

Tuning an elevator

Conformational space of the SLC23 transporter UraA
and its rational modulation by off-site mutations and
conformational-selective binders

Dissertation

zur Erlangung des Doktorgrades der Naturwissenschaften

vorgelegt beim Fachbereich 14

Biochemie, Chemie und Pharmazie

der Johann Wolfgang Goethe – Universität

in Frankfurt am Main

von

Benedikt Thomas Kuhn

aus Frankfurt

Frankfurt 2020

(D 30)

Diese Arbeit wurde vom Fachbereich Biochemie, Chemie und Pharmazie der Johann Wolfgang Goethe-Universität als Dissertation angenommen.

Dekan: Prof. Dr. Prof. Dr. Clemens Glaubitz

1. Gutachter: Prof. Dr. Klaas Martinus Pos

2. Gutachter: Prof. Dr. Volker Dötsch

Datum der Disputation:

Contents

Zusammenfassung.....	VII
Summary	XIII
1 Introduction.....	1
1.1 Transport across biological membranes	1
1.2 Secondary active transport	2
1.3 Solute carrier (SLC)	2
1.4 Superfamilies of secondary active transport.....	3
1.5 Elevator transporters	5
1.5.1 The SLC23 family.....	8
1.5.2 The 7-transmembrane segment inverted repeat fold	10
1.5.3 The uracil/H ⁺ symporter UraA from <i>E. coli</i>	14
1.6 Nanobodies	15
1.6.1 Nanobodies in structural biology	16
1.6.2 Synthetic nanobodies (sybodies).....	18
1.7 Aim of the thesis.....	19
2 Materials.....	21
2.1 Equipment	21
2.2 Chemicals.....	22
2.3 Consumables	24
2.4 Bacterial strains and Phages.....	25
2.5 Enzymes and antibodies.....	25
2.6 Commercially available Kits.....	25
2.7 Plasmids.....	26
2.8 Oligonucleotides.....	26
2.9 Liquid media and cultivation plates	27

2.10	Buffers	28
3	Methods	29
3.1	Methods in Biology.....	29
3.1.1	Alpaca immunization.....	29
3.2	Methods in Microbiology	30
3.2.1	Chemically competent <i>E. coli</i> cells	30
3.2.2	Transformation of chemically competent <i>E. coli</i> cells.....	30
3.2.3	Selection of <i>E. coli</i> transformants on LB-agar plates.....	30
3.2.4	Glycerol stock preparation	31
3.2.5	Production of M13KO7 helper phages	31
3.2.6	Production of M13 phages for phage display	32
3.2.7	Phage quantification.....	32
3.2.8	Radioisotope whole cell transport assay.....	33
3.3	Molecular biological methods.....	34
3.3.1	Site-directed mutagenesis.....	34
3.3.2	FX-cloning of PCR products into pINIT_cat.....	35
3.3.3	Plasmid preparation and sequencing of pINIT_cat	36
3.3.4	Plasmid preparation and sequencing of pDX plasmid.....	36
3.3.5	Sub-cloning of inserts from pINIT_cat into pBX expression vectors	36
3.3.6	Cloning of nanobody sequences from pDX to pSb_init.....	36
3.4	Methods in Biochemistry	37
3.4.1	SDS-polyacrylamide gel electrophoresis (SDS-PAGE).....	37
3.4.2	Coomassie staining.....	37
3.4.3	In-gel GFP fluorescence	38
3.4.4	Western blotting	38
3.4.5	Production and purification of UraA variants	38
3.4.6	Reconstitution of UraA _{WT} into proteoliposomes.....	40
3.4.7	<i>In vitro</i> biotinylation of AVI-tag containing UraA variants	40
3.4.8	PEG-5000 maleimide labeling of UraA antigens.....	40
3.4.9	Crosslinking of UraA _{L80C-M143C}	41
3.4.10	Biopanning.....	41
3.4.11	Enzyme linked immunosorbent assay	42
3.4.12	Selection of synthetic nanobodies against UraA _{WT}	43
3.4.13	Production and purification of nanobodies and sybodies	43
3.4.14	Preparation of UraA-GFP inside-out vesicles	44
3.4.15	Pulldown of nanobodies and sybodies by inside-out vesicles	44

3.4.16	Melting curve analysis by FSEC.....	45
3.4.17	Differential scanning fluorimetry	45
3.4.18	Cysteine accessibility assay	46
3.4.19	Co-crystallization of UraA with sybodies.....	46
3.4.20	Scintillation proximity assay	47
3.5	Biophysical methods.....	48
3.5.1	X-ray diffraction data collection and processing.....	48
3.5.2	Hydrogen-deuterium exchange mass spectrometry.....	48
4	Results	49
4.1	Conformation specific binder selection	49
4.1.1	Alpaca immunization	50
4.1.2	Phage display selection	51
4.1.3	Temperature dependent ELISA	55
4.1.4	Selection of sybodies against UraA	57
4.2	Nanobody characterization	59
4.2.1	Thermal stabilization of UraA _{WT} by selected binders	60
4.2.2	Transport inhibition reveals epitope of binders.....	63
4.2.3	Conformation mapping of binders	65
4.3	Conformational modulation of UraA.....	69
4.3.1	Identification and manipulation of conformational hinges in UraA	70
4.3.2	Functional analysis of inter-domain linker variants in UraA	72
4.3.3	Biochemical characterization of UraA _{G112P} , UraA _{G320P} and UraA _{P330G}	74
4.3.4	Substrate binding site accessibility in UraA _{G320P} and UraA _{P330G}	77
4.3.5	Uracil affinity of UraA _{WT} and UraA _{G320P}	79
4.4	Co-crystallization of UraA.....	80
4.4.1	Co-crystallization of UraA with Sy45	80
4.4.2	Co-crystallization of UraA _{G320P} with Sy5	82
4.4.3	Collection and processing of the UraA _{G320P} -Sy45 datasets.....	83
4.5	UraA-Sy45 co-crystal structure.....	83
4.5.1	Molecular replacement and refinement of UraA _{G320P} -Sy45	83
4.5.2	Crystal structure of UraA _{G320P} in complex with Sy45	86
4.5.3	The inward-facing cavity of UraA	90
4.5.4	The epitope of Sy45.....	90
4.5.5	Crystal contacts	92
4.5.6	Conformational transition from inward-facing to occluded in UraA	94
4.5.7	Structural alignment of UraA _{G320P} -Sy45 and UapA	96

4.6	The conformational space of UraA.....	96
4.6.1	Uracil dependent differential HDX-MS.....	97
4.6.2	Differential HDX-MS of UraA _{G320P} and UraA _{P330G}	102
4.6.3	Conformational space of UraA in DSF	105
4.6.4	Conformational thermostabilization of UraA.....	108
5	Discussion.....	110
5.1	Nanobody selection.....	110
5.1.1	Strategies and experiences.....	110
5.1.2	Conformation mapping	113
5.1.3	Nanobody and Sybody comparison.....	115
5.2	Co-crystallization of UraA.....	117
5.3	UraA-Sy45 crystal structure.....	118
5.3.1	Conformational transition from inward-facing to occluded in UraA	118
5.3.2	The substrate binding site of UraA.....	121
5.3.3	The inward-facing cavity of 7-TMIR proteins	123
5.4	Alpha-helical inter-domain linkers in UraA	126
5.4.1	UraA _{G320P}	126
5.4.2	UraA _{P330G}	130
5.4.3	Functional impact of inter-domain linkers on elevator transport in UraA.....	132
5.4.4	The oligomeric state of UraA _{G320P} and UraA _{P330G}	134
5.5	Conformational Thermostabilization	135
5.6	The conformational space of UraA in solution.....	139
5.7	Concluding remarks and outlook	141
	Supplementary information	143
	References.....	158
	List of abbreviations	170
	Declaration of collaborative work.....	173
	List of publications.....	175
	Acknowledgements	176

Zusammenfassung

Solute carrier proteine (SLCs) sind sekundär aktive Transportproteine im Menschen. Sie sind verantwortlich für vielfältige Transportaktivitäten über die Zellmembran, die zur Aufrechterhaltung des Ionenhaushalts, des Metabolismus und vielen anderen lebensnotwendigen Prozessen im menschlichen Körper dienen. Aufgrund der diversen Transportvorgänge sind nach aktuellem Stand 65 Familien von SLCs klassifiziert, basierend auf der jeweiligen Transportaktivität. Mitglieder einer Familie zeigen dabei eine Übereinstimmung der Proteinsequenz von mindestens 20%. Die große Bedeutung von SLCs für den Organismus geht einher mit Krankheiten im Falle von Dysfunktion der Transporter durch Variationen der Proteinsequenz jedoch auch mit pharmakologischen Therapieansätzen basierend auf den SLCs. Darüber hinaus stellen SLCs potenzielle Transportsysteme für pharmakologische Wirkstoffe im menschlichen Körper dar und können die Bioverfügbarkeit von Wirkstoffen durch deren Transport erhöhen sowie die zelltypspezifische Wirkstoffverteilung im Körper verbessern. Letzteres ist beispielsweise besonders bedeutsam in der Krebstherapie, wobei sich die vermehrte Präsenz einiger SLCs im Tumorgewebe zunutze gemacht werden könnte.

Strukturbiologische Ergebnisse der letzten Dekade zeigten eine Übereinstimmung der Proteinstruktur der SLC Familien 4, 23 und 26 bezüglich der Transmembrandomänen. Diese neuartige Faltung basierend auf 14 Transmembransegmenten (TM), die in zwei Proteindomänen organisiert sind, wurde *7-transmembrane segment inverted repeat* (7-TMIR) Proteinfaltung genannt. Dies beruht auf den zwei Wiederholungseinheiten, bestehend aus jeweils 7 Transmembransegmenten, die durch Inversion einer der beiden Wiederholungseinheiten zur Deckung gebracht werden können. Die Strukturanalyse verschiedener 7-TMIR Proteine in unterschiedlichen Proteinkonformationen deutete auf einen *elevator* Transportmechanismus für 7-TMIR Proteine hin. Dieser Mechanismus wurde zuvor bereits für Mitglieder anderer SLC Familien festgestellt, die sich strukturell jedoch von

den 7-TMIR Proteinen unterscheiden und deshalb auch von funktionalen Unterschieden ausgegangen werden muss. Dabei ist der *elevator* Mechanismus grundsätzlich durch eine starre Architektur einer der beiden Proteindomänen charakterisiert, die fest in der Membran verankert ist, wobei sich die zweite Domäne orthogonal zur Membranebene bewegen kann und dadurch den Transportvorgang von einer Seite der Membran zur anderen vollführt. Diese Bewegung, ähnlich eines Fahrstuhls (im englischen *elevator*), ist namensgebend für den Transportmechanismus. Nicht nur in 7-TMIR Proteinen, sondern auch in anderen *elevator* Transportproteinen, konnten alpha-helikale Verbindungselemente zwischen den beiden Proteindomänen identifiziert werden, für die aufgrund ihrer Lokalisation in Kombination mit der orthogonalen Transportbewegung ein Einfluss auf die Funktionalität zu erwarten ist. Allerdings wurde die mechanistische Bedeutung dieser alpha-helikalen Verbindungselemente bislang für keine Gruppe von *elevator* Proteinen untersucht. Die SLC Familien 4, 23 und 26 zeigen trotz der strukturellen Gemeinsamkeit Unterschiede in der Substratspezifität, sodass SLC4 Proteine als Hydrogencarbonat-Transporter, SLC23 als Ascorbinsäure-Transporter und SLC26 als Anionenaustauscher klassifiziert wurden.

Eine Erweiterung des Verständnisses von Struktur und Funktion der SLC23 Familie war das Ziel dieser Arbeit. Erzielte Forschungsergebnisse bezüglich des Transportmechanismus sind darüber hinaus, aufgrund der zuvor beschriebenen strukturellen Übereinstimmung, auch für die SLC Familien 4 und 26 von Bedeutung. Als Basis diente dafür das SLC23 Modelprotein UraA aus dem gram-negativen Bakterium *Escherichia coli*, dessen Proteinstruktur bereits in zwei Proteinkonformationen gelöst werden konnte und somit für detaillierte mechanistische Untersuchungen bestens geeignet war. Dabei wurden zwei Strategien parallel verfolgt. Zum einen wurden zwei Alpakas mit UraA immunisiert, um sogenannte *nanobodies*, die variablen Domänen von Einzeldomänen-Antikörpern gegen UraA zu selektieren. Die vorteilhaften Eigenschaften von *nanobodies* für die konformationsspezifische Stabilisierung von Proteinen sind besonders für die Proteinkristallographie geeignet und wurden im Rahmen dieser Arbeit für die Strukturanalyse von UraA genutzt. Darüber hinaus konnten konformationsspezifische *nanobodies* in dieser Arbeit auch zur Analyse der Proteindynamik verwendet werden. Zur Erweiterung der *nanobody* Diversität wurden zusätzlich zu den *nanobodies* auch synthetische *nanobodies* (*sybodies*) verwendet.

Die zweite Strategie zur mechanistischen Erforschung von UraA beruhte auf den bereits erwähnten alpha-helikalen Verbindungselementen zwischen den beiden Proteindomänen, deren funktionale Bedeutung ungeklärt ist. Strukturanalyse von verschiedenen *elevator* Transportproteinen und Vergleich der Torsionswinkel beider UraA-Strukturen im Bereich der Verbindungselemente deutete drauf hin, dass der Aminosäurerest Glycin an den Übergängen von *inter-domain linker* und *core* Domäne für die notwendige strukturelle Flexibilität verantwortlich sein könnte und ein molekulares Scharnier für den Transportmechanismus darstellt. Im Gegensatz dazu wurden Prolin-Reste am Übergang von *inter-domain linker* und *gate* Domäne identifiziert, was eine rigide Struktur erzeugt, die zur Stabilisierung der Transportbewegung dienen könnte. Diese Hypothesen wurden im Laufe der Arbeit experimentell untersucht, wobei zunächst ortsspezifische Mutagenese der Glycin-beziehungsweise Prolin-Reste durchgeführt wurde und danach die Transportaktivität der Mutanten mittels Transportexperimenten von radioaktiv markiertem uracil, dem natürlichen Substrat von UraA, ermittelt wurde. Dabei zeigte sich, dass der Aminosäureaustausch von jeweils einem Glycin-Rest im periplasmatischen als auch im cytoplasmatischen *inter-domain linker* gegen einen Prolin-Rest zum Verlust der Transportaktivität führt. Die erfolgreiche Proteinproduktion für das Transportexperiment zeigte zudem den direkten Zusammenhang zwischen dem Glycin zu Prolin Aminosäureaustausch und dem Transportverlust. Der Austausch der beiden Prolin-Reste am Übergang zur *gate* Domäne gegen Glycin-Reste resultierte ebenfalls im Transportverlust, jedoch wurde die UraA Variante P121G aus dem cytoplasmatischen Verbindungselement nicht exprimiert, sodass keine Aussage über den funktionellen Einfluss dieser Variante getroffen werden konnte. Die Bedeutung dieser Position für die allgemeine Proteinstabilität wurde jedoch indirekt durch deren Fehlproduktion aufgezeigt. Die drei erfolgreich produzierten UraA-Varianten G112P, G320P und P330G wurden zur weiteren biochemischen Analyse rekombinant produziert und gereinigt, wobei in der Größenausschlusschromatographie eine erhöhte Dimerisierung von UraA_{G320P} im Vergleich zum Wildtyp und eine vollständige Dimerisierung von UraA_{P330G} festgestellt wurde. UraA_{G112P} hingegen zeigte keine Veränderung des oligomeren Zustands. UraA_{G320P} und UraA_{P330G} zeigten zudem eine Erhöhung der Schmelztemperatur um 10 °C sowie die Fähigkeit uracil zu binden, sodass ein trivialer Ursprung des Transportverlusts in beiden UraA-Varianten ausgeschlossen werden konnte. Mittels eines cystein-spezifischen Fluoreszenzmarkers, dessen kovalente Bindung an einen eingefügten Cystein-Rest in der Substratbindestelle von

UraA kinetisch verfolgt wurde, konnte eine reduzierte Öffnungswahrscheinlichkeit der Substratbindestelle für beide UraA Varianten festgestellt werden. Basierend auf diesen Ergebnissen wurde eine Veränderung des konformationellen Raumes beider UraA-Varianten als Ursache für den Verlust der Transportaktivität angenommen. Zur endgültigen Bestätigung dieser Hypothese wurde die Proteindynamik beider UraA-Varianten und die des Wildtyps mittels differenziellem Wasserstoff-Deuterium-Austausch untersucht. Die Ergebnisse zeigten ebenfalls Änderungen im konformationellen Gleichgewicht beider UraA-Varianten jedoch auch signifikante Unterschiede zwischen beiden UraA-Varianten. So konnte für UraA_{G320P} ein Konformationsraum mit größerer Präferenz für die geschlossene Konformation festgestellt werden, wobei die Population der einwärtsgerichtete Konformation ebenfalls beobachtet werden konnte. Erstere wurde jedoch bei Zugabe von Uracil vermehrt beobachtet. Einen ähnlichen Effekt von Uracil wurde auch für den Wildtyp beobachtet. Für UraA_{P330G} war ein viel geringerer Effekt nach Zugabe von Uracil zu beobachten und eine größere Eingeschränktheit des Konformationsraums, was auch in der Schmelzpunktanalyse mit ansteigenden Uracilkonzentrationen beobachtet wurde. Für UraA_{P330G} ist daher eine überwiegend geschlossene Konformation festgestellt worden, die womöglich nur geringfügig für die beobachtete Substratbindung verändert wird. Die UraA Variante G320P wurde daher für die Kristallstrukturanalyse in Kombination mit konformationsspezifischen *nanobodies* bevorzugt, da der erhöhte Schmelzpunkt einen größeren Erfolg versprach und die UraA Variante als nicht vollständig arretiert befunden wurde, sodass die *nanobodies* unterschiedliche Konformationen stabilisieren konnten. Dabei konnten Proteinkristalle von UraA_{G320P} in Kombination mit dem sybody Sy45 als auch mit Sy5 erhalten werden. Hingegen der beiden publizierten UraA Kristallstrukturen wurde für die Kristallisation mit UraA_{G320P} und den sybodies keine Zugabe von Uracil für eine ausreichende Probenhomogenität benötigt.

Die UraA_{G320P}-Sy45 Kristallstruktur konnte mit einer Auflösung von 3.1 Å gelöst werden und zeigte eine einwärtsgerichtete Konformation, die sich jedoch von der bereits publizierten UraA-Struktur in derselben Konformation stark unterscheidet. Die deutliche Verschiebung der Transmembransegmente 6 und 7 in der publizierten Struktur, die bislang eine genaue Analyse der Konformationsänderung von einwärtsgerichtet nach geschlossen erschwerte, ist in der von Sy45 stabilisierten einwärtsgerichteten Struktur nicht zu beobachten. Im Gegenteil ist die *gate* Domäne sehr ähnlich zu jener aus der publizierten geschlossenen Struktur, wodurch die besagte Konformationsänderung nun analysiert werden konnte. Daraus wurde deutlich, dass

die Translation der *core* Domäne von einwärtsgerichtet nach geschlossen anhand einer 17° Rotation um eine Rotationsachse parallelverlaufend zu den Transmembransegmenten 5 und 12 beschrieben werden kann, ohne großen Beitrag der *gate* Domäne. Die Übergänge von *core* Domäne zu *inter-domain linker* wurden dabei als Scharniere für die Translation identifiziert. Anhand der Konformationsänderung konnte der Einfluss der beiden Aminosäure-Substitutionen G320P und P330G und deren Auswirkungen auf die Transportaktivität untersucht werden. Dabei wurde deutlich, dass G320P die Torsionswinkel der Position 320 und des vorangehenden Aminosäurerest Val-319 beeinflusst, sodass eine verlangsamte Kinetik für die Konformationsänderung hin zur auswärtsgerichteten Konformation aufgrund von geometrischen oder sterischen Gründen angenommen werden kann. Für die Position P330G wurde deutlich, dass die lokal rigide Struktur notwendig ist, um die Translation der *core* Domäne und des *inter-domain linkers* mechanisch an die *gate* Domäne zu koppeln, um die relative Translation beider Domänen zu erzielen. Die Aufweichung dieser mechanischen Kopplung durch Austausch des Prolin-Rests gegen den flexiblen Glycin-Rest resultiert folgerichtig in dem beobachteten, stark verringerten Konformationsraum mit geringer Proteindynamik. Die Auswirkungen beider UraA-Varianten auf den Konformationsraum konnten auch anhand unterschiedlicher Schmerlzpunktverschiebungen durch konformationsspezifische *nanobodies* oder *sybodies* beobachtet werden.

Diese Arbeit beschäftigt sich darüber hinaus mit Strategien zur konformationsspezifischen oder epitop-gerichteten Selektion von *nanobodies* und präsentiert eine Selektionspipeline zur Identifikation von *nanobodies* mit identischer und unterschiedlicher Konformationspezifität, die auf einer Kombination von Epitopkartierung und gleichzeitiger Bindung zweier unterschiedlicher *nanobodies* beruht. Im Falle von gleichzeitiger Bindung kann für beide *nanobodies* eine gemeinsam stabilisierte Konformation und unterschiedliche Epitope festgestellt werden. Im Falle von Konkurrenz der *nanobodies* werden Informationen der Epitopkartierung herangezogen, um sterische von konformationeller Konkurrenz zu unterscheiden. Dieses Verfahren führte zur Selektion von Sy45 und Sy5 zur Stabilisierung zweier unterschiedlicher Konformationen und reduzierte die Anzahl an Proben für die Kristallisation.

Die oben beschriebenen Ergebnisse zur Proteindynamik in UraA und den beiden UraA-Varianten in Kombination mit den konformationsspezifischen *nanobodies* und *sybodies* erlaubten zudem eine Korrelationsanalyse der Thermostabilisierung von UraA und dessen

Konformationsfreiheit. Zusammen mit Ergebnissen aus der Literatur konnte dadurch eine direkte Korrelation der beiden festgestellt werden und somit das Konzept der konformationellen Thermostabilisierung erstellt werden.

Summary

Solute carrier (SLC) are related to various diseases in human and promising pharmaceutical targets but more structural and functional information on SLCs is required to expand their use for drug design and therapy. The 7-transmembrane segment inverted (7-TMIR) fold was identified for the SLC families 4, 23 and 26 in the last decade thus detailed analysis of the structure function relationship of one of these families might also yield insights for the other two. SVCT1 and SVCT2 from the SLC23 family are sodium dependent ascorbic acid transporters in human but structural analysis of the SLC23 family is exclusively based on two homologs – UraA from *E. coli* and UapA from *A. nidulans* – yielding two inward-facing and one occluded conformation. In combination with outward-facing conformations from SLC4 transporters, and additional information from the SLC26 family, an elevator transport mechanism for all 7-TMIR proteins was identified but detailed mechanistic features of the transport remain elusive due to the lack of multiple conformations from individual transporters.

To increase the understanding of 7-TMIR protein structure and function in this study, the transport mechanism of SLC23 transporters was analyzed by two strategies including selection of alpaca derived nanobodies and synthetic nanobodies against UraA as prokaryotic model protein of the SLC23 family. The second strategy involved mutagenesis of UraA at functional relevant positions regarding the conformational change during transport. Therefore, available structures of 7-TMIR proteins and less related elevator transporters were analyzed and a common motif identified – the alpha helical inter-domain linkers. The proposed rigid body movement for transport in combination with the characteristic alpha helical secondary structure of the linkers connecting both rigid bodies led to the hypothesis of functional relevance of the linkers and a conformational hinge being located in close proximity to the linkers. These positions were identified and used to modulate the biophysical properties of the transporter. Mutagenesis at three relevant positions led to loss of transport functionality

and these UraA variants could be recombinantly produced and purified to further examine the underlying mechanistic effects. The variants UraA_{G320P} and UraA_{P330G} from the periplasmic inter-domain linker showed increased dimerization and thermal stability as well as substrate binding in solution. The substrate affinity of UraA_{G320P} was identified to be 5-fold higher compared to the wildtype. The solvent accessibility of the substrate binding site in UraA_{G320P} and UraA_{P330G} revealed reduced open probability that indicated an altered conformational space compared to UraA_{WT}. This phenomenon was analyzed in more detail by differential hydrogen-deuterium exchange mass spectrometry and the results supported the hypothesis of a reduced open probability and gave further insights into the impact of the two mutations in the periplasmic inter-domain linker in UraA.

This thesis further presents strategies for phage display selection of nanobodies with epitope bias and a post selection analysis pipeline to identify nanobodies with desired binding characteristics. Thereby, whole cell transport inhibition highlighted periplasmic epitope binders and conformational selectivity. A cytoplasmic epitope could be identified by pulldown with inside-out membrane vesicles for one cytoplasmic side binder. Thermal stabilization analysis of the target protein in differential scanning fluorometry was performed in presence of two different nanobodies to identify simultaneous binding by additional thermal stabilization respectively competition by intermediate melting temperatures. Combination of epitope information with simultaneous DSF could be used to identify the stabilization of different UraA conformations by a set of binders and presents a general nanobody selection strategy for other SLCs. Synthetic nanobodies (sybodies) were also included in the analysis pipeline and Sy45 identified as promising candidate for co-crystallization that gave rise to UraA_{WT} crystals in several conditions in presence or absence of uracil. Similar crystals could be obtained in combination with UraA_{G320P} that were further optimized to gain structural information on this mutant. The structure was solved by molecular replacement and the model refined at 3.1 Å resolution confirming the cytoplasmic epitope of Sy45 as predicted by the selection pipeline. The stabilized conformation was inward-facing similar to the reported UapA structure but significantly different to the previously reported inward-facing structure of UraA. The structure further confirmed the structural integrity of the UraA mutant G320P. Despite the monomeric state of UraA in the structure, the gate domain aligned reasonably well with the gate domain of the previously published dimeric UraA structure in the occluded conformation and allowed detailed analysis of the conformational transition in UraA from

inward-facing to occluded by a single rigid body movement. Thereby little movement in the gate domain of UraA was observed in contrast to a previously reported transport mechanism. Core domain rotation around a rotation axis parallel to the substrate barrier was found to explain the major part of conformational transition from inward-facing to occluded and experimentally supported the hypothesized mechanism by Chang et al. (2017). Additionally, the conformational hinge around position G320 in UraA could be identified as well as the impact of the backbone rigidity introduced by the highly conserved proline residue at position 330 in UraA on the conformational transition. This position was found to serve as anchoring point the inter-domain linker and determines the coordinated movement of inter-domain linker and core domain. The functional analysis further highlighted the requirement of alpha helical secondary structure within the inter-domain linker that serves as amphipathic structural entity that can adjust to changed core-gate domain distances and angles during transport by extension/compression or bending while preserving the rigid linkage.

The applied strategies to modulate the conformational space of UraA by mutagenesis at the hinge positions in the inter-domain linkers is transferrable to other transporters and might facilitate their structural and functional characterization.

Further, this study discusses the conformational thermostabilization of UraA that is based on increased melting temperatures upon restriction of its conformational freedom. The term 'conformational thermostabilization' introduced by Serrano-Vega et al. (2007) could be experimentally supported and the direct correlation between the conformational freedom and thermostabilization was qualitatively analyzed for UraA. The concept of conformational thermostabilization might help in characterization of other dynamic transport systems as well.

1 Introduction

1.1 Transport across biological membranes

Biological membranes are a major prerequisite for life. They define cell boundaries and allow compartmentation within cells, both essential for evolution of higher organisms. The membrane is composed of amphiphilic phospholipids that self-assemble in aqueous solution due to the hydrophobic effect to form a bilayer with the polar head groups being in contact with the aqueous solution and burying the hydrophobic acyl chains in the middle of the bilayer. This architecture is responsible for the semi-permeable character of biological membranes which prevents free diffusion of solutes over the membrane. In order to maintain cell homeostasis, transport of ions and metabolites across the membrane is necessary and a variety of proteins evolved that enable the passage of solutes over the membrane and that are categorized according to their working mechanism.

Channels, pores and passive carrier allow passive transport over membranes in the direction of the concentration gradient. Thus, no energy is required for transport but the generation of concentration gradients is not achieved by these transport proteins. This process requires consumption of energy and cells use transport proteins that couple energy consumption to the transport event for this purpose. ATP-binding cassette transporters and ATPases use ATP hydrolysis, the universal energy source in biological systems, for transport catalysis. Due to the direct coupling of transport and ATP hydrolysis, these transporters are called primary active. In this way, metabolites and nutrients are transported in both directions over the

membrane depending on the transporter's mechanism but irrespective of the solute concentration gradient. Therefore, primary active transporters are also used to build-up electrochemical gradients over the membrane such as proton or sodium ion gradients that are essential for life and the semi-permeability of the biological membrane allows to maintain these gradients.

1.2 Secondary active transport

The electrochemical gradients over membranes built-up by primary active transport systems serve as indirect energy source for secondary active transport systems. Due to the indirect coupling of ATP hydrolysis and transport this process is called secondary active. The energy stored in electrochemical gradients is consumed by secondary active transporters by transporting one substrate along its gradient – the co-substrate – and the transport mechanism of the transporter allows coupling of a second solute being transported against its gradient to the first process. Thereby, several mechanisms exist depending on the transport direction of the individual substrates with symporters transporting the substrates in the same direction and antiporters in opposing directions. The concept of alternating access was developed decades ago by Jardetzky (1966) to explain these transport mechanisms suggesting the transporter to alternate between open conformations that allow substrate binding or release from one site of the membrane to the substrate binding site of the transporter while being inaccessible from the other site. The classical model used conformational change of the transporter for transport while the substrate remains bound to the substrate binding site of the transporter. Substrate and co-substrate bind at distinct binding sites and simultaneously in symporters while the transported substrate is replaced by the co-substrate in antiporters in case of a shared binding site. As symporters often use proton or sodium ion gradients to couple transport, the respective co-substrate is also known as coupling ion in these cases.

1.3 Solute carrier (SLC)

Secondary active transporters and passive uniporters in human are classified in 65 distinct solute carrier (SLC) families with over 400 human genes in total (Hediger et al., 2018). The classification is based on transport function rather than on sequence homology (Schumann et al., 2020) though a minimal sequence identity of 20-25% is required within a distinct SLC family

(Hediger et al., 2004). SLCs transport a broad range of important substrates such as amino and fatty acids, inorganic ions, neurotransmitters, nucleotides, purines, sugars, vitamins and drugs (Hediger et al., 2004). Consequently, a significant number of 82 SLCs are related to human diseases (Schumann et al., 2020) whereas Mendelian diseases result from gene polymorphism of SLCs and cause for example inflammatory bowel disease, gout, jaundice, Rotor syndrome, diabetes, bladder or breast cancer and hypertension. 20% of identified SLC mutations were related to Mendelian diseases (Lin et al., 2015) but only 13 SLC families are targeted by drugs that are SLC5 (type-II diabetes), SLC6 (epilepsy), SLC9 (hypertension), SLC12 (diuresis), SLC18 (Huntington's disease), SLC22 (gout), SLC25 (osteoporosis), SLC29 (vasodilator) and SLC65 (hypercholesterolemia; Rask-Andersen et al., 2013; Wang et al., 2019). Hence, SLCs seem to be understudied compared to other protein families such as the nuclear receptors or GPCRs. However, the pharmacological potential of SLC exceeds the treatment of diseases presented above as SLCs are potential drug transporters that could improve the bioavailability of certain drugs and the expression profile of SLCs in different cell types could be exploited for cell type-specific drug delivery for example in treating tumor cells (Nakanishi et al., 2011).

1.4 Superfamilies of secondary active transport

Secondary active transporters are often specific regarding their substrates resulting in a large variety of individual transporters that evolved to catalyze different transport reactions that are required in biological systems. Though relatively low sequence similarity, transporters that evolved from a common ancestor share the same protein fold or similar structural features that are used to categorize the transporters. The major facilitator superfamily (MFS) is the largest of secondary active transporter superfamilies with 80 distinct families. In the model organism *E. coli*, 25% of all transporters are members of the MFS (Bosshart et al., 2019) with 70 individual genes (Quistgaard et al., 2016). In human, 100 MFS genes are found which represents the largest clan within the solute carrier classification (Höglund et al., 2011). Some of the best studied members of the major facilitator superfamily are the lactose transporter LacY (Kaback et al., 2019) and the multidrug transporter EmrD (Yin et al., 2006) both from *E. coli* and the human glucose transporters GLUT1-4 from the SLC2 family (Yan et al., 2017). Structural analysis of MFS members revealed a 12 transmembrane segment fold built-up of four repeat units that arrange in two pseudo symmetric domains with the substrate binding site in the center of the protein (Abramson et al., 2003; Huang et al., 2003). Transport is

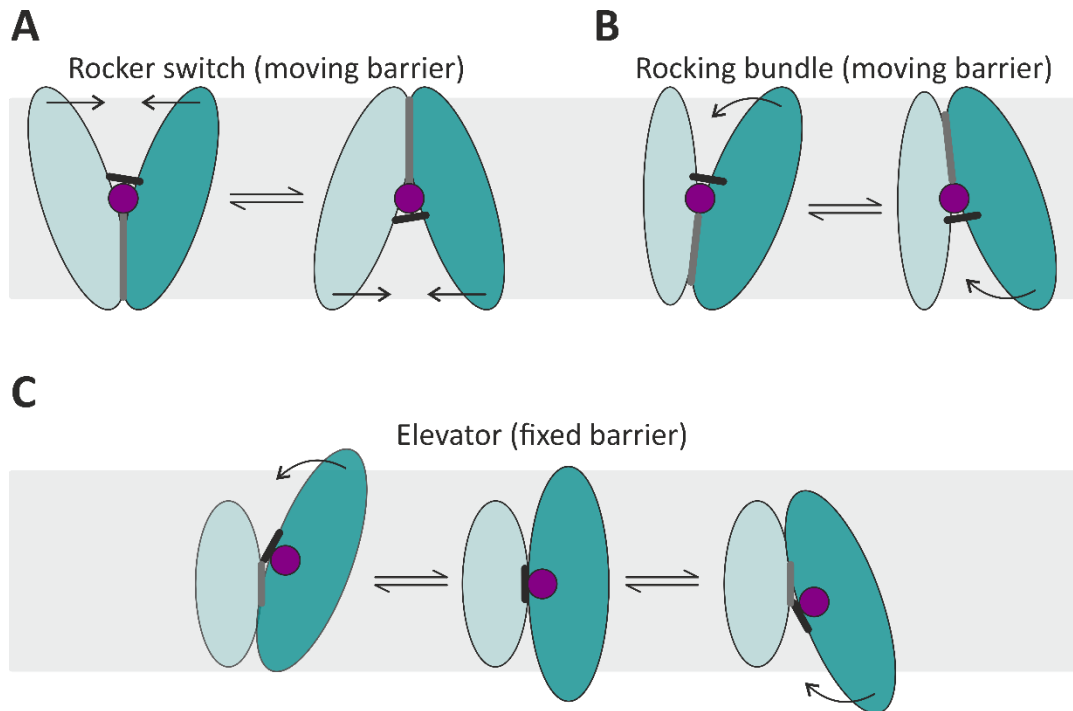


Figure 1: Transport mechanisms of secondary active transporters. The three major transport mechanisms of secondary active transport in cartoon representation adapted from Drew and Boudker (2016) with slight changes. (A) The rocker switch mechanism as found in MFS transporters with the two domains (light and dark cyan) and the sandwiched substrate in purple. The substrate barrier (grey) is moving during transport while the substrate remains at the same position with respect to the membrane. A gate is represented as black line. (B) The rocking bundle mechanism as observed for LeuT-fold proteins with similar moving barrier as for rocker switch but with asymmetric domain movement during transport. (C) Elevator mechanism as found in Glt_{Ph} . The barrier is fixed and the substrate is moved along with the transport domain. The indicated gate is not observed for all elevator transporters.

performed by the rocker switch mechanism (**Figure 1A**), a conformational change of both domains that moves the barrier for the substrate while keeping it bound at the same position and thereby allowing alternating access (Drew and Boudker 2016).

The amino acid-polyamine-organocation (APC) superfamily is the second largest following the MFS with 18 distinct families (Bosshard et al., 2019). APC members function as solute:cation symporters or solute:solute antiporters. LeuT, a leucin transporter from *A. aeolicus* is a well-studied member of the APC superfamily with a characteristic tertiary structure that served as basis for the LeuT-fold (Yamashita et al., 2005). The protein consists of 10 transmembrane segments built-up of two 5-TM inverted repeats that arrange in two domains not related by pseudosymmetry in contrast to MFS members (Shi et al., 2013). The inverted repeat topology was most likely created by gene duplication and fusion (Khafizov et al., 2010) that resulted in an ancestor protein that subsequently evolved into different transporters. Even though LeuT-fold members with monomeric activity as BetP were reported (Perez et al., 2011), the dimer or trimer, respectively, is believed to be the active form of most LeuT-fold members

(Pozoni et al., 2018). A characteristic feature of the LeuT-fold are two discontinuous transmembrane helices that build a cavity in the center of the transport domain serving as substrate binding site whereas the dipole moment of unwound helices is used for substrate binding (Screpanti et al., 2007). The conformational change of the transport domain with respect to the scaffold domain allows alternating access whereas the underlying mechanism is called rocking bundle (Drew and Boudker, 2016). In contrast to the rocker switch mechanism, only one domain, the transport domain, is undergoing a conformational change. However, both mechanisms share a moving barrier while the substrate itself is not moved during transport (**Figure 1B**).

Beside rocker switch and rocking bundle, a third mechanism exists for several transporters that is called elevator mechanism. It was first reported for Glt_{ph} , a eukaryotic glutamate transporter homologue from *P. horikoshii* (Yernool et al., 2004; Reyes et al., 2009). The mechanism involves an asymmetric conformational change of the transport domain with respect to the scaffold domain, similar to the rocking bundle mechanism, but the elevator transport features a fixed barrier and movement of the substrate around this barrier in order to allow alternating access (**Figure 1C**). The transport domain therefore moves perpendicular to the lipid bilayer like an elevator. Thus, the prerequisite for elevator transport is substrate binding performed exclusively by the transport domain to allow substrate movement around the barrier. In Glt_{ph} , substrate binding and subsequent translocation is controlled by a gate (Reyes et al., 2009) which is not found in all elevator transporters. Beside the SLC1 family with Glt_{ph} , elevator transport was also observed or suggested for SLC4, SLC9, SLC10, SLC13, SLC23, SLC26, SLC28 and additional protein families that do not belong to the SLC classification such as AbgT, 2HCT and the PTS system (Garaeva et al., 2020).

1.5 Elevator transporters

The elevator transport mechanism is relatively new compared to rocker switch and rocking bundle but more and more transporters were identified to share this mechanism and detailed analyses of several transporters e.g. Glt_{ph} , the prototype of elevator transport, increased the understanding of this transport mechanism in the past decade (**Figure 2A**). Despite the different structural architecture of known elevator transporters and the different substrate specificity ranging from inorganic ions, nucleobases, organic anions to amino acids, several

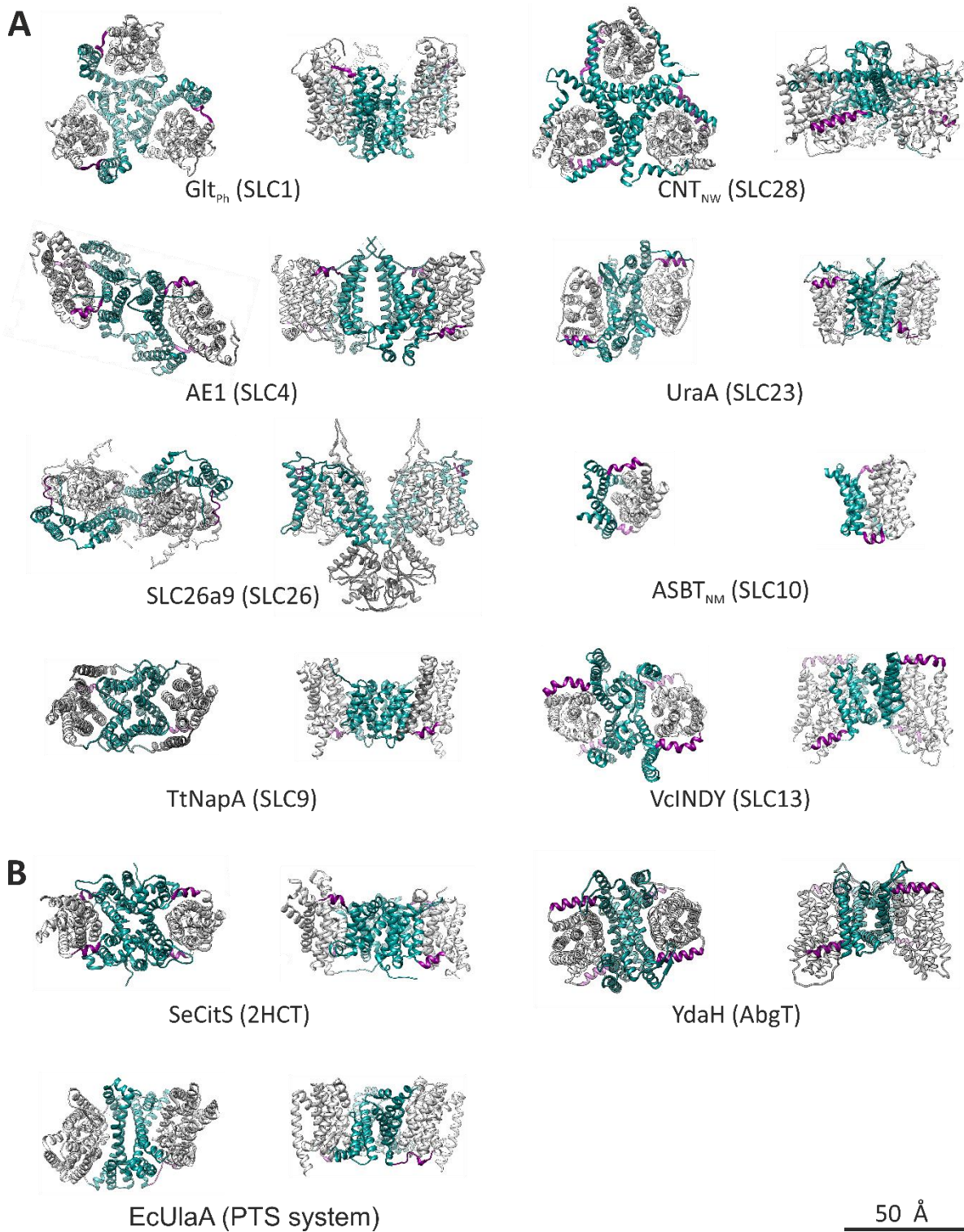


Figure 2: Elevator transporters. (A) Structures of known solute carriers with elevator transport mechanism in extracellular top view (left) and side view (right). Transport domains are shown in light grey and scaffold domains in cyan color. Additional domains or transmembrane segments are shown in dark grey. The mostly alpha helical inter-domain linkers connecting both domains are highlighted in purple. (B) Same representation as in (A) for non-SLC elevator proteins. All structures are drawn to scale. PDB codes of depicted structures and corresponding references: Glt_{ph}: 2NWL, Boudker et al., 2007; CNT_{NW}: 5L26, Hirschi et al., 2017; AE1: 4YZF, Arakawa et al., 2015; UraA: 5XLS, Yu et al., 2017; SLC26a9: 6RTC, Walter et al., 2019; ASBT_{NM}: 3ZUX, Hu et al., 2011; TtNapA: 5BZ3, Coincon et al., 2016; VciINDY: 4F35, Mancusso et al., 2012; SeCitS: 5A1S, Wöhlert et al., 2015; YdaH: 4ROC, Bolla et al., 2015; EcUlaA: 4RP8, Luo et al., 2015

structural motifs are shared by most elevator transporters. First, elevator transporters oligomerize to form dimers or trimers with the only exception being the monomeric ASBT from the SLC10 family (**Figure 2A**). The transport domains are located at the periphery with the scaffold domains forming the inter-protomer interface in the oligomeric assembly. The inter-domain interactions between scaffold and transport domain are mostly hydrophobic in nature allowing movement of the transport domain perpendicular to the membrane plane. The scaffold domains of several elevator transporters do not fully span the bilayer due to their reduced length which was observed to cause membrane thinning (Garaeva et al., 2020) and this effect might even be enhanced upon oligomerization. The physiological relevance of membrane thinning was suggested to reduce the substrate translocation path length across the membrane and thereby minimize the required elevator movement of the transport domain. Along with membrane thinning, bilayer deformations introduced by Glt_{Ph} and VcINDY were observed that could be a general feature of elevator transport and contribute as a driving force (Zhou et al., 2019).

The substrate binding site architecture varies between the members of different elevator transport families, but all fulfill the prerequisite of substrate binding exclusively performed by the transport domain. The SLC1, SLC13 and SLC28 family as well as members from 2HCT, AbgT and the PTS system feature hairpins that do not span the full bilayer and thereby build a cavity for the substrate. Conformational change of the hairpin-2 loop was further observed as part of the gating mechanism in Glt_{Ph} (Zomot et al., 2013). As alternative to hairpins, discontinuous transmembrane helices are found in transporters from the SLC4, SLC9, SLC10, SLC23 and SLC26 family that allow substrate coordination.

Beside these shared structural and functional motifs in elevator transport that are well covered in literature, an unstudied structural motif exists– the alpha helical inter-domain linker – connecting scaffold and transport domain (**Figure 2**). Due to the rigid body movement of transport domain with respect to the scaffold domain for transport, the linkage of both domains necessarily features a functional relevance. The protein structures suggest the inter-domain linker to extend the rigidity of the scaffold domain towards the transport domain in the plane of the membrane. For transporters with more than one conformation structurally analyzed e.g. SeCitS (Wöhlert et al., 2015) a change in the angle between inter-domain linker and adjacent transmembrane segment of the transport domain was observed with the special case in SeCitS being a fusion of both alpha helices resulting in an elongated TM (**Figure 2B**).

The alpha helical inter-domain linker could contribute to the conformational hinge for elevator transport as hypothesized by Chang et al., (2017). The functional role of the alpha-helical secondary structure in the inter-domain linkers is unclear.

1.5.1 The SLC23 family

The SLC23 family consists of two sodium dependent ascorbate transporters in human (SVCT1 and SVCT2), an orphan transporter (SVCT3) and a pseudo gene (SVCT4; Bürzle et al., 2013) whereas prokaryotic SLC23 homologs are nucleobase transporters. Thus, SLC23 proteins are known as nucleobase-ascorbate family (NAT) or nucleobase cation symporter 2 family (NCS2; Gournas et al., 2008). The SLC23 family (**Figure 3** and **Supplementary figure 1**) can be further subdivided in three groups, based on the transporter's substrate specificity (Bürzle et al., 2013). Xanthine/uric acid transporters in bacteria, plants and fungi, uracil transporters only found in bacteria and ascorbic acid transporters in vertebrates (de Koning et al., 2000) build the three subgroups. SLC23 members feature a signature motif (Koukaki et al., 2005; [Q/E/P]-N-x-G-x-x-x-T-[R/K/G]) whereas the first position correlates with the substrate specificity (Oliveira et al., 2018; **Figure 3**). Xanthine/uric acid transporters hold a glutamine residue at this position, uracil transporters a glutamic acid and ascorbic acid transporters a proline. As mentioned for solute carriers in general, the human SLC23 transporters SVCT1 and SVCT2 play an important role in health and disease. As humans lost the enzyme L-gulonolactone oxidase for ascorbic acid synthesis during evolution (Drouin et al., 2011), the uptake of the essential antioxidant ascorbic acid from diet and transport by SVCT1 and SVCT2 is obligatory (Padayatty et al., 2003). SVCT1 is present in epithelial tissues of kidney, intestine, liver, lung and skin (Wohlrab et al., 2017) and SVCT2 in almost every cell of the human body (Michels et al., 2013). Despite its antioxidant properties, ascorbic acid was further found to have anti-tumor effects (Gao et al., 2007) underlining its importance for human health. Consistently, dysfunction of SVCT1 or SVCT2 are related to several diseases. Scurvy is caused by absence of ascorbic acid in the diet leading to reduced hydroxylation thus instability of collagen. Scurvy was common among sailors that spend months on the open sea lacking fresh, ascorbic acid containing food. Ascorbic acid deficiency was also reported to accelerate early arteriosclerosis (Babaev et al., 2010) and dysfunction of SVCT1 or SVCT2 may lead to cellular scurvy even though ascorbic acid is present in the diet (May et al., 2011) due to impaired ascorbic acid uptake. SVCT1 was observed to have a deep impact on tissue development

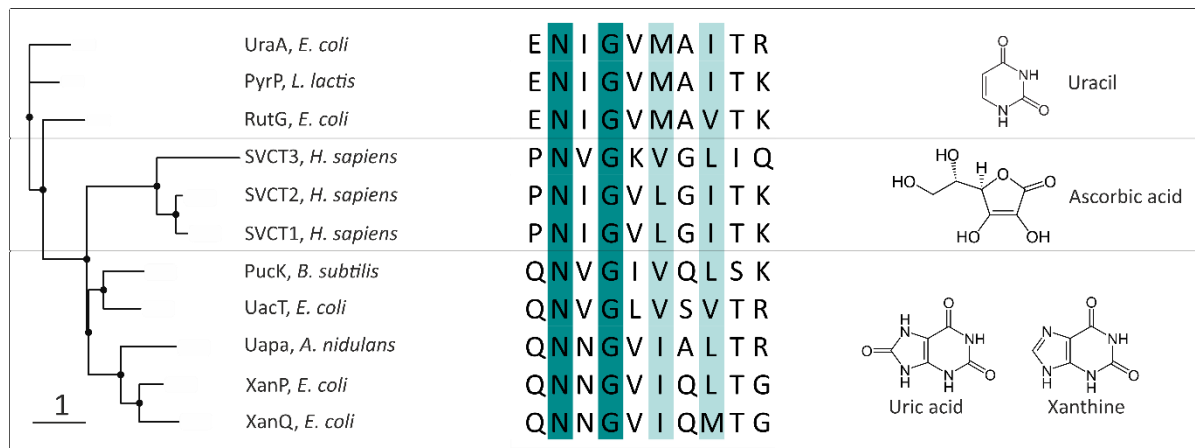


Figure 3: Diversity of the SLC23 family. (left panel) Phylogenetic tree based on sequence alignment of the three human SLC23 transporters and representative non-vertebrate SLC23 transporters covering the full SLC23 substrate spectrum. (middle panel) Selected part of the sequence alignment showing the SLC23 signature motif: [Q/E/P]-N-x-G-x-x-x-T-[R/K/G]. Sequence conservation is indicated by a color code from white to cyan. (right panel) Structural formulas of SLC23 substrates. Substrate specificity divides the SLC23 family into three groups (prokaryotic uracil transporters, vertebrate ascorbic acid transporters and uric acid/xanthine transporters found in bacteria, fungi and plants) and is correlates with the first amino acid in the signature motif. Human SVCT3 is an orphan transporter. The alignment was performed with Clustal Omega (Madeira, Park et al., 2019) and the phylogenetic tree created with NGPhylogeny (Lemoine et al., 2019).

(Zhang et al., 2018) and a variant was found to cause respiratory failure and intracerebral hemorrhage (Sotiriou et al., 2002). In addition, SVCT1 was reported to modulate the risk of Crohn's disease (Shaghghi et al., 2013) and a variant was suggested to be associated with aggressive periodontitis (de Jong et al., 2014). A variant of SVCT2 was identified to influence the gastric cancer risk (Duell et al., 2013) and a different variant caused preterm birth delivery (Erichsen et al., 2005). The pharmacological relevance of SVCT1 and SVCT2 is underlined by SVCT2 being inhibited by Diclophenac following a non-competitive mechanism (Dalpiaz et al., 2004) and their role as potential drug delivery systems. Ascorbic acid is a potential target for drug conjugation (Dalpiaz et al., 2005) for subsequent transport by SVCT1 and SVCT2 as shown for the HIV-protease inhibitor saquinavir (Luo et al., 2011). Thereby, the bioavailability of saquinavir could be improved and this strategy could be applied to other drugs.

The more complicated recombinant production of human proteins with post translational modifications led to selection of homologous SLC23 proteins. The uracil/H⁺ symporter UraA from *E. coli* (Andersen et al., 1995) and the purine/H⁺ symporter UapA from *A. nidulans* (Diallinas et al., 1989) represent the best studied homologs of the SLC23 family especially regarding structural biology. A monomeric inward-facing crystal structure of UraA with bound substrate uracil was the first high resolution structure of a SLC23 family member (Lu et al., 2011) showing the 7-transmembrane segment inverted repeat fold with in total 14

transmembrane segments (1.5.2). Beforehand the SLC23 topology was based on hydropathy plots suggesting a 12 transmembrane segment topology (Kosti et al., 2010). The dimeric inward-facing UapA structure with bound xanthine (Alguel et al., 2016) and the dimeric occluded UraA structure with bound uracil (Yu et al., 2017) highlighted the dimeric assembly of both proteins which is suggested for all SLC23 members. Both inward-facing structures of UraA and UapA respectively revealed differences regarding the gate domains while showing good structural alignment of both core domains. Despite UraA and UapA, no structural information of SLC23 members is available.

1.5.2 The 7-transmembrane segment inverted repeat fold

The 7-transmembrane segment inverted repeat (7-TMIR) fold was first identified by Lu et al. in 2011 in the crystal structure of UraA (PDB: 3QE7). The crystal structures of SLC26Dg (Geertsma et al., 2015; PDB: 5DA0) and the anion exchanger 1 (AE1; Arakawa et al., 2015; PDB: 4XZF), members from the SLC26 respectively SLC4 family, revealed that the 7-TMIR fold was not unique to the SLC23 family but also present in the two other families despite the low sequence similarity of only 15% (Chang et al., 2017). In contrast to SLC4 and SLC26, that feature additional soluble domains at the N- respectively C-terminus, both located in the cytoplasm, the SLC23 family lacks soluble domains. Thus, it is highly membrane-embedded and most compact (Chang et al., 2017).

The 7-TMIR fold consists of two repeat units each built-up of 7 transmembrane segments (**Figure 4A**). The two repeat units form a tertiary structure with two domains – core and gate (**Figure 4B**). The former consists of the first four transmembrane segments of both repeats and the gate domain of the last three TMs, respectively. Both repeat units can be structurally aligned upon inverting one repeat unit by 180° though the sequence identity between the two repeats is only about 10% (Chang et al., 2017), a phenomenon that was previously discussed for LeuT-fold transporters (Khafizov et al., 2010). The core domain features two interrupted transmembrane helices TM3 and TM10 that build a short antiparallel beta-sheet in the middle of the core domain (**Figure 5A**). The resulting cavity serves as substrate binding site based on several crystal structures with co-crystallized substrate (Lu et al., 2011; Yu et al., 2017; Alguel et al., 2016) and the partial positive charge of the interrupted alpha-helices at their N-termini, resulting from unpaired amide hydrogens, might be used for substrate coordination (Chang et al., 2017). Thereby, the discontinuous helices are not unique to the 7-TMIR fold but found in

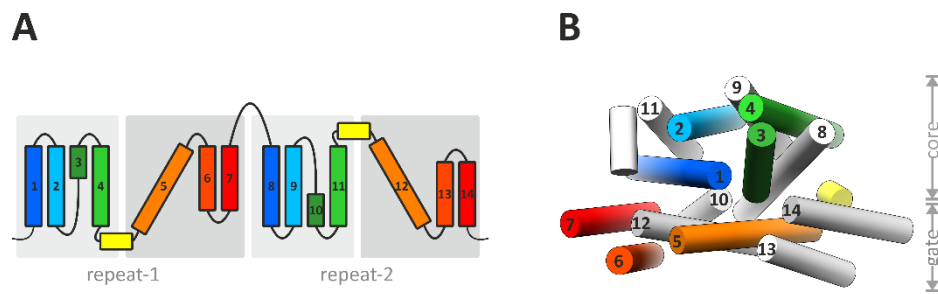


Figure 4: The 7-transmembrane segment inverted repeat fold. (A) Topology diagram of 7-TMIR proteins with 14 transmembrane segments built-up of two 7TM repeat units (TM1-TM7 and TM8-TM14) with the cytoplasmic space at the bottom. Two short alpha helical inter-domain linkers connect both domains (yellow). Both repeats are connected by a longer linker and assemble in a tertiary structure consisting of two domains – core and gate – whereas the first four TMs of each repeat belong to the core and the last three to the gate domain (B). Adapted from Chang et al. (2017) with the structure of UraA (PDB: 5XLS, Yu et al., 2017) used in (B).

several secondary active transporters (Screpanti et al., 2007). The substrate binding site formed by these discontinuous helices suggests binding and thus transport exclusively performed by the core domain which serves as transport domain. Despite the reported interaction of Tyr-342 in the gate domain of UraA with the substrate uracil (Lu et al., 2011), the gate domain is not directly involved in substrate coordination but responsible for dimerization and serves as a scaffold domain (Chang et al., 2017). Structural alignment of the core domains from AE1, UraA and SLC26Dg in three different conformations indicated the rigid body movement of the core domain during conformational transition following an elevator type mechanism (**Figure 5B**) and the reasonable structural alignment of the respective gate domains further supported the rigid body movement (**Figure 5C**). Thereby, a core domain movement of 6 Å perpendicular to the plain of the membrane was approximated (Chang et al., 2017; **Figure 5D**). This postulated displacement is significantly lower compared to Glt_{Ph} (SLC1), that was reported to move 18 Å perpendicular to the plain of the membrane (Garaeva et al., 2020). From the structural alignment, a putative transport mechanism was deduced by Chang et al. (2017) including the gate domain as static scaffold with TM5 and TM12 as substrate barrier. The core domain would rotate around an axis parallel to the barrier leading to alternating access of the substrate binding site and the inter-domain linkers connecting core and gate domain would serve as hinges for the rigid body movement. In contrast to Glt_{Ph}, the available 7-TMIR protein structures do not feature a structural gate suggesting that transport is facilitated without a gating function.

Beside the discontinuous helices that form the substrate binding site framework, several amino acid side chains were observed to be important for transport in 7-TMIR proteins especially the two substrate binding site flanking residues in TM8 and TM10 (**Figure 5B**). The

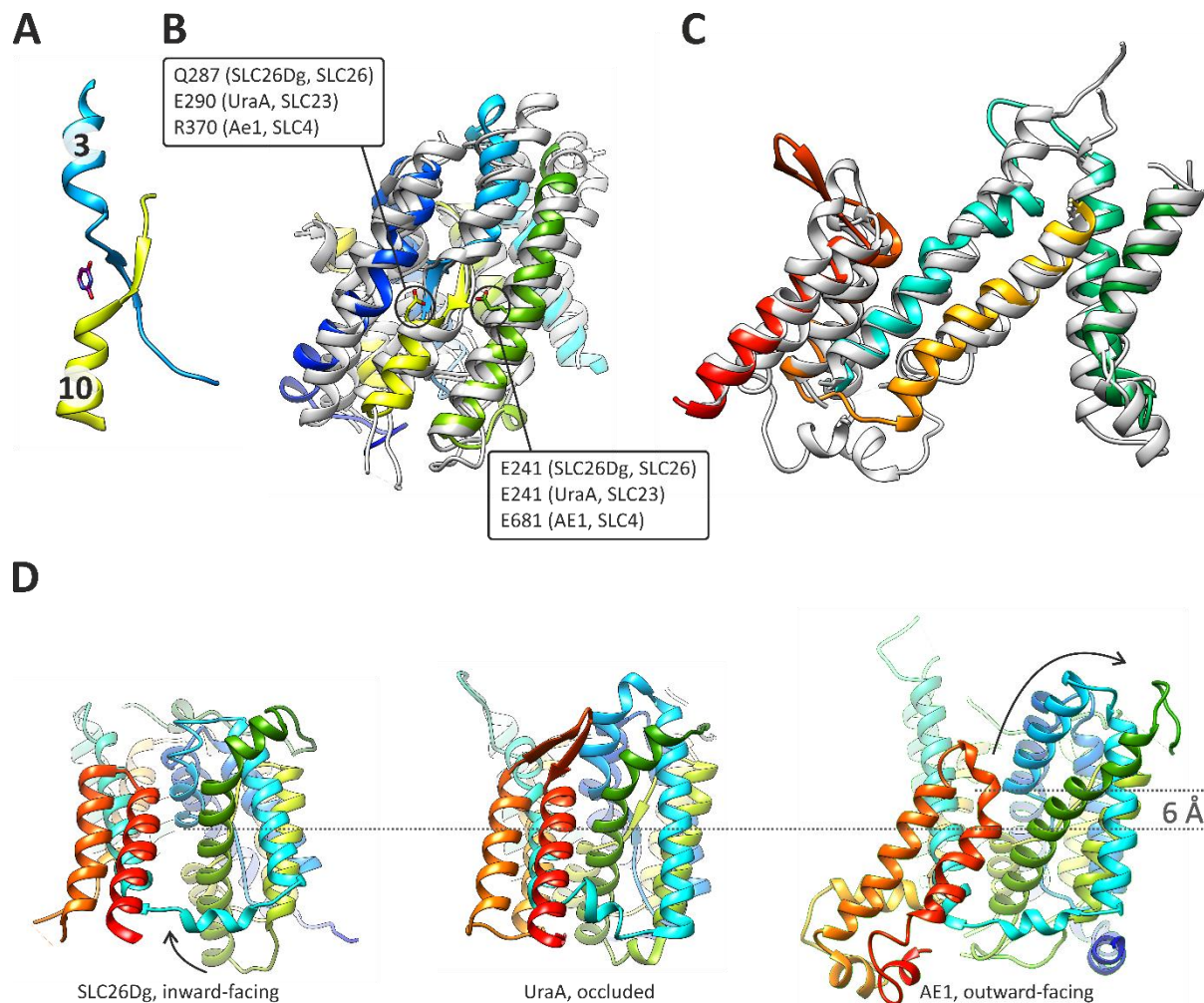


Figure 5: Substrate binding site in 7-TMIR proteins and rigid body movement. (A) Substrate binding site of UraA with bound uracil as representative for other 7-TMIR proteins. The binding site is formed by the discontinuous transmembrane segments 3 and 10 that build a short antiparallel beta-sheet in the center of the membrane. The substrate is coordinated between the N-terminal ends of the alpha helices TM3 and TM10. (B) Structural alignment of the core domain from outward-facing AE1 (SLC4; PDB: 4YZF, Arakawa et al., 2015, grey), occluded UraA (SLC23; PDB:5XLS, Yu et al., 2017, chainbow) and inward-facing SLC26Dg (SLC26; PDB: 5DA0, Geertsma et al., 2015, grey) with the two side chains involved in substrate coordination indicated with view on the gate domain facing side. (C) Structural gate domain alignment using the same structures and color code as in (B) with view on the core domain facing side. (D) Structures of inward-facing SLC26Dg, occluded UraA and outward-facing AE1 highlighting the core domain movement during transport as indicated by black arrows. Structures were aligned and drawn to scale. The substrate binding site is displaced by 6 Å during transport. Panel A, B and D were adapted from Chang et al. (2017) with slight changes.

former was shown to be important for substrate binding in UraA (Glu-241) and UapA (Glu-356) and amino acid substitution led to reduced transport activity (Lu et al., 2011; Alguel et al., 2016). This position was further suggested to be important for coupling (Chang et al., 2017). The second residue (Glu-290 in UraA) represents the first position of the presented NCS2 signature motif (**Figure 3**) and is important for substrate binding and specificity.

The domain interface of 7-TMIR proteins is mostly composed of hydrophobic residues that suggest variable, less specific inter-domain interactions during elevator transport. While the

7-TMIR fold is similar in all three SLC families (SLC4, SLC23 and SLC26), the dimerization via the gate domains and the resulting dimer interfaces are different. The SLC23 family forms the largest dimer interface with TM5, TM6, TM12 and TM13 mostly involved in dimerization (Alguel et al., 2016; Yu et al., 2017). The dimer interface of the SLC4 family is smaller with contribution of TM6 and TM12 and the TM5-TM6 and TM6-TM7 loops resulting in a less tight assembly (Arakawa et al., 2015, Thurtle-Schmidt and Stroud 2016; Coudray et al., 2016) and the dimer interface of SLC26 built-up of TM14 only (Chang et al., 2019; Walter et al., 2019) is the smallest. However, the cytoplasmic C-terminal STAS-domain was found to dimerize as well (Walter et al., 2019) suggesting reduced need for strong inter-protomer interactions via the gate domains for dimerization in SLC26 compared to SLC4 and SLC23. The dimer interface variation between the three families points towards oligomerization being established at a later step in the evolution of 7-TMIR proteins. In line with this hypothesis is the impact of dimerization on transport activity that was also observed to be different between the three families. While AE1 from the SLC4 family was functional as monomer (Lindenthal and Schubert 1991), transport activity of a monomeric UraA variant was depleted (Yu et al., 2017). Thereby, additional experiments suggested that transport activity of an UraA protomer only depends on dimerization and not on the transport activity of the second protomer in the dimer. The activity of UapA was reduced by co-expression of the UapA wildtype and a non-functional UapA variant. This was interpreted as evidence for transport activity only by the UapA-wt homodimer and not by a heterodimer (Alguel et al., 2016) suggesting that activity of both protomers in the dimer is required for transport in contrast to UraA (Byrne, 2017). Dimerization in SLC26Dg was found to be functional relevant and a functional interaction between protomers in the dimer was discovered (Chang et al., 2019). Thereby the molecular mechanism underlying the functional effect of dimerization in 7-TMIR proteins is still unclear, but a gate-gate domain effect could be hypothesized. However, an indirect effect based on deformations of the bilayer upon elevator movement cannot be excluded as discussed by Holzhüter et al. (2020). Such bilayer deformations were observed for Glt_{ph} and VcINDY (Zhou et al., 2019) as well as for Glt_{tk} (Arkhipova et al., 2020).

1.5.3 The uracil/H⁺ symporter UraA from *E. coli*

The uracil/H⁺ symporter UraA from *E. coli* serves as model protein for the human SVCT1 and SVCT2 especially regarding protein crystallography for structural biology due to the straightforward protein production in large amounts in *E. coli*. The *uraA* gene was first described by Andersen et al., (1995). It was identified to code for an uracil transporter in *E. coli* by selection for uracil uptake deficiency in combination with uracil-phosphoribosyltransferase activity and cytosine uptake activity. An *uraA* mutant was identified to result in loss of uracil uptake and the transport could be successfully complemented by recombinant expression of *uraA*. The molecular weight of UraA was calculated based on the amino acid sequence to be 45 kDa but its migration on SDS-PAGE was shown to result in a band at slightly lower molecular weight (Andersen et al., 1995). Later functional analyses revealed an affinity for the substrate uracil with a K_d of 410 nM (Lu et al., 2011) respectively 143 nM (Yu et al., 2017). The Michaelis-Menten constant was determined by whole cell transport assays ranging from 210 nM (Botou et al., 2018) to 570 nM (Yu et al., 2017) and the corresponding turnover numbers can be calculated from the reported V_{max} values ranging from 0.1 to 40.9 min⁻¹, whereas the variation is probably caused by the error-prone protein quantification in whole cells. Compared to other 7-TMIR proteins, the substrate affinity of UraA appears relatively high and the turnover number low. For comparison, the K_m value of UapA for xanthine was determined to be 9 μ M (Amillis et al., 2001) and the transport rate of the AE1 is 10⁵ ions per second (Reithmeier et al., 2016). The motor protein Prestin from the SLC26 family moves with

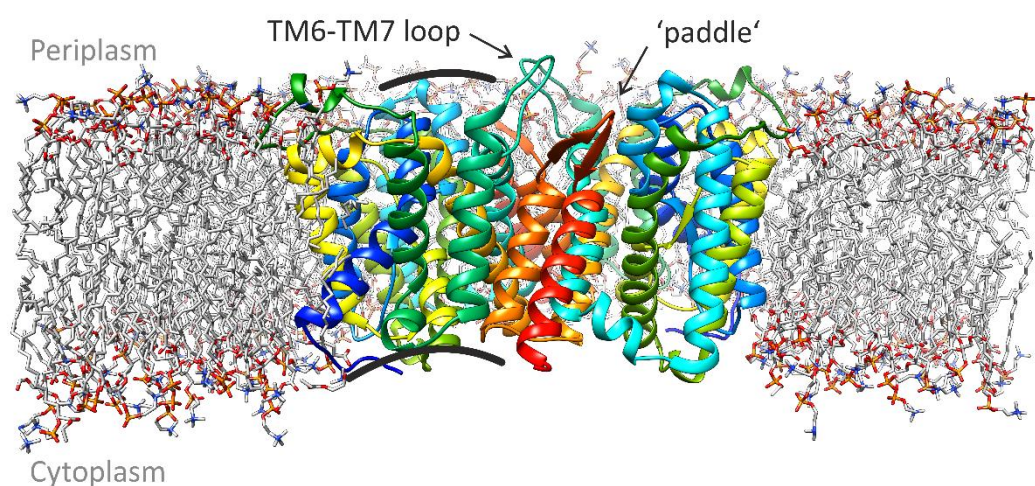


Figure 6: MemprotMD simulation of dimeric UraA. The occluded conformation of UraA with simulated DPPC bilayer (Newport et al., 2019; Yu et al., 2017). The structure is highly membrane-embedded with the periplasmic TM6-TM7 loop in contact with the aqueous solution. The TM13-TM14 loop features an antiparallel beta-sheet ('paddle') that is lying in the plain of the lipid headgroups with polar side chains pointing towards the aqueous solution and hydrophobic residues interacting with the lipid acyl chains. Membrane deformations are induced by the UraA dimer as indicated for protomer A with black lines.

a frequency of 20 kHz (Dallos and Fakler, 2002), demonstrating the functional diversity of 7-TMIR fold proteins despite the structural similarity. The structure of UraA is highly membrane-embedded (Newport et al., 2019; **Figure 6**) without additional soluble domains. It shows a unique structural feature which is an antiparallel beta-sheet in the TM13-TM14 loop lying in the interface of the lipid headgroups and their acyl chains that was not observed in other 7-TMIR protein structures. The functional relevance of the so called 'paddle' is unknown. Distortions of the lipid bilayer as mentioned above for Glt_{Ph}, Glt_{Tk} and VcINDY were also observed in the MemprotMD simulation of the dimeric, occluded UraA structure (**Figure 6**) next to TM6 and TM7 as indicated.

1.6 Nanobodies

Conventional IgG antibodies consist of two heavy and two light chains that build the typical Y-shape with the two paratopes, the antigen binding sites, at the respective ends (**Figure 7A**). Both paratopes are built-up by the variable fragments of the light and heavy chain that feature three characteristic loops in their protein fold that are responsible for antigen recognition, the complementarity determining regions (CDRs). The IgG paratope is thus distributed over two polypeptide chains which complicates the production of IgG derived binding proteins as biochemical tools. Antibody fragments (Fab or scFv) can be prepared (**Figure 7A**) either by proteolysis of IgG yielding Fab fragments or recombinant expression of fusion proteins containing a heavy and light chain connected by a linker yielding scFv. These fragments were successfully used as crystallization chaperones with individual advantages and disadvantages (Griffin et al., 2011). Heavy chain only antibodies (Hamers-Casterman et al., 1993) that are found in camelids next to conventional antibodies contain their complete paratope on a single polypeptide chain (**Figure 7B**). Similar antibodies - the IgNAR - were found in sharks (Greenberg et al., 1995). The variable domain of the heavy chain only antibodies can easily be produced as individual protein in *E. coli* and was named 'nanobody', due to the small fragment size of only 15 kDa. The superior biochemical properties such as solubility, stability, production yield and antigen affinity make nanobodies widely used tools in various applications ranging from structural biology (Steyaert et al., 2011) and imaging (Beghein et al., 2017) to diagnostic and therapy (Hu et al., 2017). Recently, two nanobodies were reported showing high binding affinity for short polypeptide tags (Virant et al., 2018; Götzke et al., 2019) that are suited for

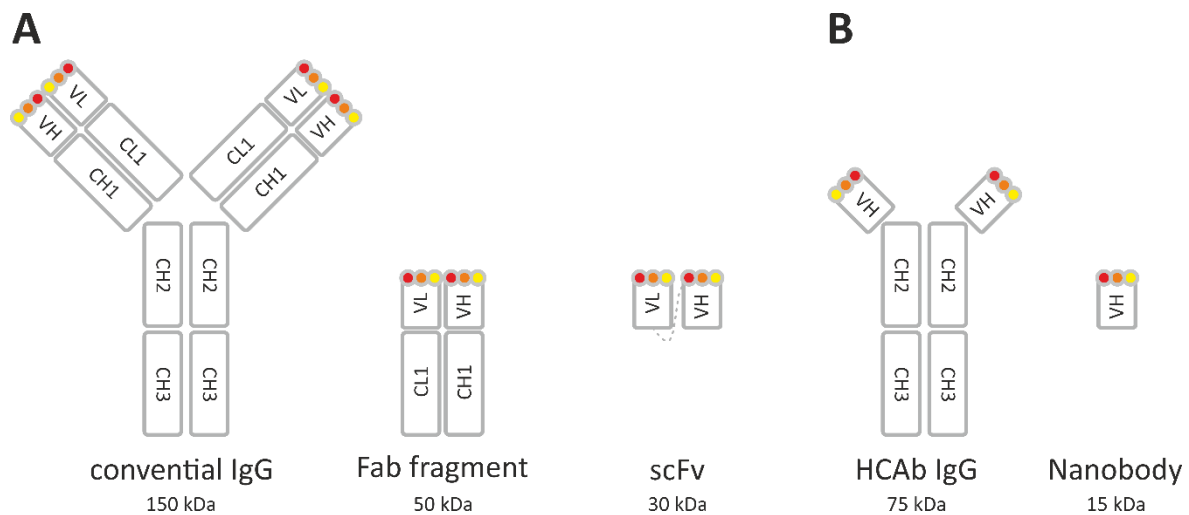


Figure 7: Conventional IgG and heavy chain only antibody. Conventional IgG, HCAb IgG and derived antibody fragments adapted from Holliger et al. (2005). The three CDRs are indicated as yellow, orange and red circles. Variable domains and constant domains are named with V and C, respectively, and the light and heavy chain with L or H. (A) Conventional IgG antibody scheme with two heavy and two light chains in the classical Y-shape with two paratopes. The derived Fab fragment contains the full paratope on two polypeptide chains and the scFv on only one chain. (B) Heavy chain only antibody from camelids (HCAb IgG) with the full paratope on a single peptide chain. The derived variable region of the heavy chain only antibody is known as nanobody.

affinity purification of target proteins and super-resolution microscopy further extending the nanobody tool kit.

The CDR3 of heavy chain only antibodies is longer compared to the CDR3 of conventional antibodies resulting in nanobody binding to protein cavities that often represent unique epitopes not detected by conventional antibodies (De Genst et al., 2005; Bannas et al., 2017). As consequence, the detected epitopes are mostly three dimensional whereas conventional antibodies often bind to linear epitopes (Forsström et al., 2015). Hence, nanobodies bind to the folded state of the target protein and cannot be used for western-blot detection but represent a valuable tool to study target proteins in their folded state in many applications.

1.6.1 Nanobodies in structural biology

Nanobodies are used as tool in structural biology for several applications. However, they are mostly known for their function as crystallization chaperones that are used in protein crystallography to improve the crystallization success. This is achieved by increasing the conformational homogeneity of the sample and in case of membrane proteins also by increasing the hydrophilic surface for specific, hydrophilic crystal contacts (Carpenter et al., 2008). The first reported crystallization chaperone in membrane protein crystallography was a Fv fragment that stabilized the Cytochrome c oxidase from *P. denitrificans* (Iwata et al.,

1995). The straightforward production of nanobodies in large amounts that are required for crystallography and their beneficial binding properties resulted in various membrane protein crystal structures with a nanobody as crystallization chaperone in the past decade. Thereby, the structures of the β 2-adrenergic receptor stabilized in native conformations by two nanobodies underlined the power of nanobodies in membrane protein crystallography (Rasmussen et al., 2011a, Rasmussen et al., 2011b). As proteins tend to crystallize in a preferred conformation, nanobodies are suited to achieve stabilization of alternative conformations in crystallization and thereby reveal the conformational space of dynamic proteins. Further, SeMet-labeled nanobodies with additionally introduced methionine residues were used to solve an RNase A nanobody co-crystal structure using the single-anomalous dispersion technique (SAD) without labeling of the target protein (Tereshko et al., 2008).

The resolution revolution in single particle cryo-EM made it the gold standard in structural biology of larger membrane proteins (Kühlbrandt 2014). A particle size below 100 kDa was the major limitation for single particle cryo-EM but recent publications reporting structures of proteins with molecular weight of 85 kDa solved at 2.7 Å or 4.2 Å resolution, respectively, (Herzik Jr. et al., 2019; Huang et al., 2020) indicated that this limitation will successively be overcome. Nanobodies are useful tools also for single particle cryo-EM regarding the conformational specific stabilization of target proteins. However, the small nanobody size prevents additional benefit regarding the particle size. To overcome this limitation, a fusion protein of nanobody and a scaffold protein HopQ from *H. pylori* was recently designed and named 'megabody' (Uchanski et al., 2019). The extension of the beta1 and beta2 strands of the nanobody into the beta-sheet of HopQ served as rigid fusion to increase the overall particle size while preventing flexible domain movements. However, the fusion was not sufficiently rigid to prevent blurring of the megabody's HopQ domain as visible in the three-dimensional model of the GABA_A β 3 receptor (Uchanski et al., 2019). Nevertheless, the developed megabody improved the structure determination by reducing the preferred orientation of particles resulting in a 2.5 Å structure of the GABA_A β 3 receptor. The second megabody generation might feature improved inter-domain rigidity based on a different scaffold or additional inter-domain linkage and thereby improve their contribution to the effective particle size.

Beside particle size and preferred orientation, a third hurdle in single particle cryo-EM exists that complicates structure solution for some proteins that is a pseudo symmetry in heterooligomeric proteins that prevents structural distinction of the individual protomers. This can be overcome by addition of a nanobody that specifically binds to one protomer of the heterooligomeric complex (Hofmann, Janulienė and Mehdipour et al., 2019) as shown for the heterodimeric ABC-transporter TmrAB from *T. thermophilus* with a conformational unselective nanobody binding to the nucleotide binding cassette of TmrB. This resulted in structural distinction of protomer A and B without affecting the conformational freedom of the transporter and allowed structural analysis of the conformational space of TmrAB in several states by single particle cryo-EM.

1.6.2 Synthetic nanobodies (sybodies)

Despite the presented advantage of nanobodies as tool, the major limitation that prevents the use of nanobodies as a routine method in every laboratory is probably the time consuming and laborious selection procedure with the major bottleneck being the immunization of a camelid. To overcome this limitation several synthetic libraries were created (Moutel et al., 2016; Ju et al., 2017; McMahon et al., 2018; Zimmermann et al., 2018). These libraries were designed for *in vitro* selection of synthetic nanobodies which accelerates the selection procedure, reduces sample consumption and avoids immunization of animals. In addition, selection conditions such as the temperature and ligand or detergent concentration can be controlled to a higher level *in vitro* making synthetic libraries a promising alternative especially for complicated target proteins such as membrane proteins. However, affinity maturation as performed by the immune system (Eisen and Siskind 1964) cannot directly be accomplished *in vitro* leaving the possibility of lower affinity binders derived from synthetic libraries. Even though *in vitro* affinity maturation could be performed in a second selection step (Wu et al., 1998) the issue could alternatively be overcome by a library diversity higher than the usually used diversity of 10^8 to 10^9 . The only reported synthetic libraries with increased diversity are the three sybody libraries with theoretical diversity of 10^{12} (Zimmermann et al., 2018). In contrast to other synthetic libraries, sybodies are based on three stable nanobody scaffolds with characteristic CDR3 architecture for shape complementarity towards different epitopes (**Figure 8**). Further, randomization was not performed throughout the whole CDRs but at

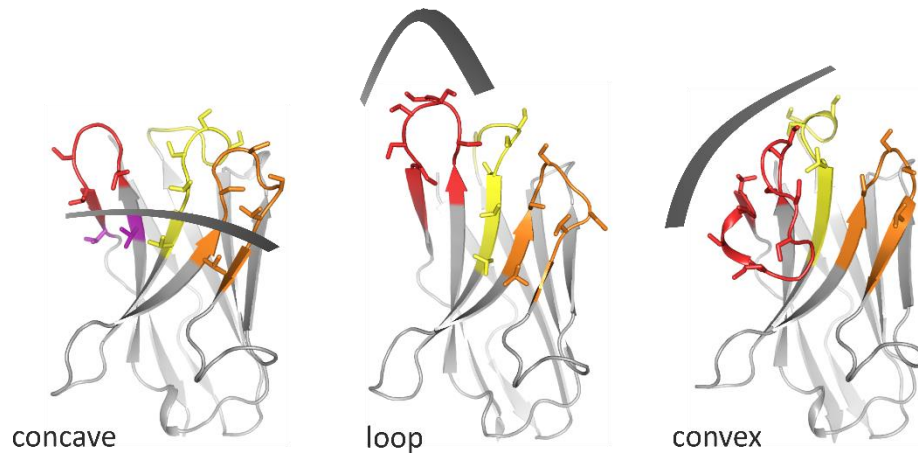


Figure 8: The three sybody libraries with defined paratope architecture. The three sybody libraries (concave, loop and convex) with defined paratopes for improved epitope shape complementarity are based on three stable nanobody scaffolds. The three CDRs from CDR1 to CDR3 are colored in yellow, orange and red. The three libraries differ in CDR3 length resulting in different paratope shapes. The figure was adapted from Zimmermann et al. (2018).

defined positions to maintain the overall fold and protein stability. Further, randomization followed a defined amino acids composition in order to exclude cysteines and enrich favorable residues for antigen binding such as tyrosine, serine or threonine. Sybodies were shown to yield binders with sufficient binding affinity (Zimmermann et al., 2018) and were successfully used as crystallization chaperones for the ABC transporter TM287/288 from *T. maritima* (Hutter et al., 2019), the ABC transporter IrtAB from *M. tuberculosis* (Arnold, Weber and Gonda et al., 2020) and the human KDEL receptor (Bräuer et al., 2019).

1.7 Aim of the thesis

The thesis aimed to improve the mechanistic understanding of SLC23 transporters on a structural and function level on the basis of the model protein UraA from *E. coli*. Though, three SLC23 crystal structures and additional 7-TMIR structures from the SLC4 and SLC26 family are reported, the elevator transport mechanism is not characterized in detail due to the lack of different conformations from an individual transporter. The mechanistic aspects underlying the transport especially the role of the alpha helical inter-domain linkers with putative hinge function are not understood. The study focused on conformational specific stabilization of UraA by a diverse set of binders for conformational arrest selected with a developed selection pipeline that groups binders with similar conformational selectivity. Second, 'off-site' mutations at identified mechanistically relevant positions were performed for functional modulation of the transporter based on the alpha helical inter-domain linkers. Both strategies

could be combined for structural characterization of UraA which resulted in an inward-facing conformation that allowed detailed analysis of the conformational transition from inward-facing to occluded. The structure gave insights into the functional relevance of the alpha helical inter-domain linkers that were further analyzed regarding their impact on the conformational space of UraA.

2 Materials

2.1 Equipment

Table 1: List of laboratory equipment

Item	Machine	Supplier
Camera	Nikon D700	Nikon GmbH
Crystal loop	Dual Thickness MicroLoops LD	MiTeGen, LLC
Crystal loop	18 mm Mounted CryoLoop	HAMPTON RESEARCH CORP.
Crystalfarm	Rigaku Gallery 700	Rigaku Corporation
Crystallization robot	Rigaku CrystalMation™	Rigaku Corporation
Extruder	LiposoFast	AVESTIN, Inc.
Fast-Prep	Fast-Prep 24	MP Biomedicals, LLC
Fermenter	NLF 30 L	Bioengineering AG
Fluorescencespectrometer	Fluorolog-3	HORIBA, Ltd.
FSEC	1260 Infinite Series	Die Agilent Technologies, Inc.
HPLC	SEC Azura P4.1S	KNAUER Wissenschaftliche Geräte GmbH
HPLC	SEC Azura UVD2.1S	KNAUER Wissenschaftliche Geräte GmbH
Imager	Image Quant Las400	GE Healthcare
Mass spectrometer	SYNAPT G2-Si	Waters GmbH
Microscope	Nikon SMZ 1500	Nikon GmbH
PCR cycler	Mastercycler ep gradient s	Eppendorf AG
Plate reader	Tecan Infinite M200	Tecan Group AG
Pressure cell homogenizer	FPG12804	Stanstedt fluid power LTD
Pressure cell homogenizer	Gaulin	APV
qPCR	Rotor-Gene Q	QIAGEN N.V.
Scintillation counter	Hidex 300SL	Hidex Deutschland Vertrieb GmbH
SEC column	Sepax SRT-10C SEC-300	Sepax Technologies, Inc.
SEC column	Superdex 200 Increase 10/300 GL	GE Healthcare

Item	Machine	Supplier
SEC column	Superdex 200 Increase 5/150 GL	GE Healthcare
SPA counter	MicroBeta Trilux 1450 LSC	PerkinElmer, Inc.
Spectrophotometer	ND-1000	Thermo Fisher Scientific Inc.
Weighing scale	Scale Quintix	Sartorius AG
Western blot	TransBlot Turbo Transfer System	Bio-Rad Laboratories, Inc.

2.2 Chemicals

Table 2: List of chemicals

Item	Supplier
[5,6- ³ H]-uracil	Hartmann Analytic GmbH
1,10-Phenanthroline monohydrate	VWR International LLC
2-Mercaptoethanol	Carl Roth GmbH + Co. KG
2-Propanol	Carl Roth GmbH + Co. KG
7-Diethylamino-3-(4'-maleimidylphenyl)-4-methylcoumarin	Sigma-Aldrich Chemie GmbH
Acetic Acid	Carl Roth GmbH + Co. KG
ADA	Carl Roth GmbH + Co. KG
Adenosin-5'-triphosphoric acid disodium salt	Carl Roth GmbH + Co. KG
AESBF hydrochloride	Carl Roth GmbH + Co. KG
Agar powder, food grade	AppliChem GmbH
Agarose	Carl Roth GmbH + Co. KG
Ammonium chloride	Carl Roth GmbH + Co. KG
Ammonium formate	Sigma-Aldrich Chemie GmbH
Ammonium peroxidsulfate	Carl Roth GmbH + Co. KG
Ammonium sulfate	Carl Roth GmbH + Co. KG
Ampicillin monosodium salt	Carl Roth GmbH + Co. KG
Benzamidine hydrochloride hydrate	Carl Roth GmbH + Co. KG
Benzamidine hydrochloride hydrate	Carl Roth GmbH + Co. KG
Bromophenolblue	Carl Roth GmbH + Co. KG
Cacodylic acid sodium salt trihydrate	Carl Roth GmbH + Co. KG
Calcium chloride dihydrate	Carl Roth GmbH + Co. KG
Chloramphenicol	Carl Roth GmbH + Co. KG
Coomassie brilliant blue R-250	Carl Roth GmbH + Co. KG
Copper sulfate	Carl Roth GmbH + Co. KG
D-(+)-Glucose	Carl Roth GmbH + Co. KG
D-Biotin	Carl Roth GmbH + Co. KG
Desoxynucleotid triphosphate mix	Thermo Fisher Scientific, Inc.
Dimethyl sulfoxide	Carl Roth GmbH + Co. KG
DL-Dithiothreitol	Carl Roth GmbH + Co. KG
Ethanol ≥ 99.8 %	Carl Roth GmbH + Co. KG
Ethanol 96 %, MEK 1%	Carl Roth GmbH + Co. KG
Ethylen glycole	Carl Roth GmbH + Co. KG
Ethylendiaminetetraacetic acid disodium salt dihydrate	Carl Roth GmbH + Co. KG
Gerbu Adjuvant FamaTM	GERBU Biotechnik GmbH

Item	Supplier
Glycerol 86 %	Carl Roth GmbH + Co. KG
Glycerol 99.5 %	Carl Roth GmbH + Co. KG
Glycine PUFFERAN \geq 99 %	Carl Roth GmbH + Co. KG
HEPES	Carl Roth GmbH + Co. KG
Heptane-1,2,3-triol	VWR International LLC
Hydrochloric acid solution 6N	Carl Roth GmbH + Co. KG
Imidazole	Carl Roth GmbH + Co. KG
IPTG	Carl Roth GmbH + Co. KG
Kanamycin sulfate	Carl Roth GmbH + Co. KG
L-(+)-Arabinose	Carl Roth GmbH + Co. KG
L-(α)-Phosphatidylcholine (PC) Soy	Sigma-Aldrich Chemie GmbH
Lithium sulfate monohydrate	Carl Roth GmbH + Co. KG
Magnesium acetate tetrahydrate	Carl Roth GmbH + Co. KG
Magnesium chloride hexahydrate	Carl Roth GmbH + Co. KG
Magnesium sulfate heptahydrate	Carl Roth GmbH + Co. KG
Manganese (II) chloride tetrahydrate	Carl Roth GmbH + Co. KG
MES	Carl Roth GmbH + Co. KG
Methanol	Carl Roth GmbH + Co. KG
Methoxypolyethylene glycol 5000 maleimide	Sigma-Aldrich Chemie GmbH
Milk powder Rapilait	Migros
MOPS	Carl Roth GmbH + Co. KG
N, N, N', N'-Tetramethylethylenediamine	Carl Roth GmbH + Co. KG
n-Decyl- β -D-maltopyranoside (DM)	GLYCON Biochemicals GmbH
n-Nonyl- β -D-glucoside (NG)	GLYCON Biochemicals GmbH
n-Octyl- β -D-glucoside (OG)	GLYCON Biochemicals GmbH
para-nitrophenylphosphate	Carl Roth GmbH + Co. KG
PEG-400	Sigma-Aldrich Chemie GmbH
PEG-8000	Sigma-Aldrich Chemie GmbH
PMSF	Carl Roth GmbH + Co. KG
p-nitrophenyl phosphate	Carl Roth GmbH + Co. KG
Potassium acetate	Carl Roth GmbH + Co. KG
Potassium chloride	Carl Roth GmbH + Co. KG
Potassium iodide	Carl Roth GmbH + Co. KG
Potassium phosphate dibasic	AppliChem GmbH
Potassium phosphate monobasic	AppliChem GmbH
Potassium sodium tartrate tetrahydrate	Carl Roth GmbH + Co. KG
Rotiphorese gel 40 (37.5:1)	Carl Roth GmbH + Co. KG
Serva DNA stain G	SERVA Electrophoresis GmbH
Sodium acetate	Carl Roth GmbH + Co. KG
Sodium chloride	Carl Roth GmbH + Co. KG
Sodium dodecyl sulfate pellets	Carl Roth GmbH + Co. KG
Sodium hydrogen carbonate	Carl Roth GmbH + Co. KG
Sodium hydroxide pellets	Carl Roth GmbH + Co. KG
Sodium phosphate dibasic	Carl Roth GmbH + Co. KG
Sodium phosphate monobasic dihydrate	Carl Roth GmbH + Co. KG
Sodium sulfate	Carl Roth GmbH + Co. KG
Thiamine	Carl Roth GmbH + Co. KG

Item	Supplier
Tris(hydroxymethyl)aminomethane	Carl Roth GmbH + Co. KG
Triton X-100	AppliChem GmbH
Trypton Biochemica	AppliChem GmbH
Tween 20	AppliChem GmbH
uracil	Carl Roth GmbH + Co. KG
Yeast extract BioChemica	AppliChem GmbH
Zinc acetate dihydrate	Carl Roth GmbH + Co. KG

2.3 Consumables

Table 3: List of consumables

Item	Supplier
Centrifuge concentrator Amicon Ultra 50 kDa MWCO 1.5 mL	Merck KGaA
Centrifuge concentrator Amicon Ultra 50 kDa MWCO 15 mL	Merck KGaA
Centrifuge concentrator Amicon Ultra 50 kDa MWCO 50 mL	Merck KGaA
Fast-Prep tube 2 mL	Bio-Rad Laboratories, Inc.
Roti-Fluoro PVDF membrane 0.2 µm	Carl Roth GmbH + Co. KG
Whatmann paper	Thermo Fisher Scientific Inc.
Syringe sterile filter 0.2 µm	VWR International LLC
Bio-Beads SM2	Bio-Rad Laboratories, Inc.
Cell disruption media 0.1 mm glass beads	Scientific Industries, Inc.
Desalting Column Econo-pac 10DG	Bio-Rad Laboratories, Inc.
Desalting Column Microspin 6	Bio-Rad Laboratories, Inc.
PeqGOLD 1 kb DNA ladder	PEQLAB Biotechnologie GmbH
SERVA Triple Color Protein Standard II	AppliChem GmbH
HisPur™ Nickel nitrilotriacetic acid resin	Thermo Fisher Scientific, Inc.
Streptavidin PVT	PerkinElmer, Inc.
400 nm pore diameter polycarbonate filter	AVESTIN, Inc.
450 nm pore diameter cellulose nitrate filter	Sartorius AG
Rotiszint Eco Plus scintillation liquid	Carl Roth GmbH + Co. KG
MRC-3 Crystallization plate	SWISSCI LTD
Maxi 48-well Crystallization plate	SWISSCI LTD
Nunc-Immuno™ MicroWell™ 96-well solid plates	Sigma-Aldrich Chemie GmbH

2.4 Bacterial strains and Phages

Table 4: List of bacterial strains and phages

Strain	Genotype
<i>E. coli</i> MC1061	F- λ - Δ (ara-leu)7697 [araD139]B/r Δ (codB-lacI)3 galK16 galE15 e14- mcrA0 relA1 rpsL150(StrR) spoT1 mcrB1 hsdR2(r-m+)
<i>E. coli</i> TG1	<i>glnV44 thi-1 Δ(lac-proAB) Δ(mcrB-hsdSM)5(rk⁻mk⁻)F' [traD36 proAB⁺ lacI^R lacZΔM15]</i>
<i>E. coli</i> DB3.1	F- <i>gyrA462 endA1 glnV44 Δ(sr1-recA) mcrB mrr hsdS20(rB-, mB-) ara14 galK2 lacY1 proA2 rpsL20(Smr) xyl5 Δleu mtl1</i>
<i>E. coli</i> JW2482	<i>lacI+rrnBT14 ΔlacZWJ16 hsdR514 ΔaraBADAH33 ΔrhaBADLD78 rph-1 Δ(araB-D)567 Δ(rhaD-B)568 ΔlacZ4787(::rrnB-3) hsdR514 rph-1 ΔuraA745::kan</i>
M13K07 helper phage	Invitrogen, ThermoFisher Scientific, Inc.

2.5 Enzymes and antibodies

Table 5: List of enzymes and antibodies

Item	Supplier
Phusion High Fidelity DNA Polymerase	New England Biolabs GmbH
Sapl	New England Biolabs GmbH
T4 ligase	Thermo Fisher Scientific, Inc.
BirA	Geertsma laboratory stock
HRV-3C protease	Geertsma laboratory stock
Lysozyme	AppliChem GmbH
DNAseI	AppliChem GmbH
Trypsin	Carl Roth GmbH + Co. KG
Anti-6-His peroxidase	F. Hoffmann-La Roche AG
Goat anti-mouse IgG alkaline phosphatase conjugate	Sigma-Aldrich Chemie GmbH

2.6 Commercially available Kits

Table 6: List of commercially available Kits

Item	Supplier
Zyppy plasmid Miniprep Kit	Zymo Research Europe GmbH
Zymoclean™ Gel DNA Recovery Kit	Zymo Research Europe GmbH
DNA Clean & Concentrator Kit	Zymo Research Europe GmbH
Immobilon Western Chemiluminescent HRP substrate	Merck KGaA

2.7 Plasmids

Table 7: Plasmids used in this study

Plasmid name	Purpose and characteristics	Reference
pINIT_cat	mutagenesis, sequencing and archiving of UraA variants	Geertsma et al. (2011)
pBXC3GH	recombinant expression of UraA variants from pBAD with C-terminal HRV-3C cleavage site, GFP fusion and 10-His-tag	Geertsma et al. (2011)
pBXCA3GH	recombinant expression of UraA variants from pBAD with C-terminal Avi-tag, HRV-3C cleavage site, GFP fusion and 10-His-tag	Geertsma et al. (2011)
pSB_init	Nanobody/Sybody sequencing, archiving and recombinant expression from pBAD with PelB leader sequence, C-terminal Myc-tag and 6-His-tag	Zimmermann et al. (2018)
pDX	Phagemid for display of proteins as M13 PIII-fusion protein. Recombinant nanobody expression from Lac promoter with PelB leader sequence, C-terminal 6-His-tag and EPEA-tag	Hofmann, Januliene, Mehdipour et al. (2019)

2.8 Oligonucleotides

Oligonucleotides used in this study as primers for PCR were purchased from Microsynth AG in genomic scale purified by desalting. The lyophilizate was dissolved to 100 μ M in ddH₂O, briefly vortexed and stored at -20 °C.

Table 8: Mutagenesis and sequencing primers used in this study.

Primer name	Primer sequence (5' to 3')
UraA mutagenesis primer:	
A31C_for	TCG CCA TGT TTG GTT GCA CCG TCC TGG TGC
A31C_rev	GCA CCA GGA CGG TGC AAC CAA ACA TGG CGA
M143C_for	CGT AGC TGC CGG TTG CGC GGG TTT ACT CC
M143C_rev	GGA GTA AAC CCG CGC AAC CGG CAG CTA CG
I252C_for	CTG GTA GTA ACG GCT AAT TGC GTC AAA AAA GAT CTG C
I252C_rev	GCA GAT CTT TTT TGA CGC AAT TAG CCG TTA CTA CCA G
G320P_for	GCT TTC CTG CGT CCC GAA ACT GGC TGC CG
G320P_rev	CGG CAG CCA GTT TCG GGA CGC AGG AAA GC
P330G_for	CTA TCC AGA TGA TCG GCT TGC CGG TGA TGG GC
P330G_rev	GCC CAT CAC CGG CAA GCC GAT CAT CTG GAT AG
G320A_for	CTT TCC TGC GTC GCT AAA CTG GCT GC
G320A_rev	GCA GCC AGT TTA GCG ACG CAG GAA AG
P330A_for	CTA TCC AGA TGA TCG CAT TGC CGG TGA TG
P330A_rev	CAT CAC CGG CAA TGC GAT CAT CTG GAT AG
K110P_for	CTT TTA TCG TGA AGC CGG CGG GGA CCG GCT G
K110P_rev	CAG CCG GTC CCC GCC GGC TTC ACG ATA AAA G
A111P_for	CTT TTA TCG TGA AGA AAC CGG GGA CCG GCT GGC TG
A111P_rev	CAG CCA GCC GGT CCC CGG TTT CTT CAC GAT AAA AG
G112P_for	TTA TCG TGA AGA AAG CGC CGA CCG GCT GGC TGG AC
G112P_rev	GTC CAG CCA GCC GGT CGG CGC TTT CTT CAC GAT AA
T113P_for	GTG AAG AAA GCG GGG CCG GGC TGG CTG GAC GTG

Primer name	Primer sequence (5' to 3')
T113P_rev	CAC GTC CAG CCA GCC CGG CCC CGC TTT CTT CAC
G114P_for	GAA GAA AGC GGG GAC CCC GTG GCT GGA CGT GCT G
G114P_rev	CAG CAC GTC CAG CCA CGG GGT CCC CGC TTT CTT C
W115P_for	GAA AGC GGG GAC CGG CCC GCT GGA CGT GCT GTT TC
W115P_rev	GAA ACA GCA CGT CCA GCG GGC CGG TCC CCG CTT TC
P121G_for	GGA CGT GCT GTT TGG CCC TGC GGC AAT GG
P121G_rev	CCA TTG CCG CAG GGC CAA ACA GCA CGT CC
C318A_for	CTA TCC TGC TTT CCG CCG TCG GTA AAC TGG
C318A_rev	CCA GTT TAC CGA CGG CGG AAA GCA GGA TAG
C61S_for	CTG TAT CTC TTC ATC TCT AAA GGG AAA ATT CCG G
C61S_rev	CCG GAA TTT TCC CTT TAG AGA TGA AGA GAT ACA G
C97S_C102S_for	CTG GGC GGC TTT ATT ATG TCC GGC GTG CTG TTC TCC CTG GTT TCT TTT ATC GTG
C97S_C102S_rev	CAC GAT AAA AGA AAC CAG GGA GAA CAG CAC GCC GGA CAT AAT AAA GCC GCC CAG
L80C_for	CCT TTA TTT CAC CGG TAT GCT TAC TGT TGC CGT TAG G
L80C_rev	CCT AAC GGC AAC AGT AAG CAT ACC GGT GAA ATA AAG G
pDX_seq_for	GAG CGG ATA ACA ATT TCA CA
pINIT_fw	GAG TAG GAC AAA TCC GC
pINIT_rev2	TGG CAG TTT ATG GCG GGG CGT
p5	ATA ATA GCT CTT CGA GTC AGN KGC ARY TSG TRG AGT CTG GGG G
p7	ATA ATA GCT CTT CCT CCG GAG ACG GTG ACC SGG GTC CCY TKG C

2.9 Liquid media and cultivation plates

Table 9: Composition of media and cultivation plates

Item	Composition
LB medium	1% tryptone (w/v), 0.5% yeast extract (w/v), 0.5% sodium chloride (w/v)
2YT medium	1.6% tryptone (w/v), 1% yeast extract (w/v), 0.5% sodium chloride (w/v)
TB medium	1.2% tryptone (w/v), 2.4% yeast extract (w/v), 0.4% glycerol (v/v), 17 mM KH ₂ PO ₄ , 72 mM K ₂ HPO ₄
LB-agar	LB medium, 1% agar (w/v)
2YT-agar	2YT medium, 1% agar (w/v)
H-top-agar	1% tryptone (w/v), 0.8% NaCl (w/v), 0.7% agar (w/v)
M9-agar	0.6% Na ₂ HPO ₄ (w/v), 0.3% KH ₂ PO ₄ (w/v), 0.05% NaCl (w/v), 0.1% NH ₄ Cl (w/v), 0.024% MgSO ₄ (w/v), 0.0022% CaCl ₂ , 0.0005% thiamine (w/v), 0.4% D-glucose (w/v), 1% agar (w/v)

2.10 Buffers

Table 10: composition of buffers used in this study.

Buffer name	Buffer composition
10x DNA sample loading dye	50% glycerol (w/v), 0.05% bromophenol blue (w/v), 100 mM EDTA
10x SDS-PAGE running buffer	246 mM Tris, 1.92 M glycine, 1% SDS (w/v)
50x TAE buffer	2 M Tris, 1 M acetic acid, 50 mM EDTA (pH 8.0)
5x SDS-PAGE sample buffer	120 mM Tris-HCl, pH 6.8, 50% glycerol (w/v), 100 mM DTT, 2% SDS (w/v), 0.1% bromophenol blue (w/v)
Alpaca immunization buffer	100 mM NaPi pH 7.2, 130 mM NaCl
Competent cells buffer-1	30 mM potassium acetate, 50 mM MnCl ₂ , 0.1 M KCl, 10 mM CaCl ₂ and 15% glycerol (w/v)
Competent cells buffer-2	10 mM Na-Mops pH 7.0, 75 mM CaCl ₂ , 10 mM KCl and 15% glycerol (v/v).
Coomassie de-staining solution	10% MeOH (v/v), 7% acetic acid (v/v)
Coomassie staining solution	0.1% Coomassie brilliant blue R-250 (w/v), 40% MeOH (v/v), 10% acetic acid (v/v)
ELISA buffer-1	PBS, 0.2% DM (w/v)
ELISA buffer-2	PBS, 0.2% DM (w/v), 0.2% milk powder (w/v)
ELISA development buffer	50 mM NaHCO ₃ pH 8.2, 50 mM MgCl ₂
FastPrep buffer	20 mM HEPES, 150 mM NaCl, 1 mM MgCl ₂ , 20 µg/mL DNaseI, 1 mM PMSF
FastPrep buffer-2	PBS, 1 mM MgCl ₂ , 20 µg/mL DNaseI and 1 mM PMSF
Nanobody elution buffer	50 mM KPi, pH 7.5, 300 mM NaCl, 300 mM Imidazole
Nanobody lysis buffer	50 mM KPi, pH 7.5, 300 mM NaCl, 1 mM MgSO ₄ , 20 µg/mL DNaseI, 1 mg/mL Lysozyme, 15 mM Imidazole, 1 mM PMSF
Nanobody size exclusion buffer	10 mM HEPES, pH 7.5, 150 mM NaCl
Nanobody wash buffer	50 mM KPi, pH 7.5, 300 mM NaCl, 50 mM Imidazole
PBS	137 mM NaCl, 2.7 mM KCl, 10 mM Na ₂ HPO ₄ , 1.8 mM KH ₂ PO ₄
PBS-G	PBS, 15% glycerol (v/v)
PBS-T	PBS, 0.1% Tween-20 (v/v)
Transport inhibition buffer	50 mM NaPi pH 6.5, 0.2 % D-glucose
Uptake buffer-1	50 mM KPi pH 7.2, 1 mM MgCl ₂
Uptake buffer-2	50 mM KPi pH 6.5, 1 mM MgCl ₂ , 0.2% D-glucose (w/v)
UraA elution buffer	20 mM HEPES pH 7.5, 150 mM NaCl, 10% Glycerol, 0.2% DM
UraA lysis buffer	50 mM KPi, pH 7.5, 150 mM NaCl, 1 mM MgSO ₄ , 20 µg/mL DNaseI, 1 mg/mL Lysozyme
UraA size exclusion buffer-1	20 mM HEPES pH 7.5, 150 mM NaCl and 0.2% DM
UraA size exclusion buffer-2	10 mM HEPES pH 7.5, 150 mM NaCl and 0.2% DM
UraA vesicle buffer	20 mM HEPES pH 7.5, 150 mM NaCl, 10% Glycerol
UraA wash buffer	20 mM HEPES pH 7.5, 150 mM NaCl, 10% Glycerol, 0.2% DM, 50 mM Imidazole
Western blot transfer buffer	48 mM Tris, 39 mM glycine, 20% MeOH (v/v)

3 Methods

3.1 Methods in Biology

3.1.1 Alpaca immunization

Alpaca immunization was performed with 100 µg UraA_{WT} proteoliposomes for the alpaca NUBIA and 100 µg DM-solubilized UraA_{WT} for OXA. Both samples were prepared in alpaca immunization buffer, mixed in a 1:1 volumetric ratio with Gerbu Adjuvant FamaTM and subcutaneously injected. The immunizations were performed four times over a period of six weeks. Blood samples were taken four days after the respective injection to monitor the immune response by ELISA with the serum used as primary antibody against immobilized DM-solubilized UraA_{WT} (3.4.11). Four days after the final antigen injection, peripheral blood lymphocytes were isolated. The RNA was purified and converted to cDNA by reverse-transcription, the repertoire amplified by PCR and nanobody genes were cloned into the phage display compatible pDX phagemid (Hofmann, Janulienė, Mehdipour et al., 2019) a derivative of pMESy4 (Pardon et al., 2014). The immune libraries resulting from the two immunized alpacas were prepared outside of this study by Katharina Holzhüter following a published protocol (Pardon et al., 2014) with slight deviations. The libraries were named OXA and NUBIA according to the animal they derived from with a maximal diversity of 2×10^8 respectively 4×10^8 .

3.2 Methods in Microbiology

3.2.1 Chemically competent *E. coli* cells

Chemically competent *E. coli* MC1061 (Casadaban et al., 1980) and *E. coli* DB3.1 (Hartley et al., 2000) were prepared as follows. 500 mL 2YT-medium were inoculated with an overnight culture to OD₆₀₀ of 0.05 and the culture was grown at 37 °C to OD₆₀₀ of 0.6 in a shaking incubator. Cells were harvested at 5,000 x g for 15 minutes and the pellet resuspended in 750 mL cold competent cells buffer-1. The cells were centrifuged at 500 x g for 15 minutes and the pellet resuspended in 75 mL cold competent cells buffer-2. Aliquots of 100 µL cell suspension were flash frozen in liquid nitrogen and stored at -80 °C.

For small scale production of competent *E. coli* BW25113 Δ *uraA* cells (Baba et al., 2006), 5 mL LB medium were inoculated with 1% overnight culture (v/v) and grown to OD₆₀₀ of 0.3 to 0.6. Aliquots of 1 mL volume were centrifuged for 30 seconds at 9,000 x g in a table-top centrifuge. The cell pellet was resuspended in 500 µL of freshly prepared 100 mM CaCl₂ and incubated on ice for 30 minutes. Cells were collected at 9,000 x g for 30 seconds and resuspended in 100 µL of 100 mM CaCl₂ and directly used for transformation.

3.2.2 Transformation of chemically competent *E. coli* cells

Transformation of chemically competent *E. coli* cells was performed by addition of 50 to 100 ng plasmid DNA to 100 µL chemically competent *E. coli* cells of the respective strain followed by 10 minutes incubation on ice. The cells were heat shocked for 45 seconds at 42 °C in a water bath and afterwards incubated for 5 minutes on ice. 400 µL LB medium were added and the cells incubated for 1 hour at 37 °C. The sample was centrifuged for 1 min at 9,000 x g, the supernatant discarded and the pellet resuspended in 200 µL fresh LB medium. The sample was plated on LB-agar plates as described below (3.2.3).

3.2.3 Selection of *E. coli* transformants on LB-agar plates

E. coli transformants were selected on LB-agar plates containing either 34 µg/mL chloramphenicol or 100 µg/mL ampicillin for selection of pINIT_{cat} respectively pBX transformants. The whole transformation sample of 200 µL volume was split in 20 and 180 µL and the two fractions were each plated on a 10 cm LB-agar plate. Plates were incubated overnight at 37 °C in an incubator. For short term storage, plates were sealed with parafilm

and stored at 4 °C and for long term storage glycerol stocks were prepared as described (3.2.4).

3.2.4 Glycerol stock preparation

For long term storage of *E. coli* strains, glycerol stocks were prepared as follows. 5 mL LB medium containing the appropriate antibiotic for selection were inoculated with a single colony from a LB-agar plate and incubated overnight at 37 °C in a shaking incubator. The overnight culture was supplemented with 20% glycerol (w/v), transferred to a cryo-tube, snap frozen in liquid nitrogen and stored at -80 °C. Glycerol stocks were used for long term storage of strains and plasmids and as starting culture for large scale protein production or whole cell transport assays.

3.2.5 Production of M13KO7 helper phages

M13KO7 helper phages were prepared for phage display selection of nanobodies. *E. coli* TG1 cells were streaked on M9-agar plates and grown at 37 °C for 48 hours. A single colony was picked and cultivated in 5 mL 2YT medium until an OD₆₀₀ of 1.0 was reached. The M13KO7 phage stock was 10-fold diluted in 2YT with a dilution series ranging from 10⁻¹ to 10⁻¹¹ and 60 µL of each dilution were used to infect 500 µL of *E. coli* TG1 cells for 10 minutes. 6 mL H-top-Agar at 37 °C was added to each sample and the sample directly poured on a 2YT-agar plate. The plates were incubated overnight at 37 °C. A plaque from the 10⁻¹⁰ dilution plate was used to infect 50 mL *E. coli* TG1 culture grown to OD₆₀₀ of 1.0 and the culture was incubated at 37 °C for 4 hours. The culture was diluted into two times 1000 mL 2YT medium and grown for 1 hour at 37 °C before the addition of 10 µg/mL Kanamycin. The cultivation was continued overnight at 37 °C. *E. coli* TG1 cells were removed from the sample by centrifugation at 6,000 x g for 25 minutes at 4 °C. Phages were precipitated from the supernatant by addition of 4% PEG-8000 and 500 mM NaCl for 90 minutes on ice and harvested by centrifugation for 30 minutes at 6,000 x g and 4 °C. The pellet was resuspended in PBS and phages precipitated with 4% PEG-8000 and 500 mM NaCl for 20 minutes on ice and harvested by centrifugation for 30 minutes at 4,000 x g and 4 °C. The phages were resuspended in PBS-G, frozen in liquid nitrogen and stored at -80 °C.

3.2.6 Production of M13 phages for phage display

The preparation of M13 phages for phage display was performed using a similar protocol as for the M13KO7 helper phages with slight changes. *E. coli* TG1 cells carrying the pDX phagemid with the OXA- respectively NUBIA-library were grown in 60 mL 2YT-Amp¹⁰⁰ medium to an OD₆₀₀ of 0.5 with an inoculum of 150-fold the size of the library in case of the OXA-library and 300-fold library size for the NUBIA-library. The cultures were infected with 400-fold excess of M13KO7 helper phages for 30 minutes at 37 °C without shaking. The *E. coli* TG1 cells were separated from the helper phages by centrifugation for 10 minutes at 3,000 x g and resuspended in 2YT-Amp¹⁰⁰-Kan²⁵ and cultivated overnight at 37 °C for phage production. Phages displaying nanobodies from the OXA or NUBIA-library, respectively, were further purified as described for the helper phages (3.2.5).

3.2.7 Phage quantification

M13 phages displaying nanobodies from the OXA- and NUBIA-library and M13KO7 helper phages were quantified spectrophotometrically and by colony assay. For the first the absorbance at 269 nm and 320 nm was measured and the concentration of virions calculated according to Sambrook and Russel (2001; **Equation 1**).

$$\text{virions/mL} = \frac{(A_{269} - A_{320}) \cdot 6 \times 10^{16}}{\text{number of bases/virion}} \quad (1)$$

Phage quantification by the colony assay was performed by infection of log phase *E. coli* TG1 with 10-fold dilutions of the respective phage stock. After 30 minutes incubation, the number of infected cells in each sample was analyzed by spotting 5 µL culture on LB-Agar-Amp¹⁰⁰ plates for M13 phage quantification respectively LB-Agar-Kan⁵⁰ for M13KO7 phage quantification. The plate was incubated overnight at 37 °C and the number of colonies was estimated and corrected by the dilution factor of the phage stock to quantify the colony forming units (**Supplementary figure 2** and **Supplementary figure 3**). The spectrophotometric quantification generally yielded 2 to 5-fold higher phage concentration compared to the colony assay indicating that not all isolated phages were infectious.

3.2.8 Radioisotope whole cell transport assay

3.2.8.1 Radioisotope whole cell transport in *E. coli* BW25113 Δ *uraA*

Radioactive transport was performed in *E. coli* BW25113 Δ *uraA* from the Keio collection (Baba et al., 2006). Chemically competent cells were transformed with the pBXC3GH plasmid carrying the sequence of the respective UraA variant. 10 mL TB-Amp¹⁰⁰/Kan⁵⁰, 1 mM MgCl₂ were inoculated with 100 μ L from an overnight culture and grown at 37 °C to an OD₆₀₀ of 1.0 to 1.5. Gene expression was induced by addition of 10⁻⁴% L-arabinose (w/v) and cultivation continued for one hour. Cells were collected at 2,500 x g and 4 °C for 10 minutes, the supernatant discarded and the pellet resuspended in 10 mL uptake buffer-1 and stored on ice overnight. The cells were collected for 10 minutes at 2,500 x g and 4 °C and resuspended in uptake buffer-2 to an optical density at 600 nm of 24.

The whole cell transport was performed as follows. 180 μ L uptake buffer at 25 °C were supplemented with 10 μ L cell suspension and stirred for 2 minutes at 25 °C for cell energization. To start the transport, 10 μ L substrate mix in uptake buffer were added and transport was allowed for 30 seconds. Afterwards, 100 μ L reaction mix were immediately quenched by diluting in 2 mL ice cold uptake buffer-2, filtered and washed with additional 2 mL buffer. The dried filters were dissolved in 4 mL Rotiszint®eco plus scintillation liquid overnight and the next day scintillation counting was performed for 1 minute per sample using a Hidex 300SL (Hidex).

The successful protein production in the cells used for radioisotope whole cell transport was controlled by SDS-PAGE and subsequent in-gel fluorescence of the whole cell lysates to detect the UraA-GFP fusion protein. Therefore, 400 μ L of the prepared cell suspension were centrifuged for 5 minutes at 17,000 x g and the cell pellet frozen and stored at -20 °C until further use. The pellet was thawed and resuspended in 200 μ L FastPrep buffer and the cell suspension transferred to a FastPrep tube containing 300 mg glass beads. Cell lysis was performed by 2 times 20 seconds FastPrep with 4 m/s² at room temperature using a FastPrep-24 (M.P. Biomedicals). The samples were cooled on ice for 5 minutes between the lysis cycles. 12.8 μ L cell lysate were mixed with 4 μ L 5x SDS-PAGE sample buffer and 3.2 μ L 10% SDS (w/v) and 5 μ L sample were loaded on 12% SDS-PAGE (3.4.1) and subsequently analyzed by in-gel fluorescence detection of the UraA-GFP fusion protein (3.4.3).

3.2.8.2 Transport inhibition in *E. coli* MC1061

Transport inhibition of UraA induced by nanobody or sybody binding was performed in whole cells using the endogenous UraA in combination with recombinantly expressed nanobodies and sybodies. *E. coli* MC1061 carrying the pSb_init plasmid with the respective binder sequence (Zimmermann et al., 2018) served as strain for transport inhibition analysis while *E. coli* BW25113 Δ uraA carrying pSb_init with a control nanobody served as a negative control. Cells were grown in 10 mL TB-Cam³⁴ containing 1 mM MgCl₂ for 3 hours at 37 °C. Expression was induced by addition of 0.01% L-arabinose (w/v) and cultivation continued at 37 °C for 1 hour. Cells were collected at 2,500 x g and 4 °C for 10 minutes, washed two times with uptake inhibition buffer and the cell density was adjusted to an OD₆₀₀ of 1.2. The radioactive transport experiment was performed with 450 μ L cell suspension pre-incubated in a water bath at 30 °C for 2 minutes and started by addition of 4.5 μ L of 1 μ M ³H-uracil. At different timepoints 100 μ L were taken from the sample and immediately quenched in ice cold transport inhibition buffer, filtered and washed with another 2 mL buffer. The filters were dried, dissolved in 4 mL ROTISZINT®eco plus and the samples stored overnight at room temperature. The radioactive uptake was determined by scintillation counting for 1 minute.

Nanobody and sybody production in the cells used for radioisotope transport was verified by SDS-PAGE (3.4.1) and subsequent western blot analysis (3.4.4). Cells from 1 mL cell suspension were collected by centrifugation for 5 minutes at 17,000 x g and the pellet resuspended in 100 μ L FastPrep buffer-2. Cells were supplemented with 300 mg glass beads and treated as described before (3.2.8.1). Cell debris and glass beads were removed by centrifugation for 10 minutes at 17,000 x g and the supernatant supplied with 5x SDS-PAGE sample buffer. 10 μ L of each sample were loaded on a 15% SDS-PAGE, run at 140 V for 75 minutes and the gel used for subsequent western blotting (3.4.4).

3.3 Molecular biological methods

3.3.1 Site-directed mutagenesis

Mutations in the *uraA* sequence were introduced by a megaprimer PCR approach (Barik 1993) using QuickChange primers designed by the web-based tool PrimerX and synthesized by the Microsynth AG. The first PCR reactions (reaction 1; **Table 11** and **Table 12**) were performed

with the pINIT_for primer in combination with the reverse QuickChange primer (reaction A) or the pINIT_rev primer in combination with the forward QuickChange primer (reaction B) to create megaprimers with complementary overhangs that were combined and amplified in a second PCR (reaction 2; **Table 11** and **Table 12**). For the second PCR only pINIT_for and pINIT_rev were used as primers. Both PCR reactions use the touchdown protocol to decrease side products derived from unspecific priming (Don et al., 1991). Primer and side products were removed from the PCR products after the second PCR by preparative TAE-agarose gel electrophoresis using 1% TAE-agarose containing 1.4% SERVA DNA Stain G. The PCR product with the approximate size of 1500 base pairs corresponding to the UraA gene was cut out from gel and further purified by using the Zyppy gel extraction kit according to the manufacturer's instructions. The concentration of the purified PCR product was determined spectrophotometrically and the insert cloned into the plasmid pINIT_cat by FX-cloning (3.3.2; Geertsma et al., 2011).

Table 11: Composition of megaprimer touchdown PCR reaction 1 and 2 for site directed mutagenesis

compound	amount (reaction 1)	amount (reaction 2)
DNA template	1 ng	1 μ L of each product from reaction 1
Phusion DNA polymerase	0.5 μ L	0.5 μ L
5x HF Phusion buffer	10 μ L	10 μ L
dNTPs (10 mM)	1 μ L	1 μ L
for primer (5 μ M)	5 μ L	5 μ L
rev primer (5 μ M)	5 μ L	5 μ L
ddH ₂ O	to 50 μ L	to 50 μ L

Table 12: Thermocycling protocol for megaprimer touchdown PCR reaction 1 and 2

step	temperature	time (reaction 1)	time (reaction 2)
initial melting	98 °C	3 minutes	3 minutes
melting	98 °C	15 sec	15 sec
annealing	63 °C (-0.5 °C/cycle)	30 sec	30 sec
elongation	72 °C	30 sec	60 sec
melting	98 °C	15 sec	15 sec
annealing	56 °C	30 sec	30 sec
elongation	72 °C	30 sec	60 sec
final elongation	72 °C	10 min	10 min

} 14 cycles
} 14 cycles

3.3.2 FX-cloning of PCR products into pINIT_cat

FX-cloning was performed according to the protocol described in Marino et al., (2017). In short, 50 ng pINIT_cat plasmid and 5-fold molar excess of purified PCR product were digested with 10 units Sapl restriction enzyme for 1 hour at 37 °C in a volume of 10 μ L. After 20 minutes

heat inactivation of Sapl at 65 °C, 0.5 µL (2.5 Weiss units) T4 DNA ligase and 1 mM ATP were added and the sample incubated for 1 hour at room temperature. After heat inactivation, 5 µL sample were transformed into chemically competent *E. coli* MC1061 cells and selected on LB-agar plates containing 34 µg/ml chloramphenicol (3.2.2; 3.2.3).

3.3.3 Plasmid preparation and sequencing of pINIT_cat

A single colony from a LB-agar selection plate was picked and cultivated overnight at 37 °C in LB-Amp-Cam³⁴. Cells were collected by centrifugation at 3,000 x g for 5 minutes in a table-top centrifuge and resuspended to 600 µL in ddH₂O. Plasmid DNA was prepped by using the Zippy plasmid Miniprep kit according to the manufacturer's instructions. The concentration of plasmid DNA was determined spectrophotometrically and 0.8 to 2 µg plasmid DNA with 30 pmol pINIT_for respectively pINIT_rev primer used for sanger sequencing performed by Microsynth AG. Resulting sequences were controlled by sequence alignment with the UraA_{WT} sequence and correct inserts sub-cloned into expression vectors as described below.

3.3.4 Plasmid preparation and sequencing of pDX plasmid

Plasmid preparation of pDX plasmids carrying a nanobody sequence was performed as described (3.3.3) from a 5 mL 2YT-Amp¹⁰⁰ overnight culture. The sample for sequencing was prepared with 0.8 to 2 µg pDX plasmid with 30 pmol pDX_seq_for primer.

3.3.5 Sub-cloning of inserts from pINIT_cat into pBX expression vectors

For sub-cloning of inserts from pINIT_cat into the expression vectors pBXC3GH and pBXCA3GH, 250 ng pINIT_cat carrying the insert and 50 ng pBX expression vector were digested with 10 units Sapl restriction enzyme and ligated with T4 DNA ligase as described (3.3.2). The product was transformed into chemically competent cells of the desired *E. coli* strain and transformants selected on LB-agar-Amp¹⁰⁰ plates (3.2.2; 3.2.3).

3.3.6 Cloning of nanobody sequences from pDX to pSb_init

The inserts of nanobodies selected by phage display were transferred from the pDX to pSb_init plasmid by PCR amplification using the p5 and p7 as forward and reverse primer, respectively, with a touchdown PCR protocol as presented (**Table 11** and **Table 12**). PCR products were

purified using the Zymoclean Gel DNA Recovery Kit and the eluted PCR fragments cloned into pSb_init as described (3.3.2).

3.4 Methods in Biochemistry

3.4.1 SDS-polyacrylamide gel electrophoresis (SDS-PAGE)

SDS-polyacrylamide gels were prepared with either 12% or 15% acrylamide (v/v), 375 mM Tris pH 8.8, 0.1% SDS (w/v), 0.1% APS (w/v) and 6.6 mM TEMED for electrophoresis of UraA respectively nanobodies. The stacking gel containing 5% acrylamide (v/v) was prepared with 125 mM Tris pH 6.5, 0.1% SDS (w/v), 0.1% APS (w/v) and 6.6 mM TEMED as depicted (**Table 13**). Gels were casted in a Mini-PROTEAN Tetra Handcast System (BioRad) and electrophoresis performed in a Mini-PROTEAN Tetra Vertical electrophoresis cell (BioRad) at 140 V for 75 to 90 minutes. The SERVA triple color protein standard II was used as protein standard. After SDS-PAGE, gels were washed in ddH₂O and further analyzed by Coomassie staining, in-gel fluorescence or western blotting.

Table 13: SDS-Polyacrylamide gel pipetting scheme

Compound	resolving gel Volume (mL)	stacking gel Volume (mL)
30 % acrylamide (v/v)	8 (12%), 10 (15%)	1.67 (5%)
1.5 M Tris pH 8.8	5	-
1.0 M Tris pH 6.8	-	1.25
10 % SDS (w/v)	0.2	0.1
10 % APS (w/v)	0.2	0.1
TEMED	0.02	0.01
ddH ₂ O to final volume	20	10

3.4.2 Coomassie staining

Coomassie staining of polyacrylamide gels after SDS-PAGE was performed by overnight incubation of the gel in Coomassie staining solution at room temperature on a rocking platform. The gel was subsequently de-stained by incubation in Coomassie de-staining solution until background signals were removed. The Coomassie de-staining solution was exchanged several times when necessary. The Coomassie stained gel was imaged using the Image Quant Las4000 (GE Healthcare) in trans illumination mode with an exposure time of 1 second.

3.4.3 In-gel GFP fluorescence

In-gel fluorescence detection of UraA-GFP fusion proteins after SDS-PAGE was performed with the Image Quant Las4000 (GE Healthcare) at an excitation wavelength of 460 nm in combination with the Y515 filter. An exponential time series of exposure times from 1 second to 8 minutes was performed. The SERVA triple color protein standard II fluorescence was recorded by excitation at 630 nm in combination with the R670BP filter and both images were digitally combined.

3.4.4 Western blotting

The polyvinylidene difluoride (PVDF) membrane was activated in methanol, washed in ddH₂O and transfer buffer. Two filter papers were soaked in transfer buffer and the western blot sandwich consisting of filter paper-1, PVDF membrane, SDS-gel and filter paper-2 constructed in the blotting chamber. Air bubbles were removed by careful rolling over the sandwich using a teflon roller. Western blotting was performed at 25 V and 100 mA for 30 minutes in the Trans-Blot Turbo Transfer System (BioRad). After transfer, the PVDF membrane was blocked overnight at 4 °C in PBS-T containing 2.5% milk powder (w/v). The membrane was washed in PBS-T to remove blocking solution and transferred to a plastic bag containing 4 mL PBS-T and 0.05 units Anti-His6-Peroxidase conjugate and incubated for 1 hour at room temperature on a rocking platform. The western blot was washed three times in 100 mL PBS-T for 5 minutes and subsequently developed by addition of 500 µL luminol and 500 µL hydrogen peroxide solution from the Immobilon Western HRP Substrate kit. Chemiluminescence was recorded with the Image Quant Las4000 (GE Healthcare) using an exponential time series from 1 second to 8 minutes of exposure.

3.4.5 Production and purification of UraA variants

UraA_{WT} and UraA variants were produced in a fermenter (Bioengineering) with 9 L TB medium containing 100 µg/mL ampicillin and 1 mM MgSO₄. Fermentation was induced by addition of 90 mL TB overnight culture of *E. coli* MC1061 pBXC3GH-UraA_{WT} or a UraA variant. UraA variants with C-terminal Avi-tag were produced from the pBXCA3GH plasmid. The cells were cultivated at 37 °C with 1.5 bar overpressure, a flow rate of 30 L per minute and 300 rpm stirring. When cells reached an OD₆₀₀ of 1.5, the temperature was stepwise lowered within one hour to 25 °C and afterwards expression under the regulation of the pBAD promoter

induced by addition of 0.01% L-arabinose (w/v; Guzmán et al., 1995). Cells were cultivated overnight at 25 °C and harvested next day for 15 minutes at 5,500 x g and 4 °C. The pellet was resuspended to a final volume of 400 mL in UraA lysis buffer and the sample stirred at 4 °C for 1 hour. PMSF was added to the sample to a final concentration of 1 mM and cells were lysed by a Menton-Gaulin homogenizer (APV) run in a cycle for two times 5 minutes with a 5 minutes cool down break in between. The sample was cooled in an ice bath throughout lysis. Cell debris was removed by centrifugation at 15,000 x g and 4 °C for 30 minutes. Membrane vesicles were collected by centrifugation at 140,000 x g for 1 hour at 4 °C and the pellet resuspended in UraA vesicle buffer using a Potter-Elvehjem homogenizer to an approximate concentration of 500 mg/mL. Membrane vesicles were flash frozen in aliquots of 10 mL in liquid nitrogen and stored at -80 °C.

For purification of UraA variants from the prepared membrane vesicles, 10 g of frozen vesicles were thawed in a water bath at room temperature, resuspended to 100 mL final volume in UraA vesicle buffer and solubilized for 1 hour at 4 °C in the presence of 1.5 % (w/v) n-decyl- β -D-maltopyranoside and 15 mM imidazole. After centrifugation for 30 minutes at 140,000 x g the supernatant was applied to batch binding with 4 mL washed and pre-equilibrated solid Ni-NTA for 1 hour at 4 °C. The sample was loaded on a BioRad gravity flow column, the column was drained and the resin washed four times with 5 column volumes UraA wash buffer. Proteins were eluted from the column by on-column cleavage using the HRV-3C protease (Hirschi et al., 2020) by addition of 4 mL UraA elution buffer containing 1.2 mg HRV-3C protease and subsequent incubation for at least 30 minutes at 4 °C. The column was subsequently drained and washed three times with 4 mL UraA elution buffer and all fractions were collected. For purification of UraA-GFP fusion protein, the protein was eluted from the column with UraA elution buffer containing 300 mM imidazole. The collected elution fractions were pooled, concentrated to a volume of 500 μ L with an Amicon Ultra-15 50 kDa MWCO concentrator at 4 °C and 3,000 x g for 5 minutes per cycle. The sample was centrifuged for 10 minutes at 13,000 x g and 4 °C prior to size exclusion chromatography to remove aggregates and the supernatant loaded on a Superdex 200 increase 10/300 GL size exclusion column equilibrated with UraA size exclusion buffer-1. If the sample was subsequently used for crystallization UraA size exclusion buffer-2 was used. Size exclusion was performed using a SEC Azura HPLC system (Knauer) with a flow rate of 0.3 to 0.6 mL/min. The elution fractions of 500 μ L volume containing the target protein were pooled and directly used for

crystallization or supplemented with 10% glycerol, flash frozen in liquid nitrogen and stored at -80 °C.

3.4.6 Reconstitution of UraA_{WT} into proteoliposomes

UraA proteoliposomes for alpaca immunization were prepared with size exclusion pure protein following a published protocol (Geertsma et al., 2008a). The Soy PC (95%) lab stock was prepared by dissolving lipids in chloroform, drying in a rotary evaporator and dissolving in 50 mM KPi, pH 7.0 to a final concentration of 20 mg/mL. Small unilamellar vesicles were formed by several sonication cycles and subsequently three freeze/thaw cycles with flash freezing in liquid nitrogen were performed to create large multilamellar vesicles that were stored in liquid nitrogen. For reconstitution, large multilamellar vesicles were thawed at room temperature and extruded 11 times through a 400 nm polycarbonate filter to form large unilamellar vesicles. These were diluted to 4 mg/mL in 50 mM KPi, pH 7.0, destabilized by addition of Triton-X100 and mixed with purified UraA_{WT} in 50 mM KPi, pH 7.5, 150 mM NaCl, 0.2% DM (w/v) to a lipid:protein ratio of 20 and incubated at room temperature for 15 minutes with gentle agitation. Detergent was removed from the sample by stepwise addition of Bio-Beads SM2 and overnight incubation at 4 °C. Bio-Beads SM2 were removed by filtration and liposomes were collected by centrifugation at 360000 x g, resuspended in alpaca immunization buffer and flash frozen in liquid nitrogen.

3.4.7 *In vitro* biotinylation of AVI-tag containing UraA variants

In vitro biotinylation was performed as described with slight changes (Kuhn et. al 2020). The IMAC pure UraA variant with C-terminal Avi-tag was supplemented with D-biotin to a protein:D-biotin ratio of 1:1.25, 10 mM MgSO₄, 10 mM ATP and 800 µg BirA enzyme and incubated overnight at 4 °C with overhead rotation. BirA was subsequently removed from the sample by reverse IMAC using 1 mL washed and pre-equilibrated solid Ni-NTA and the sample concentrated and further purified by size exclusion chromatography as described before (3.4.5).

3.4.8 PEG-5000 maleimide labeling of UraA antigens

Antigens for epitope biased phage display selection of UraA nanobodies were produced as described for UraA_{WT} (3.4.5) with addition of 3 mM DTT during cell lysis and 1 mM DTT or

5 mM 2-mercaptoethanol throughout IMAC. The reducing agent was removed from the sample using an Econopac 10DG column pre-equilibrated with 20 mM HEPES, pH 7.5, 150 mM NaCl, 10% glycerol (w/v), 0.2% DM (w/v). Labeling was started by addition of 20-fold molar excess PEG-5000 maleimide and the sample incubated for 1 hour at room temperature. Subsequently, purification of antigens was completed by size exclusion and protein containing fractions were pooled, flash frozen in liquid nitrogen and stored at -80 °C.

3.4.9 Crosslinking of UraA_{L80C-M143C}

The UraA_{L80C-M143C} antigen for pre-panning was produced from the pBXCA3GH plasmid and purified and biotinylated as described for UraA_{WT} (3.4.5; 3.4.7) but in presence of 5 mM 2-mercaptoethanol. The reducing agent was removed using an Econopac 10Dg column and oxidative crosslinking performed for 30 minutes at room temperature in presence of 0.5 mM freshly prepared copper phenanthroline. The sample was carefully vortexed at the beginning of crosslinking. The reaction was quenched by addition of 10 mM EDTA, the protein concentrated to a volume of 500 µL and purified by SEC using the Superdex 200 increase 10/300 GL column equilibrated with UraA size exclusion buffer-1. The main peak fractions were pooled, supplemented with 10% glycerol (v/v), frozen in liquid nitrogen and stored at -80 °C.

3.4.10 Biopanning

For the selection of conformational-selective nanobodies against UraA_{WT} and UraA_{Cysless-I252C}-PEG-5000, biopanning was performed with nanobody immune libraries from two alpacas. The procedure was based on a published protocol (Pardon et al., 2014) with slight changes. Nunc-Immuno™ MicroWell™ 96-well solid plates were coated overnight at 4 °C with 2 µg neutravidin per well in 50 mM NaHCO₃, pH 8.2. The plate was blocked with PBS, 2% milk powder (w/v) overnight at 4 °C shaking. After three times washing with PBS, 2 µg biotinylated antigen in selection buffer was added and immobilized for 1 hour at 4 °C with shaking. After washing three times with selection buffer, 10⁹ to 10¹² phages of the respective library in selection buffer were added per well (Appendix B) and allowed to bind for 2 hours at 4 °C. Unbound phages were washed off by 15 washing steps with selection buffer and bound phages eluted by addition of 100 µL freshly prepared 0.25 mg/mL Trypsin in PBS for 30 minutes at room temperature. The reaction was quenched by addition of 1 mM AEBSF and

the eluted phages quantified by colony assay. 50 μ L of eluted phages from each selection condition were used to infect 350 μ L *E. coli* TG1 cells at an OD₆₀₀ of 0.5 for 30 minutes at 37 °C and diluted to a final volume of 5 mL in 2YT-Amp¹⁰⁰ and cultivated overnight for library rescue.

To further increase the diversity of nanobody selection, biopanning was also performed with solid phase antigen coating. Therefore 2 μ g antigen in 50 mM NaHCO₃, pH 8.2 were directly immobilized to a well of the Nunc-Immuno™ MicroWell™ 96-well solid plate by overnight incubation at 4 °C and selections performed as described for selections using neutravidin based antigen immobilization.

3.4.11 Enzyme linked immunosorbent assay

Identification of binders from phage display sub-libraries was performed by ELISA in a 96-well format. Single colonies from phage display sub-libraries were produced by plating 50 μ L of the repertoire rescue culture from phage display on LB-Agar-Amp¹⁰⁰ containing 2% D-glucose (w/v). Single colonies were transferred to a 96-well plate containing 100 μ L LB-Amp¹⁰⁰, 2% D-glucose (w/v) and 10% glycerol (w/v) and the plate was covered with a gas permeable adhesive seal. As negative control for ELISA, an UraA unspecific clone was inoculated and an empty well with medium was used as control for potential cross contamination within the 96-deep-well block during small scale production of nanobodies. Cells were cultivated overnight at 37 °C without shaking. The generated master plates were used to inoculate 96-deep-well blocks containing 1 mL 2YT-Amp¹⁰⁰ and 0.1% D-glucose (w/v) for small scale production of nanobodies. After 4 hours cultivation at 37 °C and 250 rpm shaking in an orbital shaker, induction with a final concentration of 1 mM IPTG was performed and cultivation continued for 4 hours. The cells were collected by 10 minutes centrifugation at 4,000 x g, the supernatant was discarded, the plate frozen and stored at -20 °C until further use. For the preparation of periplasmic extracts, the 96-deep-well block was thawed, and cell pellets resuspended in 100 μ L PBS. After 30 minutes shaking, cell debris was removed by 10 minutes centrifugation at 4,000 x g and 90 μ L of periplasmic extracts were recovered for ELISA.

Nunc-Immuno™ MicroWell™ 96-well solid plates were coated with neutravidin and blocked as described (3.4.10). Between individual pipetting steps, the plate was washed three times with ELISA buffer-1. 2 μ g UraA_{WT}-Avi in ELISA buffer were added per well and incubated at 4 °C for 1 hour. 70 μ L PBS, 0.3% milk powder (w/v), 0.3% DM (w/v) and 30 μ L periplasmic extract were added followed by 1 hour shaking at 4 °C. 100 μ L Anti-6xHis peroxidase (mouse IgG;

1:1,000) in ELISA buffer-2 were added per well and allowed to bind for 1 hour at 4 °C. The secondary antibody goat-anti-mouse-AP conjugate was added as 1:5,000 dilution in ELISA buffer-2 and after three final washing steps, 100 µL ELISA development buffer containing 1 mg/mL p-nitrophenyl phosphate were added and the ELISA developed at room temperature in the absence of light. The absorbance at 405 nm was measured with a Tecan Infinite M200 (Tecan) after 45 min incubation and endpoints were measured after overnight incubation at 4 °C.

3.4.12 Selection of synthetic nanobodies against Ura_{AWT}

Synthetic nanobodies binding to Ura_{AWT} were selected by Prof. Dr. Eric R. Geertsma in collaboration with Dr. Iwan Zimmermann according to the selection procedure described in Zimmermann et al. (2020). In short one round of ribosome display followed by two rounds of phage display were performed for each of the three sybody libraries. The binding ability of sybodies from individual clones was tested by ELISA and promising clones were sequence analyzed. Unique sybodies were produced in 50 mL *E. coli* MC1061 cultures and purified by IMAC and SEC.

3.4.13 Production and purification of nanobodies and sybodies

Nanobodies and synthetic nanobodies (sybodies) were produced in *E. coli* TG1 from the pDX plasmid or in *E. coli* MC1061 from the pSb_init plasmid. A 5 L baffled culture flask containing 1 L TB medium with the appropriate antibiotic and 1 mM MgSO₄ was inoculated with 10 mL LB overnight culture and cultivated at 37 °C and 95 rpm on an orbital shaker. When cells reached an OD₆₀₀ of 1 to 1.5 the temperature was lowered to 25 °C within one hour and gene expression was induced by addition of 1 mM IPTG for expression from the pDX plasmid or 0.01% L-arabinose (w/v) for expression from the pSb_init plasmid. The cells were incubated overnight and harvested next day for 15 minutes at 5,500 x g and the cell pellet frozen and stored at -20 °C. For purification of nanobodies or sybodies, the frozen cell pellet was thawed and resuspended to a final volume of 150 mL in nanobody lysis buffer. The sample was stirred for 2 hours at 4 °C and afterwards centrifuged for 30 minutes at 15,000 x g and 4 °C. The supernatant was applied to batch binding with 2 mL solid Ni-NTA for 1 hour at 4 °C. The sample was loaded on a gravity flow column, the column was drained and washed four times with 5 column volumes nanobody wash buffer. Elution of nanobodies or sybodies was performed

by adding 5 times 1 mL nanobody elution buffer to the column. All elution fractions were collected and the protein concentration determined spectrophotometrically. Protein containing fractions were pooled and concentrated to a volume of 500 μ L in an Amicon Ultra-15 10 kDa MWCO concentrator by centrifugation cycles of 5 minutes at 3,000 x g and subsequently centrifuged for 10 minutes at 13,000 x g. The supernatant was loaded on a Sepax SRT-10C SEC-300 size exclusion column equilibrated with nanobody size exclusion buffer and the column run with 0.7 mL/min using a SEC Azura HPLC system (Knauer). The elution fractions of 500 μ L volume containing the target protein were pooled and flash frozen in liquid nitrogen as 500 μ L aliquots and stored at -80 °C. Nanobody and sybody samples could be stored at 4 °C for several weeks upon thawing.

3.4.14 Preparation of UraA-GFP inside-out vesicles

UraA-GFP inside-out-vesicles were generated according to the standard protocol for vesicle preparation described in (3.4.5) with exception of cell lysis being performed with only 1 pass through a Stansted Homogenizer according to Joshi et al. (2009). The inside-out vesicles were resuspended to 500 mg/mL in UraA vesicle buffer after ultracentrifugation and frozen as aliquots in liquid nitrogen. The orientation of inside-out vesicles was quantified by densitometry analysis of HRV-3C protease cleavage of UraA-GFP in presence and absence of protease visualized by SDS-PAGE and in-gel fluorescence (3.4.1; 3.4.3). The protease activity was verified by full cleavage of UraA-GFP upon addition of 1% Triton X-100 (v/v).

3.4.15 Pulldown of nanobodies and sybodies by inside-out vesicles

For the pulldown of nanobodies or sybodies by UraA-GFP inside-out membrane vesicles, the frozen vesicles (3.4.14) were thawed and diluted to 12.5 mg/mL in 200 μ L nanobody size exclusion buffer supplemented with 50 μ g of binder. Samples were incubated for 1 hour at 4 °C to allow equilibration and afterwards centrifuged for 15 minutes at 13,000 x g and 4 °C. The pellet was carefully washed two times with 500 μ L buffer and resuspended in 25 μ L 5x SDS sample buffer. Samples were frozen and stored at -20 °C before further analysis by SDS-PAGE and western blot (3.4.1; 3.4.4).

3.4.16 Melting curve analysis by FSEC

Melting curves of UraA_{WT}-GFP in presence and absence of nanobodies were recorded by incubating UraA_{WT}-GFP at a concentration of 0.75 mg/mL with 7-fold molar excess of the individual nanobody for 10 minutes at elevated temperatures ranging from 25 to 85 °C. Samples were centrifuged for 10 minutes at 13,000 x g to remove aggregates and 40 µL supernatant were injected into a Superdex 200 5/150 GL column and run on an Agilent HPLC with an Agilent 1260 infinity fluorescence detector with 0.2 mL/min flow rate for FSEC analysis (Kawate et al., 2006). Fluorescence of GFP was excited at a wavelength of 480 nm and detected at 530 nm. The peak intensities were normalized to the signal of the untreated sample, plotted against the temperature and fitted with a Boltzmann equation to calculate the melting temperature.

3.4.17 Differential scanning fluorimetry

For melting temperature analysis of UraA variants differential scanning fluorimetry was performed (Niesen et al., 2007; Alexandrov et al., 2008). Therefore, 90 µL sample containing 0.1 mg/mL UraA_{WT} in UraA size exclusion buffer-1 was supplied with 1.5 µL CPM dye at a concentration of 1 mg/mL in DMSO to yield a final concentration of 40 µM. The sample was incubated for 5 minutes at room temperature and aggregates were removed by centrifugation at 13,000 x g and 4 °C for 10 minutes. The supernatant was transferred to a PCR tube and the melting curve recorded from 25 to 80 °C or 90 °C with a ramp of 2 °C/min using the Rotor-Gene Q (Qiagen). The CPM fluorescence was excited at a wavelength of 365 ± 20 nm and detected at a wavelength of 460 ± 20 with the detector gain setting of -2. For data evaluation the Rotor-Gene Q software build in tool for generation of the first derivative was used and the peak maximum corresponding to the melting temperature analyzed with the Origin software. For analysis of uracil or nanobody binding the samples were preincubated at 4 °C for at least 30 minutes to allow equilibration before addition of CPM and subsequent melting.

For the analysis of simultaneous binding of nanobodies and sybodies, the saturation of UraA with the binders at the given concentrations was a crucial prerequisite. As the method was developed to serve as a high throughput tool without knowledge of affinities, the saturation of thermal stabilization was experimentally tested by using 0.1 mg/mL (2.2 µM) UraA_{WT} in combination with 11 and 22 µM nanobody in thermal melting. Measurements with two binders were performed with 11 µM of each binder and the melting temperature compared

to the melting temperatures in presence of 22 μM of the individual binders to detect additional stabilization due to simultaneous binding independent of the total concentration of nanobody.

3.4.18 Cysteine accessibility assay

For the kinetic analysis of substrate binding site accessibility, a single cysteine was introduced at position Ala-31 in UraA_{Cysless} for specific labeling with CPM, located in TM1 next to the substrate binding site without direct contribution to substrate binding. The periplasmic linker mutations were introduced into UraA_{Cysless-A31C} and the proteins produced as described (3.4.5) with the addition of 1 mM DTT in all purification buffers before size exclusion chromatography. For cysteine labeling, protein samples were diluted to 250 nM in labeling buffer and equilibrated in a quartz cuvette for 3 minutes at room temperature. 5 μM CPM in labeling buffer was added to yield the final concentrations of 200 nM protein and 1 μM CPM. CPM fluorescence was excited at 388 nm and emission recorded at 468 nm over a time course of 5 minutes with a sampling rate of 0.1 s^{-1} with the Fluorolog-3 spectrofluorometer (Horiba).

3.4.19 Co-crystallization of UraA with sybodies

For the co-crystallization of UraA_{WT} respectively UraA_{G320P} with nanobodies and sybodies the size exclusion pure UraA variant in size exclusion buffer-2 was concentrated to 8.8 mg/mL in an Amicon Ultra 0.5 50 kDa MWCO at 7,000 $\times g$ and 4 °C. The crystallization sample was prepared as shown (**Table 14**) to yield the final sample with 10 mg/mL total protein with a UraA to binder molar ratio of 1:1.2 in 9.5 mM HEPES pH 7.5, 142.5 mM NaCl, 0.16% DM (w/v), 1% OG respectively NG (w/v). For initial screening the sitting drop method was performed in a 96-well format using the Mac400 screen (Appendix A) with a drop size of 200 nL protein sample plus 200 nL mother liquor pipetted with the Rigaku CrystalMation™ system and storage in a Rigaku Gallery 700 incubator at 18 °C. Initial screening was performed in collaboration with Dr. Yvonne Thielmann from the group of Prof. Dr. Hartmut Michel from the Max Planck Institute of Biophysics, Frankfurt and the crystallization plates were pipetted by Barbara Rathmann. Initial hits were scaled up to 48-well format with 1 μL protein sample plus 1 μL mother liquor pipetted manually and stored at 18 °C.

3.4.20 Scintillation proximity assay

The uracil affinity of biotinylated UraA_{WT} or UraA variants was determined by scintillation proximity assay (Harder et al., 2012). The protein sample was diluted to 200 nM concentration in UraA elution buffer containing 200 nM ³H-uracil and increasing concentrations of unlabeled uracil (Lu et al., 2011). The samples were equilibrated for 1 hour at 4 °C and 52.5 μL of each sample were mixed in a well of a 96-well plate prefilled with 17 μL Streptavidin PVT scintillation beads at 20 mg/mL that were washed three times in UraA elution buffer. The plate was incubated for 30 minutes at 4 °C for immobilization of biotinylated UraA variants and subsequently scintillation counting was performed for 2 minutes per well at room temperature. For background correction, 1% final SDS (w/v) was added to each well and proteins unfolded for 30 minutes at 4 °C before scintillation counting. Background was subtracted from specific binding signals and the mean and standard error of triplicates calculated and plotted against the concentration of unlabeled uracil with Origin. Data was analyzed by nonlinear curve fitting in Origin with the following equation for homologous competition binding adapted from GraphPad (**Equation 2**):

$$y = \frac{B_{\max} \times \text{hot uracil}}{\text{hot uracil} + \text{cold uracil} + K_d} + \text{background} \quad (2)$$

As alternative to the competition assay, the uracil affinity of UraA_{WT} in presence or absence of Sy45 was determined by saturation assay in SPA. Therefore, 150 nM UraA were pre-incubated with 10-fold excess of Sy45 or buffer only with increasing amounts of uracil supplemented as a defined ³H-uracil/unlabeled uracil mixture. A sample volume of 52.5 μL was transferred to 96-well plate prefilled with 17 μL Streptavidin PVT scintillation beads, incubated and data collected as described above. Background binding was subtracted, counts corrected for the ³H-uracil/unlabeled uracil ratio and plotted against the total uracil concentration. The binding curve was analyzed by nonlinear curve fitting in Origin using the Langmuir isotherme.

Table 14: Composition of protein samples for crystallization screening

Sample	Volume (%)
UraA variant (8.8 mg/mL in 10 mM HEPES pH 7.5, 150 mM NaCl, 0.2% DM (w/v))	80
nanobody/sybody (19.7 mg/mL in 10 mM HEPES pH 7.5, 150 mM NaCl)	15
20% OG (w/v) or 20% NG (w/v) in ddH ₂ O	5

3.5 Biophysical methods

3.5.1 X-ray diffraction data collection and processing

X-ray diffraction data for crystal screening was collected at the P13 and P14 beamlines of PETRA III and at the X06SA and X06DA beamlines of SLS. The diffraction data yielding the UraA_{G320P}-Sy45 co-crystal structure was collected at the P13 beamline of PETRA III (Cianci et al., 2016) at a wavelength of 0.98 Å and processed using XDS and scaled using XSCALE both from the XDS package (Kabsch, 2010). The space group was determined by Pointless from the CCP4 software package (Winn et al., 2011) and data was corrected for anisotropy with the UCLA diffraction anisotropy server (Strong et al., 2006). Phases were solved by molecular replacement using Phaser-MR from the Phenix suite (Liebschner et al., 2019) with the occluded UraA structure (Yu et al., 2017; PDB: 5XLS) and a Swissmodel (Waterhouse et al., 2018) of the synthetic nanobody Sy45 as model. The structure was refined with Phenix.refine at 3.1 Å resolution. The dataset for the UraA_{G320P}-Sy45 uracil liganded structure was collected at the X06DA beamline of the SLS at a wavelength of 1.00 Å. The dataset was processed and corrected for anisotropy as described above for the apo UraA_{G320P}-Sy45 structure. The structure was solved by molecular replacement using the apo UraA_{G320P}-Sy45 structure and refined at 3.7 Å resolution.

3.5.2 Hydrogen-deuterium exchange mass spectrometry

Samples for Hydrogen-deuterium exchange mass spectrometry (HDX-MS) analysis of UraA_{WT}, UraA_{G320P} and UraA_{P330G} were prepared according to the standard protocol for protein purification (3.4.5) and flash frozen in liquid nitrogen at 2 mg/mL concentration in UraA size exclusion buffer-1 and stored at -80 °C until HDX-MS was performed by Jonathan Zöller from the group of Dr. Julian Langer from the Max-Planck-Institute of Biophysics, Frankfurt, Germany according to the procedure described in Eisinger et al. (2017). The respective UraA variant was diluted to 0.675 mg/mL and labeling with D₂O allowed for up to 45 minutes at 20 °C. Uracil containing samples were supplemented with 100 μM uracil. The hydrogen deuterium exchange was quenched by adding ice cold quenching buffer at pH 2.2. The protein was online digested with Pepsin and the resulting peptides separated by reverse phase chromatography at pH 2.2 and 0 °C. Mass spectra were recorded on a Synapt G2-Si (Waters).

4 Results

This study aimed to improve the mechanistic understanding of SLC23 transporters on a structural and functional level and develop means and methods for modulation of transporter activity ideally, both for activation and inhibition. The uracil transporter UraA from the model organism *E. coli* was selected as target protein as it is one of two SLC23 transporters with available structural information beside UapA from *A. nidulans*. Two different strategies were applied to study the conformational space of UraA by alteration of its conformational equilibrium. First, selection of a repertoire of nanobodies for diverse conformational arrest of UraA. Second manipulation of UraA function by mutating mechanistically relevant regions outside of the 'catalytic side'. Finally, the success of the two strategies was confirmed by structural characterization of UraA.

4.1 Conformation specific binder selection

A deep mechanistic understanding of transport requires detailed insights into the conformation changes associated with transport. While complete trajectories of conformational changes for a specific target protein are most instructive, these are difficult to obtain and consequently mechanisms are often inferred from comparing different conformation of different proteins. This is especially true for solute carriers for which, unlike ABC transporters, no generic inhibitors or canonical active site residues are known. Here I detail the selection of nanobodies for conformational arrest of the SLC23 transporter UraA and a facile method to assign binders into groups stabilizing distinct conformations.

The nanobody selection against UraA aimed for a very broad portfolio of binders. Therefore, generation and selection under a broad range of conditions was performed. The following section details the nanobody selection from immune libraries while the selection from synthetic libraries is presented in section 4.1.4.

4.1.1 Alpaca immunization

The variation in nanobodies was further increased by immunization of two animals (*Vicugna pacos*) with two different samples. The alpaca OXA was immunized with detergent-solubilized UraA_{WT} and NUBIA with UraA_{WT} proteoliposomes. The detergent-solubilized UraA sample was purified by IMAC and SEC (3.4.5; **Figure 9A, B**) using n-decyl- β -D-maltopyranoside, as this respective detergent was the best compromise between the smallest possible micelle and the best possible protein stability (Kunji et al., 2008). Reconstitution into soy PC liposomes was performed to a lipid:protein ratio of 20:1. Based on the recovery of UraA_{WT} following DM-resolubilization and ultracentrifugation, at least 70% of the protein was functionally reconstituted and not associated with the membrane as aggregates based on densitometry analysis in ImageJ (Schneider et al., 2012) of a Coomassie stained polyacrylamide gel after SDS-PAGE (**Figure 9C**). The immunizations were performed outside of this study by Dr. Saša Štefanić from the Nanobody Service Facility, University of Zurich, Switzerland as described (3.1). Four immunizations over a period of six weeks were performed and the immune response against detergent-solubilized UraA_{WT} was quantified by ELISA with secondary antibodies specific for the different IgG classes IgG1a, IgG1b, IgG2, IgG3a and IgG3b (**Figure 9D**). In both immunized alpacas, binding of IgG2, IgG3a and IgG3b, the heavy-chain only antibodies, to UraA_{WT} was increased during the immunizations indicating successful in vivo selection. Two immune libraries were prepared from the blood samples outside of this study by Katharina Holzhüter (3.1) following a published protocol (Pardon et al., 2014) with slight deviations. The libraries were named OXA and NUBIA according to the animal they derived from with a maximal diversity of 2×10^8 respectively 4×10^8 which was comparable to another reported immune library (Deschaght et al., 2017) and exceeded the recommended minimal diversity of 10^7 suggested by Pardon et al. (2014) by one order of magnitude.

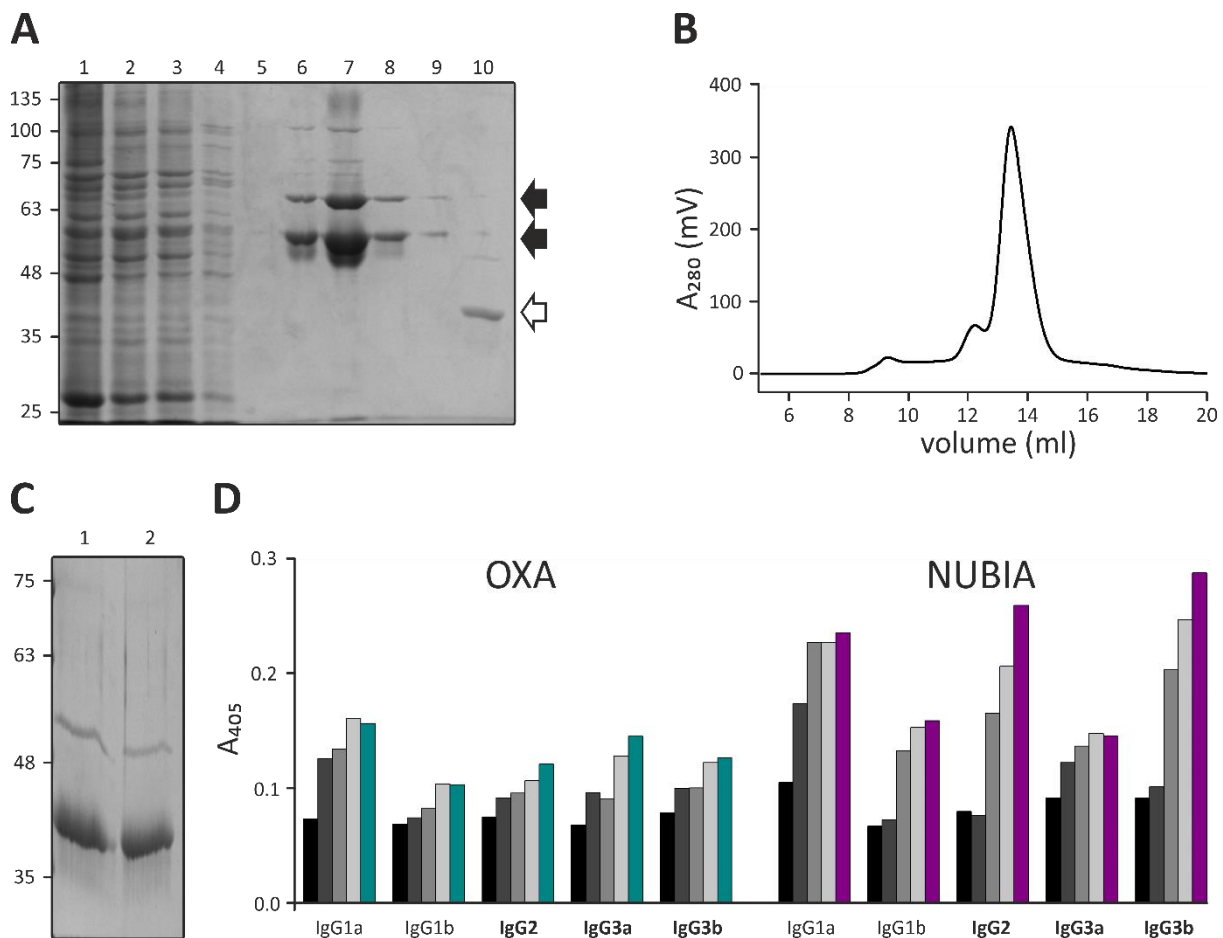


Figure 9: Alpaca immunization – sample preparation and immune response. (A) Coomassie stained SDS-PAGE gel of fractions from the IMAC purification of UraA_{WT}. Lane 1: solubilized vesicles, 2: supernatant after ultracentrifugation, 3: flowthrough, 4: 50 mM imidazole wash, 5-9: 300 mM imidazole elution fractions, 10: sample after HRV-3C protease cleavage and reverse IMAC. Black and white arrows indicate UraA_{WT}-GFP and UraA_{WT}, respectively. (B) Size exclusion chromatography of IMAC purified UraA_{WT} in 0.2% (w/v) DM. (C) Reconstitution efficiency was determined by re-solubilization of UraA_{WT} from proteoliposomes using 1% (w/v) DM. Detergent-solubilized proteoliposomes were analyzed by SDS-PAGE and subsequent Coomassie staining before (1) and after (2) ultracentrifugation for 10 minutes at 200.000 x g to remove aggregates. (D) ELISA demonstrating the immune response of the two alpacas (OXA and NUBIA) during the immunizations. Immunizations were performed on 7.11., 21.11., 05.12. and 17.12.2015 and blood samples collected four days after each immunization with color code from black (before immunization) over grey to cyan and purple (final immunization), respectively. IgG2 and IgG3 heavy chain only antibody classes are highlighted in bold. Sample preparation was performed in collaboration with Katharina Holzhüter as part of her Master studies. Immunizations were performed by Saša Štefanić from the Nanobody Service Facility, University of Zurich, Switzerland.

4.1.2 Phage display selection

For phage display selection of nanobodies against UraA_{WT}, antigens were recombinantly produced from the pBXCA3GH plasmid with a C-terminal Avi-tag fusion for specific *in vitro* biotinylation and the biotinylation efficiency was subsequently quantified to be 90% by Streptavidin induced mobility shift in SDS-PAGE (Green et al., 1990; Kuhn et al., 2020; **Supplementary figure 4**).

Biopanning was performed in various conditions including addition of substrate, counterselection with a periplasmic epitope shielded UraA variant as well as selection against a cytoplasmic shielded UraA variant as antigen. Immobilization of antigens during biopanning was achieved either indirectly using the biotin-neutravidin interaction or by direct immobilization on the plastic surface (solid phase method). All variation in the selection procedure aimed to select a diverse set of nanobodies stabilizing different conformations of UraA. As an inward-facing structure of UraA was already published at the beginning of selections (Lu et al., 2011; PDB: 3QE7; herein called UraA_{3QE7}), the procedure included strategies to enrich binders stabilizing an outward-facing conformation. Based on the ability of nanobodies to bind into cavities and substrate binding sites (De Genst et al., 2005) and assuming that these transporters adhere to the alternating access theory (Jardetzky 1966), it was hypothesized that outward-facing conformation binders would preferentially bind to the periplasmic side of UraA that features an open cavity for substrate binding in this conformation. A single cysteine was introduced into UraA_{Cysless} at position Met-143 that served as specific position for labeling of the protein with PEG-5000 maleimide. This shielded and non-biotinylated version of UraA was added during biopanning to enrich periplasmic side binders by attracting and removing cytoplasmic side binders with the counterselection antigen. A similar strategy to direct binders towards the periplasmic side was followed by using the biotinylated UraA_{Cysless-I252C} mutant that was labeled with PEG-5000 maleimide as antigen to shield potential epitopes on the cytoplasmic side of UraA (**Supplementary figure 5**). Additionally, a specific crosslinked UraA variant was prepared (UraA_{L80C-M143C}) based on the published UraA_{3QE7} structure and used for pre-panning (**Supplementary figure 6**).

A selection overview is presented in the Appendix that shows all important aspects of the 36 individual phage display selection paths (Appendix B) and a flow scheme presenting the most important aspects of phage display selection for subsequent analysis is presented in **Figure 10**.

Phages that bound during biopanning carrying the nanobody gene sequence in the phagemid were eluted, quantified (**Figure 11A, B**) and the repertoire rescued by infection of *E. coli* TG1. Subsequently, 1,012 single colonies from these sub-libraries were picked and archived in 11 master plates of 96-well format that also served as pre-culture for small scale production of nanobodies for ELISA (**Figure 11C, D**). Qualitative binding analysis of these 1,012 clones by ELISA resulted in 270 binders with a twofold signal over background which was set as

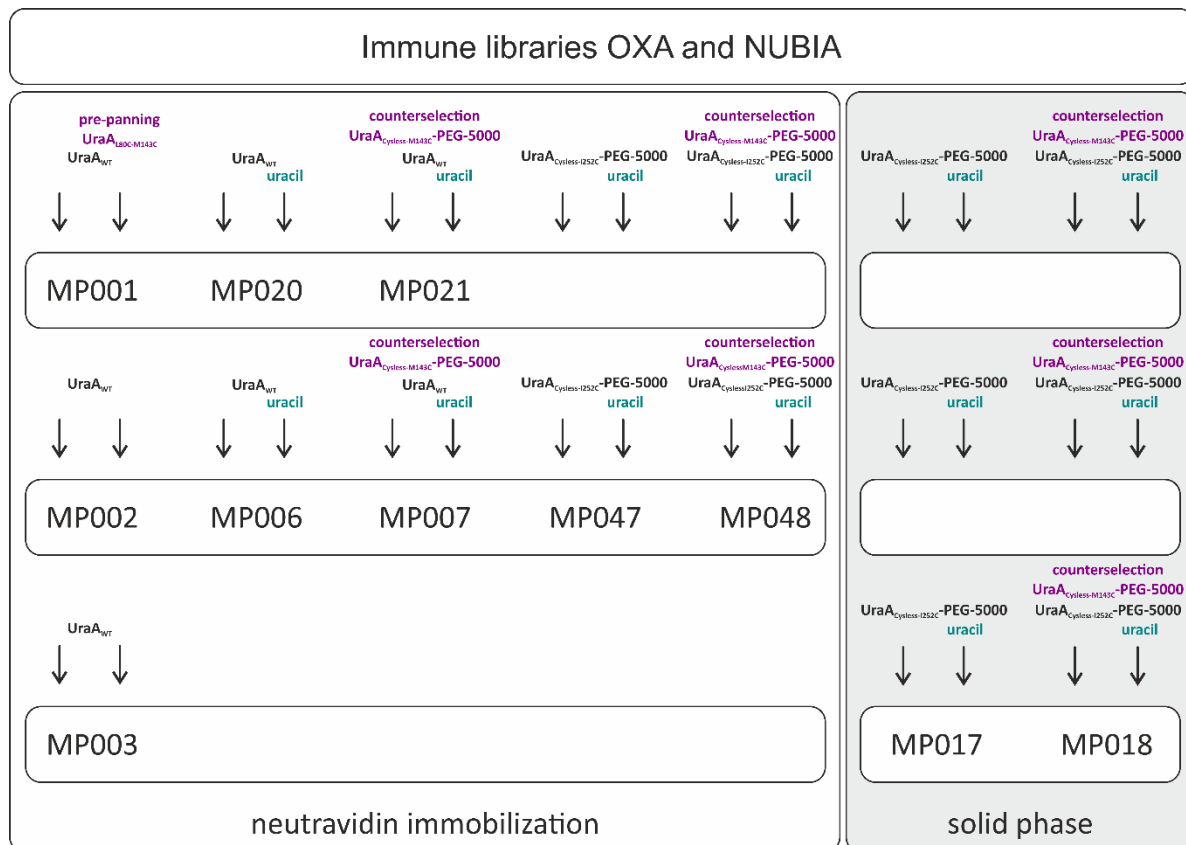


Figure 10: Phage display scheme for selection of a diverse repertoire of nanobodies against UraA. Individual selection paths are indicated by black arrows connecting the maximal three rounds of phage display selection. Each selection path was performed in parallel for the two immune libraries OXA and NUBIA which is not indicated for sake of simplicity. The used antigen for selection (UraA_{WT} and UraA_{Cysless-252C}-PEG-5000, black) and selection bias introduced by either pre-panning or counterselection (purple) or addition of uracil (cyan) is indicated with respective color code. Master plates that were created from selection output are presented in white boxes. Each master plate consists of clones from two selection paths indicated by black arrows of the two individual libraries, thus 4 individual sub-libraries. The applied antigen immobilization strategy is presented as white (neutravidin based immobilization) or grey box (solid phase method). Only selection paths resulting in ELISA analyzed master plates are presented.

threshold for binders to be ELISA positive. From these 270 binders, 88 derived from master plate MP006 that ELISA results are exemplary presented (**Figure 11C, D**) and 90 from MP007 (**Supplementary figure 7**) indicating a high enrichment within these libraries but also a potential overselection and resulting loss of diversity after two rounds of biopanning. To compensate for this, the master plates MP020 and MP021 were prepared that covered the same libraries as MP006 and MP007 after the first round of biopanning. As expected, the number of ELISA positive clones was reduced with 13 positive binders from MP020 and 7 from MP021. The ELISA results from MP001 and MP002 with only 1 positive binder were in line with a low number of eluted phages during the selection procedure. After one additional round of biopanning, the ELISA positive clones in this selection could be increased to 21 in MP003. The selections against UraA_{Cysless-1252C}PEG-5000 to direct binders to the periplasmic epitope

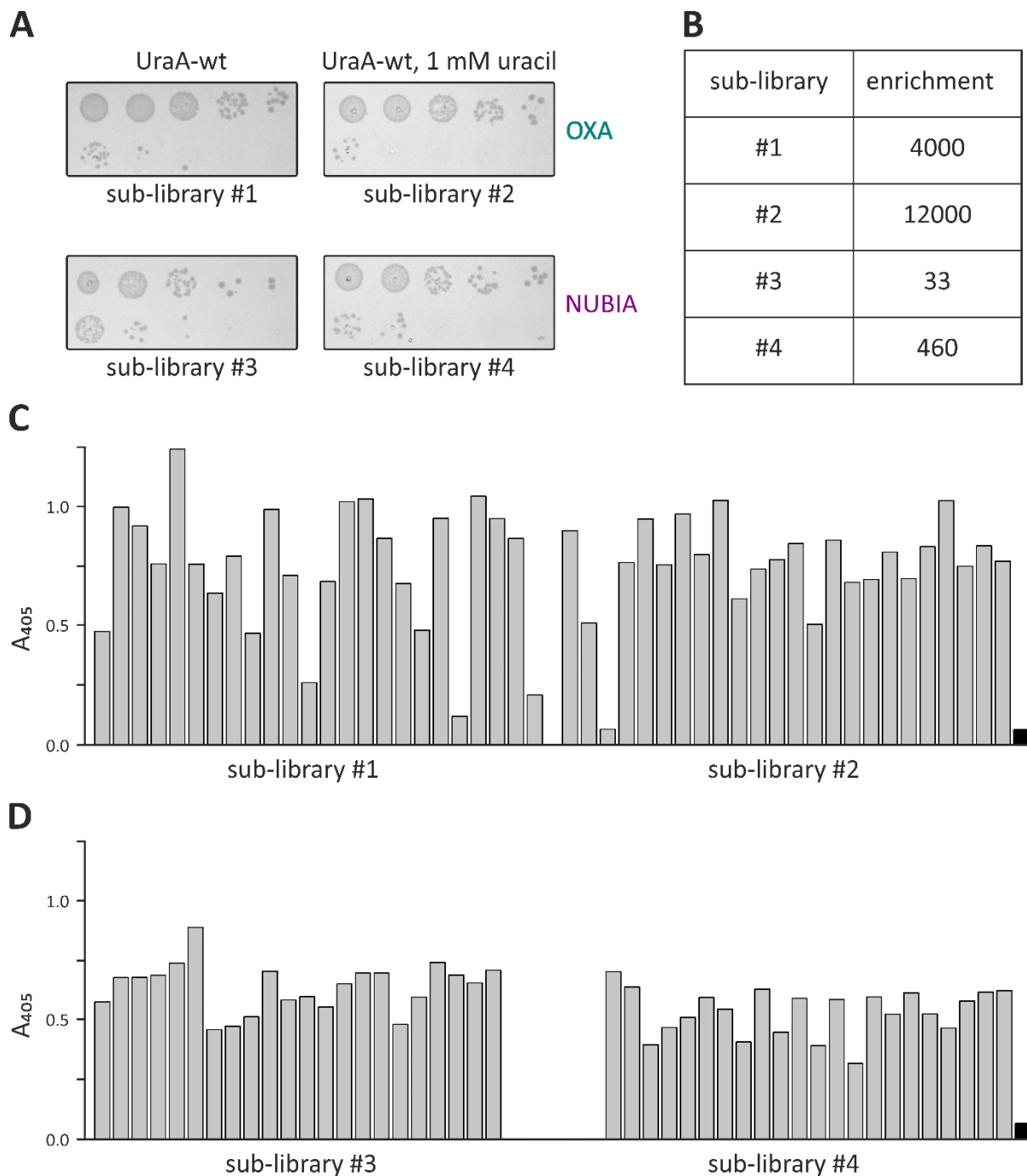


Figure 11: Phage display selection of nanobodies against UraA_{WT} and output analysis by ELISA. (A) Quantification of eluted phages by colony assay after two rounds of phage display. Selections with two libraries (OXA and NUBIA) against UraA_{WT} in presence or absence of uracil were compared to control selections devoid of UraA antigen. Derived clones were combined in the master plate MP006 (B) Enrichment of target specific nanobodies in the four sub-libraries calculated from phage quantification shown in (A). (C) Identification of UraA specific nanobodies from the OXA library from master plate MP006 by ELISA. Endpoints of ELISA after overnight development are shown. (D) Identification of NUBIA derived nanobodies as described for (C).

showed lower enrichment during selections. Only after three rounds of phage display with the solid phase strategy the enrichment was significant. ELISA with these clones against UraA_{WT} resulted in 36 positive binders from MP017 and no positive binder from MP018. The counterselection strategy with UraA_{Cysless-M143C}-PEG-5000 used for sub-libraries of MP018

abolished the enrichment of positive binders in these selections. In order to compensate for this low yield of binders regarding the UraA_{Cysless-I252C}-PEG-5000 antigen, MP047 and MP048 were prepared that covered the sub-libraries of UraA_{Cysless-I252C}-PEG-5000 after two rounds of phage display with neutravidin immobilized antigen even though the enrichment in these selections was lower compared to the UraA_{WT} selections. Consistently, the number of positive binders in ELISA with 11 from master plate MP047 and 2 from MP048 was low.

4.1.3 Temperature dependent ELISA

The large number of 270 ELISA positive clones required a high-throughput method prior to sequence analysis in order to identify potential conformational specific binders. The ELISA was reproduced for a pool of 228 clones at 4 °C and additionally performed at 20 °C in presence and absence of uracil. This strategy aimed to identify nanobodies that stabilize UraA or that show altered binding behavior dependent on uracil, both indicative of conformational selectivity.

A fraction of nanobodies showed signals on the background level in ELISA performed at 4 °C. Thus, the result from the initial ELISA could not be reproduced. Due to the high-throughput approach, overexpression and successful preparation of the periplasmic extracts was subject to batch to batch variation and low yields of added nanobodies could not be excluded in this setup. However, for a fraction of nanobodies a significant reduction in signal from ELISA performed at 4 °C to 20 °C was observed. This was often accompanied by lower ELISA signal at 4 °C compared to other binders as shown for all binders derived from master plate MP047 (**Supplementary figure 8**). This indicated conformational unspecific binding of the nanobodies (*vide infra* **Figure 15**). The same was observed for clones derived from master plate MP017 (**Supplementary figure 8**). Both resulted from selections against UraA_{Cysless-I252C}-PEG-5000 (Appendix B). Binders showing these properties were not considered for detailed analysis.

In contrast, the positive binding signal at 4 °C could be reproduced for a fraction of clones derived from selections against UraA_{WT} but with overall lower signal intensity at 20 °C (**Figure 12A**). This result was interpreted as a limiting stability of UraA_{WT} during the ELISA at 20 °C that reduced the amount of folded protein during the experiment resulting in lower ELISA signal. Following this argumentation, relatively high ELISA signals at 20 °C, as observed for Nb6D3 and Nb6E3, would be attributed to nanobodies that increase the stability of UraA_{WT} indicative of conformational specific binding. Accordingly, all ELISA signals derived from uracil

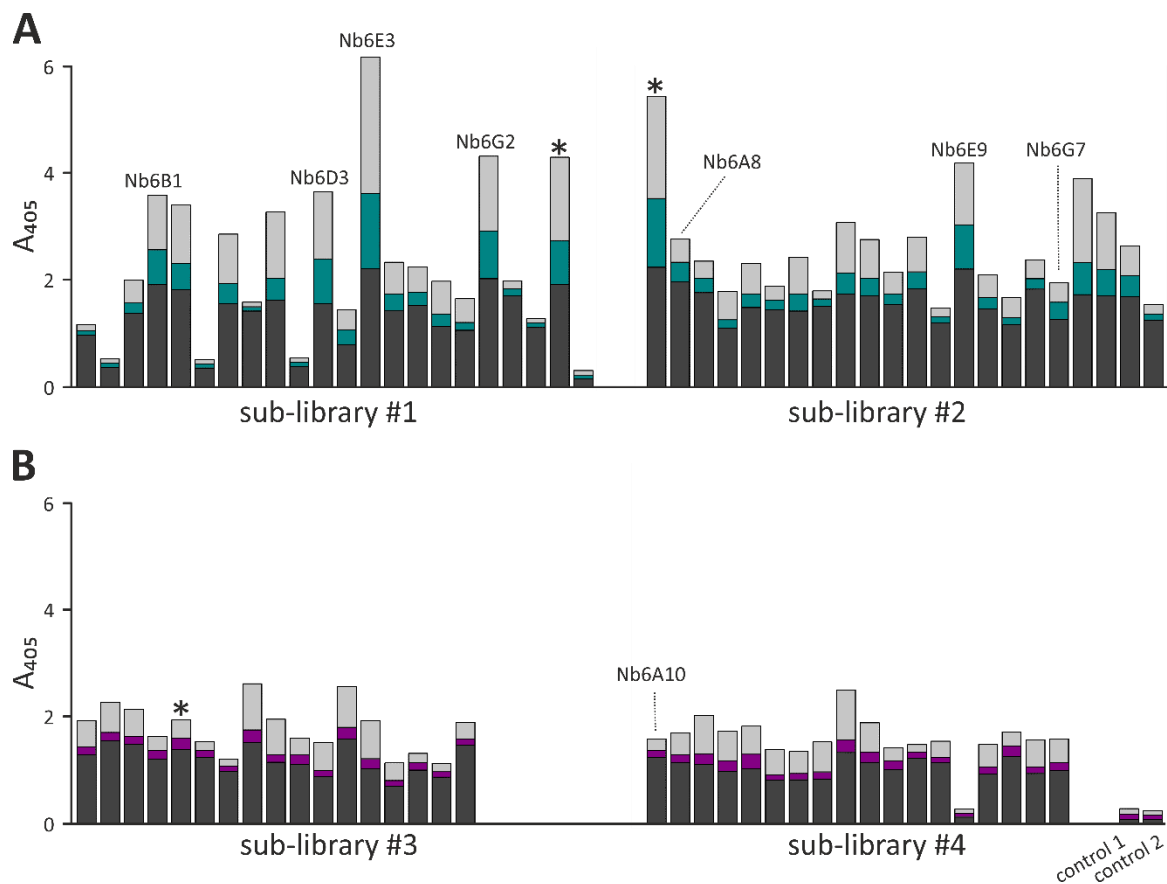


Figure 12: ELISA based binding analysis of selected nanobodies from MP006. ELISA of sub-libraries #1 to #4 from the master plate MP006 performed at 4 °C (dark grey), at 20 °C (cyan or purple) and at 20 °C in presence of 1 mM uracil (light grey). Unique nanobodies identified during selection are labeled with the name based on the master plate and well number the binder derived from. Redundant nanobodies are indicated with an asterisk. An unspecific nanobody selected against a different protein than UraA (control 1) and no addition of nanobody (control 2) served as negative controls. Unlabeled columns represent ELISA signals of nanobodies that were not sequence analyzed. Final ELISA development was performed overnight at 4 °C.

containing samples were higher compared to uracil free samples derived signals (**Figure 12**), due to the additional stabilization of UraA_{WT} by the substrate (*vide infra* **Figure 38**). Thus, ELISA in presence of uracil failed in providing information regarding the substrate competition of the tested nanobodies but indicated the limited stability of UraA_{WT} during the ELISA at 20 °C and allowed to distinguish nanobodies with stabilizing effect on UraA_{WT} from the large pool of binders.

From all 270 ELISA positive clones, in total 172 were sequence analyzed and 150 sequences could be further analyzed whereas 22 sequencing reactions were of low quality either due to double transformation or ethanol contamination in the plasmid sample from the plasmid preparation that prevented successful Sanger sequencing. The CDR3 regions of the 150 individual sequences were extracted and compared to identify unique or closely related nanobodies by using a python 2.7 based script for automated sequence analysis. This was

reasonable as sequence similarity in CDR3 of more than 80% is indicative of nanobodies derived from the same B-cell lineage that target the same epitope (Pardon et al., 2014). The sequence analysis revealed 29 unique CDR3 sequences and 121 clones were found to be closely related or identical (**Supplementary figure 9** and **Supplementary table 1**).

Only 4 of these 29 unique binders derived from the NUBIA. Though NUBIA was immunized with UraA_{WT} proteoliposomes, the increasing immune response against detergent-solubilized UraA_{WT} indicated successful *in vivo* selection (**Figure 9D**). This might indicate a loss of diversity within the NUBIA library compared to the OXA library.

Most selected binders derived from the OXA library with 25 out of 29. The nanobodies Nb3H1 and Nb17D3 were found to be highly redundant with 22 respectively 28 binders with identical CDR3 sequences among all analyzed clones. Both nanobodies showed poor binding in the ELISA at 20 °C due to non-stabilization of UraA and were therefore classified as conformational unselective binders which was experimentally confirmed by the poor thermostabilization of UraA in subsequent differential scanning fluorimetry (4.2.1). Apart from these two binders, various unique CDR3 sequences were identified with good ELISA signal intensity at 20 °C, e.g. Nb2H9, Nb6D3, Nb6E3, Nb7F3 and Nb20C3. The CDR3 sequence alignment further highlighted that 7 of the 13 unique CDR3 sequences from the OXA library derived from selection paths including counterselection with UraA_{Cysless-M143C}PEG-5000 indicating successful removal of pre-dominant nanobodies from the pool by the counterselection procedure (**Supplementary figure 9**).

4.1.4 Selection of sybodies against UraA

In addition to alpaca derived nanobodies, the synthetic sybody libraries were used to generate binders against UraA in order to further increase the binder diversity. Antigens used for selection were prepared as indicated (3.4.5; 3.4.9) and the subsequent ribosome and phage display followed by ELISA and high throughput purification of positive binders was performed outside of this work by Prof. Dr. Eric R. Geertsma in collaboration with Dr. Iwan Zimmermann from the group of Prof. Dr. Markus Seeger from the Institute of Medical Microbiology, University of Zurich, Switzerland according to a published protocol (Zimmermann et al., 2020). Counterselection was performed using the locked variant UraA_{L80C-M143C} based on the published inward-facing conformation (Lu et al., 2011) to enrich binders against uncharacterized conformations. The enrichment after two rounds of phage display was 4.3,

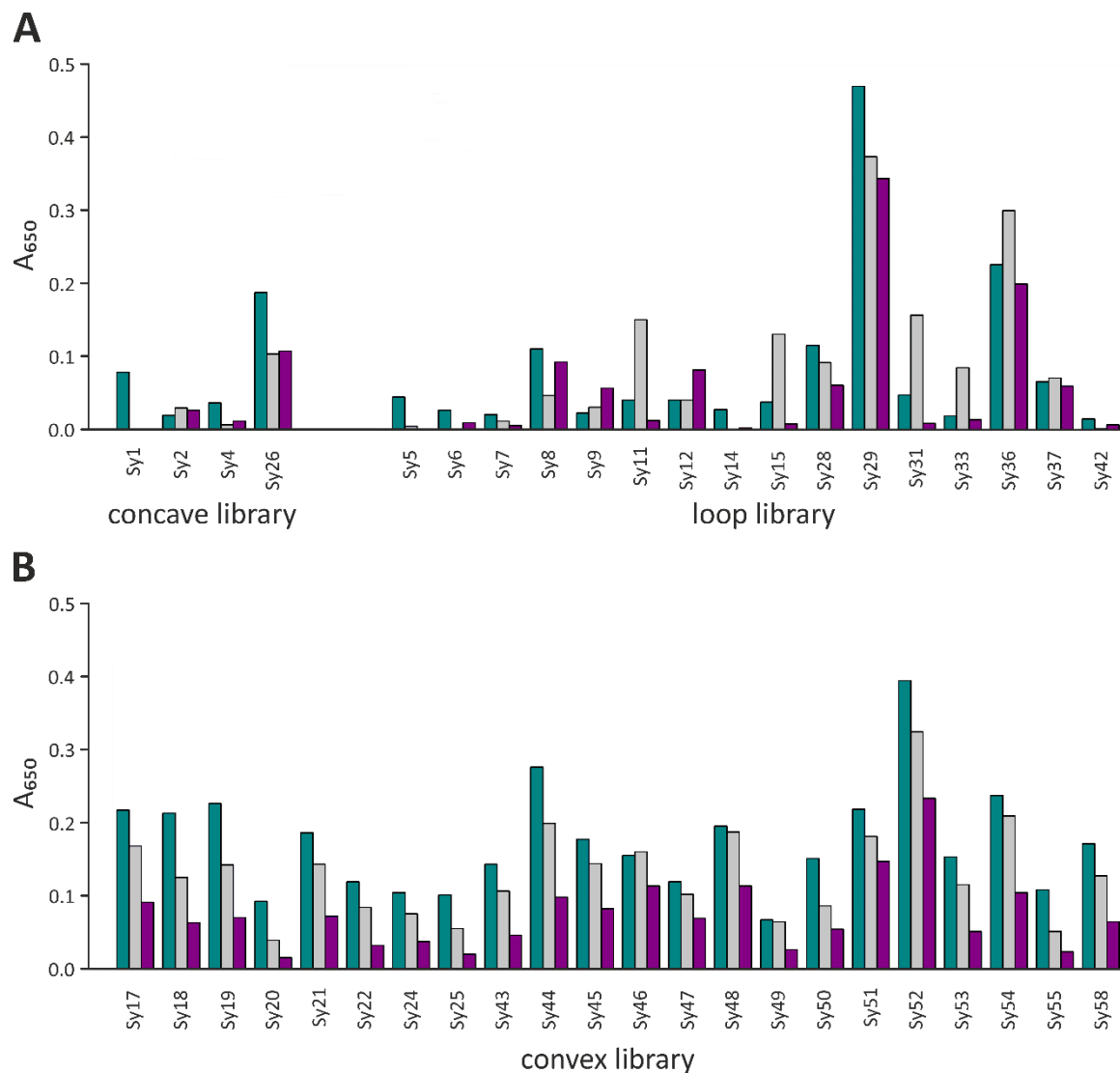


Figure 13: ELISA based binding analysis of selected sybodies. Background corrected ELISA signals of 42 unique sybodies binding to Ura_{WT} (cyan), Ura_{WT} in presence of 1 mM uracil (grey) and the inward-locked UraA mutant L80C-M143C (purple) sorted according to the three libraries the sybodies originated from (concave, loop (A), convex (B)). Sybody selection and output analysis by ELISA was performed by Prof. Dr. Eric R. Geertsma.

11.8 and 10.2 for the three libraries (concave, loop and convex) without substrate and 6.7, 19.6, 5.6 in the presence of uracil. Overall, enrichment was highest in the loop library and for the concave and loop library addition of uracil led to higher enrichment. In the convex library the opposite effect was observed. ELISA with 2 x 95 individual clones for each of the three libraries gave 96 hits in total whereof 58 were further analyzed by sequencing based on the ELISA (**Figure 13**), resulting in 40 unique sybody sequences, 13 redundant sequences and 5 sequences that could not be analyzed (**Supplementary figure 10**). The 40 unique sybodies were purified yielding 31 sybodies with a monodisperse size exclusion profile. The remaining 9 sybodies were discontinued as a result of their low expression level (7) or size exclusion profile showing multiple peaks (2). ELISA signals were larger from the convex library compared

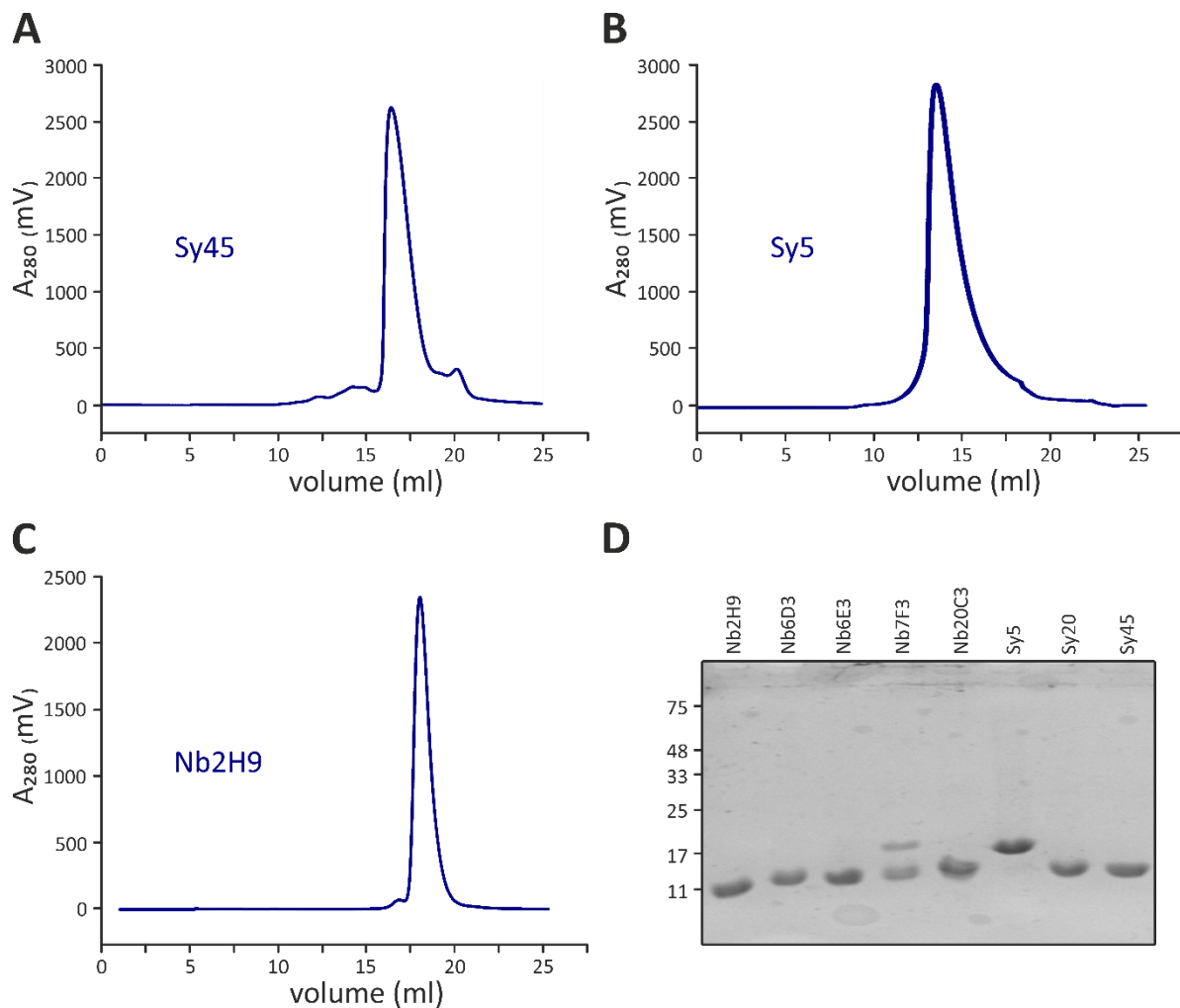


Figure 14: Purification of nanobodies and sybodies by SEC. Chromatogram of Sy45 (A), Sy5 (B) and Nb2H9 (C) from size exclusion chromatography using a Sepax SRT-10C SEC-300 column. (D) Main peak fractions were loaded on SDS-PAGE and analyzed by Coomassie staining.

to the concave and loop library with the exception being Sy29. Addition of uracil led to significantly higher signals for Sy11, Sy15, Sy31, Sy33, and Sy36, all derived from the loop library. Sy11, Sy15, Sy31 and Sy33 showed reduced binding to the crosslinked Ura_{L80C-M143C} variant. Binders from the other two libraries showed no significant uracil dependence but slightly lower ELISA signals in presence of uracil. Binding to Ura_{L80C-M143C} by binders from the convex library was generally reduced compared to Ura_{WT} binding.

4.2 Nanobody characterization

Production of a sub-selection of the selected nanobodies and sybodies was scaled up to 1 L expression cultures and after purification by IMAC and SEC (Figure 14A, B, C and Supplementary figure 11) 10 to 20 mg protein of high purity was obtained (Figure 14D). Most nanobodies eluted reproducibly at a volume of approximately 18 mL from the Sepax SRT-10C

SEC-300 column with only minor variations between the individual proteins except Nb7F3 with later elution at 21 mL (**Supplementary figure 11**). The size exclusion profiles of synthetic nanobodies mostly showed a broader elution peak in combination with pronounced variation in the elution volume for individual binders as observed for Sy5 with elution volume of 13.4 mL (**Figure 14B**). The latter may result from the increased hydrophobicity of sybodies (Zimmermann et al., 2018). However, Sy5, Sy20 and Sy45, the best characterized sybodies used in this study, showed good biochemical quality underlining that this was not a concern regarding sybodies.

4.2.1 Thermal stabilization of UraA_{WT} by selected binders

Thermal stabilization of a target protein by binding of a ligand or other binder can be related to conformational specificity of the binder (Sigoillot et al., 2019). Melting curves of UraA_{WT} in the presence and absence of nanobodies were recorded in order to identify nanobodies with this binding characteristic. Initially, melting curves were prepared by incubating the UraA_{WT}-GFP fusion construct at elevated temperatures in presence or absence of nanobodies followed by FSEC analysis (Kawate et al., 2006). By plotting the chromatogram peak intensities against the temperature, the data could be analyzed by non-linear curve fitting with a Boltzmann equation to calculate the melting temperature. In absence of nanobodies, UraA_{WT}-GFP showed a melting temperature of 49.5 ± 0.7 °C (**Figure 15A, B**) that was shifted to 59.2 ± 0.06 °C in the presence of Nb7B6 (**Figure 15B**). While this methodology allows reproducible determination of melting point, it suffers from an increased sample consumption and low throughput. In contrast differential scanning fluorimetry (DSF; Niesen et al., 2007; Alexandrov et al., 2008) requires less than 10 µg protein and allows parallel determination of melting points for 36 samples. The unfolding reaction of the target protein is monitored via the fluorophore CPM that reacts with free thiols of exposed cysteine residues via the maleimide moiety upon unfolding of the protein and thereby shows increased fluorescence intensity. Four cysteine residues are present in UraA_{WT} and inaccessible to maleimide labeling in the folded state of the protein (**Supplementary figure 12**). Upon protein unfolding the cysteines become accessible for maleimide labeling as tested by addition of PEG-5000 maleimide in presence or absence of SDS. The melting temperature of UraA_{WT} was calculated from the raw

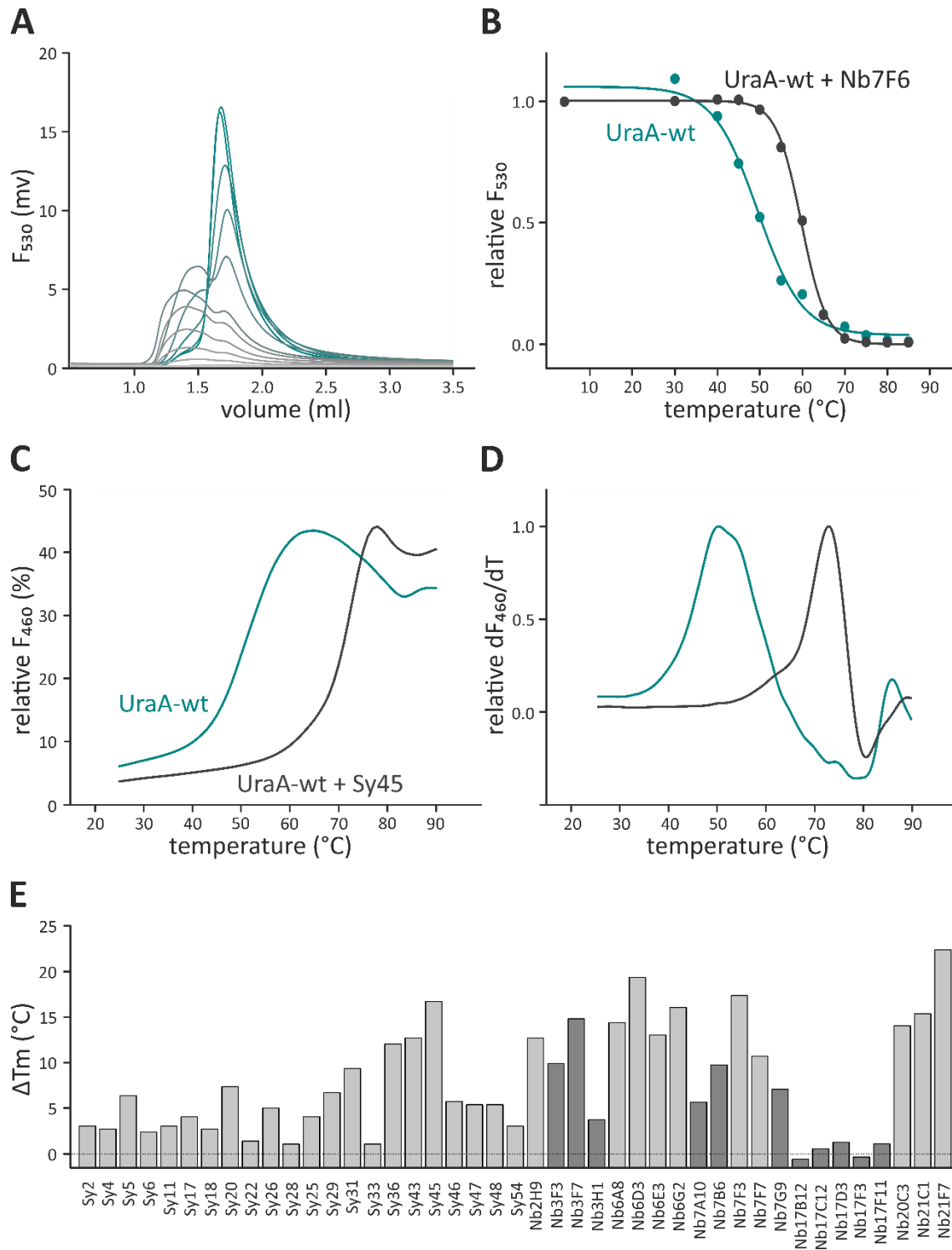


Figure 15: Thermal stabilization of UraA_{WT} by selected nanobodies and sybodies. (A) FSEC chromatograms of UraA_{WT}-GFP after thermal melting at increasing temperatures and derived melting curve for UraA wt-GFP in presence (grey) or absence (cyan) of Nb7B6 fitted with a Boltzmann equation (B). FSEC was performed with a Superdex 200 5/150 column on an Agilent HPLC with an Agilent 1260 infinity fluorescence detector with fluorescence emission and detection at 480 nm and 530 nm, respectively. (C) Differential scanning fluorimetry of UraA_{WT} (cyan) and UraA_{WT} in presence of Sy45 (dark grey). (D) The first derivative visualizes the melting temperature as its maximum. (E) Binder-induced shifts of UraA melting temperature as determined by DSF (UraA_{WT}, light grey) or FSEC (UraA_{WT}-GFP, dark grey). Expression and purification of sybodies for initial analysis was performed by Eric R. Geertsma.

data by using the maximum of the first derivative that was automatically calculated from the raw data by the Rotor-Gene Q software (**Figure 15D**). After reaching the maximum fluorescence intensity upon unfolding the signal decreased due to aggregation of the unfolded protein (**Figure 15C**). The melting temperature of UraA_{WT} was determined to be 50.2 °C showing good agreement with the calculated T_m based on FSEC (**Figure 15D**) allowing direct comparison of nanobody induced thermal stabilization of UraA determined by these two methods.

Regardless of the applied method for melting temperature determination, addition of nanobody or sybody in this screening increased the melting temperature in most cases (**Figure 15E**) whereas the largest shift was caused by Nb21F7 with +22.3 °C followed by Nb6D3 with +19.3 °C suggesting strong conformational-selective binding. Additionally, various selected nanobodies induced an increase in melting temperature of more than 10 °C. All nanobodies derived from master plate MP017 that were selected against UraA_{Cysless-1252C}-PEG-5000 did not stabilize UraA_{WT} which was in line with the low signals in ELISA performed at 20 °C and confirmed the hypothesized conformational unspecific binding of nanobodies showing this characteristic.

Among the analyzed sybodies, Sy45 stabilized UraA_{WT} with +16.7 °C thus in the range of the best alpaca derived nanobodies. However, most sybodies stabilized the target protein with shifts in T_m between +3 °C and +6 °C and thus less compared to the alpaca derived binders. Binding of Sy22, Sy28 or Sy33 induced only minor shifts of the melting temperature indicating conformational unspecific binding. However, the temperature dependent ELISA performed with the alpaca derived nanobodies already biased their selection towards thermal stabilization which was not the case for the tested sybodies and would serve as one explanation for the mostly lower stabilization of UraA by sybodies.

From the broad screening for conformational selectivity by thermal stabilization, a subset of nanobodies and sybodies was chosen for more detailed analysis. Thereby the thermal stabilization of UraA_{WT} served as one criterium next to sequence relation between certain binders, selection conditions during phage display and in the case of sybodies the library the binder originated from and the ELISA signals in presence or absence of uracil (**Figure 12**). As the aim of the selection procedure was to generate binders stabilizing many different conformations of UraA, subsequent analysis was not restricted to binders with the largest

shifts in thermal melting only. From all selected nanobodies and sybodies the following 8 binders were chosen for detailed characterization: Sy5, Sy20, Sy45, Nb2H9, Nb6D3, Nb6E3, Nb7F3 and Nb20C3. Both, Sy5 and Sy20 showed strong preference in ELISA for UraA_{WT} with reduced binding in presence of uracil or to UraA_{L80C-M143C} and the thermal stabilization of UraA in DSF suggested conformational specific binding. Sy45 was chosen based on the outstanding thermal stabilization of UraA in DSF among all sybodies. Nb2H9 was further analyzed due to the selection conditions applied during phage display including pre-panning and its reasonable binding characteristics in ELSIA and DSF. The strong thermal stabilization induced by Nb6D3 was the main criteria to further analyze this binder while Nb6E3 showed less stabilization but reproducibly yielded strongest signals in ELISA. Nb7F3 derived from a selection condition including counterselection during phage display and showed good thermal stabilization of UraA which led to its further analysis. Nb20C3 showed no outstanding binding characteristics and was selected against UraA_{WT} without any selection bias included but its CDR3 sequence similarity to Nb2H9 led to selection of Nb20C3 for subsequent analyses (**Supplementary figure 9**). The subset of binders selected for detailed analysis is presented in **Table 15** along with all important selection details and identified binding characteristics.

4.2.2 Transport inhibition reveals epitope of binders

The conformational selectivity of nanobodies and sybodies was further investigated by analyzing the transport activity of UraA_{WT} in presence of binders. As transporters undergo conformational changes in order to transport the substrate by alternating access, conformational-specific binding of a nanobody or sybody is expected to interfere with transport activity (Schenck et al., 2017). A whole cell transport assay in *E. coli* MC1061 was designed based on activity of endogenous UraA in combination with recombinantly produced nanobodies and sybodies from the pSb_init plasmid (Zimmermann et al., 2018). Thus, binders were exclusively produced in the periplasmic space due to the presence of the PelB leader sequence. The assay design allowed identification of conformational specific nanobodies and sybodies as well as their periplasmic epitope by binding induced transport inhibition. The *E. coli* BW25113 Δ uraA (JW2482) strain from the Keio collection (Baba et al., 2006) expressing a non-specific nanobody served as a negative control, while *E. coli* MC1061 expressing the same nanobody was used as positive control. From the 8 tested nanobodies and sybodies Sy20, Sy45 and Nb6E3 did not alter the transport activity of UraA (**Figure 16A**) while Nb2H9,

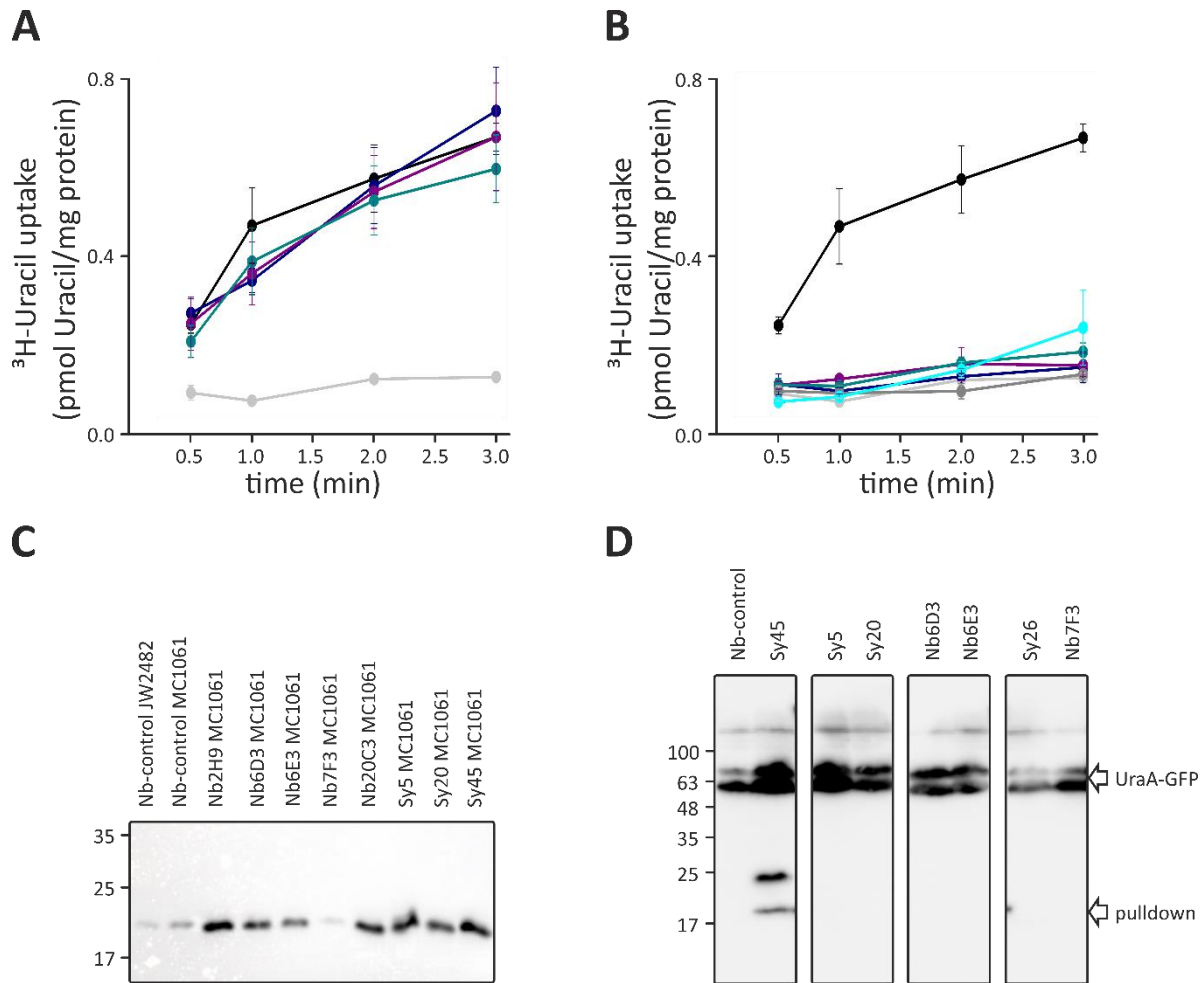


Figure 16: Whole-cell transport of ^3H -uracil by endogenous UraA in *E. coli* MC1061 in presence of recombinantly expressed nanobodies or sybodies in the periplasmic space. (A) Uracil transport in presence of Sy45 (cyan), Nb6E3 (navy) and Sy20 (purple) and a non-specific nanobody expressed either in *E. coli* MC1061 (black) or *E. coli* JW2482 (light grey) as control for transport or inhibition, respectively. (B) Uracil transport in presence of Nb2H9 (light blue), Nb6D3 (navy), Nb7F3 (purple), Nb20C3 (grey) and Sy5 (cyan) with the same controls as in panel (A). Expression of binders from the pSb_init plasmid was confirmed by anti-His western blotting (C). Pull-down of selected binders with inside-out vesicles containing UraA_{WT}-GFP recombinantly produced from the pBXC3GH plasmid. Pull-down was visualized by anti-His western blotting.

Nb6D3, Nb7F3, Nb20C3 and Sy5 reduced the uracil uptake to the level of the negative control (**Figure 16B**). The presence of all binders during the transport reaction was controlled by western blotting (**Figure 16C**). Based on these results, a periplasmic epitope for Nb2H9, Nb6D3, Nb7F3, Nb20C3 and Sy5 could be identified and their conformation specific binding mode as suggested before by thermal stabilization of UraA_{WT} could be confirmed. In the case of Sy20, Sy45 and Nb6E3 no direct evidence for a cytoplasmic epitope could be achieved. The maintained transport activity of UraA could be explained by a cytoplasmic epitope of the respective nanobody or sybody or a non-conformational specific binding to a periplasmic epitope that did not affect transport activity. As all binders were selected against detergent-solubilized UraA it might be that binders did not bind to the protein when

embedded in the lipid bilayer. As the conformational selectivity of Sy45, Sy20 and Nb6E3 was indicated before by stabilization of UraA_{WT} in differential scanning fluorimetry, a cytoplasmic epitope for these binders was most likely the reason for remaining transport activity. To test the cytoplasmic epitope theory, inside-out vesicles were prepared containing UraA_{WT}-GFP produced from the pBXC3GH plasmid in *E. coli* MC1061. The orientation of inside-out vesicles was verified by cleavage of the HRV-3C protease site preceding the GFP in UraA-GFP with HRV-3C protease and subsequent SDS-PAGE and was quantified to be 88% inside-out (**Supplementary figure 13**) based on densitometry analysis of in-gel fluorescence intensity of protease cleaved free GFP and UraA_{WT}-GFP performed with ImageJ (Schneider et al., 2012). The inside-out vesicles were used for pulldown of binders recognizing a cytoplasmic UraA epitope that were subsequently visualized by SDS-PAGE and western blotting (**Figure 16D**). From the tested binders, only Sy45 was successfully pulled down by the inside-out vesicles, which confirmed a cytoplasmic epitope for Sy45. Sy20 and Nb6E3 showed no pulldown thus direct experimental evidence for the cytoplasmic epitope of these two binders could not be created. Consistent with the periplasmic epitope identified by transport inhibition, Nb7F3, Sy5 and Nb6D3 did not show pulldown by inside-out vesicles.

In summary, side specific transport inhibition and pulldown, that took advantage of the natural *E. coli* membrane sidedness, were used to extract epitope information for the subset of 8 binders. This led to epitope identification of six binders whereas five were binding to a periplasmic epitope and only Sy45 to a cytoplasmic epitope. The cytoplasmic epitope of Sy20 and Nb6E3, respectively, as suggested by the remaining transport activity, could not be confirmed by pulldown likely due to poor binding to UraA when embedded in the lipid bilayer or fast dissociation kinetics of the binders.

4.2.3 Conformation mapping of binders

Identification of conformational selectivity and low-resolution epitope mapping was successfully performed for the subset of 8 binders by transport inhibition and thermal stabilization of UraA. However, the aim to stabilize different conformations of UraA required a concluding selection criterium that allowed differentiation of stabilized UraA conformations. Therefore, simultaneous binding of two different binders was tested by additional thermal stabilization of UraA in differential scanning fluorimetry. In general, the shift in melting

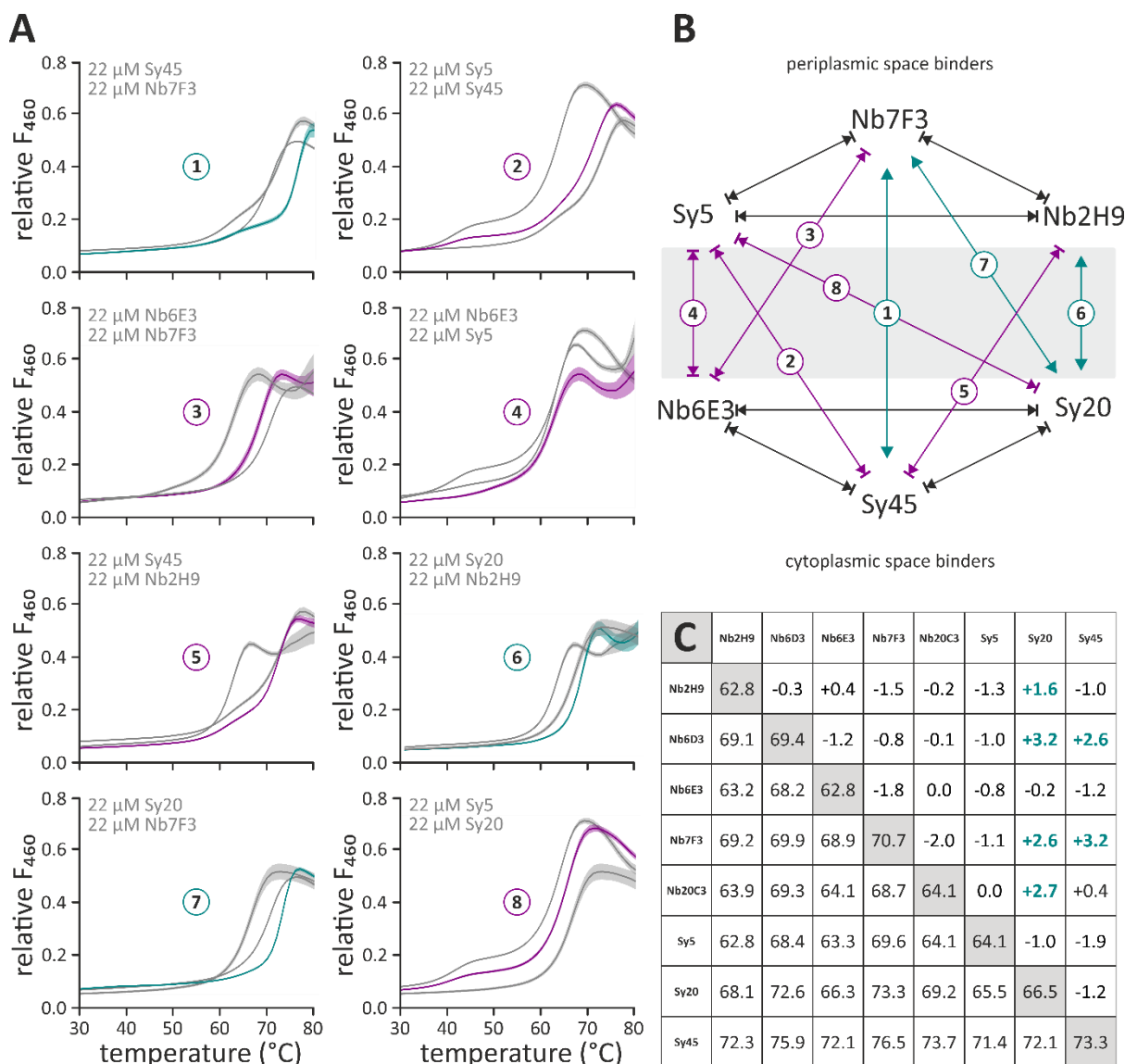


Figure 17: Simultaneous binding analysis of nanobodies and sybodies. (A) Thermal melting analysis of UraA_{WT} by DSF in presence of two different binders at 11 μ M each (cyan: additional stabilization, purple: competition) compared to single binder melting reactions in grey. Presented are the mean values of triplicates and corresponding standard errors. (B) Schematic representation of binder interactivity with the membrane indicated as grey box causing spatial separation of periplasmic space binders (Nb7F3, Sy5 and Nb2H9) and cytoplasmic space binders (Nb6E3, Sy45 and Sy20). Simultaneous binding of two binders is shown by a cyan arrow and conformational competition by purple lines with numbers as crossreference to data presented in (A). Competition that was not attributed to stabilization of different conformations is indicated as black line. Nb20C3 and Nb6D3 are not included in (B) due to identical interactivity as Nb2H9 or Nb7F3, respectively, as presented in (C). (C) Overview of all binder combinations for the set of 8 different binders with the diagonal presenting the T_m of UraA_{WT} in presence of 22 μ M of the individual binder. The lower left corner represents the T_m values of UraA_{WT} in presence of 11 μ M of each of the two tested binders. The upper right corner shows the shifts in the T_m of UraA_{WT} calculated by subtraction of the combined melting temperature (lower left corner) from the higher T_m of UraA_{WT} in presence of only one binder (diagonal).

temperature of a protein upon ligand binding depends on the ligand concentration (Scott et al., 2016) and in this case on the binder concentration. In order to guarantee the saturation of UraA thermal stabilization by the individual binders at 5-fold molar excess (11 μ M), the UraA melting temperature in presence of 10-fold molar excess (22 μ M) was also determined and

both measurements were compared (**Supplementary figure 14**). As control, the nanobodies and sybodies were also analyzed in absence of UraA to identify interfering signals introduced by the binders alone. These controls showed comparably low signals for all binders except Nb6E3 and Nb20C3 that gave rise to increase in fluorescence above 70 °C. These nanobody derived signals were also visible in the melting curves of UraA in presence of one of these binders as additional signal but did not hamper melting temperature determination (**Supplementary figure 14**). Regarding the saturation of the melting temperature in presence of 11 μM and 22 μM nanobody or sybody, all samples except Nb6E3 showed similar melting curves and melting temperatures. For the addition of 11 μM Nb6E3, a second transition at approximately 50 °C was present representing probably unbound UraA_{WT} but the second transition of the UraA_{WT}-Nb6E3 complex showed a similar melting temperature as observed in the sample with 22 μM Nb6E3. Consequently, an increased melting temperature of UraA_{WT} in presence of two different binders both at a concentration of 11 μM compared to the melting temperature induced by 22 μM of an individual binder can be assumed to rely on simultaneous binding of the two binders. A trivial effect based on different amounts of binders present in the sample and unsaturated UraA could be excluded.

The thermal shift assay with Sy45 and Nb7F3 showed additional stabilization of UraA_{WT} by +3.2 °C in presence of 11 μM of Sy45 and Nb7F3 compared to the melting temperature in presence of 22 μM Sy45 (**Figure 17A**). The additional stabilization to an absolute T_m of 76.5 °C indicated the simultaneous binding of Nb7F3 and Sy45 to UraA_{WT} in an conformational specific manner and as consequence these two binders are likely to stabilizing the same conformation of UraA – the inward-facing conformation (*vide infra* **Figure 27**). The same analysis with Sy5 and Sy45 respectively Sy5 and Nb7F3 resulted in intermediate melting temperatures compared to the melting analysis with a single binder indicative of a competition between Sy5 and Sy45 or Nb7F3, respectively (**Figure 17C**). Valuable information was retrieved from competition when a trivial, steric competition, due to overlapping epitopes, could be excluded based on epitope analysis as in case of Sy45 and Sy5. Hence, Sy5 was identified to stabilize a different conformation than Sy45 and Nb7F3. In case of Nb7F3 and Sy5 an epitope overlap could not be excluded as both inhibit UraA transport activity by binding to a periplasmic epitope (4.2.2). However, the opposing thermal stabilization of UraA resulting from these binders in combination with Sy45 indicated the conformational competition though an additional steric competition between Sy5 and Nb7F3 might exist.

The simultaneous binding analysis of Sy5, Sy45 and Nb7F3 illustrated that the combination of thermal melting and low-resolution epitope mapping yields relative information on the stabilized UraA conformation. In order to identify more conformations of UraA, that are stabilized by selected binders, the simultaneous DSF analysis was extended to the full set of 8 binders following the example of Sy45, Nb7F3 and Sy5 (**Figure 17C**). The analysis revealed simultaneous binding of Nb6D3 with Sy45 identified by a T_m -shift of +2.6 °C and competition with Nb7F3 indicated by reduction in T_m of -0.8 °C (**Figure 17C**). Thus, Nb6D3 was identified to stabilize the inward-facing Sy45 conformation (*vide infra* **Figure 27**).

The analysis for Nb6E3 showed competition with Sy5 and Nb7F3 (**Figure 17B**) that could be identified as conformational competition based on the cytoplasmic epitope of Nb6E3 and periplasmic epitope of Sy5 and Nb7F3. Nb6E3 thus stabilized UraA in a different conformation than Sy5 and Nb7F3, representing a third identified UraA conformation next to the Sy5 and Sy45 conformation.

Sy20 showed simultaneous binding with Nb2H9 and Nb7F3 but Nb2H9 did not interact with Sy45 as observed for Nb7F3 (**Figure 17B**). Therefore, Nb2H9 could not be identified to stabilize a unique conformation different from the Sy45/Nb7F3 conformation. The analysis for Nb20C3 revealed a similar pattern as observed for Nb2H9. The network of Sy45, Sy20, Nb7F3 and Nb2H9 suggested an inward-facing conformation specificity for Sy20 like Sy45 (*vide infra* **Figure 27**) but slightly different allowing simultaneous binding with both Nb7F3 and Nb2H9 on the periplasmic side. A conformational unspecific binding mode of Sy20 as explanation was excluded due to the thermal stabilization of UraA by Sy20 and the conformational competition of Sy20 with Sy5.

In summary, the nanobody and sybody selection led to identification of three binders stabilizing UraA in distinct conformations: Nb6E3, Sy5 and Sy45. Structural and functional studies on UraA with focus on only these three binders would significantly increase the mechanistical understanding of transport in UraA and other 7-TMIR proteins. In addition, similar patterns of competition and stabilization of Nb7F3 and 6D3 revealed the Sy45 conformation of UraA being stabilized by these two binders and allowed to focus on only one of these binders for further characterization of UraA. Similar patterns of Nb2H9 and Nb20C3 suggested the same conformation stabilized by both binders but whether this conformation

was distinct from the Sy45 conformation remained elusive due to the contradicting simultaneous binding with Sy20.

Table 15: The subset of 8 diverse binders and their identified binding properties and characteristics. All binders were selected against UraA_{WT}.

	selection bias	induced ΔT_m of UraA (°C)	epitope	stabilized conformation
Nb2H9	pre-panning, UraA _{L80C-M143C}	13.9 ± 0.3	periplasmic side	-
Nb6D3	-	20.6 ± 0.5	periplasmic side	Sy45
Nb6E3	-	13.9 ± 0.4	cytoplasmic side	unique
Nb7F3	counterselection, UraA _{Cysless-M143C-PEG-5000}	21.8 ± 0.3	periplasmic side	Sy45
Nb20C3	-	15.1 ± 0.4	periplasmic side	-
Sy5	-	15.1 ± 0.3	periplasmic side	unique
Sy20	-	17.6 ± 0.2	cytoplasmic side	-
Sy45	uracil	24.4 ± 0.4	cytoplasmic side	inward-facing

4.3 Conformational modulation of UraA

The second strategy applied for conformational specific stabilization of UraA, beside the nanobody based approach, involved site-directed mutagenesis at mechanistically relevant positions in UraA_{WT} in order to manipulate its conformational space. A preliminary knowledge of the transport mechanism was required for identification of suitable positions. Therefore, UraA_{3QE7} and UraA_{5XLS} (Lu et al., 2011, Yu et al., 2017) and structures from the SLC4 and SLC26 family were analyzed and a shared structural feature of elevator transport identified – the alpha-helical inter-domain linkers connecting transport and scaffold domain (**Figure 2**). The prerequisite for elevator transport being the transport domain movement of several angstrom with respect to the scaffold domain along with the rigid secondary structure of the inter-domain linkers connecting both domains led to the hypothesis of a modulation of transport domain movement by these inter-domain linkers. Thereby, a rigid connection of the inter-domain linkers to the scaffold domain and the alpha-helical fold of the linker itself would build a solid framework around the transport domain supporting elevator movement of the latter. Consequently, the connection of inter-domain linker to transport domain would constitute a conformational hinge as postulated by Chang et al. (2017), that determines the

conformational space of the transporter. Consistently, manipulation of these conformational hinges would alter the conformational space of UraA.

4.3.1 Identification and manipulation of conformational hinges in UraA

In order to manipulate the conformational space of UraA via its conformational hinges, crucial residues in the putative hinge regions of UraA were aimed to be identified based on altered dihedral angles of residues in UraA_{5XLS} and UraA_{3QE7}, the two published UraA structures (**Figure 18**). On the cytoplasmic side of UraA, larger differences in dihedral angles were observed at position Lys-110 and Ala-111, at the transition of TM4 to the inter-domain linker. On the periplasmic side, this effect was more significant with a hot-spot at position Cys-318 and Val-319 at the transition from TM11 to the inter-domain linker. Only minor changes were observed within the alpha-helical part of both inter-domain linkers due to the secondary structure. Differences in the dihedral angles were less prominent and distributed over a wider range on the gate domain facing side of both inter-domain linkers, in line with the hypothesis of a more rigid linkage of gate domain and inter-domain linker. Based on this analysis, hinge regions in UraA could be identified at the transition from core domain to both inter-domain linkers at the stated residues as highlighted in the upper panel (**Figure 18**). In addition, a more general analysis based on sequence alignment of 3067 UraA homologs with a minimal and maximal sequence identity to UraA of 40% and 99%, respectively, was performed with focus on the inter-domain linkers and adjacent positions, visualized as sequence logos (**Figure 18**). Two conserved proline residues were identified at position 121 and 122 in UraA suggesting a structurally rigid linkage of gate domain and periplasmic inter-domain linker. Positively charged and hydrophobic amino acids were found in the center of the cytoplasmic inter-domain linker with a highly conserved tryptophan residue at position 115 in UraA, reflecting the secondary structure with the amphipathic helix lying horizontally in the lipid bilayer following the positive inside rule (von Heijne, 1989). Sequence conservation was lower on the core domain facing side of the inter-domain linker with the exception being a highly conserved glycine residue at position 112 in UraA that implied a more flexible linkage of core domain and inter-domain linker. This residue was observed to succeed the potential cytoplasmic hinge at position 110 and 111 suggested by the dihedral angle analysis. Thus, proline scanning ranging from position 110 to 115 was performed to cover the whole range of

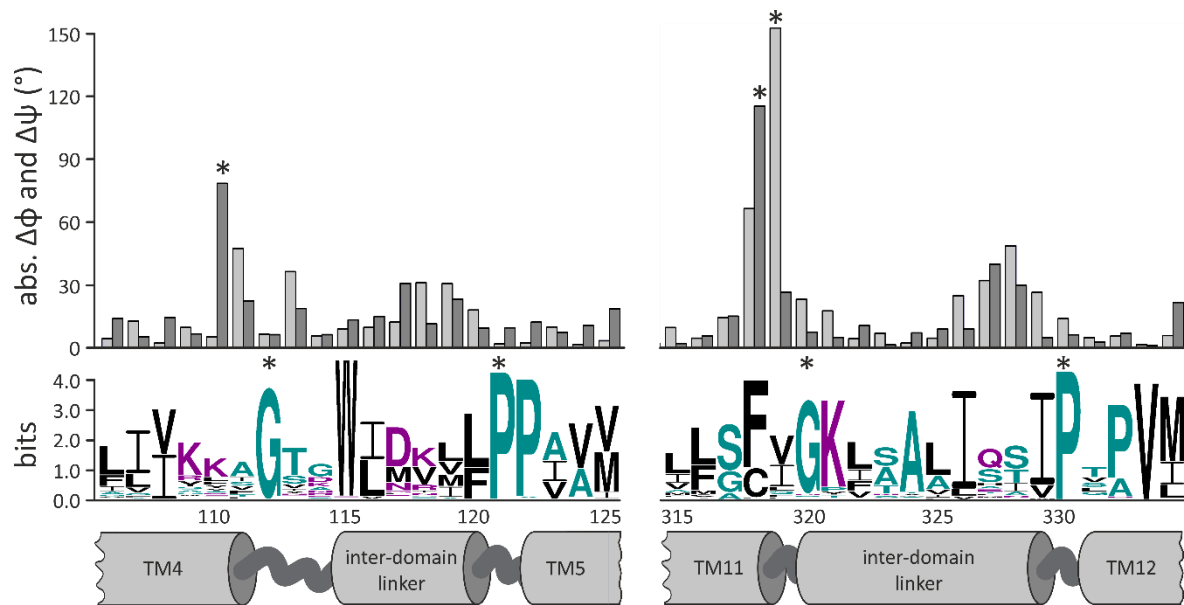


Figure 18: Bioinformatic analysis for identification of conformational hinges in UraA. Absolute differences in dihedral angles ($\Delta\phi$, grey; $\Delta\psi$, dark grey) of the two published UraA structures (PDB: 3QE7 and 5XLS) in the inter-domain linker regions. The potential conformational hinges at position 110, 318 and 319 are highlighted by an asterisk in the upper panel. Sequence alignment of 3067 UraA homologs with a minimal and maximal sequence identity of 40% and 99%, respectively, performed by Clustal Omega (Madeira, Park et al., 2019) and visualized as sequence logo, created by WebLogo 3 (Crooks et al., 2004). The putative relevant positions G112, P121, G320 and P330 in UraA are highlighted with an asterisk in the middle panel. A cartoon representation of both inter-domain linkers with adjacent transmembrane segments of the core (TM4 and TM11) and the gate (TM5 and TM12) domain is depicted in the lower panel.

putative functional relevant positions in the cytoplasmic inter-domain linker of UraA in order to identify and manipulate the conformational hinge.

The periplasmic inter-domain linker featured a highly conserved proline at position 330 in UraA. A second proline was identified at position 332 but with less conservation and the intermediate amino acid at position 331 was not conserved. This finding suggested a rigid architecture of the periplasmic inter-domain linker on the gate domain facing side similar to the observation for the cytoplasmic inter-domain linker. The alpha-helical part of the inter-domain linker was mostly built-up by small and hydrophobic amino acids in line with an amphipathic nature of the alpha helix as is observed more commonly for helices at the membrane interface. This was further illustrated by two conserved isoleucine residues at positions 326 and 329 in UraA pointing towards the hydrophobic center of the lipid bilayer. The core domain facing side of the inter-domain linker featured two conserved positions with Gly-320 and Lys-321. The strong conservation of the glycine residue suggests that the connection between the core domain and the linker needs to be more flexible. Additionally, Gly-320 was found to be located next to the identified hot-spot at Cys-318 and Val-319 that showed significant changes in the dihedral angle analysis. Thus, proline substitution was

performed at position 320 in order to influence the local flexibility at this and the preceding position.

The rigid connection of both inter-domain linkers to the gate domain with the PP-motif on the cytoplasmic side and the P-x-P-motif on the periplasmic side was manipulated by glycine substitution at position 121 and 330 to increase the flexibility at these positions. Site-directed mutagenesis of most tested UraA variants was performed by Dogukan Özkul as part of his Master studies and the UraA variants A111P, T113P, G114P and W115P were created by Sebastian Falkner.

4.3.2 Functional analysis of inter-domain linker variants in UraA

The impact of the linker variants of UraA on the uracil transport activity was determined by whole cell transport assays. The UraA variant E241A-H245A-E290A holding mutations in three residues that are crucial for uracil binding (Lu et al., 2011), served as negative control. The proline scanning in the cytoplasmic inter-domain linker ranging from position 110 to 115 yielded a reduced transport rate for UraA_{G112P} and UraA_{P121G} to the level of the negative control at an uracil concentration of 0.25 μM (**Figure 19A**). Other UraA variants from the cytoplasmic inter-domain linker showed reduced activity compared to UraA_{WT} but less severe. Thereby, position 111 was least effected by the proline substitution with 80% remaining activity in contrast to position 110 and 114 with only 30% remaining activity. Analysis of the periplasmic inter-domain linker variants showed no transport activity for UraA_{G320P} and alanine substitution at position 320 resulted in increased transport rates but not significantly higher than the background. UraA_{P330G} showed similar low transport rates as UraA_{G320P} but the activity could be restored by alanine substitution to 70% of the wildtype activity. The recombinant expression of UraA variants from the plasmid pBXC3GH for whole cell transport was tested by loading cell lysates on SDS-PAGE and subsequent in-gel fluorescence detection of the UraA-GFP fusion proteins (**Figure 19B**; Geertsma et al., 2008b). Purified UraA_{WT}-GFP was loaded on the same SDS gel as protein standard. The expression test showed similar band intensities for the UraA proline mutants at the cytoplasmic inter-domain linker ranging from position 110 to 115 suggesting successful expression and protein folding of these variants for the transport assay (Drew et al., 2001). UraA_{P121G} could reproducibly not be detected by in-gel fluorescence suggesting impaired protein folding or stability of UraA_{P121G} resulting in protein degradation. The periplasmic inter-domain linker variants showed reduced, but significant in-

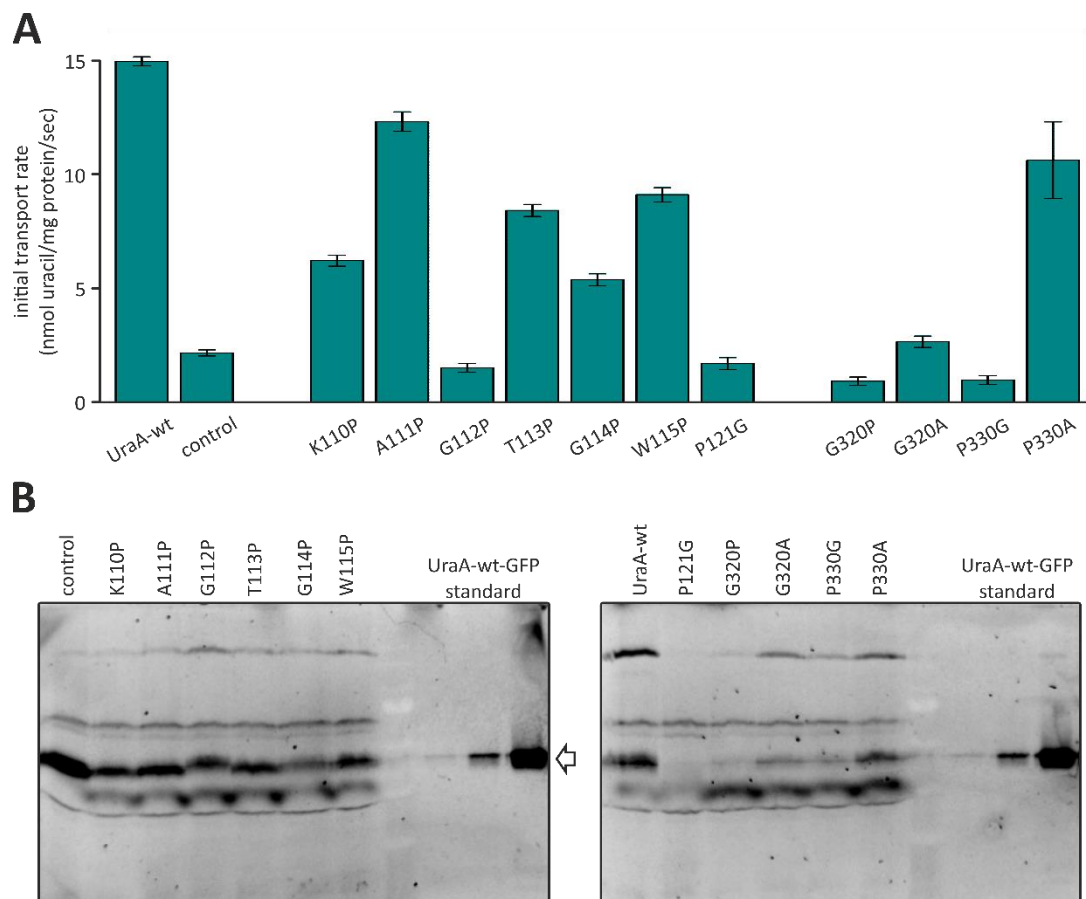


Figure 19: Functional analysis of inter-domain linker variants. (A) Initial uptake rates of UraA_{WT} and the tested variants measured by radioactive whole cell transport in presence of 0.25 μ M uracil (2.5% 3 H-uracil) in *E. coli* BW25113 Δ uraA. Transport reactions were quenched after 30 seconds and cells collected by fast filtration. The UraA variant E241A-H245A-E290A with impaired uracil binding served as negative control and was prepared by Katharina Holzhüter. (B) Expression test of UraA-variants from the same batch of cells used for transport experiments. Purified UraA_{WT}-GFP was loaded as protein standard for in-gel fluorescence detection of UraA-GFP fusion proteins.

gel fluorescence intensities for UraA_{G320P}, UraA_{G320A} and UraA_{P330G} compared to UraA_{WT}, suggesting a partial reduction in transport activity caused by the lower amount of transporters present. However, the complete loss of transport activity must be based on an additional functional effect.

Based on these results, the UraA variants G112P, G320P and P330G were selected for detailed biochemical analysis as the impaired transport revealed a major impact of the three conserved positions on UraA translocation, in line with a suspected hinge function. The three UraA variants were produced in large amounts in a 9 L culture grown in a fermenter and isolated by IMAC and SEC as described (3.4.5). The isolated UraA variants were analyzed by SDS-PAGE and Coomassie staining indicating high sample purity and no protein degradation (**Figure 20**).

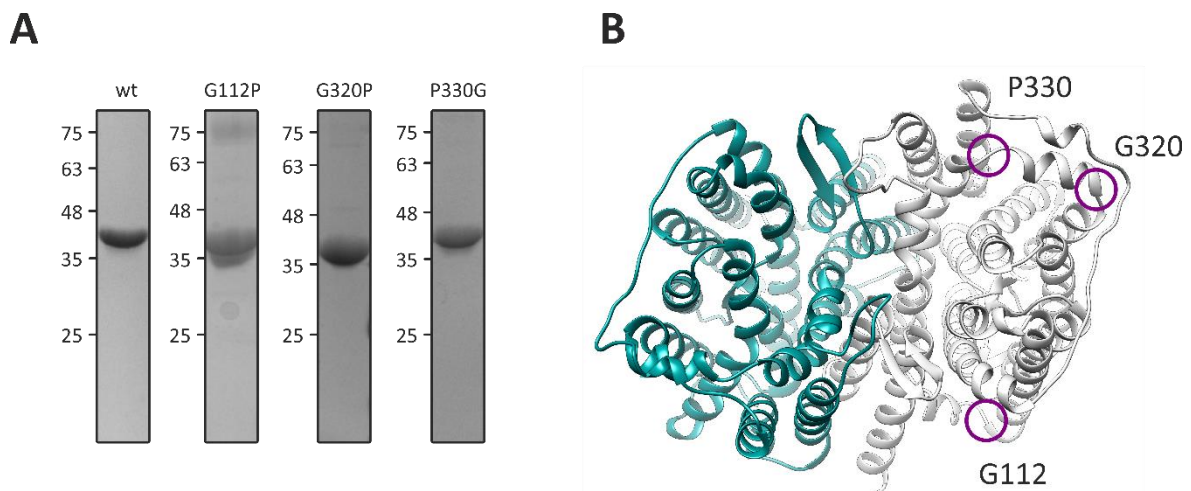


Figure 20: Purification of inter-domain linker variants of UraA. (A) UraA variants were purified by IMAC and SEC from detergent solubilized membrane vesicles yielding highly pure protein as visualized by SDS-PAGE and Coomassie staining. (B) Top view on the dimeric occluded structure of UraA with the first protomer in cyan and the second in light grey. Positions of substituted amino acids for creation of UraA variants are indicated by purple circles and labeled accordingly. Purification of UraA_{G112P} was performed by Dogukan Özkul as part of his Master studies.

4.3.3 Biochemical characterization of UraA_{G112P}, UraA_{G320P} and UraA_{P330G}

Size exclusion chromatography performed as last step in the purification of UraA_{G112P}, UraA_{G320P} and UraA_{P330G} revealed deviations in the elution profile of UraA_{G320P} and UraA_{P330G} compared to UraA_{WT} indicative of an altered oligomeric state. The chromatogram for UraA_{WT} showed a main elution peak at 13.25 mL with a small shoulder at 12.2 mL. These two fractions were assigned to monomeric and dimeric forms of UraA based on static light scattering by Yu et al. (2017). Thereby, the elution volumes of the monomeric and dimeric form of UraA by considering the additional molecular weight of the DM micelle (33 kDa) were in line with the calibration curve for the Superdex 200 increase 10/300 GL column provided by the manufacturer with elution of Aldolase (158 kDa) at 12.6 mL and Conalbumin (75 kDa) at 14 mL. Even though the fraction of dimer in UraA_{WT} was minor in the analytic size exclusion, it was observed to be approximately 10% in preparative size exclusion chromatography using larger protein amounts (**Figure 21**), suggesting a concentration dependent monomer-dimer equilibrium. UraA_{G112P} revealed a similar elution profile as UraA_{WT} with the monomer eluting at 13.25 mL, suggesting a similar monomer dimer equilibrium as observed for UraA_{WT}. UraA_{G320P} showed an increased dimer fraction of approximately 30% eluting at 12.1 mL which was also observed to underlie a certain batch to batch variation and concentration dependence (**Figure 21**) while the monomer elution was shifted to 13.1 mL compared to

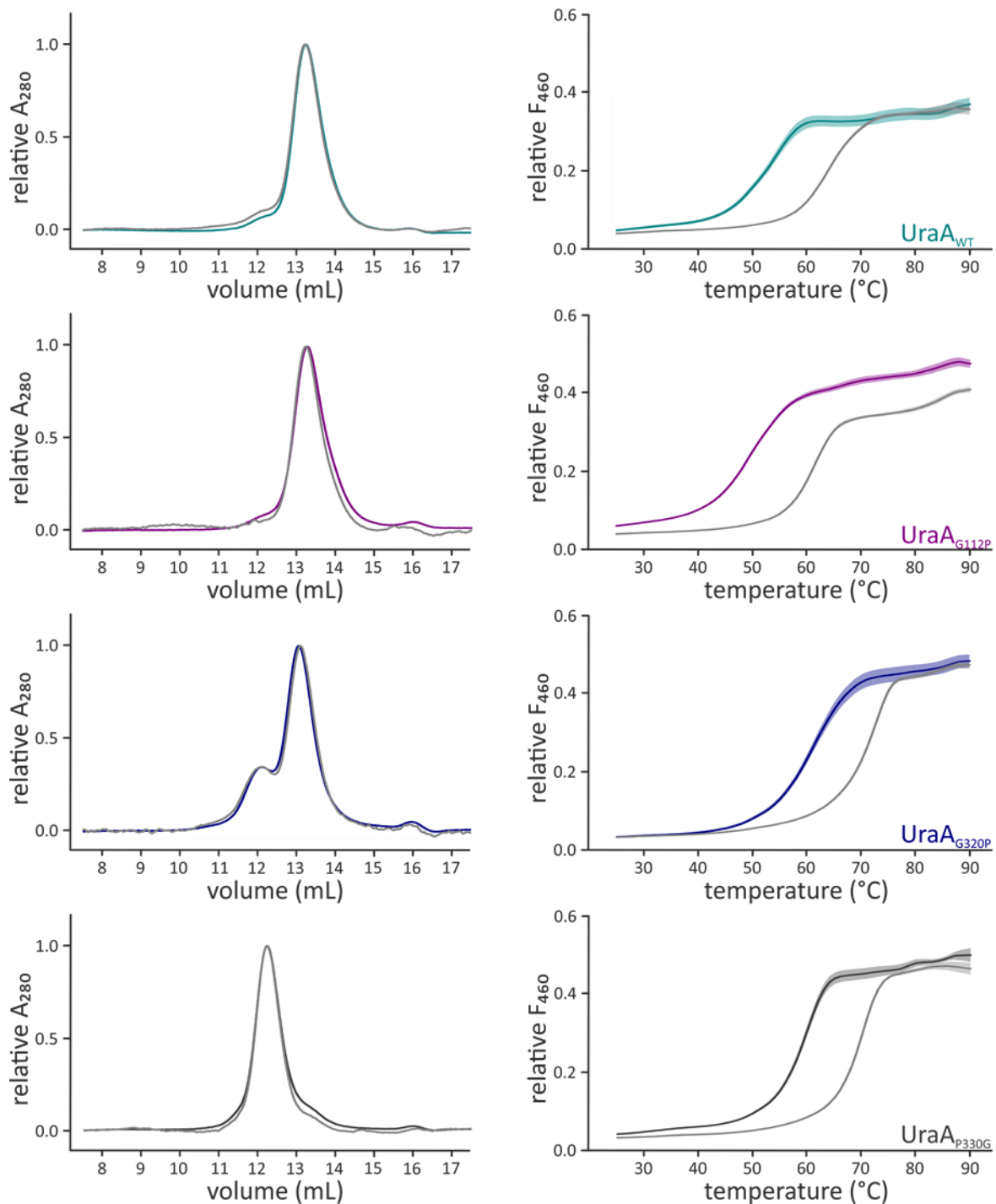


Figure 21: Biochemical characterization of UraA inter-domain linker variants. (left panel) Analytical size exclusion in presence and absence of 1 mM uracil using 100 μ g of purified protein on a Superdex 200 increase 10/300 GL column at a flow rate of 0.4 mL/min for UraA_{WT} (cyan), UraA_{G112P} (purple), UraA_{G320P} (blue) and UraA_{P330G} (grey). Elution profiles from samples containing 1 mM uracil are shown in light grey color. The signals were normalized to the peak maximum for better visualization. (right panel) Differential scanning fluorimetry for melting temperature analysis in presence or absence of 1 mM uracil shown as mean of triplicates and its standard error. The relative fluorescence of CPM was excited at a wavelength of 365 ± 20 nm and detected at a wavelength of 460 ± 20 nm using a detector gain of -2. All samples containing uracil are shown in light grey color.

UraA_{WT}, which could result from overlapping of the two peaks. UraA_{P330G} was almost exclusively dimeric with a peak at 12.23 mL and a small shoulder at 13.5 mL that could represent a small fraction of monomeric protein. In summary, the size exclusion chromatograms showed a good protein quality for the introduced inter-domain linker mutants with significant effects of the amino acid substitutions G320P and P330G on the oligomeric state of UraA. The analytical size exclusion was also performed in presence of the substrate uracil but without any effect on the elution profiles. Thus, binding of uracil did not affect the oligomeric state of the tested UraA variants.

The UraA inter-domain linker variants were further characterized by differential scanning fluorimetry in order to determine the melting temperature in presence and absence of uracil as quantitative measure for substrate binding. The resulting melting curve for UraA_{WT} yielded a melting temperature of 54.2 °C that was shifted to 61.5 °C upon addition of uracil due to stabilization of the protein by uracil binding (Scott et al., 2016). A melting profile with reduced melting temperature of 49.2 °C was observed for UraA_{G112P} with a shift to 61.6 °C in presence of uracil. In contrast, UraA_{G320P} showed a significant thermal stabilization with a melting temperature of 61.4 °C similar to UraA_{WT} in presence of uracil and addition of uracil to UraA_{G320P} further shifted the melting temperature to 72.2 °C confirming that the *ab initio* thermal stabilization of UraA_{G320P} was not based on co-purification of uracil but rather represented an intrinsic property of this UraA variant. UraA_{P330G} was also found to be thermostabilized with similar melting temperature as UraA_{G320P} of 59.9 °C and additional stabilization by uracil binding with a T_m of 70.2 °C. Beside the shift in melting temperature of UraA_{G320P} and UraA_{P330G}, the transition of protein unfolding during thermal melting was steeper compared to UraA_{WT} suggesting increased sample homogeneity. As differential scanning fluorimetry revealed uracil binding for all three inter-domain linker variants, the reduced transport capacity of all three mutants did not originate from structural distortions within the substrate binding site that would lead to impaired uracil binding. The significant increase in thermal stability of UraA_{G320P} and UraA_{P330G} in combination with the altered monomer to dimer ratio in size exclusion chromatography and the potential increase in sample homogeneity observed in the melting curves suggested an effect on the conformational equilibrium in these two variants. A causative relationship between thermostabilization and dimerization might be deduced from these results. However, UraA_{P330G} that showed almost complete dimerization was slightly less stabilized compared to

the partially dimeric UraA_{G320P}. Further, a predominant contribution of dimerization to thermostabilization should result in two melting events for UraA_{G320P}, one for each oligomeric state, assuming a slow monomer/dimer equilibrium which was not observed. This suggests no direct causative relationship of thermostabilization and oligomerization.

4.3.4 Substrate binding site accessibility in UraA_{G320P} and UraA_{P330G}

A potential alteration in the conformational space of UraA_{G320P} and UraA_{P330G} was experimentally analyzed by a cysteine accessibility assay while the variant UraA_{G112P} was not further analyzed regarding its conformational properties as it showed less promising biochemical characteristics. The elevator transport of UraA implies alternation between distinct conformations – inward-facing, outward-facing and occluded (**Figure 5D**). In order to test whether the reduced functionality of UraA_{G320P} and UraA_{P330G} was based on altered conformational equilibria between these states as suggested by the increased thermostability, a cysteine was introduced at position Ala-31 (**Figure 22A**) that is located near the substrate binding site but does not contribute to uracil coordination. This cysteine was used for specific maleimide labeling using the fluorophore CPM to test the substrate binding site accessibility in context of the inter-domain linker mutations. Labeling of Cys-31 was expected for the outward-facing and inward-facing conformations and not for the occluded conformation. The suggested alterations in the conformational equilibrium of UraA_{G320P} or UraA_{P330G} would result in changed accessibility of the substrate binding site for CPM thus different kinetics of fluorescence increase. The desired UraA variants were produced in the context of UraA_{Cysless} and purified as described (3.4.5; 3.4.8). The cysteine accessibility was analyzed by following the fluorescence intensity after addition of CPM (**Figure 22B**). The experiment was performed by Tim Gemeinhardt as part of his Master studies. The resulting data was analyzed by non-linear curve fitting with Origin using an exponential function to extract kinetic information of the CPM labeling reaction. The rate constant for UraA_{Cysless-A31C} and the positive control cysteine mutant UraA_{Cysless-M143C} holding a surface exposed cysteine at the periplasmic side of TM5, were 0.478 min⁻¹ and 0.375 min⁻¹, respectively. This indicated a high accessibility of the substrate binding site in UraA_{Cysless-A31C} (**Figure 22D**). For UraA_{Cysless-A31C-G320P} and UraA_{Cysless-A31C-P330G}, these rates were reduced with 0.230 min⁻¹ and 0.256 min⁻¹. The slower kinetics in A31C labeling in context of the G320P and P330G substitutions suggested reduced open probability of the substrate binding site for these two variants compared to UraA_{WT}.

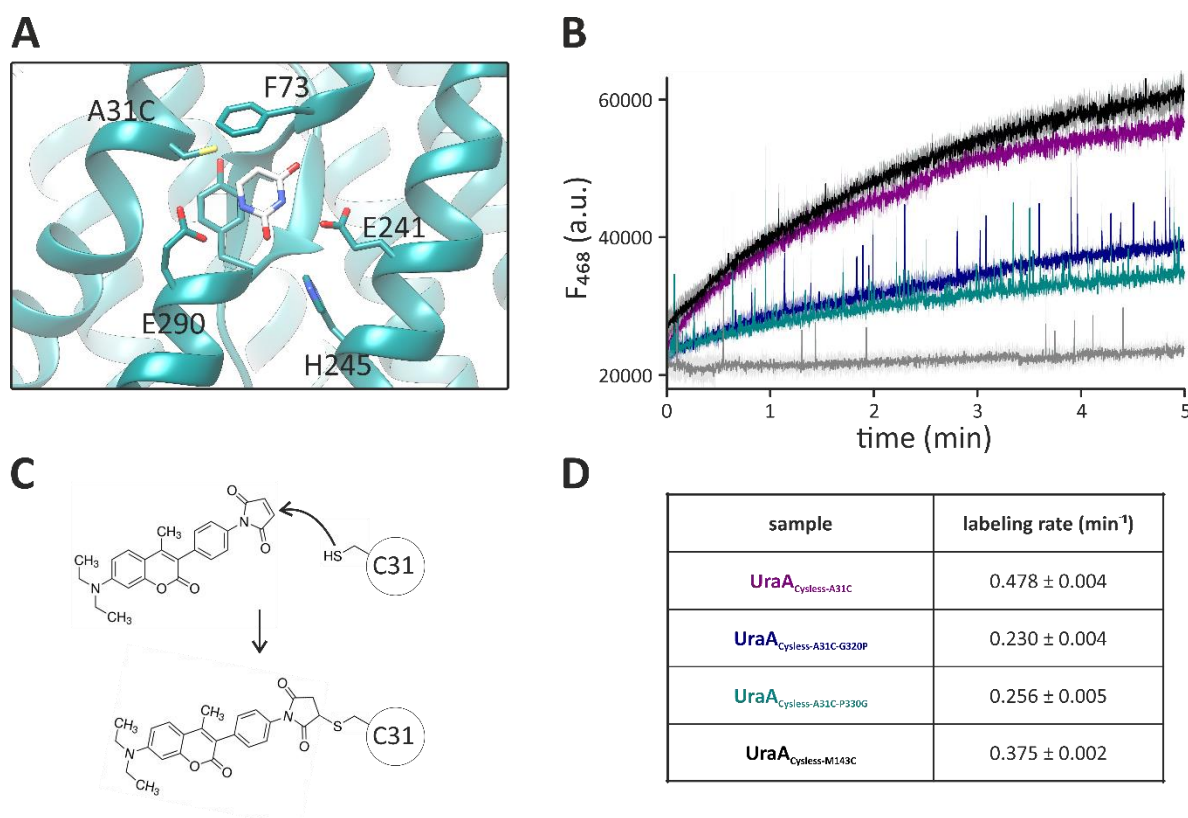


Figure 22: Substrate binding site accessibility analysis by specific cysteine labeling. (A) A single cysteine was introduced at position Ala-31 of UraA_{Cysless} to report on the substrate binding site accessibility upon addition of CPM. The tested UraA variants were diluted to 200 nM concentration in labeling buffer containing 1 μM CPM. (B) CPM fluorescence was excited at 388 nm and emission recorded at 468 nm using the Fluorolog-3 spectrofluorometer (Horiba). The mean and standard error calculated from at least three measurements per sample are shown. UraA_{Cysless} was used as negative control (grey) and UraA_{Cysless-M143C} as positive control (black). (C) The maleimide moiety of CPM reacts with the free thiol of Cys-31 following a Michael addition. The stable product features increased fluorescence intensity. (D) Signals were fitted with an exponential function using the Origin software to extract the labeling kinetics. The cysteine accessibility assay was performed by Tim Gemeinhardt as part of his Master studies.

Consistently, the potential alteration in conformational space of UraA_{G320P} and UraA_{P330G} as hypothesized based on thermal stabilization and reduced transport activity could be qualitatively supported. A shifted conformational equilibrium towards an occluded conformation in UraA_{G320P} and UraA_{P330G} would be supported by the data but a shift towards an open conformation with decreased accessibility of position A31C compared to the predominant conformation of UraA_{WT}, could not be excluded. However, the reduced binding site accessibility strongly suggests that the interdomain linkers are functionally relevant regions that may affect the conformational space of UraA.

4.3.5 Uracil affinity of UraA_{WT} and UraA_{G320P}

While the UraA variants G320P and P330G showed additional thermostabilization in the presence of uracil, differential scanning fluorimetry only allowed qualitative analysis of binding. The shifted conformational equilibrium suggested for both UraA variants might thereby influence the uracil affinity. For quantitative uracil binding analysis, a scintillation proximity assay (Harder et al., 2012) was established using biotinylated target proteins with C-terminal Avi-tag (Fairhead et al., 2014) for specific biotinylation in combination with streptavidin-coated PVT beads. The assay was performed in collaboration with Niko Schenck as part of his Master studies. The efficiency of *in vitro* biotinylation was tested by streptavidin induced mobility shift in SDS-PAGE (Kuhn et al., 2020) and quantified to be more than 90% for all tested UraA variants (**Supplementary figure 4**). The affinity of UraA_{WT} was determined before in literature using a similar approach yielding a dissociation constant of 143 ± 7.5 nM (Yu et al., 2017) that could be reproduced in this study with a calculated K_d of 151 ± 8.0 nM (**Figure 23A**). The same binding assay with UraA_{G320P} revealed a significantly higher affinity for uracil with a K_d of 21 ± 7.0 nM (**Figure 23B**). As the substrate affinity of secondary active transporters might vary depending on the transporter's conformation with the occluded conformation theoretically featuring the highest affinity (Forrest et al., 2011), the increased uracil affinity of UraA_{G320P} compared to UraA_{WT} further supported the shifted conformational equilibrium in UraA_{G320P} as suggested before by the CPM labeling (**Figure 22**). The same

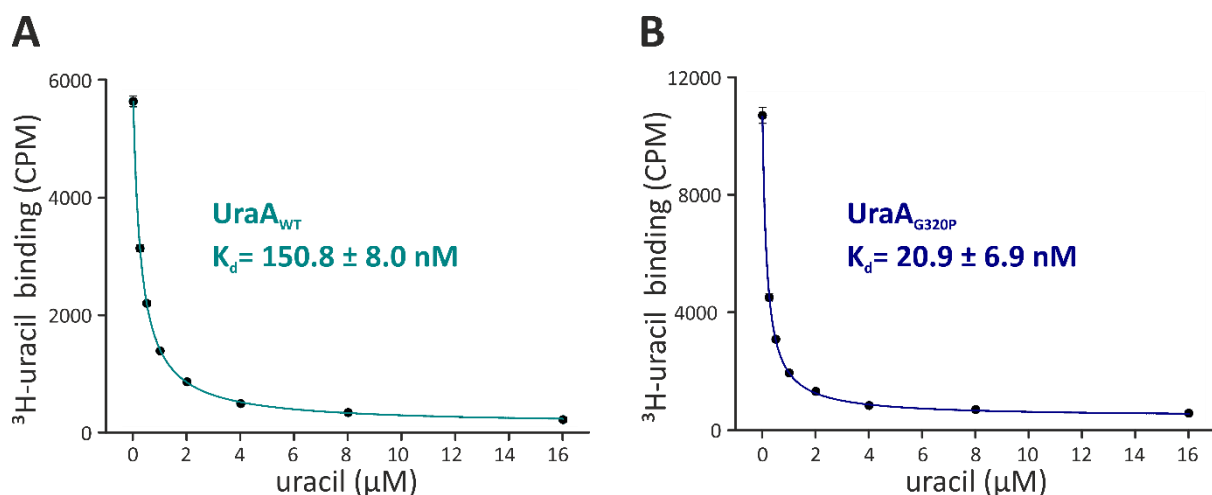


Figure 23: Scintillation proximity assay of UraA_{WT} and UraA_{G320P}. The biotinylated UraA variants at a final concentration of 150 nM were pre-incubated with final 150 nM ³H-uracil and increasing amounts of non-labeled uracil. Samples were transferred to a 96-well plate, proteins immobilized to 340 µg Streptavidin PVT beads and scintillation counted for 2 min. The background was recorded similarly for each well after addition of 1% SDS (w/v) and subtracted from the specific binding signal. Shown are the mean values from triplicates and the corresponding standard errors. The data was analyzed by non-linear curve fitting in Origin using a function for homologous competition (**Equation 2**; 3.4.20). Scintillation proximity assay was performed with Niko Schenck as part of his Master studies.

binding assay with UraA_{P330G} resulted in a similar competition but the data could not be analyzed by non-linear curve fitting and no binding affinity was extracted (**Supplementary figure 15**). The steeper transition in the competition observed for UraA_{P330G} could be indicative of a higher uracil affinity that could not be assessed reliably in the applied concentration range of uracil.

4.4 Co-crystallization of UraA

The two strategies for the manipulation of the conformational space of UraA with conformational-selective binders and mutations in the postulated hinges of the inter-domain linkers resulted in the selection of Sy45 and Sy5 beside other binders and the thermostabilized UraA variant G320P. Sy45 and Sy5 were shown to stabilize different conformations of UraA and the variant G320P showed characteristics beneficial for crystallization with increased thermal stability and sample homogeneity. Despite the lack of transport activity and the shifted conformational equilibrium featured by this UraA variant, a complete conformational lock of the transporter was not observed, making this variant an ideal target for crystallization. Both strategies were combined by performing co-crystallization to increase the mechanistic insights on UraA and to analyze the structural properties of UraA_{G320P}.

4.4.1 Co-crystallization of UraA with Sy45

Initial co-crystals of UraA/Sy45 complexes were achieved by using UraA_{WT} for crystallization. Crystals grew in several crystallization conditions of the Mac400 screen (Appendix A) at 18 °C using the sitting drop vapor diffusion method with a drop size of 200 nL. The condition consisting of 50 mM magnesium acetate, 50 mM HEPES, pH 7.5, 30% PEG-400 (v/v) with 1% OG (w/v) as additive in the protein sample showed crystal growth after 2 days and initial diffraction to 13 Å resolution (**Figure 24C**). This hit was reproduced and further optimized in a grid screen (Newby et al., 2009) with magnesium acetate concentrations ranging from 10 to 200 mM and increased drop size of 1 µL. During the optimization, it was found that the UraA_{G320P} mutant and the addition of 1% NG (w/v) instead of 1% OG (w/v) were beneficial for crystallization and crystal diffraction. Crystals of UraA_{G320P} with Sy45 grew within one week in a condition consisting of 75 mM magnesium acetate, 50 mM HEPES, pH 7.5, 38% PEG-400 (v/v) and diffracted to 3.7 Å resolution. The space group was identified to be P2₁ with the unit cell parameters: 85.2 Å, 115.3 Å, 94.2 Å, 90°, 100.8°, 90°. Further optimization and screening of

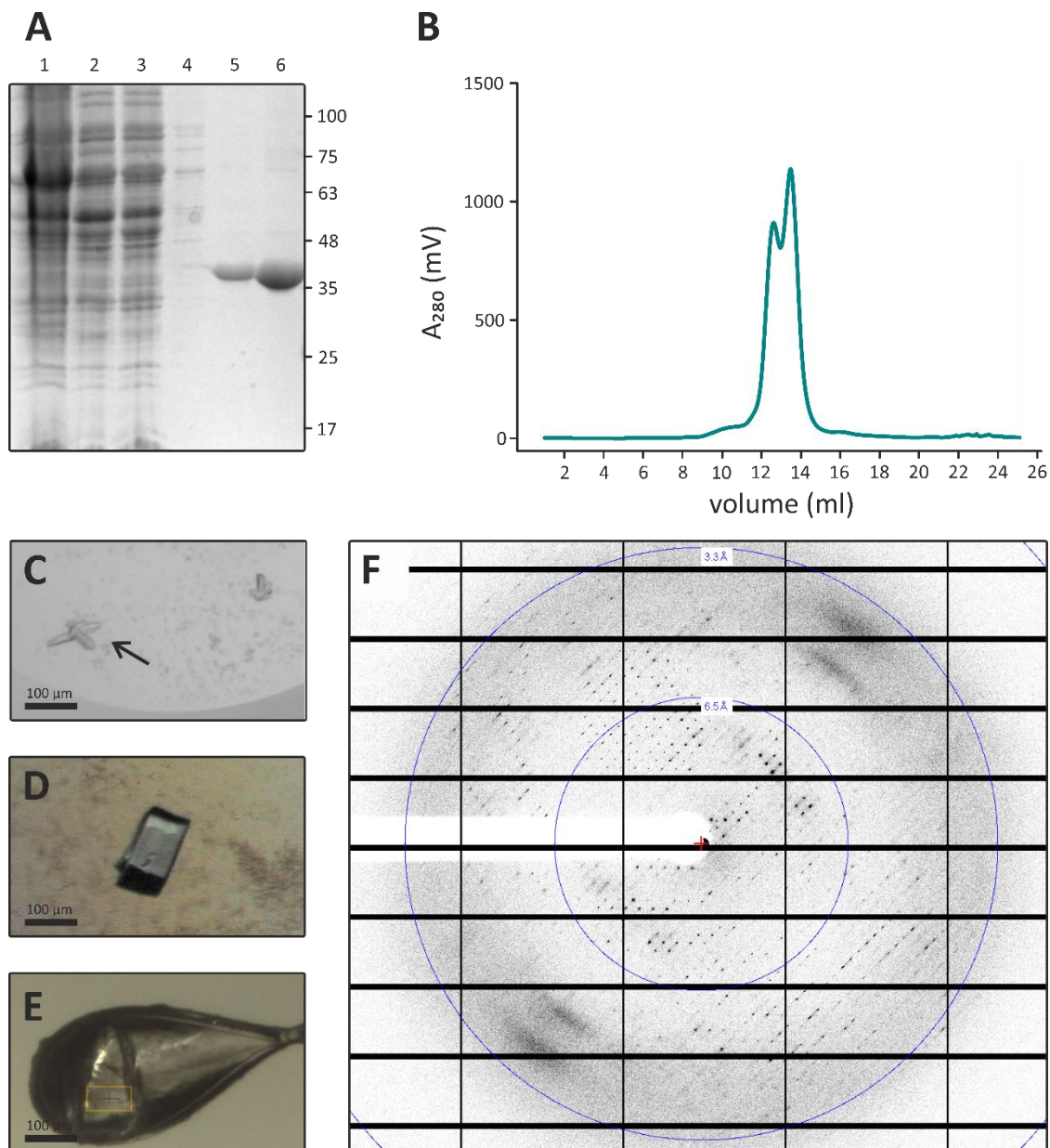


Figure 24: Co-crystallization of UraA_{G320P} and Sy45. (A) Purification of UraA_{G320P} by IMAC with the fractions 1: solubilized vesicles, 2: supernatant after ultracentrifugation, 3: flowthrough, 4: 50 mM imidazole wash, 5: elution by on-column cleavage with 3C protease, 6: sample after size exclusion chromatography loaded on SDS-PAGE followed by Coomassie staining. (B) Size exclusion chromatography of UraA_{G320P} on a Superdex 200 increase 10/300 GL column equilibrated with 10 mM HEPES pH 7.5, 150 mM NaCl, 0.2% n-decyl-β-D-maltopyranoside. (C) Initial crystals of UraA_{WT} with Sy45 diffracting to 13 Å resolution. (D) Representative crystal of UraA_{G320P} co-crystallized with Sy45 and the same crystal shown in a nylon loop with 200 to 300 μm diameter before data collection at the X06DA beam line of the SLS (E). The yellow rectangle indicates the size of beam centered on the crystal. (F) X-ray diffraction image of an UraA_{G320P}-Sy45 crystal diffracting to a resolution below 3.0 Å. Pipetting of crystallization plates for initial crystallization screening was performed by Barbara Rathmann from the MPI of Biophysics, Frankfurt, Germany

additives e.g. glycerol, ethanol, DMSO, benzamidine hydrochloride and heptane-1,2,3-triol (Michel, 1983) as well as pH optimization resulted in the best diffracting crystals in the condition consisting of 50 mM magnesium acetate, 50 mM Tris, pH 8.4, 34% PEG-400 (v/v), 0.1% benzamidine hydrochloride (w/v) in presence of 1% NG (w/v). Crystals grew within one week in a 1 μL sitting drop (**Figure 24D**), were fished with a nylon loop and immediately frozen

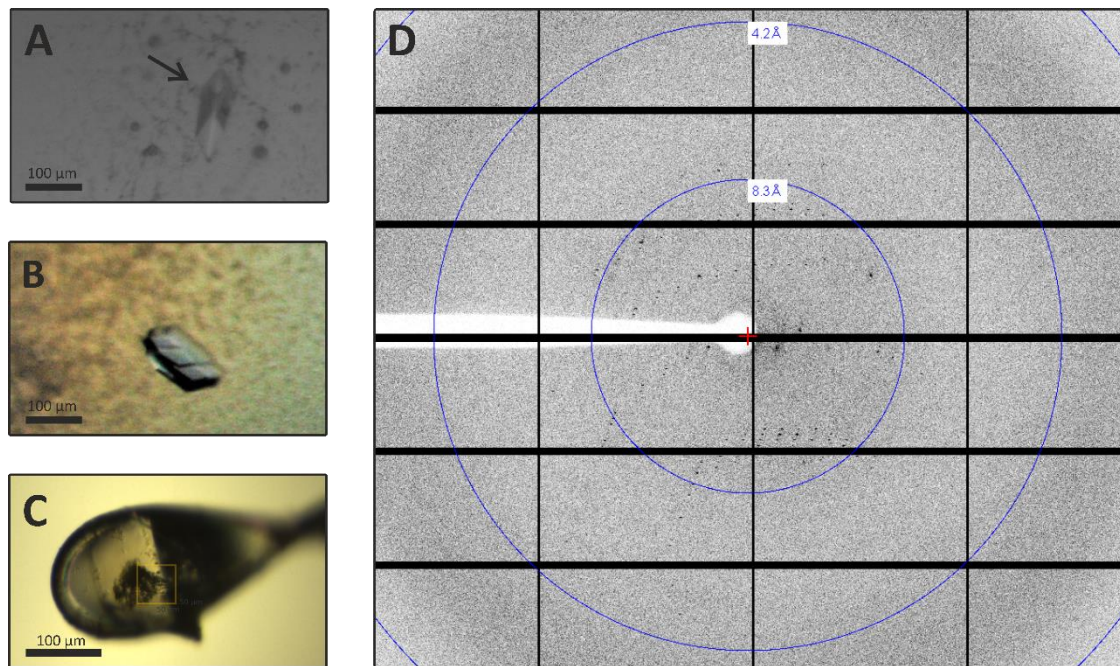


Figure 25: Co-crystallization of UraA_{G320P} and Sy5. (A) UraA-Sy5 crystals could only be obtained with the thermal stabilized mutant UraA_{G320P} in the condition containing 50 mM sodium cacodylate, pH 5.5, 50 mM magnesium acetate and 34% PEG-400 (v/v). (B) Optimized crystal of UraA_{G320P} co-crystallized with Sy5 resulting from a grid screen and increased drop size of 1 μ L. (C) UraA_{G320P}-Sy5 crystal in a 200 to 300 μ m nylon loop at the X06SA beamline of the SLS and corresponding X-ray diffraction image with anisotropic diffraction to 4 \AA resolution (D). Pipetting of crystallization plates for initial crystallization screening was performed by Barbara Rathmann from the MPI of Biophysics, Frankfurt, Germany

by plunging the loop into liquid nitrogen. The best crystal diffracted anisotropically to 2.8 \AA resolution (**Figure 24F**). The same crystallization condition with addition of 1 mM uracil gave rise to crystals of UraA_{G320P}-Sy45 in presence of uracil with similar morphology.

4.4.2 Co-crystallization of UraA_{G320P} with Sy5

For co-crystallization of UraA with Sy5 initial screens with the Mac400 screen (Appendix A) were performed using UraA_{WT} at 18 $^{\circ}$ C with the sitting drop vapor diffusion method which did not yield any crystals. The same screening was therefore repeated with UraA_{G320P} and resulted in several conditions with initial crystals whereof the condition containing 50 mM sodium cacodylate, pH 5.5, 50 mM magnesium acetate and 34% PEG-400 (v/v) showed best crystal morphology (**Figure 25A**). This condition was optimized by using grid-screens and the drop size was increased to 1 μ L in a 48-well plate for generation of larger crystals (**Figure 25B**). Though crystal quality improved during the optimization process, diffraction remained anisotropic for all tested crystals and could not be improved below 4 \AA resolution (**Figure 25D**) hampering the generation of a high-resolution structure.

4.4.3 Collection and processing of the UraA_{G320P}-Sy45 datasets

The synchrotron X-ray diffraction data for the UraA_{G320P}-Sy45 apo dataset was collected at the beamline P13 operated by EMBL Hamburg at the PETRA III storage ring (DESY, Hamburg, Germany; Cianci et al., 2017). The dataset for the UraA_{G320P}-Sy45 structure in presence of 1 mM uracil was collected at the X06DA beamline of the SLS (Paul-Scherrer-Institute, Villigen, Switzerland). All crystallographic data obtained was processed with the software XDS (Kabsch, 2010). The space group P2 was selected by the software as highest symmetry space group with reasonable fit. The screw axis resulting in the correct space group P2₁ was identified by Pointless from the software package CCP4. The dataset for the UraA_{G320P}-Sy45 apo structure was reprocessed in space group P2₁ and analyzed with Xtriage that reported the existence of moderate anisotropy of the diffraction data. This was further investigated using the UCLA diffraction anisotropy server (Strong et al., 2006) that identified strong anisotropy with suggested resolution limits by the server of 3.7 Å, 3.2 Å and 2.8 Å along the three axes. The dataset was reprocessed at 2.5 Å to extract as much high-resolution data as possible for subsequent ellipsoidal truncation and anisotropic scaling by the UCLA diffraction anisotropy server. The merging statistics for the UraA_{G320P}-Sy45 diffraction data set from XSCALE before and after ellipsoidal truncation and anisotropic scaling are shown in the supplements (**Supplementary figure 17**). The resolution limits chosen by the server were 3.7 Å, 3.2 Å and 2.6 Å along the three axes.

For the UraA_{G320P}-Sy45-uracil structure, a similar procedure was applied as anisotropic diffraction was observed. The data was processed at 3.0 Å in XDS and scaled with XSCALE before ellipsoidal truncation and anisotropic scaling by the UCLA diffraction anisotropy server. The resolution limits along the three axes were chosen by the server to be 3.9 Å, 3.7 Å and 3.0 Å. Merging statistics before and after anisotropy correction are presented in the supplements (**Supplementary figure 18**).

4.5 UraA-Sy45 co-crystal structure

4.5.1 Molecular replacement and refinement of UraA_{G320P}-Sy45

The UraA_{G320P}-Sy45 co-crystal structure was solved by molecular replacement using phaser-MR of the Phenix software suite. The number of UraA_{G320P}-Sy45 complexes in the

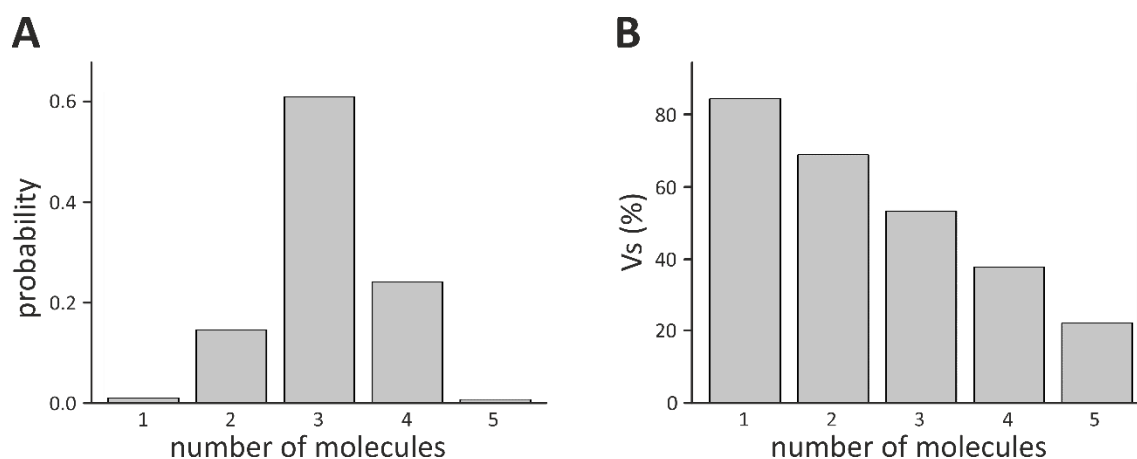


Figure 26: Matthews coefficient analysis of the UraA_{G320P}-Sy45 X-ray diffraction dataset. The Matthews Probability Calculator (Kantardjiev et al., 2003) was used with the space group P2₁, the unit cell parameters (87.14 Å, 118.11 Å, 94.93 Å, 90.00° 100.42° 90.00°) and a molecular weight of 60 kDa assuming a one to one stoichiometry of UraA_{G320P} (45 kDa) and Sy45 (15 kDa). (A) Overall probability distribution for one to five molecules in the asymmetric unit with the highest probability of 0.6 for three copies of UraA_{G320P}-Sy45 and a corresponding solvent content (Vs) of the asymmetric unit of 53.4 % (B).

asymmetric unit was calculated by the Matthews Probability Calculator (Kantardjiev et al., 2003; **Figure 26**) resulting in the highest probability for three protein complexes with a solvent content of 53.4%. As type-II membrane protein crystals are known to have a higher solvent content (Moraes et al., 2014) than crystals from soluble proteins due to the size of the detergent micelle, only two complexes of UraA_{G320P}-Sy45 were assumed for molecular replacement with a corresponding solvent content of 68.9%. A unique solution in space group P2₁ was found with log-likelihood gain (LLG) of 321 and a translation function Z (TFZ) score of 16 indicating a correct molecular replacement solution with two UraA_{5XLS} protomers as search models. A Sy45 model was generated with SWISS-MODEL (Waterhouse et al., 2018) based on the structure of the lysozyme binding nanobody (De Genst et al., 2006) that served as scaffold for the convex sybody library. Two copies of the Sy45 model were searched while the two copies of UraA_{5XLS} were kept at the positions that were identified in the first round of molecular replacement yielding no clear solution. One round of rigid body refinement of the initial solution for the two UraA_{5XLS} protomers in Phenix.refine (Afonine et al., 2012) and visual inspection of the electron density in Coot (Emsley et al., 2004) revealed a relatively good agreement of the core domains with the crystallographic data but poor correlation between the inter-domain linkers and gate domain with the electron density. The statistics after initial refinement yielded values for R-work and R-free of 50% and 51%, respectively. The different orientation of the gate domain with respect to the core domain compared to UraA_{5XLS} suggested a different conformation of UraA present in the crystal. Molecular replacement was

performed with the two core domains kept at the identified positions and two gate domains as search model with truncated TM5-TM6 loop (Abergel et al., 2013). A unique solution was found with LLG of 1090 and TFZ score of 17.1 with the gate domains placed at their former positions in the asymmetric unit but shifted towards the periplasmic side with respect to the core domain. Rigid body refinement with the improved model resulted in a better fit to the experimental data with R-work of 46% and R-free of 47%. Additional density on the cytoplasmic side of UraA became visible which was attributed to Sy45. The model of UraA was fixed in the identified positions and a new molecular replacement performed in order to place two copies of Sy45 in the electron density but no clear solution was found with the best TFZ score of 6. The molecular replacement was repeated but with a CDR3 truncated version of the Sy45 model which resulted in the final solution with LLG of 1630 and a TFZ score of 26. The two copies of Sy45 were placed by phaser-MR in the additional density that was visually identified before. The model was refined using Phenix.refine with grouped ADP, reciprocal space refinement and the option to use non-crystallographic symmetry (NCS) restraints in the beginning of refinement. NCS was removed from the refinement protocol after several refinement cycles and real space refinement was added. For the last rounds of refinement TLS was used with one TLS group per protomer.

Additional density became visible that was successfully modeled in Coot with detergent molecules present in the crystal condition being either NG or DM. Furthermore, additional density in the substrate binding site was observed but as uracil was neither added nor co-purified in significant amounts based on analysis by differential scanning fluorimetry (**Figure 21**) the density could not be modeled with an uracil molecule. Initial trials to fit the glucose moiety of a NG molecule in the density proved incorrect and the additive benzamidine that was present in the crystallization condition could not be modeled without introducing clashes. This indicated a smaller molecule with almost spherical shape located in the substrate binding site. A Tris molecule present in the crystallization condition was therefore modeled as it features a positively charged amine that could interact with Glu-241. The UraA_{G320P}-Sy45 co-crystal structure was refined at a resolution of 3.1 Å (**Table 17**).

The UraA_{G320P}-Sy45 structure crystallized in presence of uracil was solved by molecular replacement using the UraA_{G320P}-Sy45 apo structure resulting in a single solution from Phaser with LLG of 5150 and a TFZ score of 41.6. The structure was refined in Phenix.refine at 3.7 Å resolution using real and reciprocal space refinement, grouped ADP and reference model

restraints using the UraA_{G320P}-Sy45 apo structure. Additional density was modeled in Coot with uracil in the substrate binding site and NG or DM molecules in the inter-protomer interface respectively. For the last rounds of refinement TLS was used with one TLS group per protomer and the model restraints were removed from the refinement protocol.

Table 17: Refinement statistics for the solved crystal structures of UraA_{G320P} in presence of Sy45.

	UraA _{G320P} -Sy45	UraA _{G320P} -Sy45-uracil
Beamline	P13, PETRA III (Desy, Hamburg, Germany)	X06DA, SLS (PSI, Villigen, Switzerland)
Wavelength	0.98	1.00
Resolution range	29.53 - 3.1 (3.211 - 3.1)	49.42 - 3.7 (3.832 - 3.7)
Space group	P 1 21 1	P 1 21 1
Unit cell	87.14 118.11 94.93 90 100.424 90	86.25 116.81 94.29 90 100.485 90
Unique reflections	29454 (1341)	19370 (1607)
Completeness (%)	85.51 (39.26)	97.89 (81.57)
Wilson B-factor	73.36	50.79
Reflections used in refinement	29454 (1341)	19361 (1607)
Reflections used for R-free	1484 (64)	988 (79)
R-work	0.2401 (0.3581)	0.2516 (0.2878)
R-free	0.2607 (0.3846)	0.2845 (0.3120)
Number of non-hydrogen atoms	8464	8233
macromolecules	7956	7941
ligands	508	292
Protein residues	1071	1069
RMS (bonds)	0.002	0.002
RMS (angles)	0.44	0.47
Ramachandran favored (%)	98.31	95.48
Ramachandran allowed (%)	1.69	3.86
Ramachandran outliers (%)	0	0.66
Rotamer outliers (%)	0	0
Clashscore	4.86	6.67
Average B-factor	65.08	76.92
macromolecules	64.32	77.19
ligands	77.12	69.65
Number of TLS groups	4	4

4.5.2 Crystal structure of UraA_{G320P} in complex with Sy45

Two strategies for gaining further structural information on UraA with nanobody or sybody selection and conformational space manipulation of UraA could be combined and resulted in the UraA_{G320P}-Sy45 co-crystal structure (**Figure 27**). The asymmetric unit consists of two UraA_{G320P} molecules each bound to one Sy45. Sy45 binds at the cytoplasmic side of each UraA

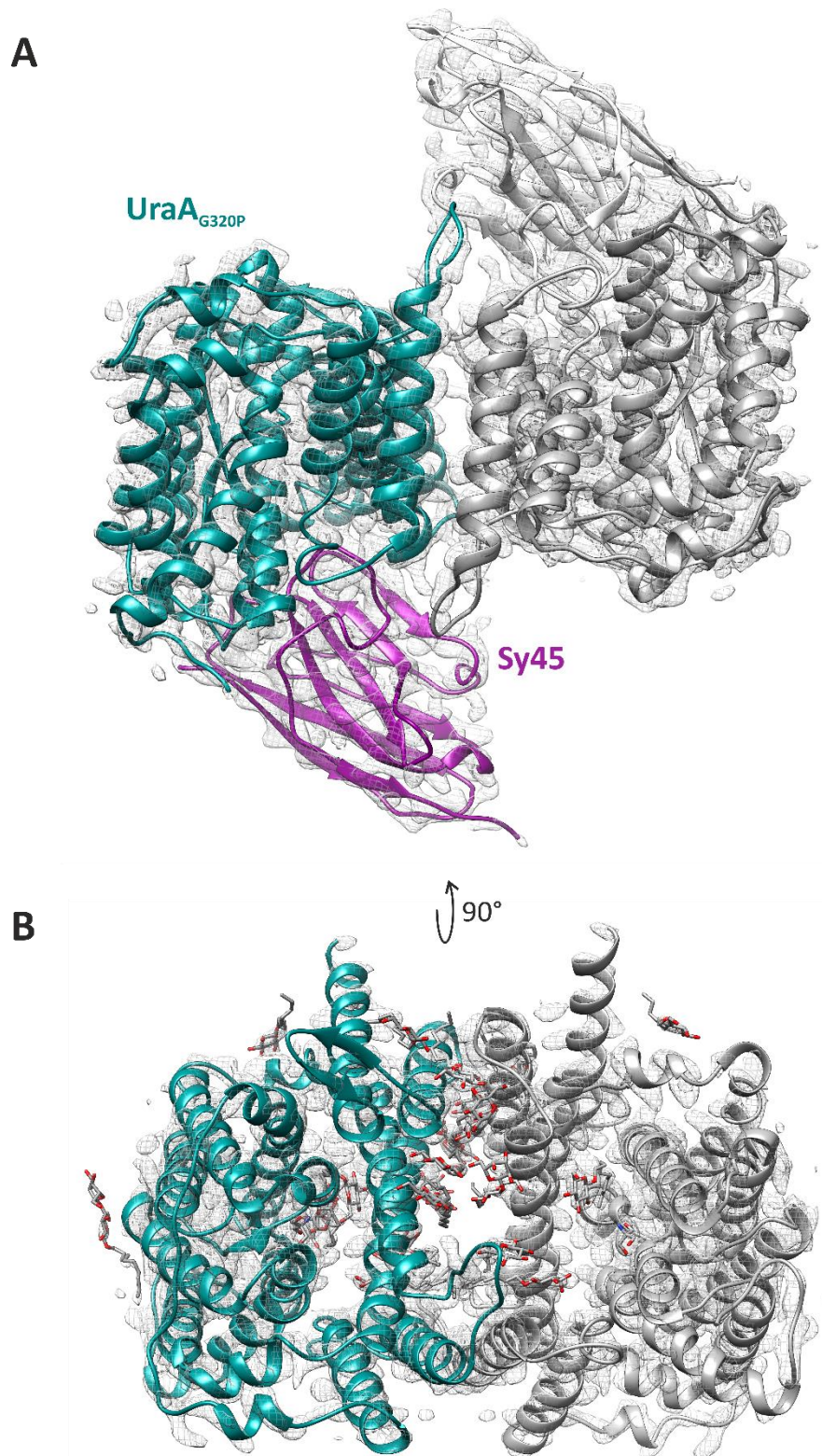


Figure 27: UraAG320P-Sy45 co-crystal structure. (A) Asymmetric unit of the UraAG_{320P}-Sy45 co-crystal structure with the UraA protomers show in cyan and grey and sybodies in purple and grey. The electron density was contoured at 2 sigma. Both protomers are stabilized by Sy45 in an inward-facing conformation. The two monomers are assembled via their gate domains with one protomer rotated by 160° compared to a physiological dimer. (B) The empty space in the gate-gate domain interface is filled with structured DM and NG molecules shown as grey sticks. The two Sy45 protomers were removed for better visualization.

protomer into a relatively large cavity that allows solvent accessibility of the substrate binding site. Thus, the UraA_{G320P}-Sy45 structure is inward-facing and Sy45 could be identified to stabilize this conformation of UraA. The cytoplasmic epitope of Sy45 identified in the co-crystal structure was consistent with the epitope analysis by IOV-pulldown (**Figure 16**). Even though UraA_{G320P} was more dimeric in analytical size exclusion compared to UraA_{WT}, the protein was monomeric in the structure with two monomers interacting via their gate domains but with one protomer being rotated by 160° within the membrane plane compared to the physiological dimeric assembly observed in the UraA_{5XLS} structure (Yu et al., 2017). The interaction of UraA_{G320P} with Sy45 in a one to one stoichiometry was found to hamper dimerization due to the steric clash of two Sy45 protomers in a dimer (**Figure 27** and **Figure 29**). The architecture of the gate domain prevents tight inter-protomer interactions between the two UraA protomers due to shape incompatibility in the 160 ° rotated assembly which resulted in an empty space in the gate-gate domain interface where additional electron density was observed that could be modeled with the detergent molecules NG and DM (**Figure 27B**). Additional detergent molecules were observed in the inward facing cavity, at the cytoplasmic inter-domain linker and along the 'paddle' between TM13 and TM14. Both monomers of UraA_{G320P} in the asymmetric unit show non-crystallographic symmetry and an overall RMSD of 0.3 Å thus for subsequent analysis only the structure of protomer-A was considered. The same was true for the UraA_{G320P}-Sy45-Uracil structure that structurally aligned with the apo structure with an RMSD of 0.5 Å (**Figure 41**). Structural alignment of the here presented UraA_{G320P}-Sy45 co-crystal structure with both published UraA_{WT} structures (UraA_{3QE7}, inward-facing and UraA_{5XLS}, occluded) using the MatchMaker function of Chimera resulted an RMSD of 4.6 Å for UraA_{5XLS} and a higher RMSD of 7.0 Å for UraA_{3QE7}. The core domains aligned with an RMSD of 0.7 Å and 0.5 Å, respectively, underlining the rigid body movement of the core domain during the transport cycle (Chang et al., 2017). Alignment of the gate domains yielded an RMSD of 1.9 Å for UraA_{G320P}-Sy45 and UraA_{5XLS} and an RMSD of 9.1 Å for UraA_{G320P}-Sy45 and UraA_{3QE7}. This significant deviation in the gate domain of UraA_{3QE7} from UraA_{5XLS} and UraA_{G320P}-Sy45 was not in line with a transport mechanism based on rigid body movement and the anticipated symmetry based on the inverted repeat topology. The presence of a detergent molecule binding in the TM5 and TM12 interface in UraA_{3QE7} in addition led to the decision to focus the structural analysis in this study on UraA_{5XLS} as a

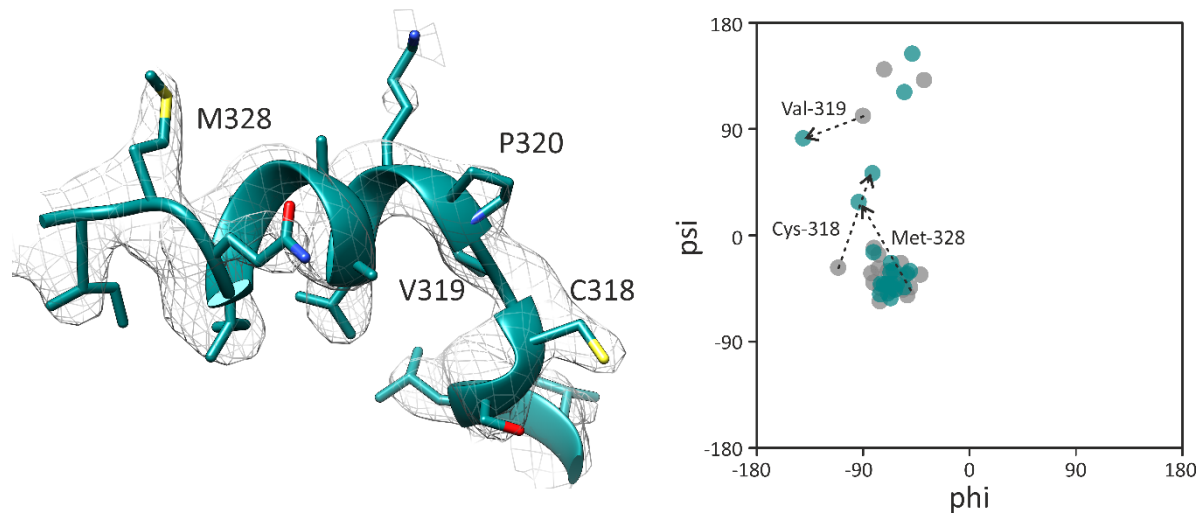


Figure 28: Position 320 with the introduced amino acid substitution glycine to proline in the inward-facing conformation of UraA. The periplasmic inter-domain linker with the electron density contoured at 1.5 sigma. The mutation site is directly located at the transition from TM11 to periplasmic inter-domain linker and the additional electron density for the pyrrolidine ring of the introduced proline is visible. The Ramachandran plot of the occluded UraA_{5XLS} structure (grey) and the UraA_{G320P}-Sy45 structure (cyan) in the range of the periplasmic inter-domain linker shows differences in the dihedral angles for the positions 318, 319 and 328.

reference structure. However, an analysis also including UraA_{3QE7} is presented in the discussion further elaborating these observations (5.3.1).

As expected from the biochemical analysis of UraA_{G320P}, the mutant globally shows the native UraA fold as suggested by the good structural alignment of the two core domains from UraA_{G320P}-Sy45 and UraA_{5XLS}. The mutation was not causing obvious distortions in the structure between TM11 and the periplasmic alpha helical inter-domain linker (**Figure 28**) and the additional pyrrolidine ring of the introduced proline residue was well represented in the electron density. Comparison of the Ramachandran plots of both UraA structures from position 315 to 335 showed changes in dihedral angles for position Cys-318, Val-319 and Met-328 within the allowed range but with position 319 shifted towards the ζ -population, unique to pre-proline residues (Ting et al., 2010). Thus, changes in dihedral angles of Cys-318 and Met-328 were most likely caused by the conformational change from occluded to inward-facing introduced by Sy45 binding and local bias of the substitution G320P on Val-319 was identified. The influence of the succeeding proline residue at position 320 on the dihedral angles of Val-319 and Cys-318 in UraA_{G320P} could be one reason for the altered conformational equilibrium observed for UraA_{G320P} in line with the hypothesis of a conformational hinge at this position. The change in dihedral angles of Met-328 further suggested this position to be involved as well in the conformational transition and consistently this contribution could apply to the whole alpha helical inter-domain linker.

4.5.3 The inward-facing cavity of UraA

The UraA_{G320P}-Sy45 structure revealed a large cytoplasmic cavity indicative of an inward-facing conformation. As the dimeric inward-facing structure of the SLC23 protein UapA from *A. nidulans* underlined a contribution of TM13 of protomer-A to the cavity of protomer-B (Alguel et al., 2016), it was reasonable to analyze the cytoplasmic cavity of UraA in the context of the dimeric protein. The dimeric inward-facing model was created by structural alignment of the gate domains in Chimera (Pettersen et al., 2004) based on the occluded dimeric UraA_{5XLS} structure. As observed for UapA, TM13 was also found to contribute to the inward-facing cavity in UraA. The cavity was mostly hydrophobic (**Figure 29A, B**) as shown by the surface representation except for the substrate binding site with the three charged residues Glu-241, His-245 and Glu-290 and comparably large with a length of 25 Å and 8 Å in both directions of the membrane plane (**Figure 29B**). The cavity was further explored using Hollow (Ho et al., 2008) with a radius of 13 Å around the C α atom of Gly-289 and its volume was calculated to be 4400 Å³ by the 3V volume calculator (Voss et al., 2010). The Tris molecule that was modeled with good agreement (**Figure 29C**) is forming various hydrogen bonds with E241, E290, and the backbone of F73 and G289 as observed for the uracil interaction in UraA_{5XLS} (**Figure 40**). Thereby, the short hydrogen bond of 2.5 Å distance between the primary amine of the Tris molecule and the carboxylic group of E241 is probably most important for binding of Tris. Besides the substrate binding site and TM5 and TM12 of the gate domain, the cavity is flanked by the cytoplasmic inter-domain linker and the TM6-TM7 loop on both sides of the protein along the gate domain. Due to the hydrophobicity of the cavity, a structured NG molecule was identified close to the substrate binding site with the hydrophobic acyl chain pointing towards the periplasmic side and the glucose moiety towards the opening of the cavity thereby shielding parts of the hydrophobic surface (**Figure 29D**). Structured detergent or lipid molecules were also observed in the inward-facing cavity of structures of the 7-TMIR proteins SLC26Dg (Geertsma et al., 2015), UapA (Alguel et al., 2016) and BicA (Wang et al., 2019; **Figure 42**).

4.5.4 The epitope of Sy45

The interaction of Sy45 with UraA was addressed experimentally by Sy45 pulldown with inside-out vesicles. The co-crystal structure confirmed the cytoplasmic epitope (**Figure 30A**) and further demonstrated that Sy45 stabilized an inward-facing conformation by binding of

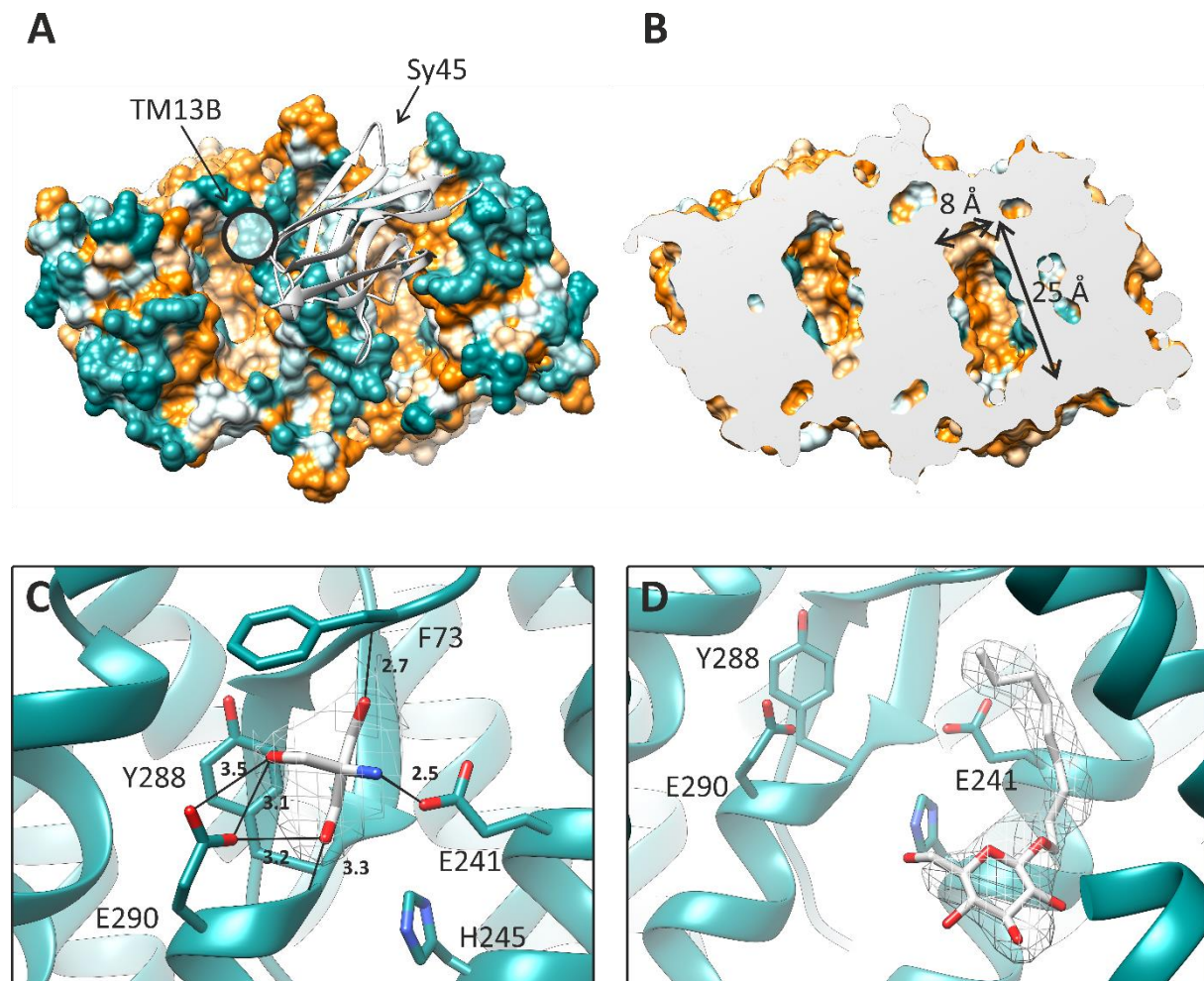


Figure 29: The inward cavity of UraA. The inward-facing conformation of UraA stabilized by Sy45 presents a large hydrophobic cavity as visualized in the surface representation of the cytoplasmic side of the UraA dimer (A) with a color scale from hydrophilic side chains colored in cyan to hydrophobic side chains in orange. The inward-facing dimeric structure was constructed based on the dimeric occluded structure of UraA (PDB: 5XLS). TM13 of protomer B contributes to the cavity of protomer A as indicated. The cavity is approximately 25 Å long ranging from cytoplasmic inter-domain linker to TM7 and is 8 Å wide (B). (C) The substrate binding site is mainly built by Glu-241, His-245, Glu-290 between the interrupted TM3 and TM10 and features a Tris molecule that was present in the crystallization condition. The electron density is contoured at 1.5 sigma. Various hydrogen bonds are formed between Tris and the substrate binding site highlighted by black lines connecting donor and acceptor atoms with inter-atomic distances in angstrom. (D) A structured NG molecule was modeled in the hydrophobic cavity filling the deeper part with its acyl chain. The electron density was contoured at 1.5 sigma. The lower part of the cavity is occupied by aromatic side chains from the CDR3 of Sy45. The bound Tris molecule was removed.

the side chains of residues Phe-101 and Tyr-103 of the CDR3 loop in the hydrophobic cavity between the core and gate domain. The size of the Sy45-UraA interface was calculated in Chimera to be 1249 Å² and involved parts of the core and gate domain of UraA and the cytoplasmic inter-domain linker (**Figure 30A**). Due to the hydrophobicity of the inward-facing cavity, the residues Phe-101 and Tyr-103 form hydrophobic interactions inside the cavity but also hydrophilic interactions were observed outside of the cavity. The residue Tyr-100 from the CDR3 loop is forming a hydrogen bond with Asp-245 from the TM8-TM9 loop of UraA with a donor-acceptor distance of 2.8 Å and Tyr-103 forms a hydrogen bond with the carbonyl

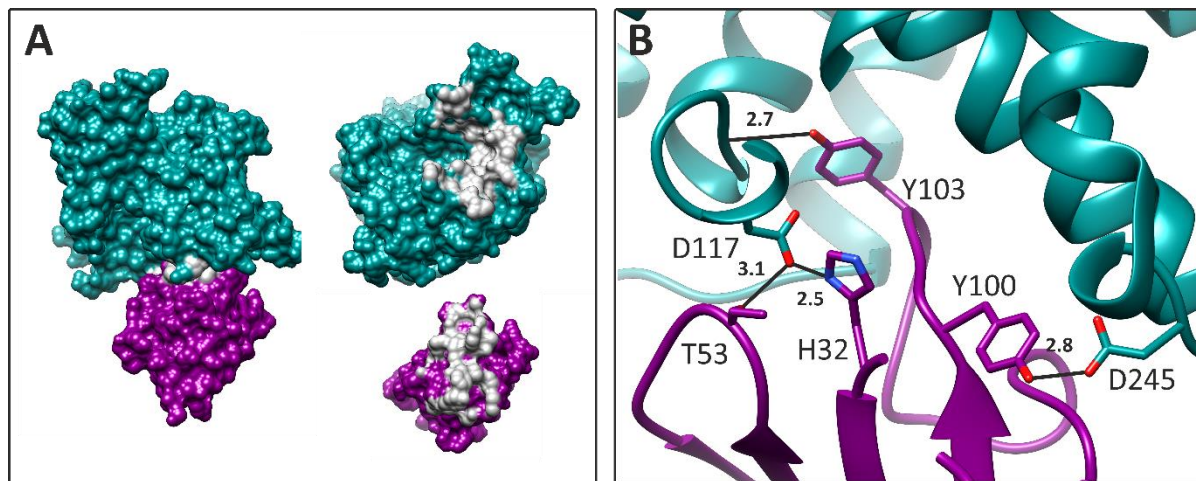


Figure 30: The epitope of Sy45. (A) Sy45 (purple) binds to the cytoplasmic side of UraA (cyan) with a binding interface of 1249 Å² (grey). (B) Aromatic side chains of Sy45-CDR3 are involved in hydrophobic interactions with the hydrophobic inward-facing cavity of UraA_{G320P}. Hydrogen bonds from Asp-117 of the cytoplasmic inter-domain linker to His-32 in CDR1 and Thr-53 in CDR2, from Tyr-100 in CDR3 to Asp-245 and from Tyr-103 in CDR3 to the backbone of Phe-120 were identified and visualized as black lines with distances labeled in angstrom. The CDR2 of Sy45 and TM4 of UraA were partially removed for better visualization.

oxygen of Phe-120 (**Figure 30B**). Other residues of the relatively long CDR3 do not contribute directly to the interaction with UraA but stabilize the loop conformation as seen for Arg-113 and Tyr-114. The CDR1 loop interacts with the cytoplasmic inter-domain linker, especially by a 2.5 Å hydrogen bond between His-32 of Sy45 and Asp-117 of UraA. CDR2 also contributes to the interaction with UraA as Leu-55 is involved in hydrophobic interactions with Val-118, Pro-121 and Pro-122. The side chain of Thr-54 is forming a hydrogen bond with Asp-117 with a donor acceptor distance of 3.1 Å. All three CDR loops of Sy45 were observed to contribute to UraA binding resulting in a large three-dimensional epitope distributed over both domains of UraA and the cytoplasmic inter-domain linker. These binding properties are indicative of strong conformational preference of Sy45 and likely to represent the molecular basis for the strong thermal stabilization of UraA upon binding of Sy45 observed in differential scanning fluorimetry.

4.5.5 Crystal contacts

Nanobodies are known to improve crystallization especially of membrane proteins by increasing the hydrophilic surface resulting in improved crystal contacts and in consequence higher resolution diffraction. UraA is completely embedded within the lipid bilayer or in the detergent micelle in solution thus addition of nanobodies respectively sybodies was expected to improve crystal contacts (**Figure 6**). A back to back interaction of two Sy45 protomers was found in UraA_{G320P}-Sy45 based on an anti-parallel beta-sheet formed by the two beta1-strands

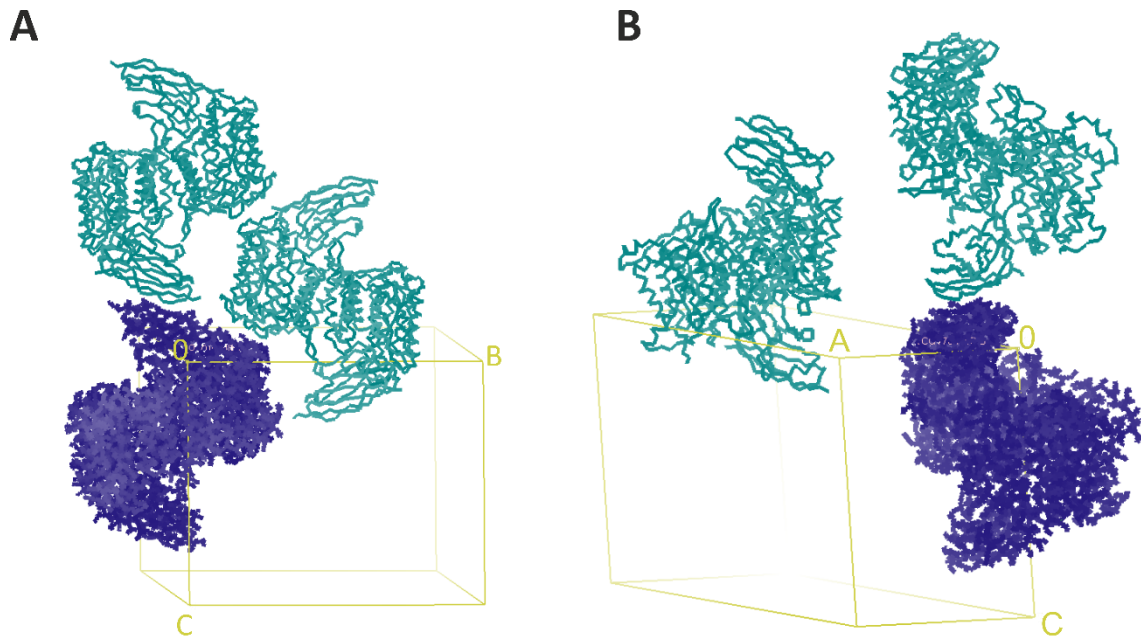


Figure 31: Crystal contacts in the lattice of UraAG_{320P}-Sy45 crystals. (A) View on the plain of the B- and C-axis with the unit cell shown in yellow, the asymmetric unit in blue and symmetry molecules in cyan. (B) View on the A-axis.

...serving as crystal contacts along the C-axis of the crystal lattice (**Figure 31A**). Along the B-axis, a salt bridge was formed between Asp-206 from the TM7-TM8 loop and Lys-64 of the TM2-TM3 loop. Additional contacts were observed between Thr-205 and Asp-260 and Asn-209 with Arg-259 and Gln-1 of Sy45. Another crystal contact along this axis was also found between Pro-13 and Leu-85. No crystal contacts could be identified along the A-axis (**Figure 31B**) indicating a contribution of unresolved loops or terminal parts of the polypeptide chains to the crystal contacts or the wrong choice of space group which was unlikely in this case due to the reasonable refinement statistics. As the C-terminus of UraAG_{320P} with additional 17 amino acid residues and the HRV-3C protease cleavage site with additional 6 residues were not resolved in the structure, a contribution of these residues to the crystal contacts was likely but could not be modeled. The C-terminal Myc-tag and 6-His-tag of Sy45 were also not resolved with 22 residues in total. It can thus be hypothesized that the crystal contacts along the A-axis in the UraAG_{320P}-Sy45 crystal lattice were formed by the unstructured C-terminal parts of UraAG_{320P} and/or Sy45 but with reduced quality. This resulted in the anisotropic diffraction of crystals with a loss in resolution along the A-axis with diffraction to 3.7 Å compared to 3.2 Å and 2.6 Å along the B- and C-axis. The best diffraction along the C-axis could be attributed to the strong Sy45-Sy45 interaction via the beta1-strands and demonstrated the potency of nanobodies as crystallization chaperones for membrane protein crystallography.

4.5.6 Conformational transition from inward-facing to occluded in UraA

The core and gate domain of UraA_{G320P-Sy45} showed good structural alignment with the individual domains of UraA_{5XLS} whereas the whole protomers aligned with a RMSD of 4.6 Å indicating a relative movement of both domains due to the conformational change from occluded to inward-facing. As the UraA mutant G320P was stabilized by Sy45, that was selected against UraA_{WT}, the inward-facing UraA_{G320P} structure was not expected to be globally biased by the G320P substitution allowing analysis of the conformational transition by comparison of UraA_{G320P-Sy45} and the occluded UraA_{5XLS} structure (Yu et al., 2017). The reasonable structural alignment of the gate domains of both structures enabled analysis of the conformational change by DynDom (Hayward, 1998; **Figure 32A**) that identified a rotation axis going through TM4 to the periplasmic side of TM11 thus near the two hypothesized hinge positions in UraA at the core domain to inter-domain linker connections. The DynDom analysis calculated a 17° rotation of the core domain around this rotation axis and a 1.3 Å translocation along the axis for the conformational transition from inward-facing to occluded. This resulted in a 10.3 Å displacement of TM1 on the cytoplasmic side, based on the C α atom distance of Leu-15, towards the periplasmic side and the gate domain (**Figure 32B**). The experimentally identified hinge next to position 320 showed a reduced angle between TM11 and the periplasmic inter-domain linker by 12.2°, as expected for a hinge position, resulting in a 7.2 Å displacement of the cytoplasmic tip of TM11 towards the gate domain based on the C α atom distance of Trp-304. Consequently, the adjacent TM10 was also displaced by 9.8 Å (Ile-291 C α to Ile-291 C α distance) towards the gate domain and thereby closing the inward-facing cavity. The rotation around the calculated axis led to helix movements away from the gate domain on the periplasmic side especially observed for TM3, TM4 and TM8 (**Figure 32D**) along with an upward movement. The rotation axis is lying in the plain of TM5 and TM12 that build the barrier for substrate translocation in the gate domain. Thus, core domain rotation around the axis results in almost orthogonal movement of the substrate binding site with respect to the TM5-TM12 barrier which is the shortest path for substrate translocation from the substrate entry to the exit site (**Figure 32C**). This translocation path was illustrated by the residues Glu-135 and Val-344 in TM5 and TM12 respectively at the substrate entry and exit site (**Figure 32E**). The distance between the two residues was measured to be 12.3 and 13.0 Å, respectively, in the two conformations and a 5.4 Å movement of Phe-73, representative of the substrate binding site, parallel to the translocation path was observed.

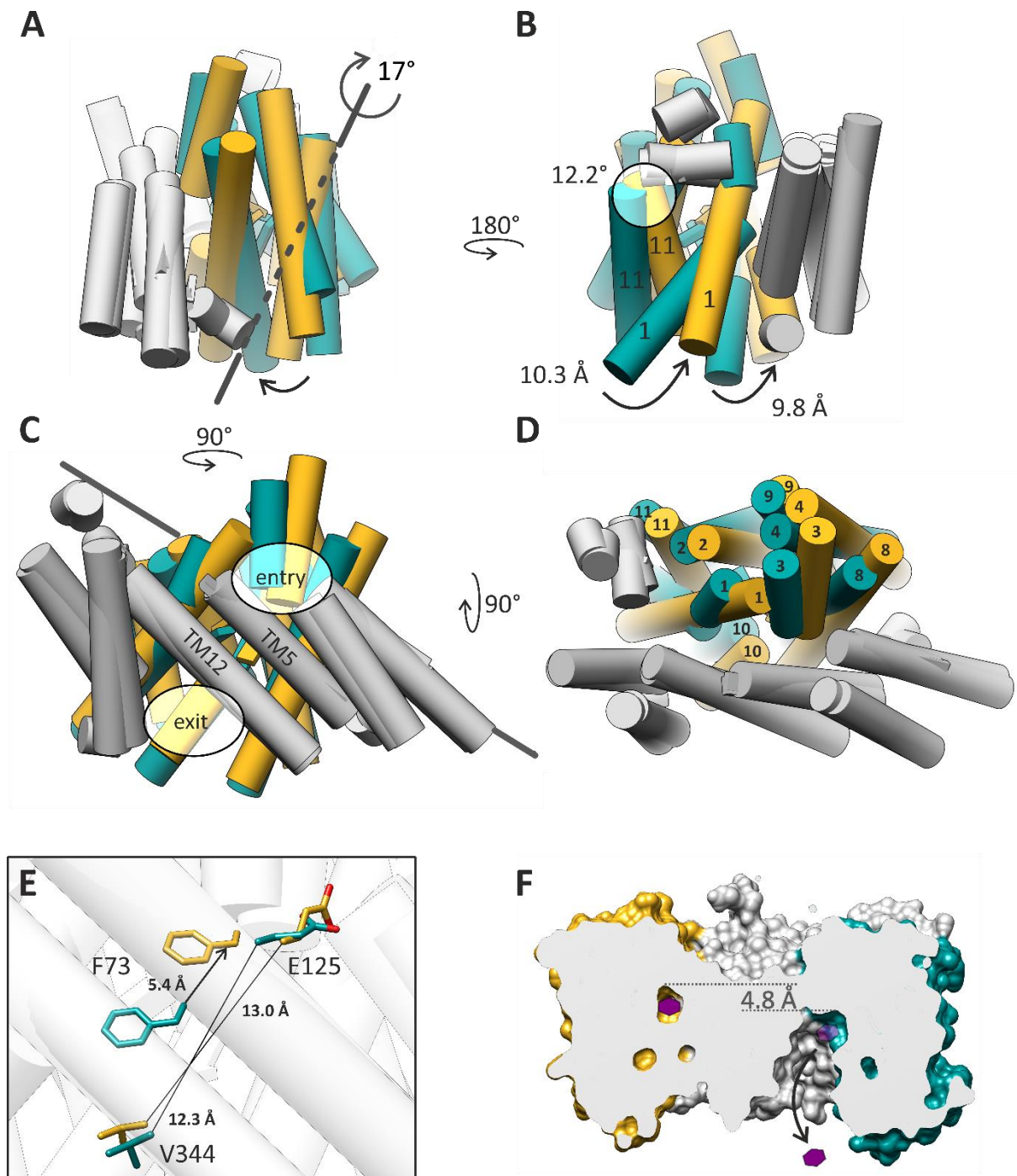


Figure 32: Conformational transition from the inward-facing to occluded conformation in UraA. (A) Rigid body movement of the core domain analyzed by DynDom (Hayward et al., 1998) reveals a rotation axis to describe the movement by a 17° rotation around the axis from inward-facing (cyan) to occluded (yellow). (B) Translocation of TM1 and TM11 on the cytoplasmic side based on the 17° rotation. (C) The rotation axis lies in the plane of TM5 and TM12 that serve as fixed substrate barrier for elevator transport. (D) Top view on the aligned conformations with labeled transmembrane sections. (E) Translocation of F73 representative for the substrate binding site translocation. F73 moves 5.4 Å along the 12 to 13 Å long substrate barrier with E125 and V344 building the end points. (F) Constructed heterodimer of UraA in the occluded and inward-facing conformation highlighting the inward-facing cavity and substrate binding site translocation.

The reasonable structural gate-gate domain alignment allowed the construction of a heterodimeric structure featuring the two conformations showing the significant difference in the cavity formed around the substrate binding site and the vertical translocation of the substrate

binding site by approximately 4.8 Å (**Figure 32F**) in line with the postulated displacement of 6 Å for the full transition from inward-facing to outward-facing in 7-TMIR proteins (Chang et al., 2017).

4.5.7 Structural alignment of UraA_{G320P}-Sy45 and UapA

The here reported UraA_{G320P}-Sy45 structure in the inward-facing conformation showed poor structural alignment with UraA_{3QE7}, previously reported to represent the inward-facing conformation of UraA (Lu et al., 2011). However, structural alignment of UraA_{G320P}-Sy45 with the inward-facing conformation of UapA (Alguel et al., 2016) resulted in an RMSD of 1.2 Å for 204 pruned atom pairs using the MatchMaker function of Chimera (**Figure 33**) indicating a similar conformation of the two structures. Alignment over the full-length proteins was poor with RMSD of 6.6 Å, due to variations in the loop regions connecting the transmembrane segments especially on the periplasmic side of the proteins. The substrate barrier build by TM5 and TM12 showed significant similarity between both structures while TM13 and TM14 were slightly displaced (**Figure 33D**). In the core domain, TM9 and TM11 showed a strong similarity (**Figure 33B**) that could be observed for TM2 as well but the elongated TM2 of UapA compared to UraA resulted in a longer TM1-TM2 loop on the periplasmic side for the former. The same was observed for TM4 but with overall reduced similarity between UraA and UapA with significant deviation at the cytoplasmic hinge, the linkage of TM4 and cytoplasmic inter-domain linker (**Figure 33A, B**). The periplasmic hinge at the linkage of TM11 and periplasmic inter-domain linker showed high similarity supporting the assumption that no major bias by the G320P substitution is present in the UraA_{G320P}-Sy45 structure (**Figure 33B, C**). Remarkably, the N-termini were observed to share a high similarity, both interacting with the TM10-TM11 loop. The structural similarity of UraA_{G320P}-Sy45 and UapA confirmed the overall structural integrity of UraA_{G320P} and supports the functional relevance of the Sy45 stabilized conformation of UraA especially in the periplasmic hinge. It further underlines the mechanistic similarity within the SLC23 family.

4.6 The conformational space of UraA

The conformational hinges of UraA at the periplasmic side was successfully manipulated in order to create phenotypic mutants suitable for conformational specific analyses. A shifted conformational equilibrium for the UraA variants G320P and P330G was deduced from altered

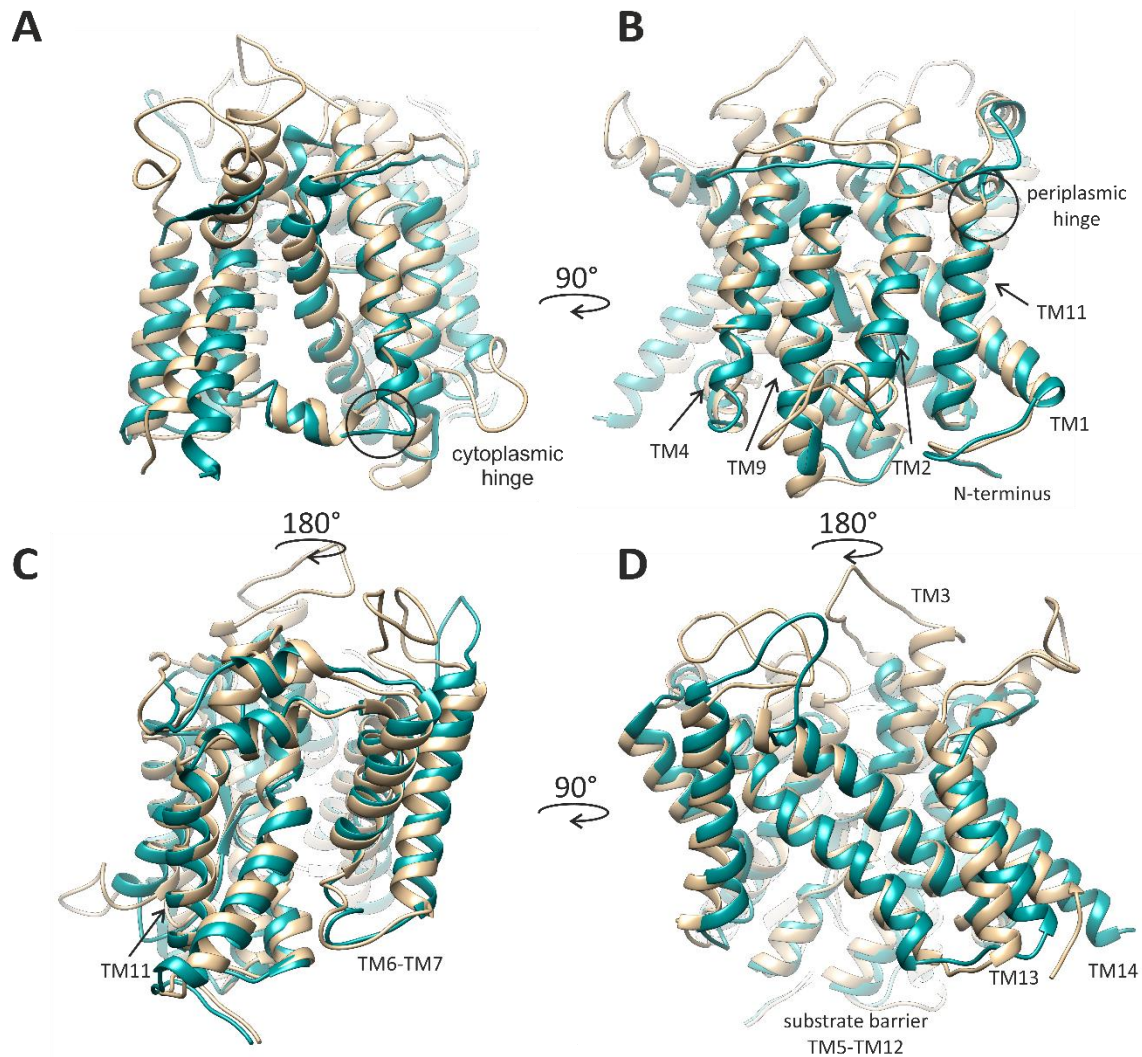


Figure 33: Structural alignment of UraA_{G320P}-Sy45 and UapA. UraA_{G320P}-Sy45 (cyan) and UapA (brown; Alguel et al., 2016) in inward-facing conformation were structurally aligned using the MatchMaker function of Chimera resulting in an RMSD of 6.6 Å for the full structures and an RMSD of 1.2 Å for 204 pruned atom pairs. (A) Side view on the cytoplasmic inter-domain linker with the periplasmic space on top. (B) Back view on the core domain. (C) Side view on the periplasmic inter-domain linker. (D) View on the gate domains with TM5 and TM12 building the substrate barrier.

substrate binding site accessibility and thermal stabilization but the absolute effect on the conformational equilibrium remained elusive. As the effect of the G320P and P330G substitution on the conformational space in UraA would also illustrate the mechanistic relevance of these positions in UraA, the conformational effect, introduced by the two variants, was studied in more detail.

4.6.1 Uracil dependent differential HDX-MS

The impact of the amino acid substitutions G320P and P330G on the conformational equilibrium in UraA was experimentally determined by differential HDX-MS (dHDX). All dHDX measurements presented were performed by Jonathan Zöllner and Dr. Julian Langer from the

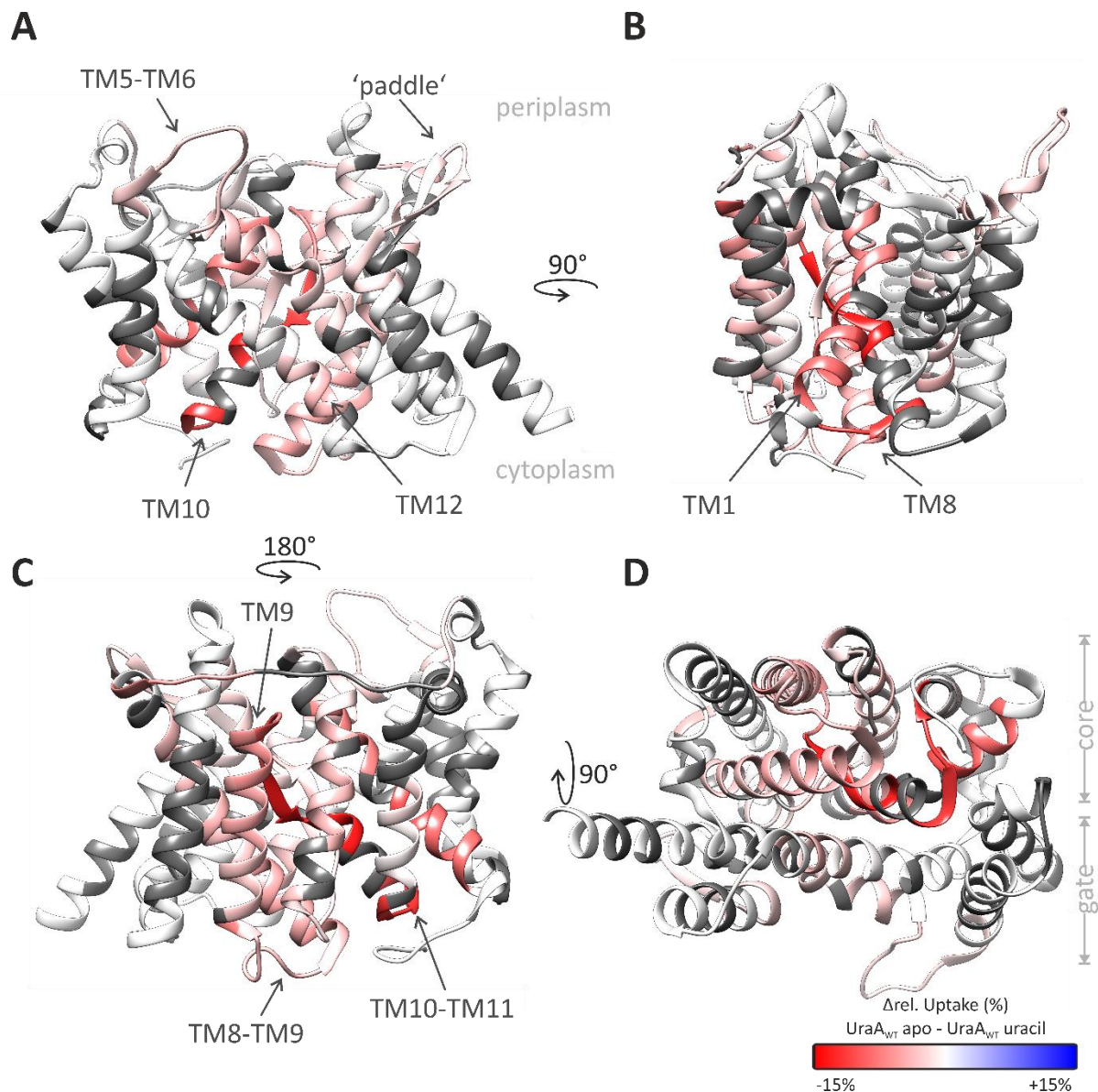


Figure 34: Differential HDX-MS of UraA_{WT}. UraA_{WT} solubilized in DM in presence and absence of 100 μ M uracil was subjected to HDX and the differential deuterium uptake plotted on one protomer of the occluded crystal structure of UraA (PDB: 5XLS). The relative differences in deuterium uptake between the UraA_{WT} apo and the UraA_{WT} uracil sample are visualized as color code ranging from -15% (red) to +15% (blue) with uncovered sections colored in dark grey. (A) Side view on the gate domain with the periplasm and cytoplasm on top and bottom, respectively. (B) Side view on gate and core domain. (C) Back view on the core domain. (D) Bottom view on core and gate domain.

MPI of Biophysics, Frankfurt, Germany. Samples of UraA variants were subjected to hydrogen deuterium exchange in the presence or absence of 100 μ M uracil for up to 45 minutes at room temperature before exchange was quenched by lowering the pH to 2.2 and cooling. Subsequent proteolysis by Pepsin followed by mass spectrometry analysis resulted in a sequence coverage of 82.4% for UraA_{WT} with 154 peptides and an average redundancy of 4.31. The sample quality throughout the 45 minutes at room temperature was verified by a long-term stability analysis of UraA_{WT} and the two inter-domain linker variants. No significant

protein aggregation was observed upon overnight incubation at room temperature (**Supplementary figure 19**). A decrease in deuterium uptake in dHDX indicates reduced solvent accessibility or increased secondary structure rigidity (Eisinger et al., 2017). A large decrease (-13%) in deuterium uptake of UraA_{WT} in the substrate binding site especially in TM10 (**Figure 34A**) and the preceding strand of the beta-sheet was observed upon uracil addition. TM1 (-10.2%) and TM8 (-5.1%; **Figure 34B**), that flank the substrate binding site, showed decreased uptake with stronger effects on their cytoplasmic sites of the helices. Apart from the substrate binding site, decreased exchange upon uracil binding was also observed in TM2 (-3.9%) and TM9 (-9.1%) and the short linker between TM10 and TM11 (-11.6%) that are not directly involved in substrate binding (**Figure 34C**). This suggested a global effect of uracil binding on UraA_{WT}, resulting not only in reduced accessibility of the substrate binding site. The gate domain showed overall less difference in HDX (**Figure 34D**) with the loop between TM5 and TM6 and the 'paddle' between TM13 and TM14 showing a slight decrease in uptake (-3.5% and -2.1%; **Figure 34A**). The midsections of TM5 and TM12 that face the substrate binding site in the gate domain and form the barrier for the substrate showed also slightly decreased uptake (-2.1% and -4.0%; **Figure 34A**). The periplasmic inter-domain linker of UraA_{WT} was not covered in HDX-MS analysis due to insufficient proteolysis while the cytoplasmic inter-domain linker was covered but showed no significant change.

The same analysis performed with UraA_{G320P} resulted in a lower coverage of 79.9% with 111 peptides and an average redundancy of 3.27. The dHDX plotted on UraA_{5XLS} overall showed similar patterns of deuterium uptake in TM1 (**Figure 35B**), TM9 (**Figure 35C**) and TM10 in presence and absence of uracil for UraA_{G320P} compared to UraA_{WT} but with slightly reduced intensity. The dHDX in TM8 with -1.3% was less compared to UraA_{WT} but higher at the cytoplasmic end of TM8 with -7.1% (**Figure 35A**). The same was true for the cytoplasmic tips of TM12 and TM13 with dHDX of -6.3% and -8.1% (**Figure 35A**). As for UraA_{WT} no change in HDX was observed at these two positions that are involved in inter-protomer interactions in the dimeric UraA_{5XLS} structure, this suggests an influence of the increased dimeric state on the deuterium uptake for UraA_{G320P}. The mutation site 320 in UraA_{G320P} showed no change in HDX upon addition of uracil (**Figure 35B**) and for UraA_{WT} this region was not covered. However, the cytoplasmic inter-domain linker was covered for both UraA variants showing reduced HDX for UraA_{G320P} with -2.6% from the cytoplasmic tip of TM4 to position 116 (**Figure 35C**) but no change was observed in TM4 of UraA_{WT}. The TM7-TM8 loop in UraA_{G320P} showed reduced HDX

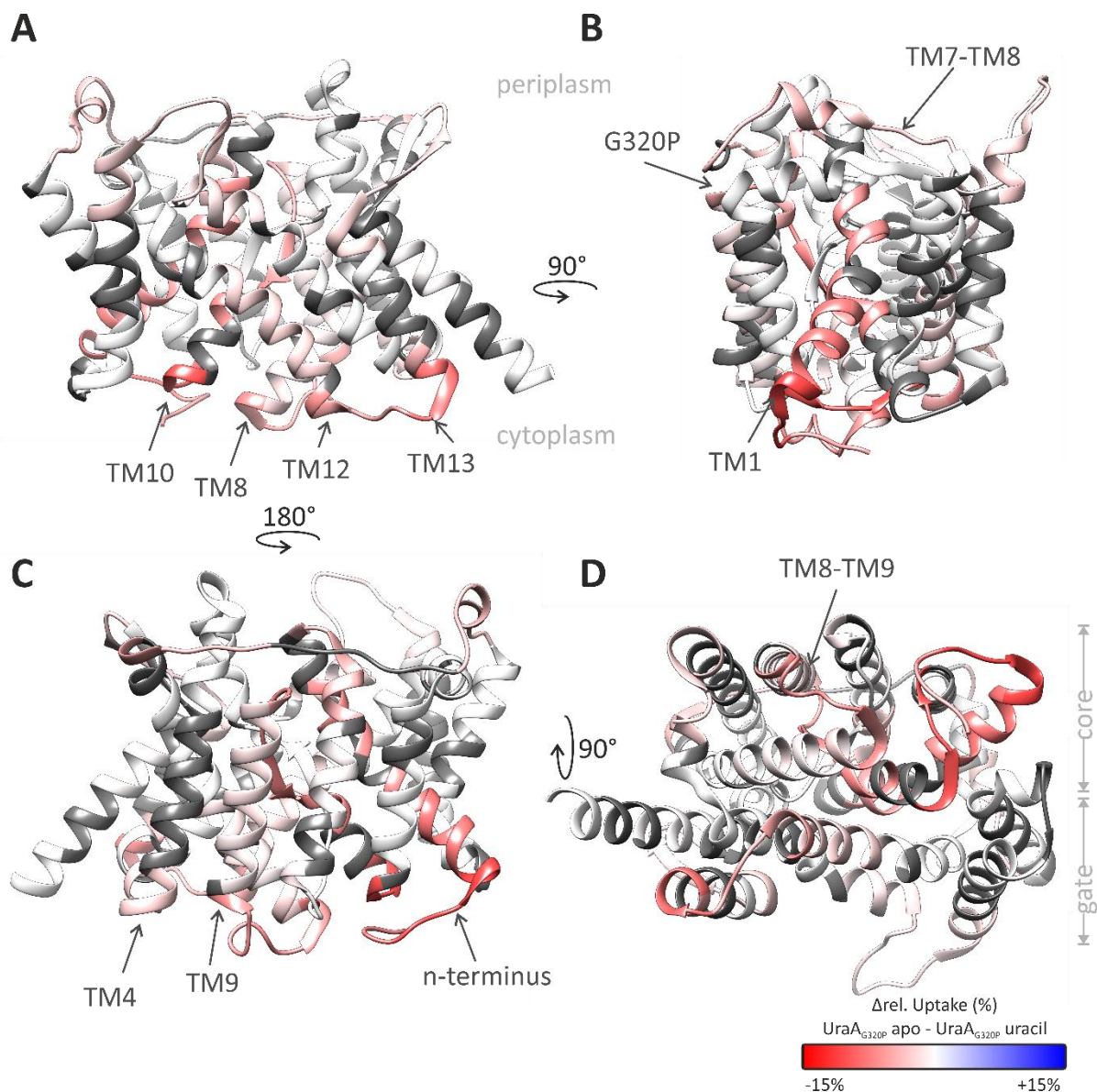


Figure 35: Differential HDX-MS of UraA_{G320P}. HDX was measured in presence and absence of 100 μ M uracil and differential deuterium uptake plotted on the occluded structure of UraA (PDB: 5XLS) with a color code ranging from -15% (red) to +15% (blue) and uncovered sequences in dark grey. (A) Side view on the gate domain with the periplasm and cytoplasm on top and bottom, respectively. (B) Side view on gate and core domain. (C) Back view on the core domain. (D) Cytoplasmic side view on core and gate domain.

with -4.6% (**Figure 35B**) that was also not observed for UraA_{WT}. Overall, this suggested a similar behavior of UraA_{WT} and UraA_{G320P} upon uracil binding with global changes but to a higher extent for the wildtype.

The dHDX analysis of UraA_{P330G} in presence and absence of uracil resulted in a higher sequence coverage of 89.2% compared to UraA_{WT} and UraA_{G320P} with 200 peptides and average redundancy of 5.17. Overall the signal intensity of dHDX was lower in UraA_{P330G} with the largest effect of uracil addition observed at the cytoplasmic tip of TM12 with -8.5% (**Figure 36A**). As observed for UraA_{G320P} the adjacent tip of TM13 showed also reduced HDX

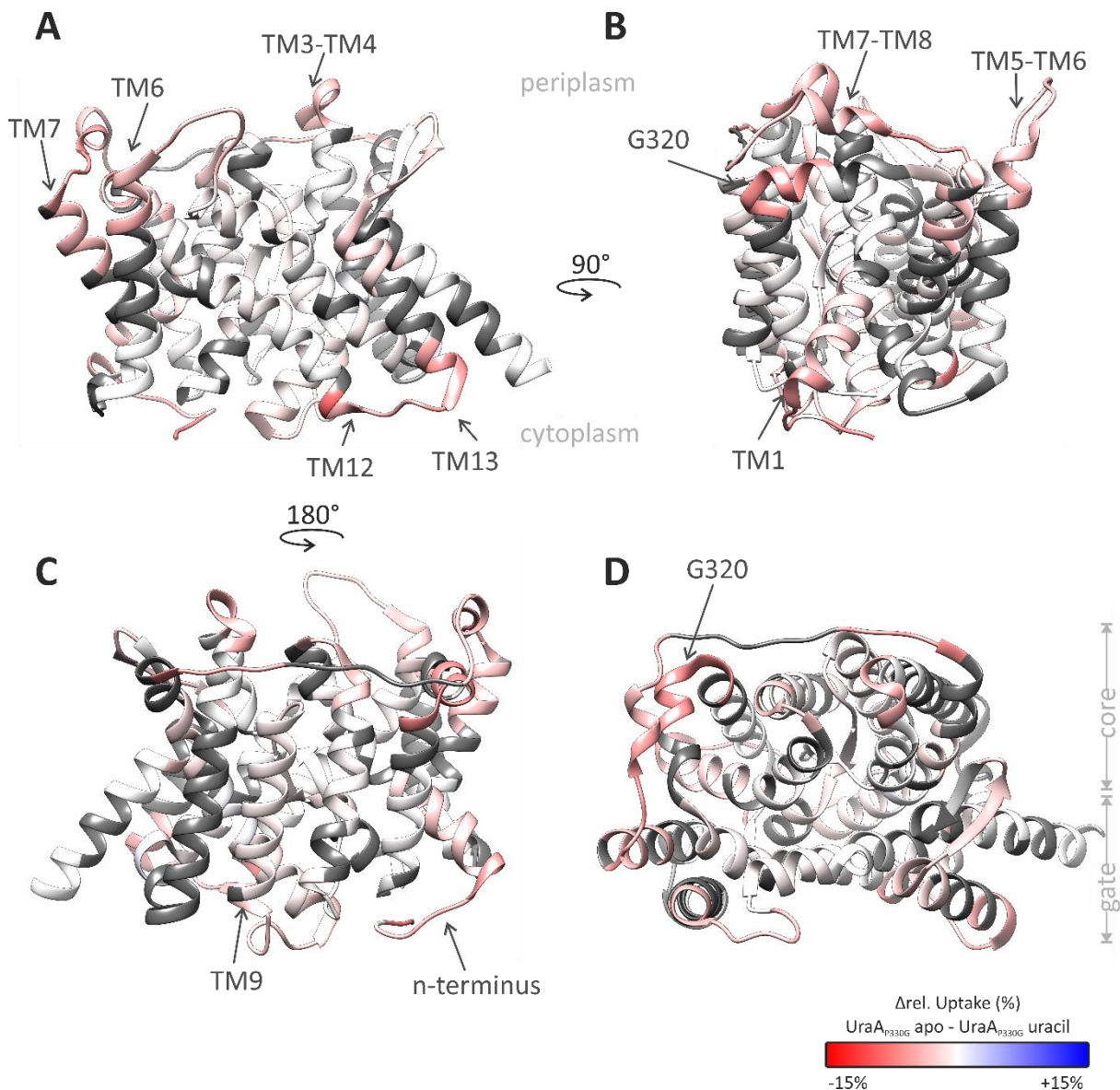


Figure 36: Differential HDX-MS of UraA_{P330G}. HDX was measured in presence and absence of 100 μ M uracil and differential deuterium uptake plotted on the occluded structure of UraA (PDB: 5XLS) with a color code ranging from -15% (red) to +15% (blue) and uncovered sequences in grey. (A) View on the gate domain in the membrane plane shows decreased HDX in the TM3-TM4 and TM12-TM13 loop and on the periplasmic side of TM6 and TM7 in presence of uracil. (B) Side view showing reduced HDX on the cytoplasmic side of TM1, in the vicinity of position G320 and in the TM5-TM6 and TM7-TM8 loops. (C) Back view on the core domain and periplasmic side view (D).

with -6.0%. As UraA_{P330G} was identified to be predominantly dimeric in size exclusion, these results might be influenced by the oligomeric state of the protein as discussed above for UraA_{G320P}. However, the strong effect at the cytoplasmic tip of TM10 with -10.0% in UraA_{G320P} was not observed for UraA_{P330G}. Similar to UraA_{G320P}, a reduced uptake was observed in the long TM7-TM8 loop especially in the short alpha helix that was not observed for UraA_{WT} (**Figure 36B**). The strong decrease in TM1 for UraA_{WT} and UraA_{G320P} was less pronounced with -3.1% dHDX (**Figure 36B**) and the same was true for TM9 (**Figure 36C**). The decreased dHDX pattern of UraA_{WT} and UraA_{G320P} in the substrate barrier forming transmembrane sections 5

and 12 was completely lost in UraA_{P330G} (**Figure 36A**). However, patterns unique to UraA_{P330G} were observed in TM7 with decreased uptake by -3.9% and in the TM3-TM4 loop with -4.6% (**Figure 36A**). Furthermore, UraA_{P330G} showed reduced HDX in presence of uracil with -6.5% at position 320 and the adjacent residues (**Figure 36D**). Overall, the effect of uracil binding was only subtle in the substrate binding site and central parts of the gate domain in UraA_{P330G} compared to UraA_{WT} and UraA_{G320P} even though substrate binding was shown by DSF suggesting a less global effect of uracil binding on UraA_{P330G} in comparison to UraA_{WT} and UraA_{G320P} and might represent a binding event without impact on global protein dynamics.

4.6.2 Differential HDX-MS of UraA_{G320P} and UraA_{P330G}

The differential HDX-MS analysis was further extended to a direct comparison of the two UraA variants with UraA_{WT} (**Figure 37**) in their apo states. Thereby, significant differences between the UraA variants became visible. For UraA_{G320P}, TM1 showed the strongest effect in HDX with a reduction of -20.1% and a reduction of -19.0% that was observed in TM9 (**Figure 37B**). Further reduction in HDX was observed for the TM10-TM11 loop (-17.5%) and the cytoplasmic side of TM8 (-16.3%) and TM3 (-9.4%). These effects were also observed for UraA_{WT} upon addition of uracil suggesting similar effects to uracil binding introduced by the G320P substitution in UraA. Additional changes in HDX of UraA_{G320P} were found in the TM7-TM8 loop especially at the alpha helical part that is in proximity to the periplasmic inter-domain linker (**Figure 37A**). HDX was changed by -14.7% and could be related to a local reduction of structural flexibility introduced by the G320P substitution that is transferred to the TM7-TM8 loop. In line with this, the position P330 showed a change by -5.4% that was neither observed for UraA_{WT} nor UraA_{G320P} upon uracil addition. Though position 320 with the introduced glycine to proline substitution was not covered in the dataset, the effect in TM7-TM8 and at position 330 suggested a local rigidification in the periplasmic inter-domain linker in UraA_{G320P}.

The TM5-TM6 loop in the gate domain of UraA_{G320P} showed reduced HDX by -11.8%. The higher dimer content of UraA_{G320P}, as observed in size exclusion chromatography, could influence the dHDX especially in the gate domain. However, the reduced HDX in the TM5-TM6 loop was also observed in the UraA_{WT} dataset upon uracil binding. The same was true for the reduction at the periplasmic side of TM5 and in TM12 that build the substrate barrier suggesting an effect independent of the oligomeric state or overlapping effects of substrate binding and dimerization leading to the complex dHDX pattern.

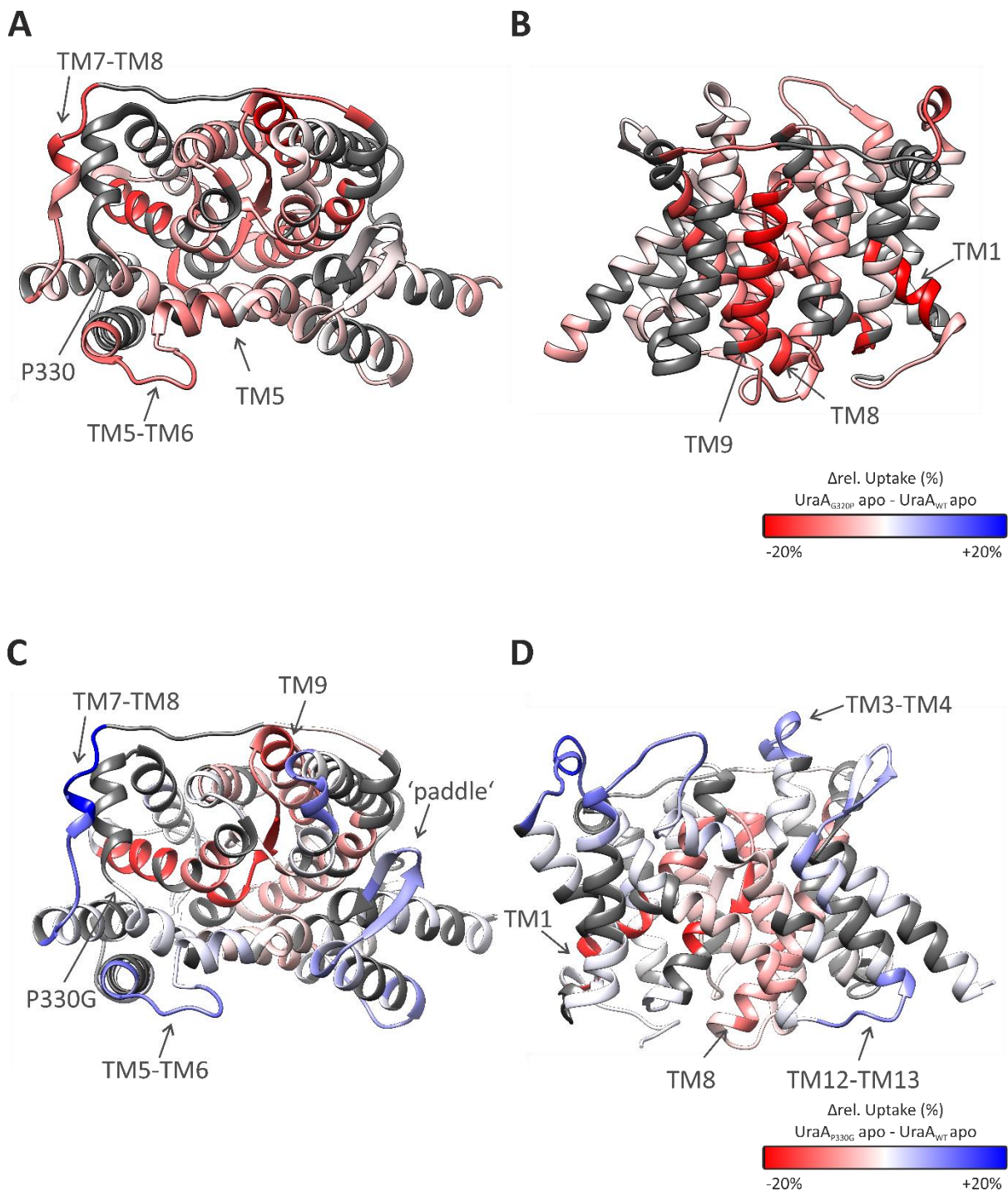


Figure 37: Differential HDX of UraA_{G320P} and UraA_{P330G} in comparison to UraA_{WT}. (A) Periplasmic side view on the occluded structure of UraA with differential HDX of UraA_{G320P} and UraA_{WT} plotted as color code ranging from -20% (red) to +20% (blue) and uncovered sequences in grey with back view on the core domain (B). (C) Differential HDX of UraA_{P330G} compared to UraA_{WT} with the same color code as in (A) in periplasmic side view and view on the gate domain within the membrane plain (D).

The correlation of dHDX in UraA_{WT} upon uracil binding and UraA_{G320P} especially in TM1, TM8 and TM9 pointed towards a conformational effect introduced by UraA_{G320P} in comparison to UraA_{WT} that was comparable to the effect introduced by addition of uracil. As the conformational transition from inward-facing to occluded in UraA (Figure 32) showed a

significant displacement of TM1, the reduced HDX in TM1 observed in UraA_{G320P} and UraA_{WT} upon uracil binding was interpreted as result of the conformational change from inward-facing to occluded. Following this interpretation, UraA_{WT} would be preferably in the inward-facing conformation and undergo a conformational change towards the occluded conformation upon uracil binding. However, increased deuterium uptake could be expected on the periplasmic side of UraA which was not observed. This could be explained by the reduced displacement of transmembrane segments on the periplasmic side compared to the cytoplasmic side in the conformational transition (**Figure 32**). Following this hypothesis, the occluded conformation would be preferred for UraA_{G320P} while the inward-facing conformation is still sampled but to a lower extent. This was in line with the overall lower effect of uracil binding on UraA_{G320P} in dHDX and with the structural data on UraA_{G320P} in the inward-facing conformation in presence of Sy45.

The dHDX-MS analysis for UraA_{P330G} in comparison to UraA_{WT} revealed significant differences between the mutant and the wildtype but also common patterns compared to the dataset of UraA_{WT} in presence of uracil. The largest difference was observed in the TM7-TM8 loop with an increase in HDX of 20.1% in UraA_{P330G} (**Figure 37C**). In line with the effect in the TM7-TM8 loop in UraA_{G320P}, where the local rigidification was hypothesized to be transferred to the loop and led to decrease in HDX, the proline to glycine substitution at position 330 suggested to increase the local flexibility at the periplasmic inter-domain linker and the TM7-TM8 loop. As the inter-domain linker was not covered, this local effect could not be observed directly at position 330. Further increase in HDX for UraA_{P330G} was observed in the TM5-TM6 loop (+9.6%), in the 'paddle' connecting TM13 and TM14 (+8.2%; **Figure 37C**) and the cytoplasmic tip of TM13 and the adjacent linker (+8.4%; **Figure 37D**). As these positions are located in the gate domain that builds the dimer interface of UraA, the high degree of dimerization of UraA_{P330G} compared to the mostly monomeric UraA_{WT} in solution might cause these changes in HDX. As the scaffold domains of elevator transporters are known to thin the membrane to reduce the substrate translocation path length, a higher solvent accessibility in the dimer could explain the observed increase in HDX. As consequence, these positions would be more shielded by the detergent micelle in the monomeric protein. The structured NG and DM molecules along TM12, TM13 and TM14 in the monomeric UraA_{G320P}-Sy45 structure would be in line with this hypothesis (**Figure 27**) regarding the 'paddle' and TM13 but not the TM5-TM6 loop. Additionally, UraA_{G320P} was also found to be more dimeric compared to UraA_{WT} and the

discussed effect of dimerization on dHDX for UraA_{P330G} should also apply for UraA_{G320P} but the respective positions showed reduced HDX in UraA_{G320P}. Therefore, the dHDX patterns in the gate domain of UraA_{G320P} and UraA_{P330G} were likely to be caused by multiple overlapping effects, oligomerization and conformational change, complicating the interpretation of this data.

Apart from the increased HDX for the mentioned position in UraA_{P330G}, the characteristic pattern of reduced HDX in TM1 and TM8 especially on the cytoplasmic side and TM9 was observed. As discussed before this could indicate a shift in conformational equilibrium towards an increased population of the occluded conformation. In contrast to UraA_{G320P} where the substitution at the inter-domain linker resulted in a global rigidification and shift towards the occluded conformation, UraA_{P330G} showed a similar conformational shift but accompanied by a gain in flexibility.

The dHDX analysis yielded relative information on the solvent accessibility of the three UraA variants that indicated conformational preferences when combined with information from the UraA_{G320P}-Sy45 structure. UraA_{WT} showed an effect of uracil binding on the whole core domain apart from local effects in the substrate binding site. The overall reduction of HDX for UraA_{WT} in presence of uracil led to the hypothesis of a conformational transition induced by uracil binding resulting in a conformation with overall less surface exposure or increased secondary structure rigidity, respectively. As the G320P substitution led to a similar effect as uracil binding, an increased population of the occluded conformation in UraA_{WT} upon uracil binding was deduced. For UraA_{G320P} the suggested occluded conformation preference was supported by the dHDX analysis but additional existence of an inward-facing conformation was indicated in line with the UraA_{G320P}-Sy45 crystal structure. For UraA_{P330G} the minor effects in dHDX suggested only a local effect upon uracil binding while the comparison with UraA_{WT} indicated major differences suggesting a conformational restriction of UraA_{P330G} in a conformation with less solvent accessibility of the core domain on its cytoplasmic side.

4.6.3 Conformational space of UraA in DSF

The observations from dHDX were further investigated by differential scanning fluorimetry. Uracil titration with substrate concentrations ranging from 1 μ M to 8 mM was performed and melting curves of UraA_{WT} in presence of these different uracil concentrations recorded. The melting curve was found to be heterogenous with a shoulder at 50 °C and a maximum signal

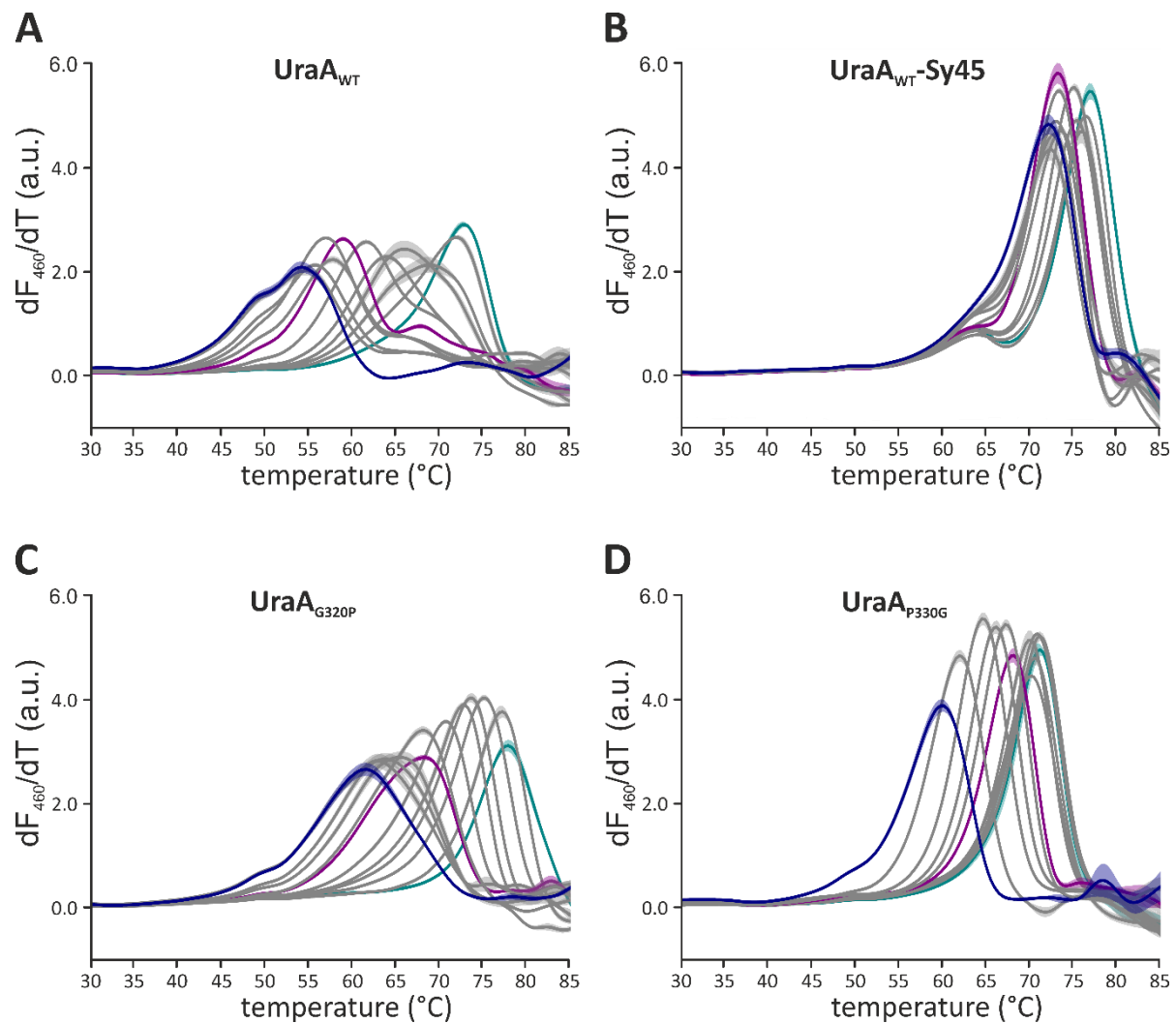


Figure 38: Conformational space of UraA altered by uracil binding. UraA_{WT}, UraA_{G320P} and UraA_{P330G} at 0.1 mg/mL concentration were titrated with increasing concentration of uracil ranging from 1 μ M to 8 mM and the shifts in melting temperature upon substrate binding were recorded. For the UraA_{WT}-Sy45 sample, 22 μ M Sy45 a 10-fold molar excess was added. Samples were equilibrated for 30 minutes before thermal melting. The first derivatives of the melting curves are shown for better visualization of the melting temperatures as peak maximum. The mean of triplicates and the standard error are presented. Samples containing no uracil are colored in blue and samples with highest uracil concentration (8 mM) in cyan. Samples containing 50 μ M uracil are highlighted in purple. (A) uracil binding stabilizes UraA_{WT} from 55 $^{\circ}$ C to 65 $^{\circ}$ C while higher uracil concentrations induce a second population with melting temperatures above 65 $^{\circ}$ C. (B) In presence of Sy45, locking UraA_{WT} in the inward-facing conformation, a more linear increase in T_m is observed. UraA_{G320P} (C) and UraA_{P330G} (D) show different profiles compared to UraA_{WT}.

displaying the melting temperature of 54.2 $^{\circ}$ C in absence of uracil (**Figure 38A**) suggesting the presence of different populations in the sample. This might be related to different conformations being in equilibrium. As the first derivative shows the steepness of the melting reaction, no conclusion could be drawn on the occupancy of the different populations based on this data. Upon titration of UraA_{WT} with the substrate uracil in the concentration range of 1 μ M to 20 μ M, the melting temperature shifted to 57.8 $^{\circ}$ C due to uracil binding while the shoulder at 50 $^{\circ}$ C remained visible and a new population at melting temperatures above 65 $^{\circ}$ C

became visible. As this population was not generated by substrate induced shift in melting temperature but rather emerged newly, this suggested a conformational transition. At uracil concentrations of 50 μM to 2 mM the signal at 65 $^{\circ}\text{C}$ became more prominent and shifted towards a melting temperature of 70 $^{\circ}\text{C}$ while the original major population with lower melting temperature further shifted to 65 $^{\circ}\text{C}$ due to the higher substrate concentration (Scott et al., 2016). This population was reduced in size at uracil concentrations above 4 mM and the main melting event was displayed by the population that emerged from a conformational change. In the presence of Sy45 that stabilizes the inward-facing conformation of UraA and reduces the conformational equilibration, the titration of uracil resulted in a less complex behavior of UraA_{WT} with more linear increase in melting temperature and overall smaller shift from 72.2 $^{\circ}\text{C}$ to 76.8 $^{\circ}\text{C}$. The reduced conformational equilibrium in presence of Sy45 resulted in steeper melting transitions suggested by the higher signal intensity in the first derivative of the melting curves (**Figure 38B**). The reduced effect of uracil binding on UraA in presence of Sy45 was also observed in the comparison of the two crystal structures UraA_{G320P}-Sy45 and UraA_{G320P}-Sy45-uracil (**Figure 41**).

The uracil titration of UraA_{G320P} in thermal melting (**Figure 38C**) showed a different melting profile compared to UraA_{WT} with a single melting event shifted from 61.5 $^{\circ}\text{C}$ without uracil to 77.8 $^{\circ}\text{C}$ in presence of 8 mM uracil. Thereby the steepness of melting was comparable to UraA_{WT} and reduced comparison to UraA_{WT}-Sy45 indicating some conformational flexibility of UraA_{G320P}. In contrast, UraA_{P330G} showed steeper transition in thermal melting comparable to UraA_{WT}-Sy45 with melting temperatures increasing from 59.9 $^{\circ}\text{C}$ to 71.2 $^{\circ}\text{C}$ (**Figure 38D**). Different to UraA_{WT} and UraA_{G320P}, the shift in T_m for UraA_{P330G} was almost saturated at an uracil concentration of 200 nM with a T_m of 70.1 $^{\circ}\text{C}$ and the observed melting profile was more homogenous as suggested by the reduced width and higher symmetry of the melting curves similar to UraA_{WT} in presence of Sy45. This could be in line with a potential higher uracil affinity of UraA_{P330G}.

The uracil titration in DSF underlined the results obtained by dHDX for UraA_{WT}, UraA_{G320P} and UraA_{P330G}. UraA_{WT} appear to feature a dynamic conformational equilibrium that become more homogeneous upon uracil addition. The proposed conformational change towards the occluded conformation was observed as newly emerging population with a higher T_m . The conformational space of UraA_{G320P} shared characteristics with UraA_{WT} but was reduced in its conformational dynamic. A conformational transition was not observed in DSF which could be

related to its *ab initio* preference for the occluded conformation. The melting profiles of UraA_{P330G} upon uracil addition were shifted to higher T_m but were not altered in shape or steepness in line with the small effect of uracil binding in dHDX. This supported the limited conformational space postulated for UraA_{P330G} with the occluded conformation being highly populated.

4.6.4 Conformational thermostabilization of UraA

Dynamic conformational space analysis of UraA_{WT}, UraA_{G320P} and UraA_{P330G} in dHDX and DSF suggested a major contribution of the introduced conformation in UraA on its thermal stability. This was indicated by the different stabilizing effects of uracil on UraA_{WT}, dependent on the presence of Sy45 and by the conformational restricted UraA variants G320P and P330G, that showed *ab initio* increased thermal stability. Consistently, modulation of the conformational space by binding of conformational-specific binders would result in different effects for the individual UraA variants. This hypothesis was tested by thermal melting analysis of UraA_{WT}, UraA_{G112P}, UraA_{G320P} and UraA_{P330G} in presence of Sy5, Sy45 and Nb6E3 that were identified to stabilize distinct conformations of UraA_{WT} (4.2.3) and thereby increase the melting temperature of UraA_{WT}. Sy45 was shown in this study to stabilize the inward-facing conformation by co-crystallization while the stabilized conformational could not be assigned for Sy5 and Nb6E3. UraA_{G320P} was thermal stabilized by Sy45 but to a lower extent as UraA_{WT} in line with its preference for the occluded conformation along with reduced population of the inward-facing conformation (**Figure 39**). UraA_{G320P} was stabilized by Sy5 to a higher degree as observed for UraA_{WT} but Nb6E3 did not stabilize this variant indicating a mismatch between the Nb6E3 conformation and the conformational space of UraA_{G320P}. UraA_{P330G} was only slightly stabilized by Sy45 in line with the reduced conformational space with much lower occupancy of the inward-facing conformation as observed in dHDX. Interestingly, Sy5 and Nb6E3 reduced the melting temperature of UraA_{P330G} underlining the impact of the conformational equilibrium on the thermal stability in UraA.

The conformational equilibrium of UraA_{G112P} was not analyzed by cysteine accessibility and dHDX in this study, as initial experiments did not indicate major alterations. Consistently, all three binders stabilized this UraA variant and the reduced stabilization by Sy45 could be related to a lower affinity for Sy45 due to the G112P substitution close to the Sy45 epitope (4.5.4), that might lead to local structural distortions.

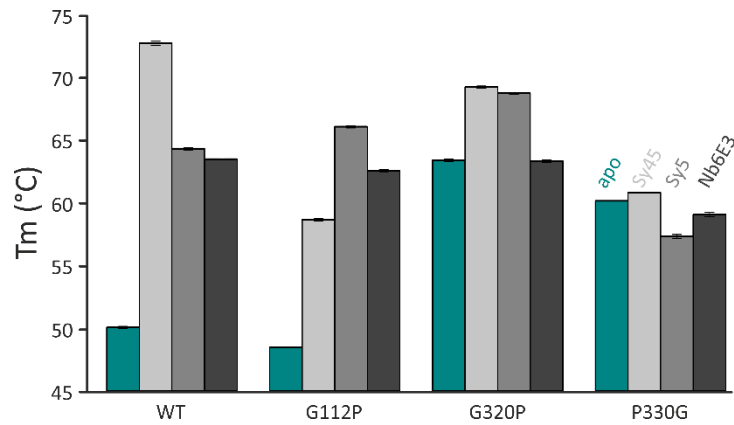


Figure 39: Conformational dependent thermal stabilization of UraA variants. Thermal melting of UraA_{WT} and the three variants UraA_{G112P}, UraA_{G320P} and UraA_{P330G} in presence of three conformational specific binders Sy45 (light grey), Sy5 (grey) and Nb6E3 (dark grey). Melting temperatures in absence of binders is presented in cyan. UraA variants were diluted to 0.1 mg/mL and incubated with 5-fold molar excess of nanobody respectively sybody before addition of CPM and subsequent thermal melting. Mean of four samples and corresponding standard errors are shown.

In summary, conformational specific binders could be used as conformational probes in order to confirm the shifted conformational equilibrium of UraA_{G320P} and UraA_{P330G} while UraA_{G112P} could be shown to feature characteristics of UraA_{WT} in the conformational range that was covered by Sy45, Sy5 and Nb6E3. Further, the postulated differences in conformational specificity of the three binders could be validated. Finally, a major contribution of the conformational equilibrium and its alteration on the thermal stability of UraA was identified.

5 Discussion

The conformational equilibrium of UraA was successfully manipulated in this study following the strategy of binder selection and amino acid substitution in conformational hinges. Aspects regarding the binder selection including the selection pipeline with the concept of conformation mapping are discussed in the first part of this chapter. The combination of these two strategies led to the UraA_{G320P}-Sy45 co-crystal structure that yielded new insights into the structure and function relationship of UraA and other 7-TMIR proteins. This is discussed in the second part. Additionally, the functional relevance of the alpha-helical inter-domain linkers in UraA, the concept of conformational thermostabilization and the conformational space of UraA are discussed in the last part.

5.1 Nanobody selection

5.1.1 Strategies and experiences

This study presented several strategies to bias nanobody selections towards certain binder characteristics and the following section will evaluate the applied strategies based on the nanobodies that resulted from these.

The binder Nb2H9 was selected from a library resulting after pre-panning the phage display library with a specific crosslinked version of UraA (UraA_{L80C-M143C}) based on the published inward-facing conformation (Lu et al., 2011; PDB: 3QE7) to remove binders stabilizing the already known conformation from the selection pool. Even though pre-panning reduced the

diversity of the library as seen on the number of eluted phages after biopanning, the unique binder Nb2H9, that could not be identified from any other selection path, was gained from this procedure. Thus, pre-panning can lead to selection of rare binders. Further, nanobodies Nb3F7 and Nb3H7 resulted from the pre-panning selection path even though binders with identical CDR3 could also be selected by different selection strategies. The success of pre-panning depends on the quality of the pre-panning antigen used and in case of conformational locking, the extent to which the antigen can be locked in one conformation. It might be beneficial to include such pre-panning after the first round of biopanning, as pre-panning in the first round may lead to an unnecessary decrease of library diversity.

A second selection strategy used in this study was based on shielding parts of the antigen surface to prevent nanobody binding and thereby bias the epitope selection. Therefore, an introduced cysteine on the cytoplasmic side of UraA was labeled with PEG-5000 to shield the cytoplasmic epitope and consequently to enrich binders targeting periplasmic epitopes. This selection path resulted in low enrichment during phage display and derived nanobodies were conformational non-selective based on lack of thermal stabilization (**Figure 15**). Among others, Nb17D3 showed these characteristics and interestingly this nanobody was also identified in selections against a homolog of UraA from *Pyramidobacter piscolens* with a sequence identity to UraA of 27.8%, that was also used for alpaca immunization. This indicated an unspecific binding mode for Nb17D3 probably to hydrophobic patches of the target protein or to the detergent micelle. A poor antigen quality during selection due to the covalently linked PEG-5000, that might keep partially unfolded proteins in solution, could be responsible for this outcome. Even though UraA_{Cysless-1252C}-PEG-5000 showed a reasonable elution profile in preparative size exclusion chromatography (**Supplementary figure 5**), unfolding during phage display cannot be excluded. Consistently, using this approach conformational-selective binders could not be selected and in fact epitope blocking using PEG-5000 even resulted in the enrichment of unspecific binders.

In addition, the shielding strategy was also applied to counterselection antigens with better outcome. From the unique binders identified, in total 7 resulted from selection paths including counterselection with the pegylated UraA variant M143C (**Supplementary table 1**). This strategy was superior as the positive selection could be performed with UraA_{WT}, the antigen that was also used for immunization, without any modifications that could complicate phage display selection. Thereby, enrichment of specific binders was expected and the selection was

less biased as phages were removed from the selection pool by counterselection but the properties of the counterselection antigen did not directly influence the properties of the selected nanobodies. However, usage of PEG-5000 for epitope shielding was found to be not the best method due to the unstructured characteristics and unpredictable shielding efficiency and the issue of unfolded protein being kept in solution as mentioned above. The better alternative might be cysteine labeling with biotin-maleimide for subsequent shielding with streptavidin whereas the low dissociation rate of the biotin streptavidin complex would prevent immobilization of the counterselection antigen. The biotin strategy would also allow to shield an epitope of the selection antigen by biased immobilization to neutravidin during selections. Whether shielding with PEG-5000 was successful in this study in directing binders to the periplasmic epitope, the initial motivation for this strategy, cannot be judged due to the limited number of nanobodies analyzed. Even though the periplasmic binder Nb7F3 was derived from a selection path including counterselection, Nb6D3 with similar periplasmic epitope (**Figure 17**) could be selected without counterselection as well. Though, the benefit of counterselection with UraA_{Cysless-M143C}-PEG-5000 cannot be estimated in detail, promising unique nanobodies such as Nb7F3 and Nb21F7 with strong thermal stabilization of UraA_{WT} in DSF could only be selected with counterselection suggesting at least a positive effect of the presented method for increased diversity of selected nanobodies (**Figure 15**).

In addition, selections were performed in presence of uracil resulting in selection of unique binders such as Nb6G7. The underlying effect could be a change in conformational space of UraA upon substrate addition (**Figure 34** and **Figure 38**) and as shown for the transporter Glt_{Ph} the substrate concentration can be adjusted to populate different transporter conformations (Arkhipova et al., 2020). Thereby, rare conformations might be more populated during selections, though conformational space may also be reduced upon substrate addition depending on the individual protein dynamics. Thus, selections in presence and absence of different substrate concentrations carried out in parallel would be advisable.

In case of UraA, no uracil dependent binding for any binder could be identified even though selections were performed in the presence or absence of uracil. The apparent absence of structural changes within the core and gate domain during transport suggests a lack of allosteric sites that could be targeted by such binders. In addition, direct competition between binder and substrate at the substrate binding site seems unlikely due to the buried nature of the uracil binding site (**Figure 29**). Though no structural information is available, the outward-

facing binding site could be less buried but the TM5-TM6 loop is likely to restrict the accessibility for periplasmic binders. Thus, uracil competition may be a rare property in the binder library in line with the experimental results.

The last selection strategy used in this study was the solid phase immobilization of UraA antigens instead of the specific biotinylated Avi-tag neutravidin immobilization method (Kuhn et al., 2020). This strategy led exclusively to binders that did not stabilize UraA_{WT} in thermal melting. This indicated unspecific binding due to potential unfolding of the antigen upon solid phase immobilization or binding to conformationally inactive epitopes. It is likely that the solid phase immobilization promoted unfolding of UraA antigens during selections making this method less favorable even though it is fast and straightforward (Nizak et al., 2005). For membrane proteins with soluble domains, which are generally less prone to unfolding upon immobilization, this effect might be less critical as for the highly membrane-embedded UraA. But it is likely that the majority of binders selected in this was would be directed towards the more stable soluble domain due to partial unfolding of the transmembrane domain. This could be exploited for certain projects but the usage of a separately expressed biotinylated soluble domain in combination with neutravidin immobilization would be more elegant.

5.1.2 Conformation mapping

From the classical nanobody analysis pipeline including ELISA and affinity determination, no conclusion can be drawn on the conformation of the target protein that is stabilized by the individual binders. This information is extremely valuable as it reduces the number of binders in subsequent applications that are mostly time-consuming and cost-intensive. However, conformational analysis of nanobodies by, for example, binding experiments requires target proteins modified to sample only a certain conformation. As the main goal of nanobody selection itself is often to achieve a conformational lock by using nanobodies as tool, the target protein is not likely to be present in such a condition that allows conformational analysis of nanobodies. In case of primary active ABC-transporters, ATP, ADP and a variety of analogs and generic active site mutations are available to capture the protein at distinct steps in the transport cycle (Barth et al., 2018). Secondary active transporters are more challenging regarding locking conformations due to the lack of generic tools for conformational arrest. Crosslinking could lock transporters in a specific conformation but would only provide negative information on binders that stabilize a different conformation and guide the

selection procedure towards the already known conformation. In conclusion, it is challenging to predict the conformation of a secondary active transporter stabilized by the individual binders in an efficient manner. HDX-MS has been used to highlight the shielding of the epitope towards the aqueous solution upon nanobody binding (Wei et al., 2014). Thereby the epitope can be mapped on the three-dimensional structure of the target protein, if available, to visualize the epitope. Whether conformational information can be retrieved from this analysis might depend on the individual target protein. The same is true for the crosslinking-MS approach presented by Pleiner et al. (2014). As presented above in this study, different epitopes may result in stabilization of the same conformation. The example of Sy45 and Nb7F3 where both binders bind from opposing sides of the membrane to UraA indicated that epitope analysis does not necessarily correlate with the stabilized conformation of the target protein.

In this study a relative conformational analysis pipeline was developed based on differential scanning fluorimetry that groups nanobodies with similar characteristics regarding their targeted conformation. As a result, the number of nanobodies that need to be screened can be strongly reduced and may approach the number of discrete conformations the transporter is expected to sample. The key element of this pipeline is that stabilization of a target protein by nanobodies can be additive leading to a further shift in T_m to higher temperatures upon binding of a second nanobody to the target protein (Sigoillot et al., 2019). On the other hand, intermediate melting temperatures were reported due to competition of two ligands for the same binding site in mixed samples compared to single ligand melting analysis (Redhead et al., 2017). This theoretical framework was transferred to the nanobody UraA interaction as last stage of the selection. In this study, the simultaneous binding of Sy45 with Nb7F3 was observed based on additional thermal stabilization in DSF (**Figure 17**) and was also observed for other combinations of binders. From this experimental result two conclusions could be drawn. First, Sy45 and Nb7F3 bind to two distinct epitopes that do not overlap which was already known from side specific transport inhibition and pulldown analysis (**Figure 16**). The second and probably more valuable conclusion was that Sy45 and Nb7F3 stabilize UraA in the same conformation. Consistently, both showed competition with a third binder Sy5 indicated by intermediate melting temperatures. Generally, the competition between binders could be due to two separate effects, the first being an epitope overlap leading to steric competition and the second being stabilization of different conformations of the target protein that results in conformational competition whereas the latter might feature steric competition in addition.

In case of Sy45, Nb7F3 and Sy5, the conformational competition of Sy5 and Sy45 was obligatory as the epitopes were located on opposing sides of the membrane (**Figure 17**). Therefore, the competition of Sy5 with Nb7F3 was necessarily conformational as well but the periplasmic epitopes of both binders could cause additional steric competition. This example showed that triangulation of simultaneous DSF results enabled to identify the nature of binder competition. However, the example further underlined that at least low-resolution epitope information is required to expand the gained information away from simultaneous binding towards relative conformational distinction.

Even though the presented pipeline does not assign the stabilized conformation, the set of binders for this subsequent analysis is minimized and suited for low throughput methods as shown in this study by co-crystallization of UraA_{G320P} with Sy45. Alternatively, cryo-EM or more dynamic methods as HDX-MS or EPR could be used for this purpose. In this study, Sy45 was found to stabilize UraA in the inward-facing conformation and Sy5 and Nb6E3 were predicted to stabilize different conformations as Sy45. Further structural biology including only these two binders could result in extensive structural information of the UraA transport cycle without further screening due to the pre-selection by the outlined approach.

In summary, the presented method allows to identify nanobodies that bind simultaneously or compete for an overlapping epitope on the target protein. The pair of simultaneously binding nanobodies might be helpful to further increased hydrophilic surface for generating better crystal contacts in crystallography or increased particle size for single particle cryo-EM. However, information from competition can be used to distinguish between different conformations stabilized by binders when combined with epitope information from any side-specific experiment such as transport or pulldown or HDX-MS and crosslinking-MS. The simultaneous binding analysis is not limited to differential scanning fluorimetry but could also be based on surface plasmon resonance spectroscopy or bio-layer interferometry.

5.1.3 Nanobody and Sybody comparison

The newly introduced sybody libraries (Zimmermann et al., 2018) serve as a convenient alternative to classical *in vivo* selections with focus on membrane protein applications (Zimmermann et al., 2020). In general, conformational stabilization of target proteins by nanobodies might raise the question whether the captured conformation represents a native state of the protein and in case of synthetic nanobodies this concern might be enhanced.

Given the better control over sample quality and selection condition *in vitro*, this intuitive concern regarding synthetic nanobodies appears incorrect but experimental evidence is still limited due to the small number of publications regarding sybodies ((Hutter et al., 2019; Arnold, Weber and Gonda et al., 2020; Bräuer et al., 2019). The selections of nanobodies and sybodies against the same target protein – UraA – performed in this study represent a rare case that allows comparison of nanobodies and sybodies.

Both selection methods resulted in more than 25 individual binders and large-scale production and purification resulted in comparable protein yields for sybodies and nanobodies. However, from the initial set of 40 sybodies, 9 were discarded based on unfavorable biochemical properties (polydisperse size exclusion profiles and/or low protein yields), while all tested nanobodies behaved well. *In vivo* antibody maturation may lead to selective enrichment of binders with improved biochemical properties, whereas for synthetic libraries the selection for these characteristics takes place during the panning. Nevertheless, sybodies with good to excellent biochemical behavior are easily identified (**Figure 14** and **Supplementary figure 11**). Initial thermal stabilization of UraA suggested conformational selectivity for a significant fraction of selected binders. Though alpaca-derived nanobodies overall led to larger shifts in T_m of UraA_{WT} in initial analyses with lower excess of binders, Sy5, Sy20 and Sy45 showed comparable stabilization of UraA_{WT} in later thermal melting experiments (**Figure 17**). Induced transport inhibition of endogenous UraA was observed by Nb7F3 and other nanobodies but also by Sy5 suggesting binding to a native conformation of UraA as the introduction of an artificial conformation within the lipid bilayer appears unlikely. The same conclusion could be drawn for Sy45 based on the positive pulldown by inside-out vesicles. The physiological relevance of the Sy45 stabilized UraA conformation was further supported by the simultaneous binding of Sy45 and Nb7F3 or Nb6D3 to UraA and the similarity to the UapA structure (Alguel et al., 2016; **Figure 33**). In summary, the selected nanobodies and sybodies against UraA could be used as complementary tools to study the conformational space of UraA and advantages and disadvantages of both selection procedures were observed: while the generation of nanobodies takes more time, the average protein quality of the binders is slightly better, 10-fold more target protein is required compared to sybodies. Based on this experience, sybodies could be recommended as additional approach to conventional nanobodies to increase the diversity of binders as observed in this study with the unique

binder Sy5 but should be considered with higher priority for selections requiring defined and well controlled selection conditions.

5.2 Co-crystallization of UraA

Co-crystallization of UraA was performed with several binders whereof Sy45 and Sy5 yielded the best crystals as presented (**Figure 24** and **Figure 25**). In addition, our conformation analysis suggested that both stabilize different conformations (**Figure 17**). While in combination with Sy45 and UraA_{WT}, crystals could be obtained in several conditions with reasonable diffraction, Sy5 co-crystals were only achieved in combination with UraA_{G320P} and in a lower number of conditions. As Sy5 stabilizes the same conformation in UraA_{WT} and UraA_{G320P} the reason for its improved crystallization behavior was most likely the increased thermal stabilization of the UraA_{G320P}-Sy5 complex with a T_m of 68.7 °C compared to 63.2 °C for UraA_{WT}-Sy5. In case of Sy45, the thermal stabilization of UraA_{WT} with a T_m of 72.0 °C was higher compared to UraA_{G320P} (68.4 °C) and crystals could be obtained with UraA_{WT} in combination with Sy45. Even though stabilization of Sy45 with UraA_{G320P} was reduced, crystals were obtained as well (**Figure 39**). This example illustrated a general observation during co-crystallization of UraA. It was found that a thermal stability of the complex above 65 °C resulted in better crystallization respectively crystallization trials with a complex stability below 65 °C were mostly unsuccessful.

UraA_{WT} was previously crystallized in complex with the substrate uracil, resulting in two reported structures (Lu et al., 2011; Yu et al., 2017). The thermal stability of UraA_{WT} in presence of uracil was investigated in this study and a complex pattern of substrate binding and probably conformational changes was observed by differential scanning fluorimetry (**Figure 38**). The melting temperature was highly concentration dependent but 1 mM uracil that was used during the crystallization of the two published structures led to an increased melting temperature of UraA_{WT} to above 65.3 °C as determined in this study. This underlines the importance of thermal stabilization for successful crystallization of UraA. Consistently, crystals of UraA without substrate could only be obtained in this study by increasing the thermal stability of UraA by addition of nanobodies or sybodies. Further beneficial effects of nanobodies in crystallization in general were seen in crystal packing. UraA exclusively holds a membrane embedded domain and may therefore be more prone to less favorable crystal

contacts based on hydrophobic interactions (**Figure 6**; Carpenter et al., 2008). The crystal contacts in the UraA-Sy45 structure illustrated this with the best resolution along the C-axis with the Sy45-Sy45 interaction as crystal contact (**Figure 31**). However, the lattice of UraA-Sy45 also showed that crystal contacts along the B-axis were based on UraA-UraA interactions only and the contacts along the C-axis could not be modeled highlighting an additional aspect of UraA crystallization. Despite good crystal morphology, it was found that all tested co-crystals of UraA grown in the presence of DM but without the addition of the short chain detergents OG or NG did not diffract below 4.5 Å resolution. The smaller micelle of OG and NG compared to DM probably improved the UraA-UraA crystal contacts. Thus, crystal screening at a later stage of the study was exclusively performed with addition of either 1% OG or 1% NG. Mostly, both detergents resulted in crystals of similar morphology. Short chain detergents are known to feature a reduced micelle size resulting in tighter crystal packing, less unstructured water and potentially better crystal contacts (Sonoda et al., 2011). This effect was also observed for UraA crystals in this study even though the number of initial conditions giving rise to crystals in presence of DM only was reduced by addition of OG or NG. However, the relatively large number of structured detergent molecules in the UraA_{G320P}-Sy45 structure showed that the addition of NG not only resulted in better crystal contacts by reducing the size of the micelle as the interface between the two protomers in the asymmetric unit was filled with detergent mostly NG that also supported the assembly in the asymmetric unit. Further, the inward-facing cavity was filled with a structured NG molecule that stabilized the inward-facing cavity (**Figure 29**). In contrast to the NG molecule in the UraA_{3QE7} structure, which glucose moiety participated in substrate binding and which acyl chain penetrated the TM5-TM12 interface within the plane of the membrane, the NG molecule in the UraA_{G320P}-Sy45 co-crystal structure did not create such artifacts and had a similar behavior as detergent molecules in the inward-facing cavity of other 7-TMIR protein structures (**Figure 42**).

5.3 UraA-Sy45 crystal structure

5.3.1 Conformational transition from inward-facing to occluded in UraA

The presented UraA_{G320P}-Sy45 structure visualized an inward-facing conformation of UraA similar to reported inward-facing structures of other 7-TMIR proteins such as UapA, SLC26Dg,

SLC26a9 and BicA but with significant differences to the previously reported inward-facing structure UraA_{3QE7} (Lu et al., 2011). UraA_{3QE7} was previously used by Yu et al. (2017) in combination with the dimeric, occluded UraA_{5XLS} to analyze the transport mechanism of UraA. Thereby, deviations in TM6 and TM7 hampered structural alignment of both gate domains to visualize the core domain movement during the transport cycle and the authors could not exclude local disruption of the TM6-TM7 structure in UraA_{3QE7} (Yu et al., 2017). Structural alignment of both core domains revealed a rotation of TM5 and TM12 around an axis orthogonal to the core-gate domain interface, which was attributed to the conformational transition by the authors (Yu et al., 2017). The effect of the NG molecule present between TM5 and TM12 in UraA_{3QE7} and its impact on the local structure was not discussed in this context. The TM5 and TM12 movement during conformational transition was also analyzed for UapA by Yu et al. (2017) showing only minor displacement of the C-terminal part of TM12.

The new UraA_{G320P}-Sy45 structure allowed improved modelling of the transition from the inward-facing to occluded conformation in UraA. The here proposed mechanism is based on a static gate domain architecture and is thus in contrast to the previously reported mechanism by Yu et al. (2017; **Figure 40A, B**). The static character of the gate domain during transport is promoted by the rigid dimeric assembly as observed in UraA_{5XLS} that would potentially be disrupted by extensive movements in TM5 and TM12. This is in line with the functional relevance of dimerization in UraA (Yu et al., 2017) that does not imply cooperativity as would be expected for a mechanism including larger gate domain movements. The rigid body movement of the core domain could be described by a 17° rotation around an axis lying parallel to the substrate barrier and confirmed the mechanism proposed by Chang et al. (2017). The hypothesized conformational hinges could be identified in the transition from core domain to inter-domain linker with the crucial positions Gly-112 and Gly-320 and the rotation axis runs close to these hinge positions as expected. TM5 and TM12 of the gate domain remain static and build the substrate barrier while the rigid body movement of the core domain moves the substrate almost orthogonal to the barrier. This movement may simply be extended to reach the outward-facing state by rotation around the identified axis. Alternatively, a different path may be required to reach the outward-facing conformation. The latter was previously discussed for the nucleosid transporter CNT from *N. wadsworthii* (Hirschi et al. 2017; **Figure 2**), that could be crystallized in distinct intermediate states and that would be important for preventing unspecific ion leakage.

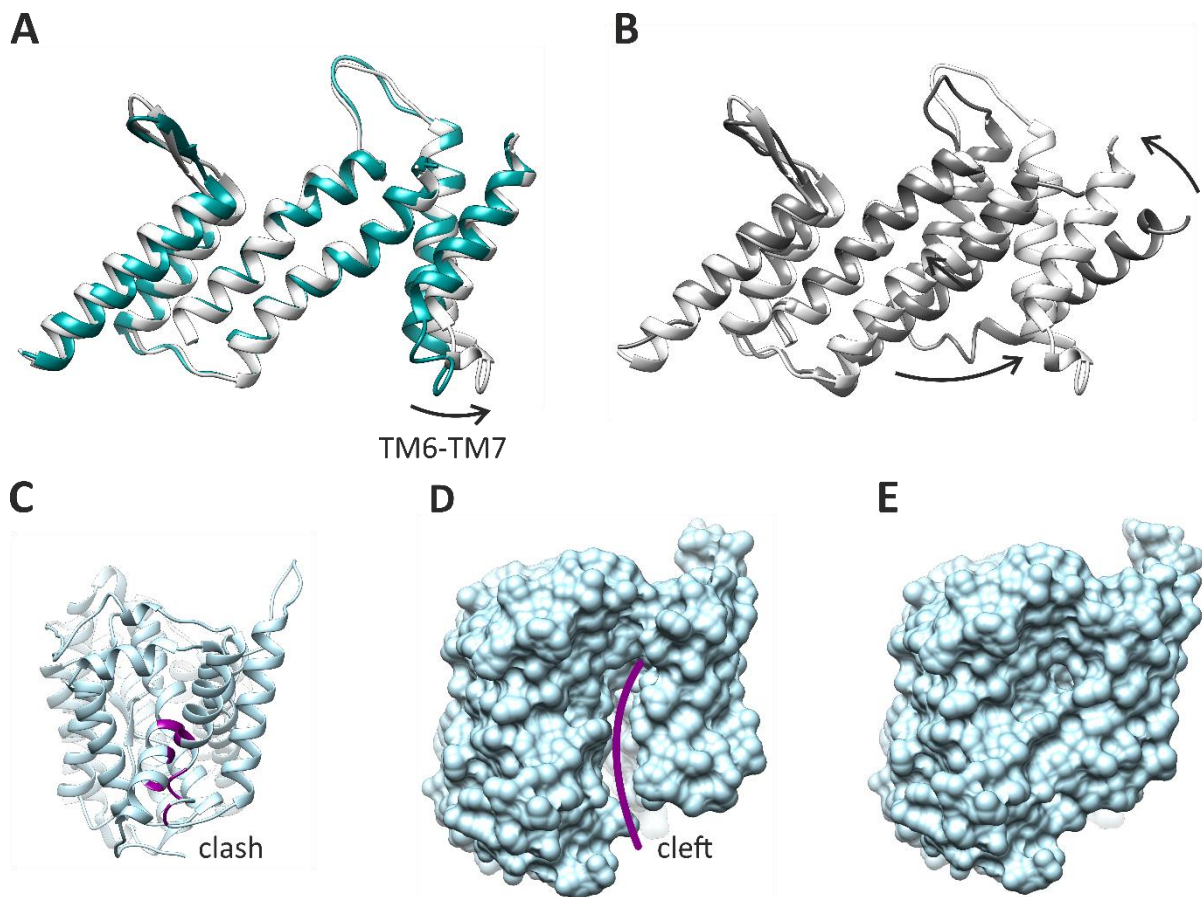


Figure 40: Structural rearrangements in the gate domain of UraA in conformational transition. (A) Structural alignment of the gate domains of UraA_{5XLS} (grey) and UraA_{G320P-Sy45} (cyan) with a RMSD of 1.4 Å. The cytoplasmic TM6-TM7 loop shifts away from TM12 during transition from inward-facing to occluded. TM5 and TM12 do not show significant rearrangements. (B) Gate domain of UraA_{3QE7} (dark grey) aligned to UraA_{5XLS} (light grey) as in (A) with a RMSD of 4.6 Å. TM12 moves towards TM5 during transition from UraA_{3QE7} to UraA_{5XLS} and TM6 and TM7 are completely displaced. Movements are indicated by black arrows. To visualize the impact of the TM6-TM7 loop displacement, two chimeric structures of UraA were prepared based on UraA_{5XLS} and UraA_{G320P-Sy45} (C) Chimera-1 of UraA consisting of core domain from UraA_{5XLS} and gate domain from UraA_{G320P-Sy45} with clashes between TM1 and TM7. The structure is shown as side view with periplasmic space on top and cytoplasmic space at the bottom. (D) Chimera-2 of UraA consisting of gate domain from UraA_{5XLS} and core domain from UraA_{G320P-Sy45} in surface representation highlighting a cleft between TM1 and TM7. (E) Surface representation of UraA_{G320P-Sy45} showing closing of the cleft upon TM6-TM7 loop rearrangement as shown in (A).

Despite the static gate domain, slight movements of the TM6-TM7 loop and TM7 in the gate domain were observed during transition from UraA_{G320P-Sy45} and UraA_{5XLS} (**Figure 40A**). The monomeric assembly of UraA_{G320P-Sy45} could explain slight differences in the gate domain compared to the dimeric UraA_{5XLS} not necessarily related to transport but the TM6-TM7 loop movement could also be mechanistically relevant. Structural alignment of UraA_{G320P-Sy45} and UraA_{5XLS} based on TM5, TM12, TM13 and TM14 and analysis of UraA_{5XLS} core domain and UraA_{G320P-Sy45} gate domain (Chimera-1) indicated clashes between TM1 of UraA_{5XLS} and TM7 of UraA_{G320P-Sy45} indicating that for transition from inward-facing to occluded the TM6-TM7 loop is required to move away from TM12 (**Figure 40C**). The closer location of the TM6-TM7

loop to TM12 may be a prerequisite for the inward-facing conformation but the outward movement of the loop may also support an inward-facing conformation. This was analyzed by creation of Chimera-2 based on the gate domain of UraA_{5XLS} and the core domain of UraA_{G320P}-Sy45. Chimera-2 revealed a cleft between TM1 and TM7 that would potentially allow lipids to enter the inward cavity (**Figure 40D**). This cleft is closed by the TM6-TM7 loop movement towards TM12 in UraA_{G320P}-Sy45 suggesting that this rearrangement is functionally relevant (**Figure 40E**). Conclusively, despite the static substrate barrier formed by TM5 and TM12, the TM6-TM7 loop adjusts to the core domain translocation by minor displacements and thereby prevents clashes between core and gate domain as well as diffusion of lipids into the inter-domain interface. Based on this analysis a similar functional relevance could be hypothesized for the 'paddle' between TM13 and TM14 on the periplasmic side for the outward-facing transition.

In conclusion, UraA_{G320P}-Sy45 presented an alternative inward-facing conformation compared to UraA_{3QE7} that highlighted the conformational transition from inward-facing to occluded by rigid body movement of the core domain as characteristic for elevator transporters without complicated intra-domain rearrangements. Thereby, UraA_{3QE7} and the associated postulated transport mechanism could be revised (Yu et al., 2017).

5.3.2 The substrate binding site of UraA

The inward-facing conformation of UraA stabilized by Sy45 was visualized by crystallography in presence and absence of the substrate uracil to analyze differences in the substrate binding site upon substrate binding resulting in the two structures UraA_{G320PSy45} and UraA_{G320PSy45-uracil}, whereas UraA_{G320PSy45} was the first UraA structure that could be solved without uracil being present due to the beneficial properties of Sy45 for the crystallization of UraA. However, in absence of uracil a Tris molecule was found to bind to the substrate binding site by formation of similar interactions with key residues of the substrate binding site (**Figure 29**). Therefore, no conclusion could be drawn on potential side chain rearrangements in the substrate binding site of UraA in the inward-facing conformation upon uracil binding. It could be speculated, that the high similarity between the two structures and the little side chain movements expected for Glu-241, His-245 and Glu-290 in the alpha helical secondary structure indicate that there are no major changes induced by uracil binding (**Figure 41**). Therefore, substrate binding to the inward-facing conformation could work according to the 'lock and key' model

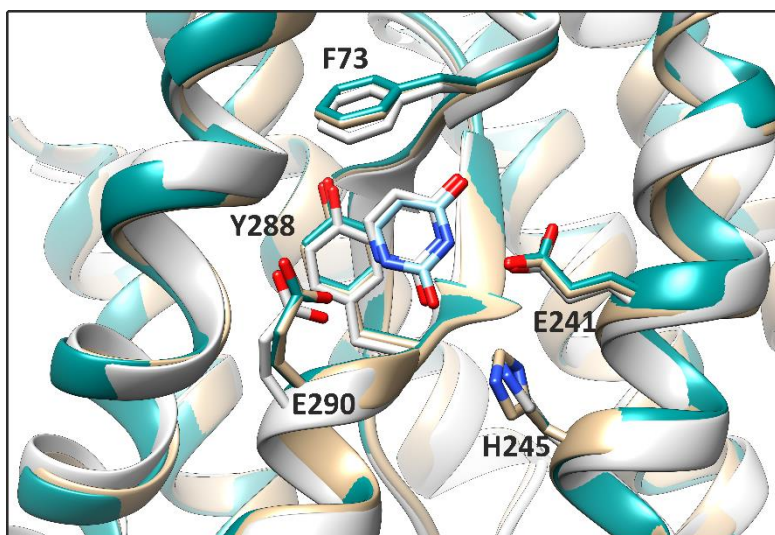


Figure 41: The uracil binding site of UraA. Structural alignment of the three core domains from occluded, liganded UraA_{5XLS} (light grey), inward-facing UraA_{G320P}-Sy45 (cyan) and inward-facing liganded UraA_{G320P}-Sy45-uracil (brown) with focus on the substrate binding site of UraA. Important residues for substrate coordination are highlighted as well as the two uracil molecules from UraA_{5XLS} and UraA_{G320P}-Sy45-uracil. The two Sy45 stabilized UraA structures do not show any major differences with a RMSD of 0.5 Å for structural alignment of the core domains. All the side chains in the substrate binding site despite the presence or absence of uracil align well. The Tris-buffer molecule of the UraA_{G320P}-Sy45 structure was removed for sake of simplicity. Comparison to UraA_{5XLS} shows only minor deviations in the side chains of H245 that is slightly rotated and E290 that is shifted towards the cytoplasmic side along with the corresponding backbone. The two uracil molecules show a similar position and orientation.

introduced by Emil Fischer in 1894 (Lichtenthaler, 1995) rather than to the induced fit (Koshland, 1958) or conformational selection model (Monod, Wyman and Changeux, 1965). Comparison with the substrate binding site of the occluded conformation UraA_{5XLS} revealed only minor differences in the side chain orientations with a slight rotation of His-245 and a shift of Glu-290 along with the backbone towards the cytoplasm. The similar architecture of the binding site in the different conformations is in line with the observed rigid body movement of the core domain during transport. Further, the contribution of the gate domain to substrate coordination in the occluded conformation involved comparably unspecific hydrophobic interactions via the side chains of I132 and I345 that did not induce any rearrangements in the substrate binding site upon conformational transition. Thereby, the limited impact of uracil binding on UraA in the crystal structures is in line with the experimental data showing increased melting temperature of only 4.6 °C upon uracil binding in presence of Sy45 (**Figure 38**) and only minor differences in the substrate binding site in uracil dependent dHDX of the conformationally restricted UraA variant P330G (**Figure 36**).

5.3.3 The inward-facing cavity of 7-TMIR proteins

The inward-facing cavity of UraA was visualized by UraA_{G320P}-Sy45 structure in this study and is located between core and gate domain allowing access to the substrate binding site built-up by side chains from Glu-241, His-245 and Glu-290 and the two discontinuous helices TM3 and TM10. Compared to UraA_{3QE7}, the inward-facing cavity in UraA_{G320P}-Sy45 was much more pronounced and the exit site formed between TM5 and TM6 plus TM13 of the opposing protomer within the dimer as predicted for the elevator transport mechanism in 7-TMIR proteins. The inward-facing structure of UapA from *A. nidulans* showed a comparable cavity as seen in UraA_{G320P}-Sy45 (Alguel et al., 2016; **Figure 42A**). UapA was locked in this conformation by introducing a thermostabilizing glycine to valine substitution at position 411 that sterically blocks core domain translocation against the gate domain due to the bulkier side chain. The inward-facing cavity of UapA was filled with two structured DDM molecules due to the hydrophobic character of the cavity comparable to the NG molecule in UraA_{G320P}-Sy45. The same was observed in the inward-facing structures of SLC26Dg and BicA (**Figure 42B**; Geertsma et al., 2015; Wang et al., 2019) where one DM or monoolein molecule, respectively, was bound in the cavity. Apart from UraA_{3QE7}, all inward-facing structures of 7-TMIR proteins (UraA_{G320P}-Sy45, UapA, SLC26Dg, SLC26a9 and BicA) showed similar large inward-facing cavities but the transported substrates (uracil, xanthine, fumaric acid and bicarbonate) are comparably small. Even though the substrate of SLC26a9 is still under debate (Walter et al., 2019) this observation raises the question whether the extended inward-facing cavity presents a mechanistic aspect of the 7-TMIR fold. The mostly hydrophobic surface of the inward-facing cavity makes a presentation towards the aqueous solution energetically unfavorable but it appears unlikely as well that lipids would bind into the cavity. Binding of lipids would potentially interfere with the transport mechanism and the main role of the TM6-TM7 loop seems to prevent diffusion of lipids into the inward-facing cavity in UraA (5.5). The rate limiting steps for symporters have been suggested to be either the substrate dissociation upon transport or the translocation without bound substrates at the end of the transport cycle (Forrest et al., 2011) which is the conformational change from the unbound inward-facing to the outward-facing conformation in case of UraA. Thereby, the presented hydrophobic inward-facing cavity could serve as a driving force for the back-translocation to the outward-facing state by energetically disfavor the unbound inward-facing conformation. Interestingly, bilayer distortions observed for elevator transporters were lately assigned to have a role in

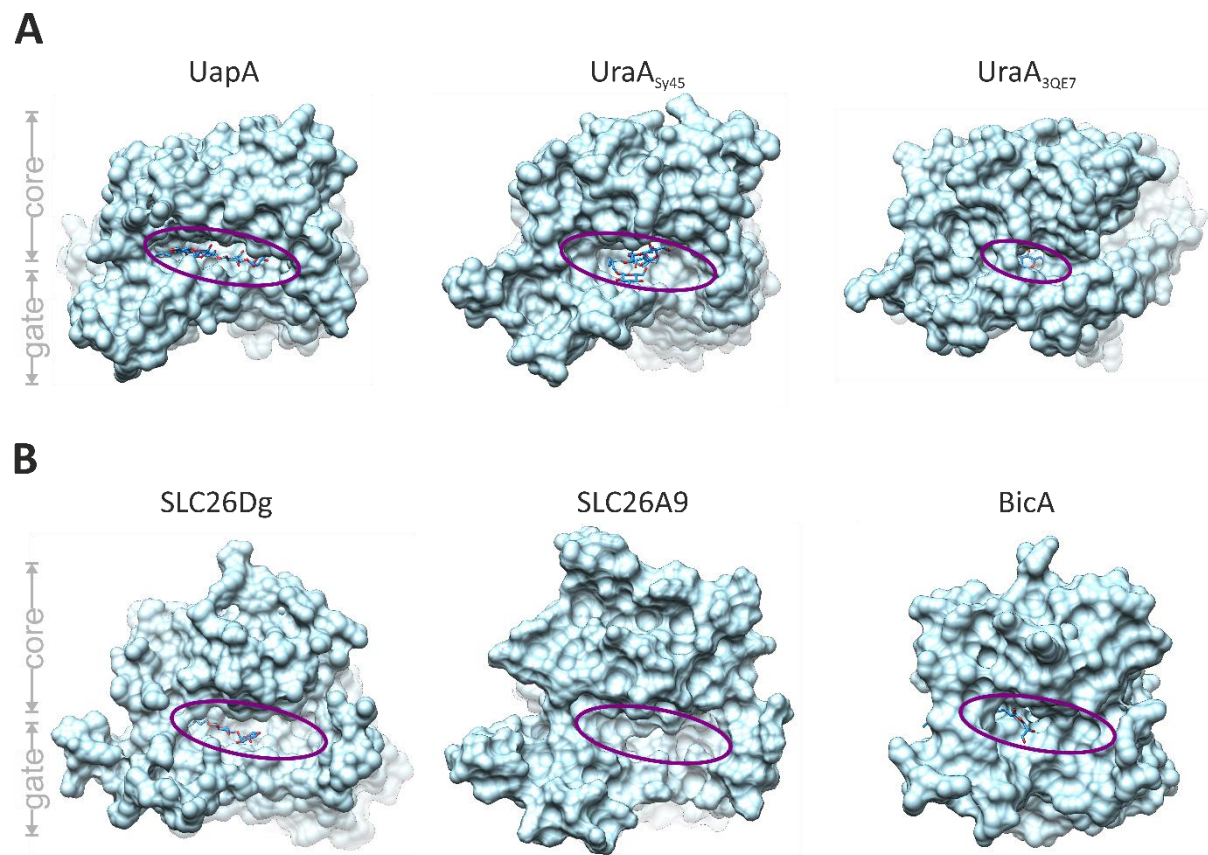


Figure 42: Inward cavity of 7-TMIR proteins. (A) Cytoplasmic view on the surface representation of structures from SLC23 members in inward-facing conformation with co-crystallized detergent molecules inside the cavity shown in stick representation. The inward-facing cavities are highlighted in purple. (B) Structures of SLC26 members in inward-facing conformation depicted as in (A).

transport energetics and cooperativity (Zhou et al., 2019; Holzhüter et al., 2020) and these would be increased by wider opening of the inward-facing cavity. Further, wide opening of the cavity implies the separation of core and gate domain over a larger area reducing the inter-domain contacts. The concept of inter-domain interface size as measure for conformational stability was first described by Akyuz et al. (2015) based on a humanized variant of Glt_{Ph} and further discussed by Wang et al. (2020) based on distinct conformations of Glt_{Ph}. In UraA, the domain interface is reduced by 17% upon transition from the occluded to inward-facing conformation and expected to represent a general feature of 7-TMIR proteins (**Figure 43**). Consistently, the transition from inward-facing to occluded becomes energetically favored due to the increased surface for hydrophobic interactions in the interface. Thus, wide opening of the cavity could be a mechanistical element to reduce the size of the inter-domain interface in the substrate bound state to facilitate re-translocation to the occluded and subsequently outward-facing conformation of the empty transporter upon substrate dissociation and would go in hand with the discussed unfavored presentation of the hydrophobic cavity to the aqueous solution.

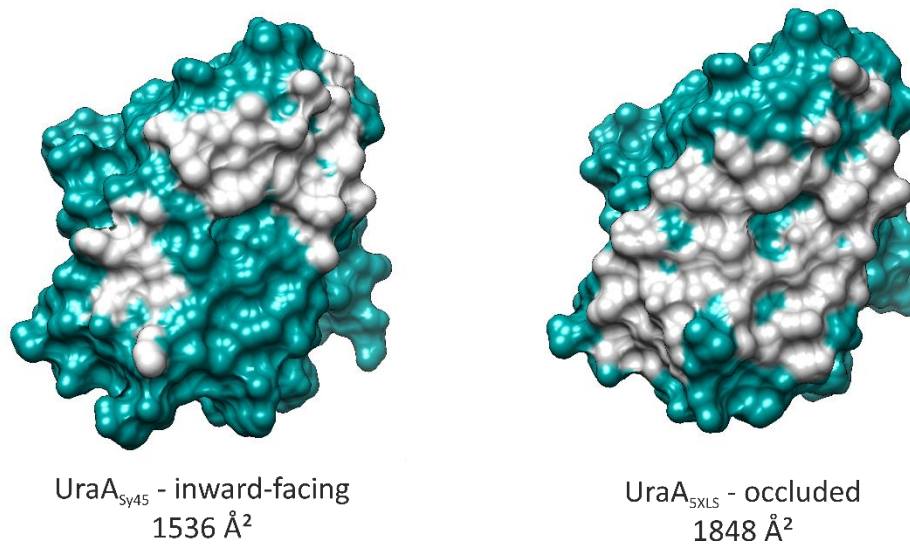


Figure 43: Conformation dependent size of the core-gate interface in UraA. Surface representation of the core domains of UraA_{G320P-Sy45} and UraA_{Sy45} in cyan with gate domain contacts highlighted in grey. The interface between core and gate domain increases from 1536 Å² to 1848 Å² upon transition to the occluded conformation. The interface size was calculated in Chimera using the solvent excluded surface area upon removal of the inter-domain linkers and the TM7-TM8 loop connecting both domains.

7-TMIR proteins are lacking a gating function as seen in other elevator transporters such as Glt_{Ph} (Zomot et al., 2013) that features two hairpins for substrate binding site opening and closing. These gating loops are involved in substrate coordination and serve as checkpoint for translocation (Pavic et al., 2019). The missing gating function in UraA and other 7-TMIR proteins in combination with the relatively static substrate binding site could be partially compensated by the wide opening of the inward-facing cavity to promote substrate dissociation upon translocation by significantly changing the structural environment around the substrate binding site. This would be in line with the observed changes in uracil affinity in presence and absence of Sy45 (**Supplementary figure 16**).

Taking all together, it appears that the wide opening of the inward-facing cavity is a mechanistical feature in 7-TMIR proteins used to facilitate the rate limiting steps, substrate dissociation and back-translocation. Thereby, opening of the cavity is coupled to the favorable inward transition in the substrate bound state of the symporters and part of the energy is stored for back translocation by introducing the unfavorable inward-facing cavity.

5.4 Alpha-helical inter-domain linkers in UraA

5.4.1 UraA_{G320P}

The UraA variant G320P was created in this study in order to manipulate the conformational space of UraA for its analysis and a functional impact of the periplasmic inter-domain linker in SLC23 was observed. UraA_{G320P} showed the typical phenotype of a conformational restricted mutant including loss of function and thermostabilization as reported in literature (Smirnova et al., 2003; Serrano-Vega et al., 2007; Alguel et al., 2016). In addition, increased uracil affinity compared to UraA_{WT} with a K_d of 21 nM and an increased dimer fraction was observed. Though dimer formation is required for functionality of UraA it was also shown that complete monomerization of UraA is not causing significant alteration of uracil affinity (Yu et al., 2017). Thus, the increased uracil affinity in UraA_{G320P} is most likely independent of the oligomeric state. In line with this argumentation were the size exclusion chromatography results that showed no alteration in the monomer-dimer equilibrium of any UraA variant in presence or absence of uracil. As shown for other transporters, the substrate affinity might depend on the protein conformation (Bianchi et al., 2016) and might be used as a driving force for transport (Forrest et al., 2011). According to the induced transition fit concept (Klingenberg et al., 2005), the substrate affinity would be highest in the occluded state of UraA. Consistently, the altered conformational equilibrium of UraA_{G320P} towards the occluded conformation as suggested by the reduced cysteine accessibility and HDX-MS analysis is likely to cause the increased uracil affinity of UraA_{G320P}. This hypothesis is in line with a study on the maltose-binding protein that showed different substrate affinities depending on amino acid substitutions in the hinge region that altered the substrate binding site opening and closing kinetics. The authors claimed that 'the intrinsic opening-rate dictates ligand dissociation' (Seo et al., 2014). Consistently, the increased uracil affinity of UraA_{G320P} can be interpreted as a direct cause of the reduced substrate binding site opening due to the larger population of the occluded conformation that prevents uracil dissociation. This is further supported by the 5-fold reduced uracil affinity of UraA_{WT} in presence of Sy45 that increases the open probability of the substrate binding site without disturbing their structure (**Supplementary figure 16 and Figure 41**).

HDX-MS analysis of UraA_{G320P} in presence and absence of uracil showed similar patterns as observed for UraA_{WT} with slightly reduced intensity. These results were interpreted as uracil

induced population of the occluded state in UraA_{WT} also indicated in the uracil titration DSF experiment and consistent with the increased uracil affinity discussed above. The increased population of the occluded state in UraA_{G320P} consequently reduced the dHDX intensity in presence of uracil for this variant. Nevertheless, similar dHDX pattern as in UraA_{WT} were found in the core domain further highlighting that UraA_{G320P} was not locked in the occluded conformation but its conformational equilibrium shifted. Additionally, DSF analysis of UraA_{G320P} with conformational-selective nanobodies and sybodies revealed strong stabilization with Sy45 that stabilizes the inward-facing conformation as shown in the UraA_{G320P}-Sy45 crystal structure. Thus, the conformational transition from occluded to inward-facing is generally allowed for the G320P variant. The presence of UraA_{G320P} in the inward-facing conformation was also supported by the reduced deuterium uptake on the cytoplasmic side in TM1 of UraA_{G320P} upon uracil addition. Interestingly, even though the melting temperature of UraA_{G320P} in combination with Sy45 was increased, the absolute melting temperature was lower compared to UraA_{WT} stabilized by Sy45 while the G320P substitution is not part of the Sy45 epitope. This underlines the difference in the energy landscape of conformational transition for UraA_{WT} and UraA_{G320P}.

Based on these experimental results for UraA_{G320P} that are all in line supporting a shifted conformational equilibrium the molecular mechanism resulting in the loss of function in UraA_{G320P} can be discussed. It is likely that the shifted conformational equilibrium resulted in low occupancy of the outward-facing conformation the prerequisite for substrate binding and transport in the whole cell transport assay as the inward-facing and occluded conformation were experimentally confirmed. As the 'return' of the empty transporter to the initial state of transport, in case of UraA the outward-facing state, was discussed to be the rate limiting step for transport (Forrest et al., 2011), the G320P mutation might sterically hamper this transition. The molecular basis might be the effect of a proline substitution on this position itself and on the preceding, neighboring residue on the dihedral angles of both (Ho et al., 2005) and in case of UraA_{G320P} this effects the dihedral angles of Val-319. Comparison of UraA_{5XLS} and UraA_{G320P}-Sy45 regarding the dihedral angles of Val-319 showed a change in the phi angle from -90° to -150° and a less pronounced change in the psi angle (**Figure 28**) shifting the dihedral angles of Val-319 towards the ζ -population, that is unique to proline preceding residues (Ting et al., 2010; **Figure 44A, B**). This suggested a local bias in the inward-facing UraA_{G320P}-Sy45 structure by the G320P substitution and underlined the steric effect of proline

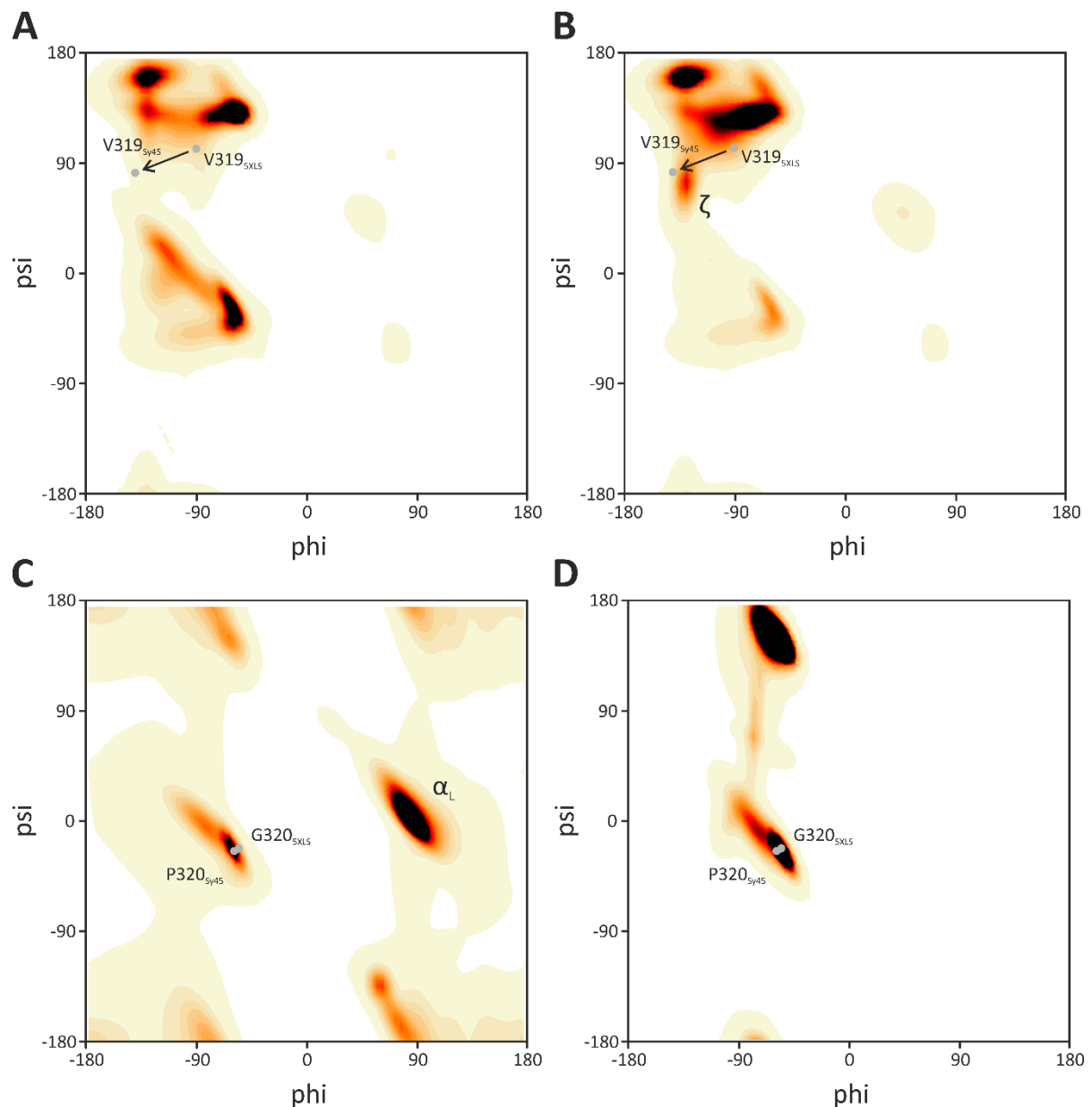


Figure 44: The G320P substitution influences the Ramachandran configuration of position 320 and 319. (A) Ramachandran plot for valine residues preceding a neighboring glycine residue representing the configuration in UraA_{WT} with probabilities shown as color code from yellow to black. (B) Ramachandran plot for proline preceding valine residues as in the UraA_{G320P} variant. Ramachandran plots were adapted from Ting et al. (2010). The Ramachandran configuration of V319 in the occluded UraA_{SXLS} and the inward UraA_{G320P-Sy45} structure is indicated for both. The G320P substitution introduces differences in the Ramachandran configuration of V319 towards the zeta population. (C) Ramachandran plot for glycine residues showing the dihedral freedom with Ramachandran configuration of G320 and P320 from UraA_{SXLS} and UraA_{G320P-Sy45} as indicated. (D) Ramachandran plot for proline residues with Ramachandran configurations indicated as in (C).

at position 320 on Val-319 that is part of the periplasmic hinge and required for conformational change. For the outward-facing conformation, this effect might be critical and result in the reduced conformational freedom. However, also the UraA variant G320A was observed to be inactive in whole-cell transport but with slightly increased transport compared to UraA_{G320P} suggesting that, despite the observed effect of proline on Val-319, the

introduction of proline is not the major reason for inactive transport but rather the loss of the conserved glycine at position 320. Consistently, the dihedral freedom for glycine residues as visualized in the Ramachandran plot (**Figure 44C**) is drastically reduced upon substitution to proline (**Figure 44D**) but also to any other amino acid though to a lower extent. Consistently, this reduction in dihedral freedom can be assumed as key element in the loss of function in UraA_{G320P} and UraA_{G320A} and a change of the dihedral angles at this position in the outward-facing conformation or in a transition state towards this conformation favored only by a glycine residue can be hypothesized. This could apply to the α_L population (Ho et al., 2005; **Figure 44C**). Interestingly, the dihedral angles of Pro-320 in UraA_{G320P}-Sy45 were almost identical to the configuration of Gly-320 in UraA_{5XLS}, in line with the occluded conformation preference of UraA_{G320P}.

Conversely to the loss of function in UraA upon introduction of the G320P substitution, the *E. coli* pyrimidine transporter RutG with 36% sequence identity to UraA together with other RutG homologs naturally feature a proline at the corresponding position in their sequence (**Figure 45**). Even though the concept of transceptors, a class of former transporters that lost their transport but gained receptor function, is known (Diallinas et al., 2017) and the G320P substitution in UraA could be interpreted as evolution from transporter to transceptor, the transport activity of RutG from *E. coli* was experimentally confirmed (Botou et al., 2018) with broader substrate spectrum as UraA and uracil transport kinetics with increased Michaelis-Menten constant (K_m) compared to UraA. This example of UraA and RutG illustrates that the effect of the G320P mutation in UraA is not transferrable to other SLC23 transporters only by comparison of the residues at homologous positions to G320 in UraA. The concept of residue co-evolution within proteins (Nicoludis et al., 2018) implies that introduction of proline at the homologous position to 320 in UraA in other SLC23 transporters during evolution could be accompanied by a second substitution that would restore the transporter's function. Sequence alignment of 3067 UraA homologs with minimal and maximal sequence identity of 40% and 99%, respectively, and same analysis for 2925 RutG homologs presented as sequence logos in the range of the periplasmic inter-domain linker (**Figure 45B, C**) illustrates shared conservation of Lys-321, Ala-324, Ile-326, Ile-329 and Pro-330 of UraA between the UraA and RutG cluster. While positions 322 and 323 in UraA show little sequence conservation the equivalent positions in the RutG cluster feature a highly conserved phenylalanine and glycine residue, respectively, whereof the glycine could be responsible for restoring the hinge

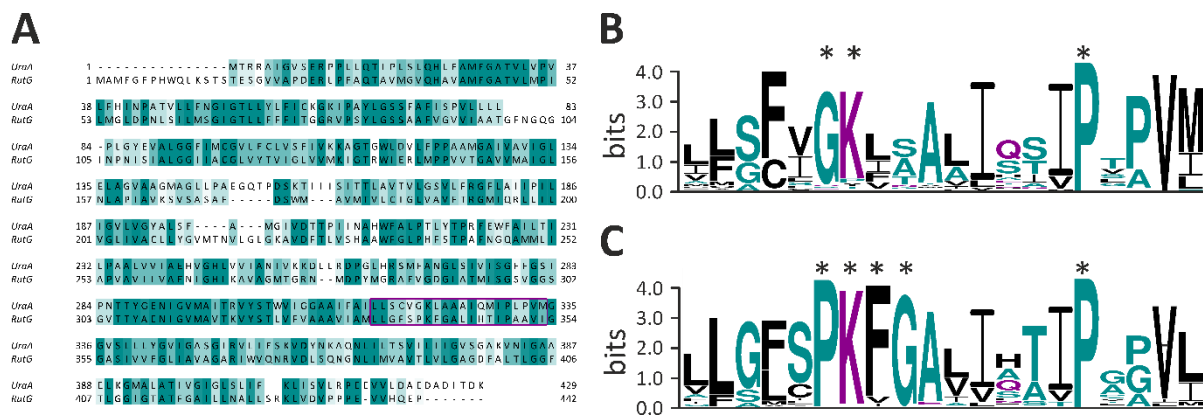


Figure 45: Sequence conservation in the periplasmic inter-domain linker of SLC23 transporters from the UraA and RutG cluster. (A) Sequence alignment of UraA and RutG. Both SLC23 transporters share 36% sequence identity. The purple box highlights the section presented as sequence logos in (B) and (C). **(B)** Sequence logo of the periplasmic interdomain linker from alignment of 3067 UraA homologs with minimal and maximal sequence identity of 40% and 90%, respectively. **(C)** Corresponding sequence logo for 2925 RutG homologs.

flexibility in the RutG cluster. The corresponding UraA variant G320P-A323G could be a promising candidate to restore the transport activity of UraA_{G320P} and confirm this hypothesis. Even though this would raise the question whether the transport mechanisms of the UraA and RutG cluster are identical or slightly different.

5.4.2 UraA_{P330G}

The position Pro-330 in UraA is highly conserved within the UraA and RutG cluster (**Figure 45**) and also present in less related SLC23 transporters such as the human SVCT1 and SVCT2 (**Supplemental figure 1**) and also found in the SLC4 and SLC26 family (**Figure 46**) which suggests a strong relevance of Pro-330 for the function of 7-TMIR proteins. This position was subjected to proline to glycine substitution in order to study the role of Pro-330 in transport function and to take advantage of its functional importance for the conformational manipulation of UraA. Glycine was chosen as substitute to contradict the backbone rigidity of the naturally occurring proline which resulted in loss of function in the whole cell transport analysis. In contrast, the P330A mutant showed transport activity with reduced rates compared to UraA_{WT} suggesting that the introduced backbone flexibility by glycine substitution in UraA_{P330G} was the major reason for loss of function rather than a proline specific effect. The strong conservation of the proline residue at this position in 7-TMIR proteins however suggests a requirement that might exceed the functional activity analysis performed in this study. The sharp transition from the periplasmic inter-domain linker to TM12 would be promoted by the missing amide hydrogen in proline at position 330 in UraA preventing hydrogen bonding of the alpha helical secondary structure and contribute to

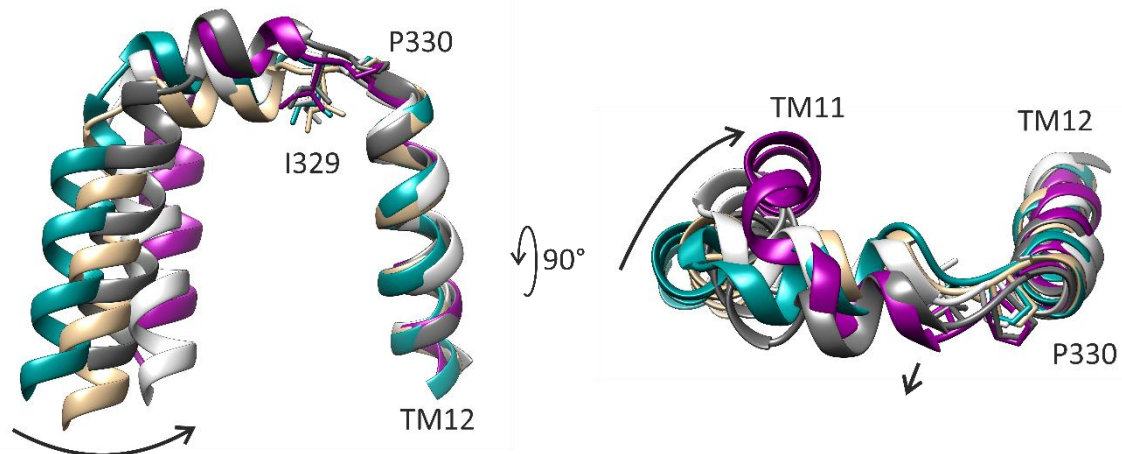


Figure 46: The periplasmic inter-domain linker in 7-TMIR proteins. The proline residue at the transition from periplasmic inter-domain linker to TM12 (P330 in UraA) serves as anchoring point for conformational transition in 7-TMIR proteins, indicated by the black arrows. Presented are the inward-facing structures UraA_{G320P}-Sy45 (cyan), SLC26Dg (dark grey; Geertsma et al., 2015) and UapA (brown; Alguel et al., 2016), the occluded UraA_{5XLS} (light grey; Yu et al., 2017) and the outward open AE1 structure (purple; Arakawa et al., 2015).

protein folding and stability. A more detailed analysis of the UraA variant P330A would be required to increase the understanding of the P330 conservation in 7-TMIR proteins. Thus, the discussion will focus on the impact of the P330G substitution. The introduced backbone flexibility in UraA_{P330G} at the transition from alpha helical inter-domain linker to TM12 of the gate domain, also shown by dHDX (**Figure 37**), led to reduced solvent accessibility of the substrate binding site in both dHDX and cysteine labeling but uracil binding was observed in DSF and SPA though the K_d could not be determined. The dHDX analysis further supported the reduced conformational flexibility of UraA_{P330G} that was also observed in DSF in presence of uracil or conformational-selective binders and by the *ab initio* thermostabilization. Further, the occluded conformation was identified as predominant in UraA_{P330G} based on dHDX and cysteine labeling while the poor stabilization of UraA_{P330G} by Sy45 in DSF showed decreased population of the inward-facing conformation in this UraA variant. Thereby, the introduction of glycine at position 330 that increases the local structural flexibility resulted in a global loss of conformational flexibility suggesting that the backbone rigidity of the naturally occurring proline compared to glycine at position 330 is required for the efficient conformational change in UraA. Structural alignment of 7-TMIR proteins in different conformations along TM12 visualizes the effect of Pro-330 for the conformational transition being the anchoring point for the periplasmic inter-domain linker that allows the sharp transition between both alpha helices. Though Pro-330 as anchoring point is barely displaced during conformational transition, it determines the defined movement of the preceding Met-328 and Ile-329 leading to a shift of the whole inter-domain linker. The hinge at position 320 in UraA leads to the large

displacement of TM11 with respect to TM12 – the conformational transition. In this mechanism, additional backbone flexibility introduced by the P330G substitution, is expected to disturb the defined movement of Met-328 and Ile-329 thus prevents the coordinated movement of inter-domain linker and core domain required for conformational transition. The underlying molecular mechanism would be as outlined for position 320 the extended dihedral angle of pre-glycine compared to pre-proline residues (**Figure 44**). However, the hinge function at position 320 in UraA_{P330G} is preserved allowing a breathing motion of the core domain uncoupled from the gate domain resulting in the experimentally observed dynamics of UraA_{P330G} in dHDX, binding analysis and cysteine labeling.

5.4.3 Functional impact of inter-domain linkers on elevator transport in UraA

The co-crystal structure of UraA_{G320P} with Sy45 and the functional analyses of UraA_{G320P} and UraA_{P330G} shed light on the functional relevance of the periplasmic inter-domain linker in UraA on conformational transition thus transport. Structural alignment of UraA_{5XLS} and UraA_{G320P}-Sy45 revealed the conformational change from inward-facing to occluded, thereby the role of the periplasmic inter-domain linker in this transition could be observed (**Figure 46**). Met-328 in the alpha helical linker underwent a slight clockwise rotation when viewed from the core domain side along the linker which leads to a subtle elongation of the alpha helical linker by 0.3 Å. Cys-318 also rotates slightly but counter-clockwise in periplasmic view down the TM11. The linker elongation and Cys-318 rotation changed the relative orientation of both alpha helices and resulted in rigid body movement of the core domain. The role of Gly-320 in this transition seems to serve as the flex point that geometrically enables the displacement of both helices. Thereby, position Pro-330 seems to be important in transferring the Met-328 backbone rotation to the upstream linker and TM11 due to the structural rigidity. This also explains the effect of the P330G substitution that lacks the structural rigidity at the transition of linker and TM12. As consequence, the Met-328 backbone rotation might be compensated by Gly-330 and the conformational transition obstructed. Based on these considerations, a mechanical coupling between gate and core domain via the inter-domain linker seems to be crucial for rigid body movement of the core domain with respect to the gate domain. Accordingly, the existence of an alpha helical inter-domain linker on the periplasmic side can be better understood. The slight elongation of the inter-domain linker during transport

requires a structure that allows a certain flexibility in length to adapt to the different distances between core and gate domain during transport either by spring like stretching and compressing of the helix, helix bending or partial helix unfolding. As this criterium would also be fulfilled by an unstructured loop, additional benefits of the alpha helical fold are expected. The observed transfer of the Met-328 movement to the hinge and TM11 and the coordinated rigid body movement requires a solid structural element connecting both positions that is why the alpha helical fold in the linker is important in addition. The effect of a lost transfer of the Met-328 movement to the hinge at position 320, due to loss of structural rigidity, is observed in the inactive P330G variant of UraA. The location of the inter-domain linker at the membrane surface further requires an amphipathic structure that is perfectly matched by an alpha helix with hydrophobic side chains pointing towards the acyl chains of the lipid bilayer and more hydrophilic residues towards the aqueous solution while the polarity of the peptide bonds is minimized in the alpha helix. These three characteristics – certain flexibility in length, structural rigidity and amphipathic in nature – determine the alpha helical structure of the periplasmic inter-domain linker.

For the cytoplasmic inter-domain linker, similar properties would be expected based on the inverted repeat symmetry in 7-TMIR proteins. Though, the functional characterization of UraA_{G112P} did not reveal a special phenotype as observed for the periplasmic inter-domain linker variants, the abolished transport activity showed the functional relevance of position G112 in UraA. Structural alignment of TM5 from UraA_{5XLS} and UraA_{G320P}-Sy45 illustrates the local conformational changes leading to the rigid body movement of the core domain from the inward-facing to occluded conformation (**Figure 47**). Thereby, Lys-110 shows the largest change in the dihedral angles leading to elongation of the alpha helical secondary structure in TM4 at position 109 to 111 in UraA_{5XLS}. The alpha helical fold of the inter-domain linker is maintained but the linker helix is slightly compressed by 0.4 Å as determined based on the C α distance of position T113 and F120. This supports the movement of TM4 towards TM5 on the cytoplasmic side. The Dihedral angle of position G112 is not altered in this translation but the glycine residue seems to be required for the flexible transition between both alpha helical structures. Further, the dihedral angle of G112 in both conformations is not allowed for any other amino acid residue including the proline residue as is the case in UraA_{G112P} (**Figure 44D**). A local structural rearrangement at position 112 in UraA_{G112P} to accommodate the pyrrolidine ring must be assumed that is most likely resulting in loss of transport. Though this UraA variant

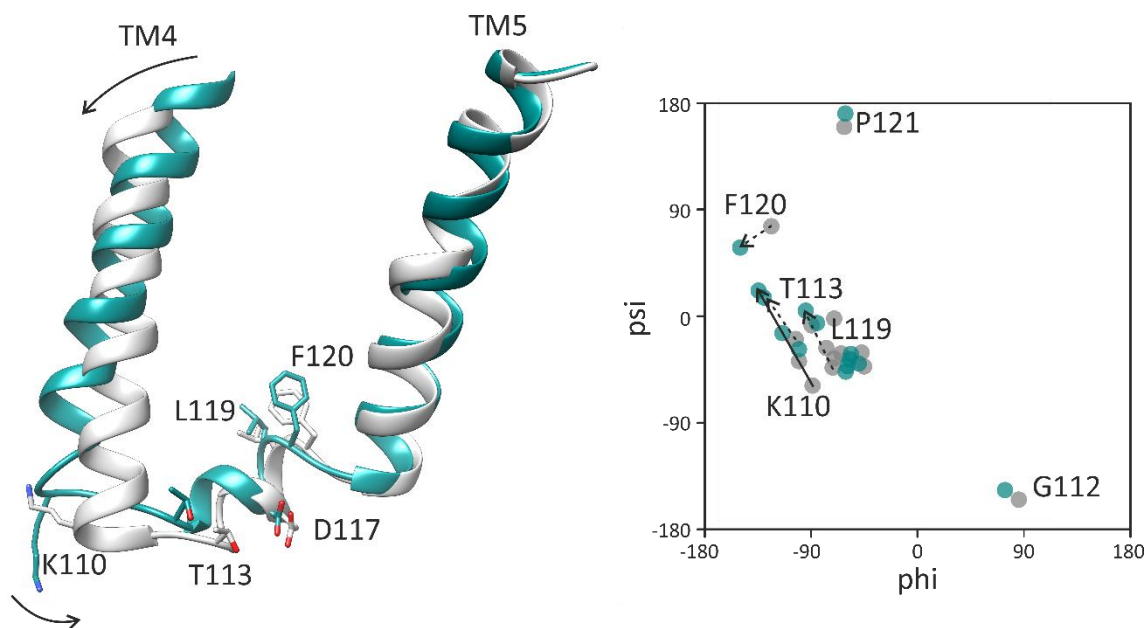


Figure 47: The cytoplasmic inter-domain linker in UraA. Structural alignment of TM5 from UraA_{G320P}-Sy45 (cyan) and UraA_{SXL5} (grey) illustrating local rearrangements at the cytoplasmic inter-domain linker during the rigid body movement of the core domain from the inward-facing to occluded conformation. The ramachandran plot showing dihedral angles of cytoplasmic inter-domain linker residues with the position K110, T113 and L119 undergoing the largest change as indicated by arrows.

could be recombinantly expressed and purified, the slightly reduced thermal stability compared to UraA_{WT} indicated this unfavorable local structural change. However, binding of the conformational-selective binders Sy5, Sy45 and Nb6E3 led to thermal stabilization suggesting no major conformational effect in UraA_{G112P}. The role of Gly112 and the cytoplasmic hinge might be less dominant for conformational transition in UraA compared to the position G320 in the periplasmic inter-domain linker but additional dynamic information on UraA_{G112P} would be required to investigate the functional role of the cytoplasmic inter-domain linker in more detail.

5.4.4 The oligomeric state of UraA_{G320P} and UraA_{P330G}

The functional relevance of dimerization in UraA and other 7-TMIR proteins was presented in several publications suggesting different impact on activity for SLC4, SLC23 and SLC26. However, for SLC23 the experimental evidence is a dimeric functional unit and inactivity of the monomer (Yu et al., 2017). The periplasmic inter-domain linker variants UraA_{G320P} and UraA_{P330G} showed either increased dimer fraction or complete dimerization, respectively, by introduction of a single amino acid substitution. Monomerization of UraA_{WT} could be achieved by introduction of tryptophan residues in the gate domain to perturb the dimer interface resulting in loss of transport activity (Yu et al., 2017) which indicated the correlation between

dimerization and transport functionality in UraA, but similar cases with increased dimerization by a single amino acid substitution as presented in this study are not reported in literature. The increased dimerization in detergent was observed in combination with inactive transport for UraA_{G320P} and UraA_{P330G}, though the substitutions were not located in the dimer interface. Thus, the increased dimer population is likely an indirect effect based on the reduced conformational freedom in the two UraA variants leading to reduced core domain translation. This is in line with the degree of conformational freedom and dimerization observed for the individual UraA variants with UraA_{P330G} being more restricted and completely dimeric and UraA_{G320P} featuring reduced conformational space in combination with partial dimerization. Accordingly, reduced core domain movements in the detergent micelle would stabilize the dimeric assembly while dynamic movements put more stress on the micelle and could cause monomerization. However, lipids in the dimer interface may also support dimerization. Consistently, UraA_{G320P} and UraA_{P330G} showed preference for the occluded conformation in solution that is causing least micelle perturbation in the dimeric assembly compared to inward-facing or outward-facing due to discoidal shape of the UraA dimer. Though more experimental evidence is required, the correlation of conformational preference, reduced conformational flexibility and increased dimer stability in detergent indicates indirect protomer crosstalk in the UraA dimer via the micelle that could also take place in the lipid bilayer as lately considered for elevator transporters (Zhou et al., 2019; Holzhüter et al., 2020).

5.5 Conformational Thermostabilization

Thermal stabilization of UraA by the substrate uracil and selected nanobodies and sybodies was applied in this study resulting in complicated melting events in case of UraA_{WT} with increasing uracil concentrations and strong variations in melting temperatures of inter-domain linker variants of UraA with conformational specific nanobodies or sybodies. Even binder induced destabilization of UraA_{P339G} was observed. These results will be discussed in the following section based on theoretical considerations regarding thermal stabilization of transport proteins in general.

Protein-ligand interactions often stabilize the protein and induce shifts in the melting temperature. Thermal shift analysis is widely known and well accepted as qualitative measure for ligand binding and often used in high throughput screening. The underlying theory is based

on the equilibrium of proteins between their native, folded and the unfolded state. Based on ligand binding exclusively performed by the folded state, which can be fairly assumed for proteins with a three dimensional ligand binding site architecture, the presence of free ligand in the sample shifts this equilibrium towards the folded state thus increases the thermal stability of the protein in thermal unfolding (**Figure 48A**). Consistently, saturation of thermal stabilization at increasing substrate concentrations is theoretically not to expected due to the resulting further shift in equilibrium (Scott et al., 2016). There are attempts to use thermal melting for quantitative binding analysis (Bai et al., 2019; Hall 2019) but the models seem not to apply to dynamic membrane proteins featuring more complicated melting profiles as observed in this study for UraA.

In case of UraA and other transport proteins, the equilibrium becomes more complex as more than one native state exist – inward- and outward-facing state and maybe an occluded state. Therefore, the simple equilibrium between the folded and the unfolded protein must be extended by the different conformations of the transporter during the transport cycle. These states can be interpreted as stable ground states but with differences regarding their absolute energy. As these ground states only represent snapshots from structural biology, higher energy states must exist representing intermediate transition states that connect the ground states (**Figure 48B**). These transition states can be considered as less stable and prone to unfolding as interactions stabilizing a ground state were lost and new interactions stabilizing a different ground state not yet established. The positive contribution of the enthalpy for protein folding would therefore be reduced while the entropic penalty of protein folding might be unchanged. Not all transition states might be prone to unfolding but it appears intuitive that a transition state in the trajectory of transport represents the origin for unfolding rather than a ground state. Consistently, thermal stabilization of transport proteins should be, next to ligand binding, also achieved by reducing the probability of the transporter to be in a less stable transition state. Practically, this would be accomplished by shifting the equilibrium towards a certain conformation either by mutations or by addition of conformational-selective binders resulting in restriction of the transporters conformational freedom (**Figure 48C**) and a reduced population of transition states. As presented in this study, addition of substrate might also impact the conformational equilibrium (**Figure 48D**), thus both effects, ligand binding and conformational restriction, might work synergistically leading to overlapping patterns of thermal stabilization or multiple populations in thermal melting (**Figure 38**; Gao et al., 2019)

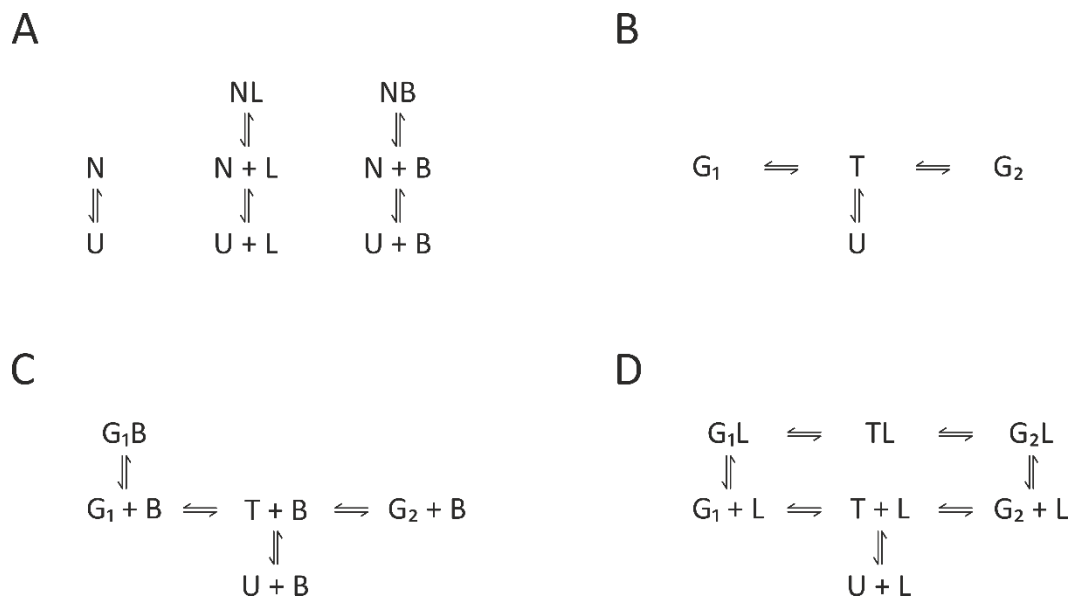


Figure 48: Equilibria models underlying the thermostabilization of proteins upon binding of ligands or binding proteins. (A) Equilibria models for thermostabilization partially adapted from Scott et al. (2016) with the native folded protein (N) in equilibrium with its unfolded state (U). Addition of ligand (L) or binding protein (B) that exclusively bind to the folded state shifts the equilibrium away from the unfolded state and leads to thermostabilization. (B) Extended model for dynamic proteins with at least two distinct conformations that are assumed as ground states (G_1 and G_2) connected by a series of transition states here denoted as 'T'. (C) Extended model from (B) with a conformational-selective binding protein shifting the conformational equilibrium towards G_1B thus away from the transition state (T) and the unfolded state (U). (D) Extended model with a conformational unspecific ligand that binds to all states with the restriction being ligand binding and unbinding only performed by the two ground states (G_1 and G_2).

making it more complicated to dissect the individual contribution to thermostabilization. Accordingly, all conformational-selective binding is expected to increase the melting temperature of the target protein due to conformational space restriction where the absolute shift in T_m would be based on the substrate or binder affinity and on the induced conformation itself.

Several examples can be found in literature where a reduced conformational freedom of the target protein based on amino acid substitutions in the protein sequence led to increased protein stability, supporting the theoretical framework presented above. These cases include the human β_1 -adrenergic receptor (Serrano-Vega et al., 2007) where six alanine substitutions led to an increased population of the antagonist bound state of the protein along with a 21 °C increased melting temperature and the LacY mutant C154G that was locked in the inward-facing conformation, as shown by crystallography (Abramson et al., 2003), and inactive transport along with increased thermal stability (Smirnova et al., 2003). Additionally, UapA was locked in the inward-facing conformation by the G411V substitution leading to loss of functional activity and thermal stabilization (Alguel et al., 2016). Interestingly, the correlation

between loss of conformational freedom and thermal stability was only touched upon by Serrano-Vega et al. (2007) named 'conformational thermostabilization' but rather interpreted as two separate events.

In case of UraA, a strong shift in thermal melting of more than 20 °C was observed by addition of Sy45 that stabilizes the inward-facing conformation (**Figure 27**) while conformational unselective binders such as Nb3H1 and Nb17D3 did not induce thermostabilization (**Figure 15**) underlining the impact of conformational restriction on thermal stabilization of UraA. Nb7F3 was identified to stabilize UraA in the same inward-facing conformation as Sy45 to more than +15 °C but simultaneous binding of Sy45 and Nb7F3 led only to an additional shift in melting temperature of +3 °C. As the melting temperature is an intensive property, T_m -shifts induced by individual nanobodies are not expected to sum up. However, this result points towards a major contribution of the conformational restriction upon nanobody binding in UraA stabilization rather than by the binding event of the nanobody itself. Interestingly, simultaneous binding of two nanobodies to a soluble version of the nucleotide binding domain (NBD) of the cystic fibrosis transmembrane conductance regulator resulted in thermal stabilization of +13 °C respectively +15 °C for individual binders and +24 °C in simultaneous binding thus almost additive thermal stabilization was observed (Sigoillot et al., 2019). As the NBD as individual protein is not expected to undergo conformational changes the theory of restricted conformational equilibria does not apply in this case. The additive thermal stabilization might be rather based on a higher degree of shielding by two nanobodies of hydrophobic patches on the NBD surface, that would normally be covered in the full transporter.

A similar effect as seen for Sy45 and Nb7F3 was observed in the uracil titration of UraA_{WT} in thermal melting in presence or absence of Sy45. The melting curves of UraA_{WT} showed strong uracil dependence with gradual T_m increase and an emerging population at uracil concentrations above 20 μM. At an uracil concentration of 8 mM, the melting temperature of UraA_{WT} was shifted by +18.6 °C from 52.2 °C to 72.8 °C. In contrast, the presence of Sy45 reduced the maximal uracil induced T_m -shift to +4.6 °C suggesting that uracil coordination in the substrate binding site of UraA_{WT} is only a minor contribution to thermostabilization compared to the major impact of the uracil binding induced alteration of conformational freedom. This is also in line with the small structural changes in the substrate binding site of UraA upon uracil coordination and the small effect of uracil binding on UraA_{P330G} in dHDX.

Based on the theoretical framework presented above, the destabilization of UraA_{P330G} in thermal melting by Sy5 and Nb6E3 can be discussed as well (**Figure 39**). Thermal destabilization by ligands or binders initially appears unintuitive but was observed in individual cases (Hamiaux et al., 2012; Yoshida et al., 2019) and explained by ligand binding to the unfolded state of the protein in literature (Scott et al., 2016). However, the conformational effect on thermal stability was not considered for this phenomenon respectively the conformational preference of ligands or binders. Sy5 and Nb6E3 were shown to thermostabilize UraA_{WT} (**Figure 39**). Thus, binding of these binders to the unfolded state of UraA_{P330G} as explanation for destabilization does not hold true in this case. As UraA_{P330G} was observed to feature only little conformational freedom compared to UraA_{WT} in dHDX (**Figure 36**) and uracil dependent DSF (**Figure 38**), it is thus likely that Sy5 and Nb6E3 each introduce a conformation that represents a higher energy state in the context of the P330G mutation in UraA but that is well tolerated by the wildtype. As consequence, the *ab initio* increased thermostability of UraA_{P330G} is reduced upon Sy5 and Nb6E3 binding respectively that expand the conformational space of UraA_{P330G} towards higher energy states and lead to negative T_m-shifts in thermal melting. Interestingly, the melting temperature of UraA_{P330G} in presence of Sy5 or Nb6E3, respectively, still exceeds the melting temperature of apo UraA_{WT}. This shows that binding of Sy5 or Nb6E3, respectively partially reverses the conformational restrictive effect of the P330G substitution on the thermal stability in UraA.

In summary, thermal stabilization of UraA not only gave insights into the conformational space of UraA and its modulation upon nanobody or uracil binding but also underlined the direct correlation between conformational restriction and thermal stability of dynamic proteins in this study. The term ‘conformational thermostabilization’ coined by Serrano-Vera et al. (2007) could be confirmed experimentally and an associated model was proposed that takes transition states as origin for unfolding events and minimization of their population by conformational restriction as basis for thermostabilization.

5.6 The conformational space of UraA in solution

The conformational space of UraA_{WT} in solution was analyzed by different methods including differential HDX, differential scanning fluorimetry in presence of substrate or conformational specific nanobodies, specific cysteine accessibility of phenotypic mutants and crystallography.

In addition, the inter-domain linker variants UraA_{G320P} and UraA_{P330G} gave insights into the conformational space of UraA. UraA_{WT} in solution was found to be present in different conformations as indicated by the heterogeneous melting curve (**Figure 38**) and the dHDX pattern (**Figure 34**). The binding of nanobodies and sybodies stabilizing different conformations (**Figure 39**) further supported this assumption. The addition of uracil to UraA_{WT} resulted in both experiments, dHDX and thermal melting, in significant changes in the conformational equilibrium of UraA_{WT}. In contrast to HDX-MS studies on the Na⁺/H⁺ antiporter NhaA from *E. coli* (Eisinger et al., 2017), where decreased uptake on one side of the protein was accompanied by uptake increase on the opposing side during conformational change due to the alternating access, uracil binding in UraA_{WT} featured reduced uptake on both sides with larger effect on the cytoplasmic side. This observation might represent a shift in conformational equilibrium from both inward-facing and outward-facing conformations towards an occluded conformation upon substrate binding. This hypothesis could be partially supported by the results obtained by differential scanning fluorimetry that showed a population with increased thermal stability emerging from the heterogeneous signal at higher uracil concentrations. This population was attributed to the occluded uracil bound conformation. However, the nature of the predominant open conformation of UraA in solution that allows uracil binding and was gradually shifted to intermediate melting temperatures at lower uracil concentration remained speculative as binding of uracil to any open conformation would result in increased melting temperature of this population. Though, the dHDX data of UraA_{WT} showed a stronger reduction of solvent accessibility for the cytoplasmic side of UraA_{WT} upon uracil addition suggesting a predominance of the inward-facing state in solution. As observed in the UraA_{G320P}-Sy45 structure (**Figure 27**), the inward-facing cavity attracted detergent molecules that might stabilize this state and reduce the kinetics for the transition to the occluded state in solution. This would explain the predominance of the inward-facing state in solution. However, this effect is not to expect in the lipid bilayer in absence of detergent, resulting in a reduced population of the inward-facing conformation. Based on these observations the impact of the UraA dynamics on uracil affinity can be better understood. The uracil affinity of UraA_{WT} was determined by other groups and in this study resulting in values for the K_d of 143 nM (Yu et al., 2017; competition), 151 nM (this study; competition), 314 nM (this study; saturation binding) and 410 nM (Lu et al., 2011; competition). However, in presence of Sy45 stabilizing the protein in the inward-facing

conformation, the affinity was reduced with a K_d of 1469 nM and the affinity of UraA_{G320P} preferring the occluded conformation was increased with a K_d of 21 nM. The individual affinity of the outward-facing UraA conformation could not be determined in this study. However, the kinetic analysis of UraA_{WT} in whole cell transport that resulted in a K_m of 490 nM (Lu et al., 2011), 570 nM (Yu et al., 2017) or 210 nM (Botou et al., 2018) could serve as reference point for to the outward-facing affinity of UraA_{WT}. Consistently, the uracil affinity for UraA_{WT} in solution seems to be conformation dependent with the highest affinity in the occluded conformation in line with theoretical considerations (Forrest et al. 2011) and lowest in the inward-facing conformation consistent with the required uracil dissociation upon transport.

5.7 Concluding remarks and outlook

This study aimed to increase the mechanistic understanding of elevator transport in UraA and other 7-TMIR proteins. Two strategies were applied: selection of nanobodies and sybodies with focus on conformational selectivity and mutagenesis in functional relevant hinge regions of UraA to manipulate the conformational freedom of UraA. Both strategies could be combined resulting in an inward-facing crystal structure of UraA_{G320P} that allowed detailed analysis of the molecular basis for conformational transition. Important positions were identified to be Gly-320 and Pro-330 and the impact of alpha helical secondary structure in the periplasmic inter-domain linker was revealed to be based on a required amphipathic rigid linkage allowing certain flexibility in length and angle.

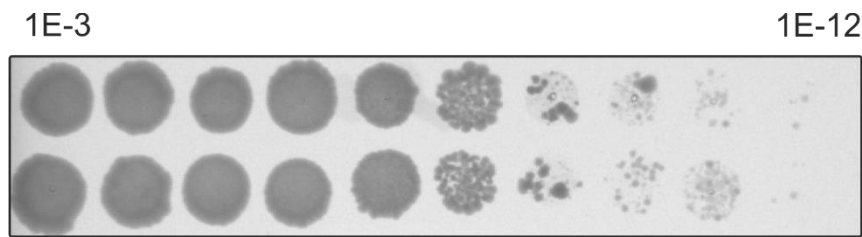
The presented concepts of nanobody and sybody selection with epitope bias and subsequent analysis taking advantage of the sidedness of the native membrane will be suitable for other transport systems as well and will enable efficient selection of conformational specific binders. The concept of conformational space alteration by mutagenesis in the hinge region was based on prior structural information but mechanistic key positions in conformational hinges could also be identified by conservation analysis and be used to thermal stabilize transporters following the presented concept of conformational thermostabilization. Though the project resulted in a crystal structure of UraA yielding new structural information, the full power of conformational space modification by nanobodies and mutagenesis could not be transferred into structural information due to the limitation of crystallization and crystal quality. However, the increased fraction of dimer in UraA_{G320P} and UraA_{P330G} will allow the reconstitution of

dimeric UraA into nanodiscs or similar protein lipid particles and the addition of nanobodies would sufficiently increase the particle size for structural analysis by single particle cryo-EM. Thus, the here presented strategies and results might be the basis for extensive structural characterization of elevator transport in UraA in the future.

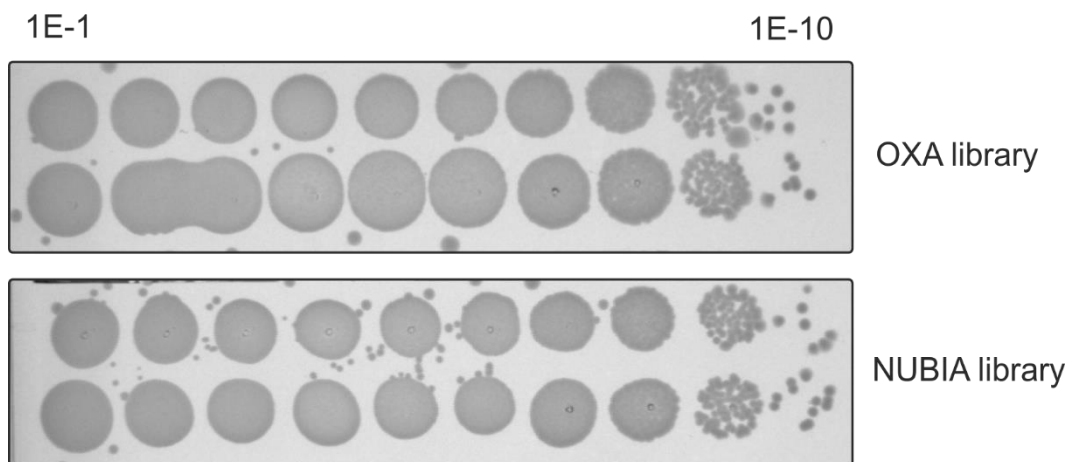
Supplementary information

<i>UraA</i>	1MTRRAIGVSRPPLLTQIPLSLQLFLAMFG	30
<i>PyrP</i>	1MHDDIILKVDKPPAASQWFLSFLQLFLAMFG	32
<i>RutG</i>	1MAMFGFPHWQ-LKSTSTESGVVAPDERLPFAQTAVMGVQAVAMFG	45
<i>hSVCT3</i>	1MSRSP LNP S QLR SVGSQDALA-PLPPPANPSTHSWDP LCGSLPWGLSCLLALQVHVMAS	61
<i>hSVCT2</i>	1	MMGIGKNTTSKSM EAGSSTEGKYDEAKHPAFFTLPPVINGGATSGEQDNEDELMAIYT-TENGLAEKSSLAETL-D-STGSLDPQRSDMIYTI EDVPPWYLCIFLGLQVYLTCS	115
<i>hSVCT1</i>	1MR-AQEDLEGRQHEHTR-DPSTPLTEPKFDMLYKIEDVPPWYLCIFLGLQVYLTCS	57
<i>PucK</i>	1PMKEQHNAQLMMLGLQLMLAMYA	24
<i>UocT</i>	1MSAIDS---QLPSSSGDRPTDEVDRLSPGKLIILGLQLVLMVYA	43
<i>UopA</i>	1MDNSIHS TDGPDSPVINSN---PKKTVRQRVRLARHLTRTEGLIGDYDGF LRP ELPMFKKDRAPPFFGLNEKIPVLLAFILGLQALAMLA	92
<i>XanP</i>	1MSVSTLESNAQPVVAQTQNSLEIYRLIEDRPPPLQTLFAACQQLFLAMFV	48
<i>XanQ</i>	1MSDIHAGSDLI FELED RPPFHQALVGAITLALAFV	37
<i>UraA</i>	31	ATVLPVPLFHINP-----ATVLLFNIGTLLYLF-----CGKIPAYIGSSFAFISPVL LLLPLG-----YEV-AL	91
<i>PyrP</i>	33	STVLPVPLVGINP-----AIALLSGLGLAHMSV-----TKFRVPAYMGSFAFYGAMTLLMKN-----GMPAIA	94
<i>RutG</i>	46	ATVLMPLMLGLDP-----NLSILMSIGTLLFFI-----TGGRVPSYLGSSAAFGVGVIAATGFGNGG-----INPNISIAL	113
<i>hSVCT3</i>	62	LLCVSHLLLCSLSPGGLSYSPQLLSASFSCOMSTLQQTW-----MGRSLP LQDPSLEFLIPALVLT SQ---KLPRAIQTPGNSLMLHLCRGPSCHGLGHWTSLQEV	166
<i>hSVCT2</i>	116	GTI AVPFLADAMCVGDQWATSQ LIGTIFFCVGLITLLQTT-----FGCR-----	161
<i>hSVCT1</i>	58	GTI AVPFLAEALCVGHDQHMVSQLIGTIFTCVGLITLLQTT-----VGI RLP LQASAFALVLPKAILALERWKCPEE E IYGNWSLP-----LNTSHIWHPRIREVQ	157
<i>PucK</i>	25	GAIVLP L VIGAAIGLN-AGQLTYL I AIDLFMC AATLLQLWRN-----RYFGI L PVLGCTFAVGPMSIGS---TYG---YGVVAVGCLN	100
<i>UocT</i>	44	GAVAVPLMIGDRGLS-K EAIAMLSSDLFCGGLVTL LQCIGI-----RFMGI RLPVIMSVTFAAVTPMIAIGMNPDIG-----LGLIF	122
<i>UopA</i>	93	GVVTPPLIISSSLSP-SDLQYLVSTSLIVCGLLSMVQITRFHIYKTPYYIGSGVLSVMGVSFII SVASGFNQMSYNGFCQLDEAG-----NR LCPFAI	189
<i>XanP</i>	49	AVITPALLICQALGLP-AQDQHIISMSLFA SVASIIQIKAWGP-----VSGLSLIQGTSFNFVAP LIMGGTALKTGAD-----VP TMM	129
<i>XanQ</i>	38	PMTVPLLVGAALQLS-AETTAYLVSMAMIASGIGTWLQVNRVGI-----VSGLSLIQSVNFSFVTVMIALGSSSMKSDGFH-----EELIM	118
<i>UraA</i>	92	GGFIMCGVLFCLVSVFVKKAGTGWLDVLPFAAMGAI VAVIGLELAGVAAGMAGLPAEQG-----T-PDSKTI I IISITLAVTVIGSVL-----	175
<i>PyrP</i>	95	QGAMTGLVYLIVALIVKFAKGWIDKVLPIVVGPIVMVIGLSLAPTAINDAMYDVANL-----KGSYLAYII IALITVLSIIVYSIY-----	179
<i>RutG</i>	114	GGI IACGLVYTVIGLVVMKIGTRWIERLMPVVTGAVVMAIGLNLA IAVKSVSASAFD-----SMMAVMTVLCIGLVAVF-----	189
<i>hSVCT3</i>	167	GAVVYGLLGGMGLL---GSPGHVFP HCGPLV LAPSLLVAGLSAHR EYVQF-----CFTH-----WGLALLVILMMVCSQHLGSCQHFVCFWRRASTSS	255
<i>hSVCT2</i>	162	-----TFELVLLFSQYARNKFPPIKYS-KKQWT	190
<i>hSVCT1</i>	158	GAIMVSSVVEVIGELL---GLPGALLNYIGPLVTPVTVLSIGLSVQAAGR-----AGS-----H-----WGISACSILLIILFSPQYLRNLTFLPVYRVW-KGLT	245
<i>PucK</i>	101	GAIIAAGL---IVVLAAGFFG-KLVRFPPVYVTVGSVMIIGLSIIP TAMNLAGGESK-----EFGSLDNVLLGFGVTAIFILLVYF-----	179
<i>UocT</i>	123	GATIAAAGF-----ITTLIAPLIG-RMLPFPPLVTVGVVITSGLSIQVGI DWAAGKGNP-----QVGNPVYLGISFAVLIIFILLTRY-----	201
<i>UopA</i>	190	IGLIGTSACCALVEILLAFVPPVYI QIIFPIVITGPTVMIIGLSIGTGFKDWAGSACMDGMCLPSATAPRPLPWGSP EFIGLGLVYVSIICERF-----	288
<i>XanP</i>	100	AALIGTLMLASCTEMVIRSVLH-LARRIITPLVSGVVMVIGLSIQVGLTSGIGGYAAMSND-----TFGAPKLLLAGVYVLLIILNRQ-----	214
<i>XanQ</i>	119	SSLLGVSFVGAFLVGGSSFILP-YLRRYITPTVSGIVVLMIGLSIKVGIIDFGGFAAKSSG-----TFGNYHGLVGLVLLVIGVFNCC-----	205
<i>UraA</i>	176	--FRGFLAIPILIGLVLYGALS FAMG-----IVDTPPIINAH-WFALPTLYTPR--FEW---FAI LTI LPAALVVAEHVRLVVTANIVKKD L L R--DPGLH	264
<i>PyrP</i>	180	--GKGF LSVVPL LGLIITGYAAMIIGKITGM-N-----IVSFTGISHAK-WLTPPMEIPFANYKWFYPSA I L TMAP IAFV TMTHEFHIIMVNSLTKKDYFK--EPGLE	280
<i>RutG</i>	209	--TRGMQRLLLVGLIVACILLYGMVTNVLGLGK-----AVDFTLVSHAA-WFGLPHFSYPAF-----NGQAMMLIAPVAVILVAENLHLKAVAGMTGRN-M--DPYMG	283
<i>hSVCT3</i>	256	HTPLPVRFLLSVLPVACVWVVSFAVFGFS-VI PQ-----ELSAPTKAPVWLPHPGGEWNP L L T--PRAAAGISMA LAASSTSLCYALCGRLLHLP P P P--PHACS	352
<i>hSVCT2</i>	191	AYK LQ LFKMFPILAI L VSWLLCFIFTVTDVFPDSTKYGFYARTDARQVGLVAPWFKVPYFPQWGLPTVS---AAGVIGMLSAVVAIIESI DDYACARLSCAPPPP--IHATN	303
<i>hSVCT1</i>	246	LRIQ LFKMFPILAI L VSWLLCFIFTVTDVFPDSTKYGFYARTDARQVGLVAPWFKVPYFPQWGLPTVS---AAAVLGMFSATLAGIIESIDDYACARLSCAPPPP--VHATN	357
<i>PucK</i>	180	--FKGFRSIAI L LGLIAGTAAAYFMC-----KVDSEVLEAS-WLHPSLFYFGPPTFE--LPAVVTMLVAIVSLESTVYVFAADI TNRRLS--EKDL	270
<i>UocT</i>	702	--AKGFMSNVAVLGLVFGFLSWMMN-----EVNLSGLHDAF-WFALVTPMFSGMPIFD--PVSILTMTAVLIIVFIESMWFALGELVGRKLS--SHDI	792
<i>UopA</i>	289	--GAPIMKSCSVVIGLIVGCLVAACG-----YFSHADIDAA- AASFIVWTFPLSVYG---PMVLP I IAVFIIICACECI RDVTATCDW SRL EVRGGTFESRIQ	382
<i>XanP</i>	216	--RNPVYLRVASLVI IAMAAGYALAWFMG-----MLPESNEPMTQLIMFPTPLYYGLGIEW---SLLPLMLVFMITILETIIDTATSDWSEQVSGPLVMKRK	310
<i>XanQ</i>	205	--RSP LRMGGALIGLVCVYIASLCLG-----MVD FSSM-RNLP LIT IHPFKYGFSSFSF---HQFLVVGTIYLLSVLEAVGDI TATAMVSRRP IQGEEYQSR LK	298
<i>UraA</i>	265	RSMFANLSTVISEFFGSTP-NTTYGELIIVMAITRYSV TWIGGAIFAILLSCVGLAAAIQMLPVMGVS LLLYGVGASIRVLI ESKYVDYNAQNLIIITSVI I IIVSGAK	381
<i>PyrP</i>	281	KTLTGDELQAIAGF IGAPP-VTSYGEIIVMAITKHSIYVIAAAVLAIVVSGIKITALLQSAPVIGGASIALFGVIAASLKI LVENKNVFDIKRNLIISSVVIVIGIGMI	397
<i>RutG</i>	284	RAFVGDGLATMISVSGVSGGSS-VTTAYAEIIVMAVTKYVLSYVFAAAVIAMLGFSFKGAL IHTAAVIGGASIVVFGLIJAVABAR IWWQNRVDSLQNGNIMAVVATLVLAGDFA	400
<i>hSVCT3</i>	354	RGLSLEGLSVAAGLLSGPMGTASSFPVKKVGLIQGSSQVAHLVGLLQVGLSPLRQLLITLIPVVEGVLVGTQAVLSA FSSFYLADIDS--GRNFIIVGFSIFMNL--L	466
<i>hSVCT2</i>	303	RGIIFVE LSCVLDIGFPTGNGSTSSSPNIEVGLITKVGRRVYQYGAAILMVLGTEIKFTALFESSDPPLGALFCTLFGMITAVELSNLQFIDLNS--SRNLFVLFGSIFIFGL--V	415
<i>hSVCT1</i>	358	RGIIFTEICCI IAGLLGTGNGSTSSSPNIEVGLITKVGRRVYQYGAAILMVLGTEIKFTALFESSDPPLGALFCTLFGMITAVELSNLQFVDMS--SRNLFVLFGSIFIFGL--V	470
<i>PucK</i>	271	KYRAEGLAII LGLLGNAPF-YTAFSQVIEIVQLSKMKSVNVAITGII LVAIGLVPKAAALTVVTPV LGGAMIVMFGMVISYIKMLSVDVLDLQ-GNLLII IASSVILGLGATT	385
<i>UocT</i>	293	RGLRVDQVGMIGGTFNSFP-HTSFSQVIEIVQLSKMKSVNVAITGII LVAIGLVPKAAALTVVTPV LGGAMIVMFGMVISYIKMLSVDVLDLQ-GNLLII IASSVILGLGATT	408
<i>UopA</i>	383	GAVLADENSVVAALATMTP-MTTFAQDNVIALTRCANRWAGYCCLLIIVAGIFAKFAAIVATNSVMCGMKTFLFASVVISQAIIVAKAPFT--RRNRFILTASMALCYGATL	496
<i>XanP</i>	311	GVLANLNSFVSAVNTFP-NSCFGDNVIEIQLTGASRYVGFVVALMLIVLGLFPVAVSGVQHIEPVLGGATLVMFGTIIAASVRIIVSRPEPLN--RRAILIALSLAVGLVGSV	424
<i>XanQ</i>	299	GVVLADELVSVIVASAVGSLP-LITFADQNVIQMTGASRYVGRITAVMLVILGLFPMIGGFTTISAVLEGAMTLMFSMIIAIIIRI IITNGLK--RRETLIVATSGLGLVGSV	412
<i>UraA</i>	382	V-----NIGAA-ELKGMALATVIGIGSLIFKLSVLRP-EVVLD AEDAD--I-----TDK-----	429
<i>PyrP</i>	398	I-----NITONLQISSVAIATLILVAVNLVLP--K-DP-SEI-----	430
<i>RutG</i>	401	L-----TIGGF-TLGGIGTATFGILNALLSRKLVDPVP-PEVHQ-EP-----	442
<i>hSVCT3</i>	416	LPWRFEA-PVLFSTGWSLDVLLHSLLTQPIFLAGLSGLFENTIPGTLQERGGGLSPFTAQEARMPKPREKAAQVYRPLFP I QNLCP I PQPLHCLCLPEPDEEGGSS	532
<i>hSVCT2</i>	467	LP SYLRQN-P-LVTGTIGIDQVLLTAMFVGGVCFIDNTIPGTFEERICR IWKVKGVGKGNK-----SDGMESYVLPFGMNI I K-----KYRCFSYLPISPTFFVYTKNG	518
<i>hSVCT1</i>	417	LPNYLEN-PGAINGTILEVDQILIVLLTTEMFVGGCLAFIDNTVPGSPFERGLIQWKAGAHANSD-----MSSSLKSYDFPIGMGIVK-----RITFLKYIPICPVFKGSSSS	575
<i>PucK</i>	386	VPA L F S S L-----SGAASLAGSGVIGSLTIAI AHV FQTQPN SADIKT-----	431
<i>UocT</i>	409	SHDFSKL-----PAVLQPLHSGIMLATSVAVVNVFNGYQHHDVKEVSDKDLK-V-R-----TVRMMMLM-----RKLK-----	476
<i>UopA</i>	497	VP TWFVGNVFPQTE NRDL EGFENAI ELVLETGFAVTA FVAMLNAI MP AEVEEIGAVTPMPVSAHNR-D-----GEAEYQSK-----QA-----	574
<i>XanP</i>	425	QPLILQFA-----PEWLNKLLSSGIIAAGGITAVINLIIPPEKQ-----	463
<i>XanQ</i>	413	DPEIFIKL-----PASIVYLVENP ICAAGLLTILNII L PGGYKQENVLPISITSAEEM--D-----	466
<i>UraA</i>			
<i>PyrP</i>			
<i>RutG</i>			
<i>hSVCT3</i>	583	-----EP E M A D L P G S G E P C E S S R E G F R S Q K-----	610
<i>hSVCT2</i>	519	LRKSDNRS S D E - D S Q A T G-----	536
<i>hSVCT1</i>	576	KDQIAIPE D T P E - N T E T A S V C T K V-----	598
<i>PucK</i>			
<i>UocT</i>	477	-----KNEHGE-----	482
<i>UopA</i>			
<i>XanP</i>			
<i>XanQ</i>			

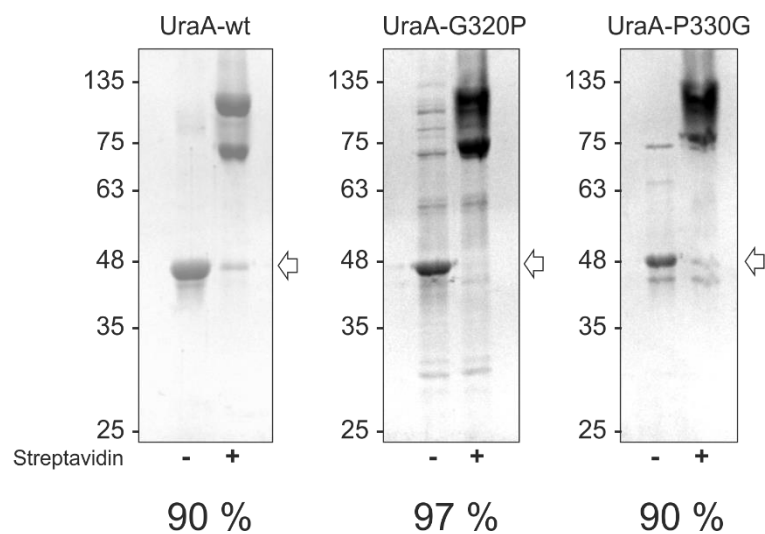
Supplementary figure 1: SLC23 alignment. Alignment of the three human SLC23 transporters with non-vertebrate transporters covering the full spectrum of substrate specificity in the SLC23 family (xanthine/uric acid, uracil, ascorbic acid). Conserved residues are highlighted by cyan color with the degree of conservation displayed in a color code from white to cyan and the signature motif visualized by a purple box.



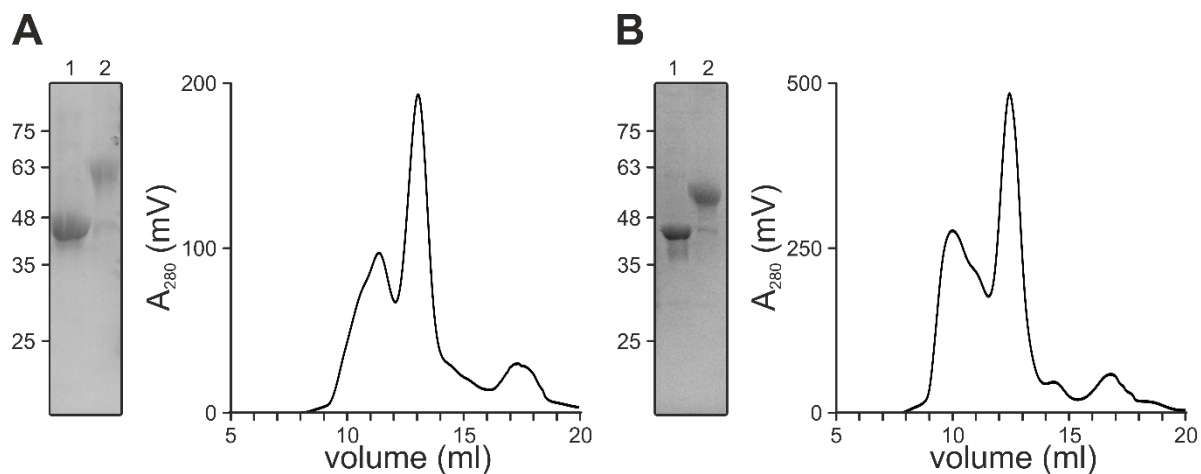
Supplementary figure 2: M13KO7 helper phage quantification. Dilutions of purified helper phages were used to infect log-phase *E. coli* TG1 that were subsequently plated as duplicates on 2YT-Agar-plates containing 50 µg/mL kanamycin. From the number of grown colonies, a helper phage concentration of 8×10^{14} colony forming units was calculated.



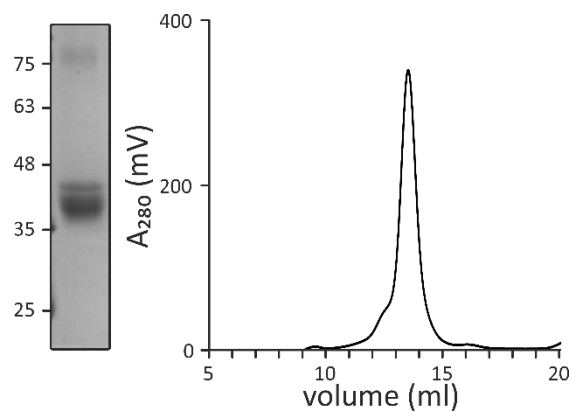
Supplementary figure 3: OXA and NUBIA phage library quantification by colony assay. The phages served as input for the first round of biopanning. Dilutions of purified phages were used to infect log-phase *E. coli* TG1 that were subsequently plated as duplicates on 2YT-Agar-plates containing 100 µg/mL ampicillin. From the number of grown colonies, a phage concentration of 1.4×10^{15} colony forming units per mL for the OXA library respectively 1.6×10^{15} colony forming units per mL for the NUBIA library was calculated.



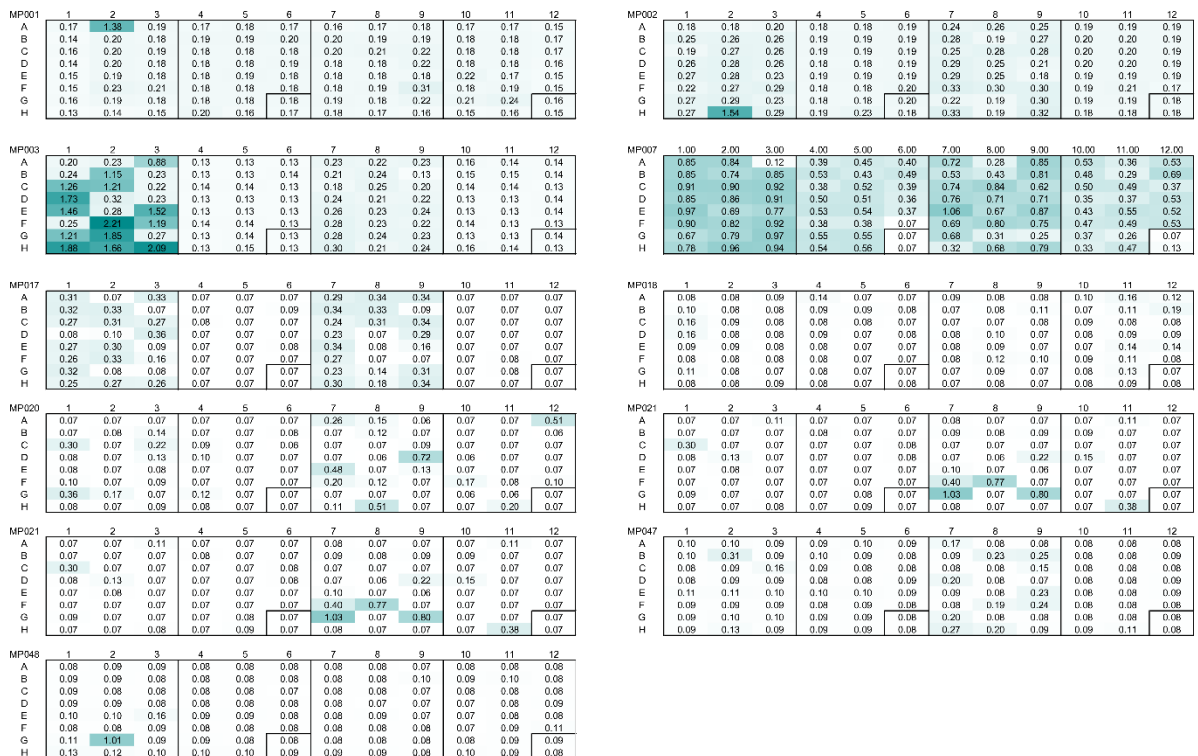
Supplementary figure 4: Biotinylation efficiency of UraA_{WT}, UraA_{G320P} and UraA_{P330G} with C-terminal Avi-tag quantified by streptavidin induced mobility shift in SDS-PAGE visualized with coomassie staining. The biotinylation efficiency was calculated based on densitometry analysis of the UraA band, indicated with an arrow, in presence and absence of streptavidin using the ImageJ software (Schneider et al., 2012).



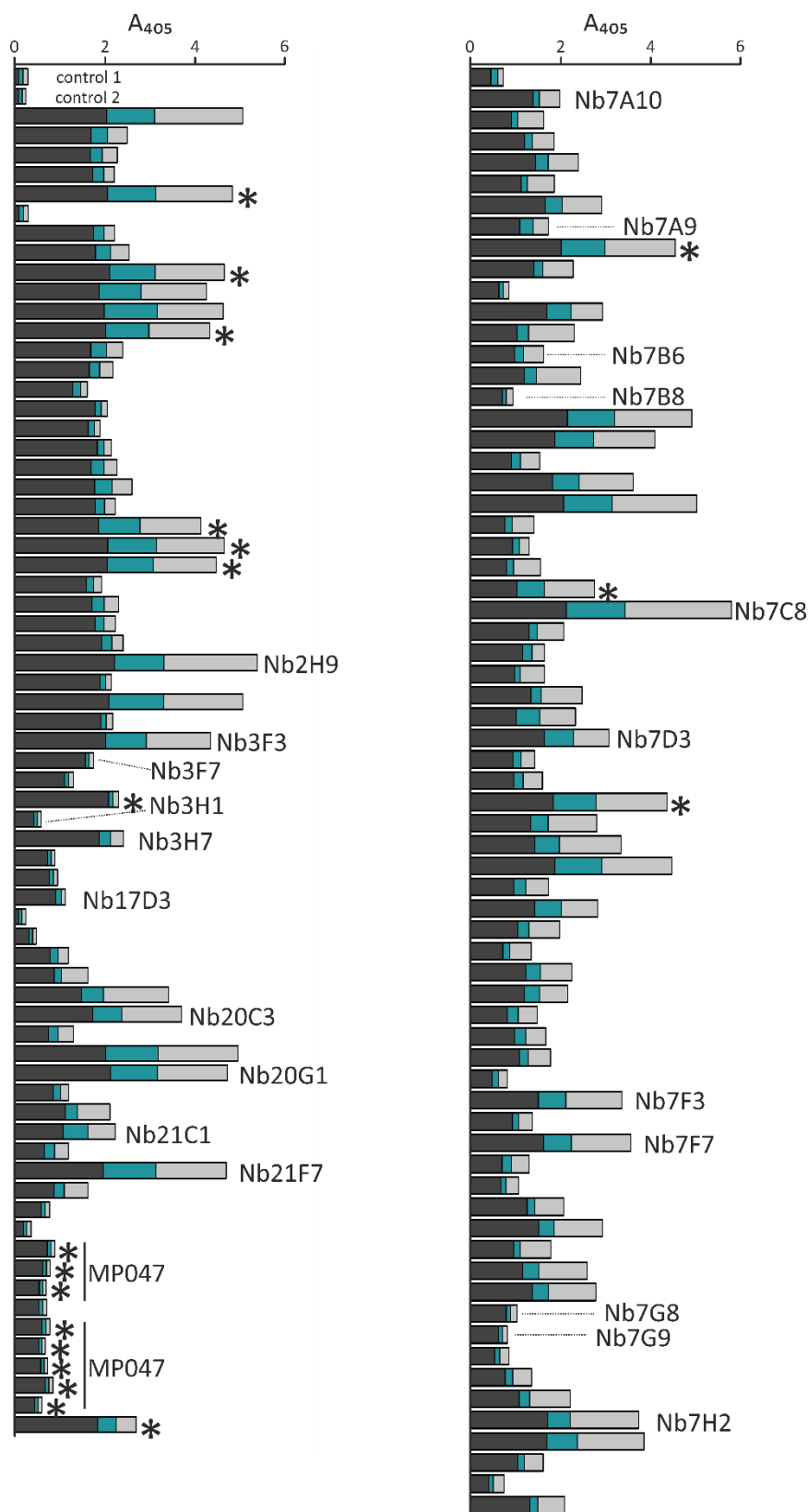
Supplementary figure 5: Preparation of antigens for nanobody selection with biased epitope. (A) Coomassie stained SDS-PAGE of UraA_{Cysless-1252C}-Avi with samples loaded as follows: 1: IMAC elution, 2: PEG-5000 labeled protein. SEC was performed as last step of purification. Only the main elution fraction was used for selections (B) Purification of UraA_{Cysless-M143C} with PEG-5000 maleimide labeling and SEC performed and presented as in (A).



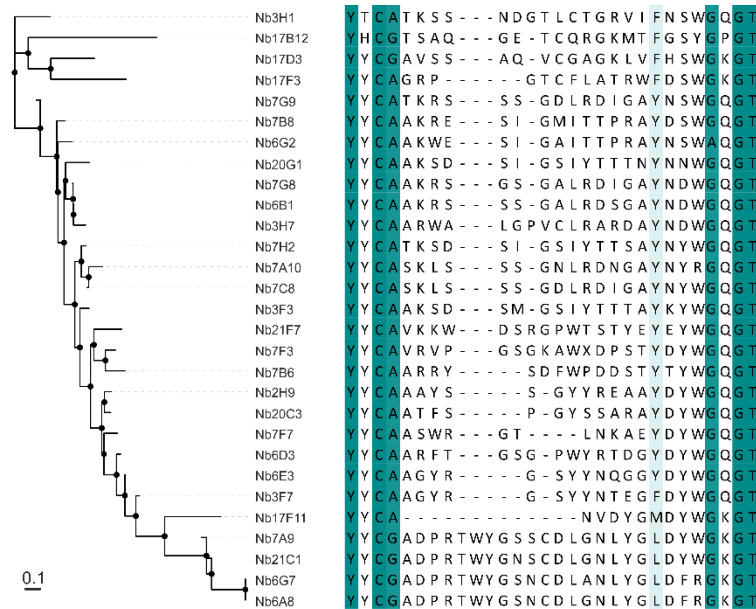
Supplementary figure 6: Preparation of crosslinked UraA_{L80C-M143C}. Coomassie stained SDS-PAGE and size exclusion chromatogram of UraA_{L80C-M143C} after oxidative crosslinking.



Supplementary figure 7: ELISA of master plates MP001, MP002, MP003, MP007, MP017, MP018, MP020, MP021, MP047 and MP048. Absorbance at 405 nm measured after overnight incubation at 4 °C indicative of nanobody binding to UraA_{WT} illustrated as color code from white (no binding) to green (high binding). The control wells G6, H6, G12 and H12 are framed.



Supplementary figure 8: ELISA of clones from master plates MP001, MP002, MP003, MP007, MP017, MP020, MP021, MP047 and MP048 with signals derived from ELISA performed at 4 °C (dark grey), at 20 °C (cyan) or at 20 °C in presence of 1 mM uracil (light grey). Unique nanobodies identified during selection are labeled with the name based on the master plate and well number. Redundant nanobodies are indicated with an asterisk. An unspecific nanobody (control 1) and no addition of nanobody (control 2) served as negative controls. Unlabeled columns represent ELISA signals of nanobodies that were not further analyzed, thus with unknown amino acid sequence.



Supplementary figure 9: Phylogenetic analysis of selected nanobodies. CDR3 sequence alignment of nanobodies selected against UraA and phylogenetic tree showing closely related and unique nanobodies. Alignment was performed with Clustal Omega (Madeira, Park et al., 2019) and the phylogenetic tree created with NGPhylogeny (Lemoine et al., 2019).

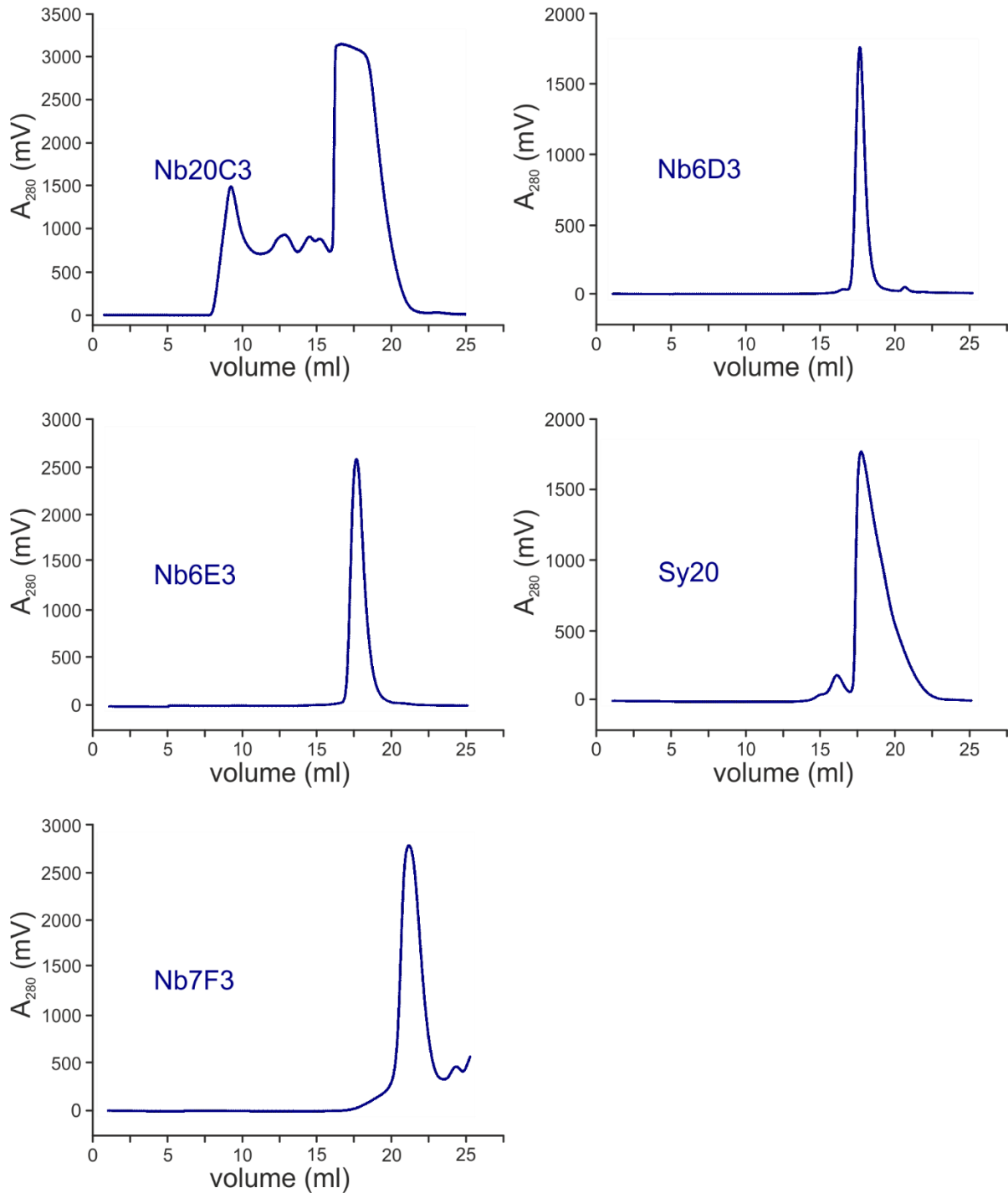
A

	CDR1	CDR2	CDR3	library
Sy1	GFPVKALV	IYSYGVMT	HVFGVRHY	concave
Sy2	GFPVSSST	IASWGWKT	EVFVGWEY	concave
Sy4	GFPVSSST	IASWGWIT	EVYVGGQY	concave
Sy5	GFPVQHNY	IVSFGHET	NVKDVGKWWHAYDY	loop
Sy6	GFPVEQEH	ISSAGQWT	NVKDDGWGWEYDY	loop
Sy7	GFPVATAW	IASWGGHT	NVKDQGEWWVEYDY	loop
Sy8	GFPVEQWT	ISSWGWWT	NVKDVGAWWASYDY	loop
Sy9	GFPVDWET	ITSWGQTT	NVKDHGEWWATYDY	loop
Sy11	GFPVSSST	ISSSGDVT	NVKDYGFWYWTMYDY	loop
Sy12	GFPVYFER	IHSWGEET	NVKDAGEWWAHYDY	loop
Sy14	GFPVxxxx	IxSxGQxT	NVKDxGWxGxxYDY	loop
Sy15	GFPVYRET	IESNGEET	NVKDYGFWYAAAYDY	loop
Sy17	GNISYISY	LFTSWGQT	AAANYGYFDPLHYNYY	convex
Sy18	GDISYIHY	LNTTYGNT	AAAFYGYQDPLDYTWYYY	convex
Sy19	GTISYIHY	LATWTGET	AAAWYGYDPLNYSY	convex
Sy20	GNISYIHY	LGTSWGST	AAANYGYNPLMDTY	convex
Sy21	GNIKYISY	LYTSYGYT	AAAGFGYASPLSSARYFY	convex
Sy22	GSIAYIHY	LWTHDGRT	AAAQFGYFDPLTEYYFY	convex
Sy24	GNISYIHY	LNTVWGWT	AAAMYGYNPLHAWDYSY	convex
Sy25	GYIQYIHY	LNTAWGET	AAAHYGYFNPLGWQQYNY	convex

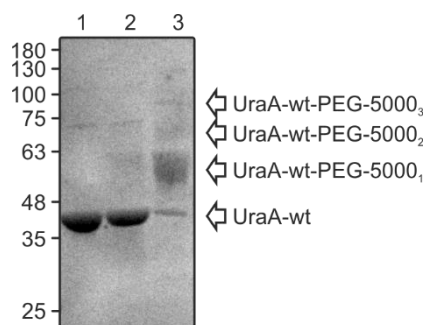
B

	CDR1	CDR2	CDR3	library
Sy26	GFPVEDAT	IASWGWQT	EVYVGAEY	concave
Sy27	GFPVxxxx	IDSWGxT	no sequence	concave
Sy28	GFPVSYQT	ITSWGWT	NVKDFGLWYDYDY	loop
Sy29	GFPVGHWT	IASYGWWT	NVKDWGTYYEYDY	loop
Sy30	GFPVxxxx	ITSWGAWT	no sequence	loop
Sy31	GFPVFNQR	IYSEGSFT	NVKDYGFWYWWLYDY	loop
Sy33	GFPVNAGE	IYSNGSYT	NVKDYGWWYWTYYDY	loop
Sy36	GFPVGWAV	INSEGQWT	NVKDWGQFLEYDY	loop
Sy37	GFPVSYAV	ISSYGSWT	NVKDYGAWFAYYDY	loop
Sy41	no sequence	no sequence	no sequence	loop
Sy42	GFPVYASQ	IYSNGQYT	NVKDHGNFHTYYDY	loop
Sy43	GAIQYISY	LSTAWGET	AAAYFGYHDPLSASRY	convex
Sy44	GYIGYIHY	LKTEVGNT	AAAWYGYDPLSYNSY	convex
Sy45	GNIAIHY	LSTTLGNT	AAAYFGYSSPLAHERY	convex
Sy46	GNIQYIHY	LGTHGGET	AAAWYGYFNPLDAYS	convex
Sy47	GNIAIYISY	LATSWGNT	AAAMYGYSDPLESNKY	convex
Sy48	GNIQYIHY	LSTSLGTT	AAAHYGYWNPLDEYHY	convex
Sy49	GYIKYIHY	LSTSWGHT	AAAWYGYNSPLNAAWY	convex
Sy50	GNIHFIHY	LSTVWGNT	AAAWIGYNDPLSKFTY	convex
Sy51	GxIxxIY	LxTxxGxT	AAAxGxxxPLxxxxYxY	convex
Sy52	GNITYIHY	LKTSTGET	AAAWYGYDPLAYNSY	convex
Sy53	GKIVFIHY	LWTQNGQT	AAAYFGYFNPLLNYY	convex
Sy54	GKIYIHY	LSTHRGET	AAAWYGYEYPLFEEHY	convex
Sy55	GYISHIHY	LKTYVGST	AAAWYGYSDPLADSHY	convex
Sy58	GNIEYIHY	LSTTWGTT	AAAMFGYYSPLTAAANY	convex

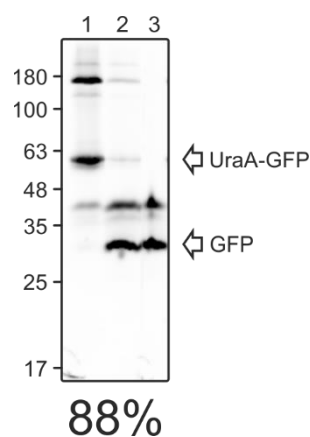
Supplementary figure 10: CDR sequences of selected sybodies after removal of redundant sequences. Binders selected against Ura_{A_{WT}} (A) or selected against Ura_{A_{WT}} in presence of uracil (B) with indicated sybody library (concave, loop, convex) the individual binders originated from. Sequences that could not be analyzed are highlighted in red.



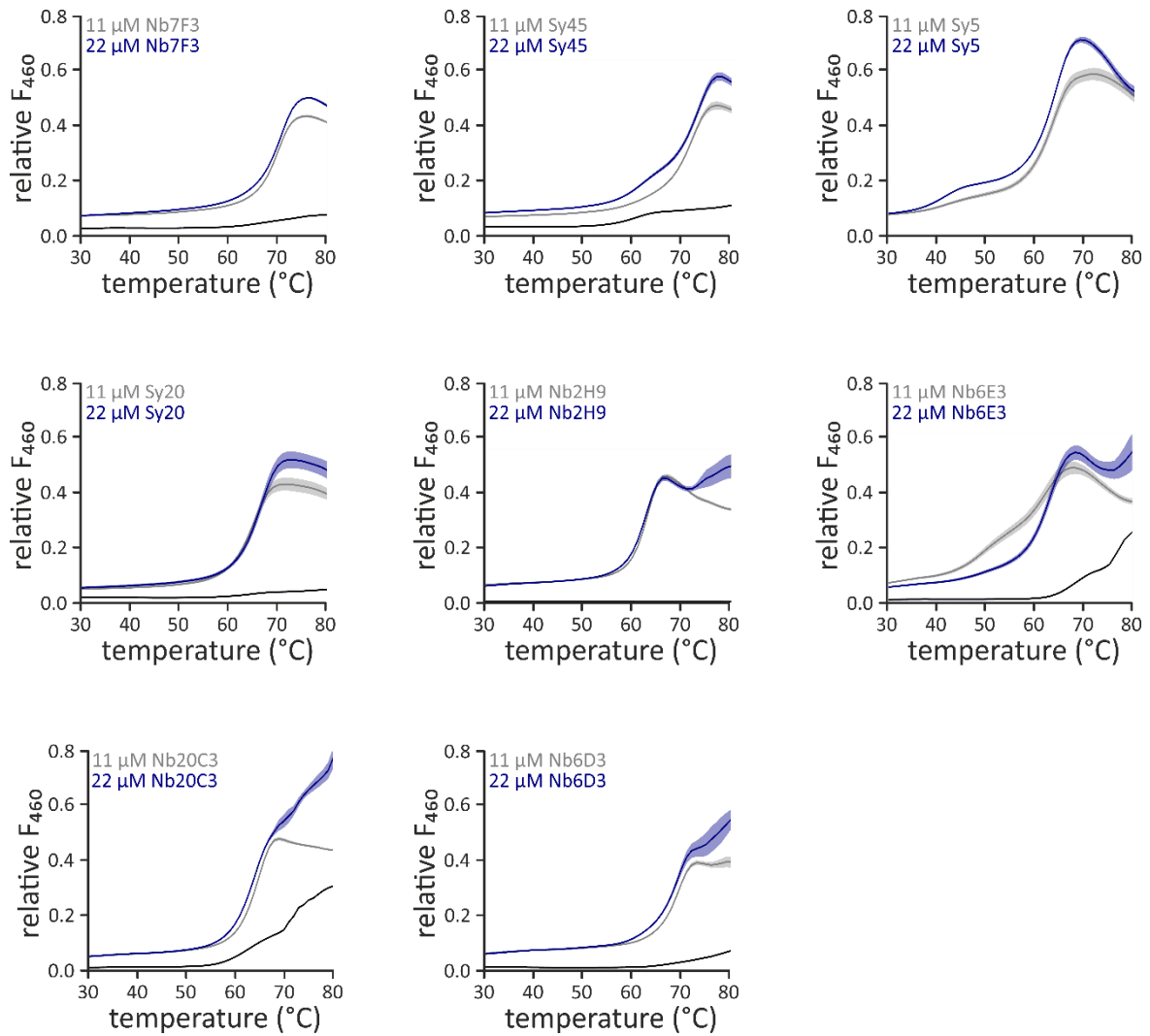
Supplementary figure 11: Purification of nanobodies and sybodies. Chromatograms of selected nanobodies and sybodies from size exclusion chromatography performed on a Sepax SRT-10C SEC-300 column.



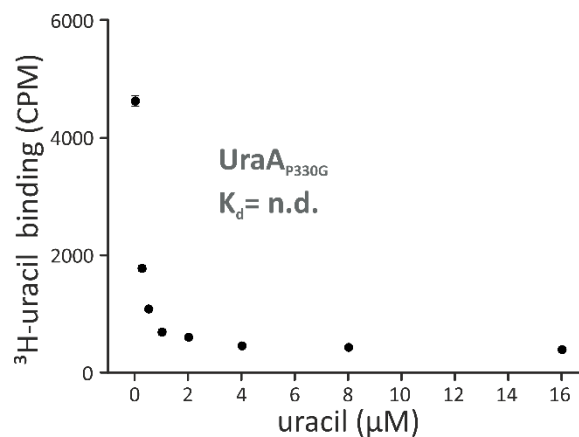
Supplementary figure 12: Solvent accessibility of the four native cysteine residues in UraA_{WT}. Accessibility was tested by PEG-5000-maleimide labeling in the folded and unfolded state. Purified UraA_{WT} was subjected to PEG-5000-maleimide labeling in presence (lane 3) or absence (lane 2) of 1% SDS (w/v) for 10 minutes at room temperature and the label induced upshift in SDS-PAGE visualized by Coomassie staining. Lane 1 shows the control sample without addition of PEG-5000-maleimide.



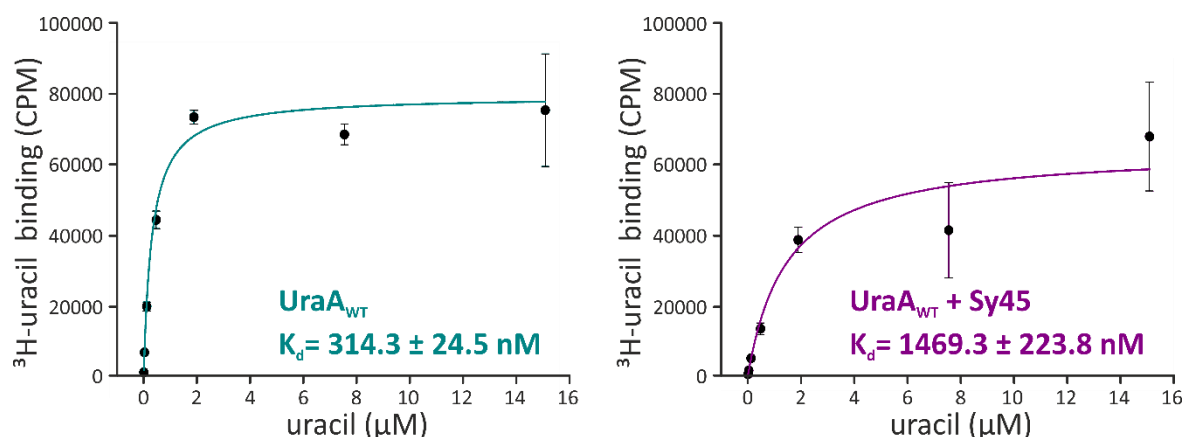
Supplementary figure 13: Inside-out vesicle orientation analysis by HRV-3C protease cleavage. Inside-out vesicles were prepared from *E. coli* MC1061 with UraA_{WT}-GFP produced from pBXC3GH plasmid. The cytoplasmic 3C-protease cleavage site was used for orientation quantification by comparing the in-gel fluorescence signal of the untreated UraA_{WT}-GFP running below 63 kDa in lane 1 with the signal in lane 2 containing the same sample with addition of 3C-protease. Densitometry analysis in ImageJ yields 88% inside-out orientation of the vesicles. The protease activity was controlled by full cleavage of UraA_{WT}-GFP in presence of 1% triton X-100 for vesicle solubilization (lane 3).



Supplementary figure 14: Simultaneous DSF. Thermal stabilization of UraA_{WT} in presence of 11 μM (grey) of nanobody or sybody as indicated or 22 μM (blue). Controls without addition of UraA_{WT} are shown in black color. For Sy5 and Nb2H9 the control curves are covered by the x-scale.



Supplementary figure 15: Scintillation proximity assay of UraA_{P330G}. UraA_{P330G} at a final concentration of 150 nM were pre-incubated with final 150 nM ³H-uracil and increasing amounts of non-labeled uracil. Samples were transferred to a 96-well plate, proteins immobilized to 340 μg Streptavidin PVT beads and scintillation counted for 2 min. The background was recorded similarly for each well after addition of 1% SDS (w/v) and subtracted from the specific binding signal. Shown are the mean values from triplicates and the corresponding standard errors. Scintillation proximity assay was performed with Niko Schenck as part of his Master studies.



Supplementary figure 16: Uracil affinity of UraA_{WT} in presence or absence of Sy45 by saturation binding assay. The uracil affinity of UraA_{WT} was analyzed by a saturation binding assay. Background corrected signals were corrected for different ratios of ³H-uracil/uracil and plotted against the total uracil concentration. The data was analyzed by non-linear curve fitting using the Origin software and Langmuir isotherme.

SUBSET OF INTENSITY DATA WITH SIGNAL/NOISE >= -3.0 AS FUNCTION OF RESOLUTION													
RESOLUTION LIMIT	NUMBER OF REFLECTIONS			COMPLETENESS OF DATA	R-FACTOR observed	R-FACTOR COMPARED expected	I/SIGMA	R-meas	CC(1/2)	Anomal Corr	SigAno	Nano	
	OBSERVED	UNIQUE	POSSIBLE										
11.18	8834	735	778	94.5%	3.2%	4.2%	8834	61.49	3.3%	99.9*	-16	0.637	640
7.91	18098	1347	1349	99.9%	3.4%	4.4%	18098	60.20	3.5%	100.0*	-20	0.632	1249
6.45	22782	1784	1784	100.0%	5.1%	5.1%	22782	43.52	5.3%	99.9*	-9	0.822	1671
5.59	27308	2047	2048	100.0%	7.9%	6.9%	27308	31.72	8.2%	99.9*	-10	0.864	1937
5.00	33237	2361	2364	99.9%	8.6%	7.7%	33237	28.15	8.9%	99.9*	-7	0.832	2257
4.56	34830	2566	2571	99.8%	8.5%	7.7%	34830	25.53	8.8%	99.9*	-8	0.811	2459
4.23	36529	2812	2809	100.1%	11.1%	10.3%	36529	19.76	11.6%	99.9*	-6	0.812	2705
3.95	41420	2984	2995	99.6%	17.2%	16.6%	41420	14.18	17.9%	99.9*	-5	0.772	2875
3.73	45454	3218	3220	99.9%	30.2%	29.8%	45454	9.33	31.3%	99.7*	-2	0.746	3107
3.54	47076	3357	3362	99.9%	53.9%	54.9%	47076	6.00	55.9%	99.2*	-1	0.694	3254
3.37	46037	3546	3556	99.7%	80.4%	83.2%	46037	3.90	83.7%	98.1*	0	0.671	3421
3.23	50649	3707	3715	99.8%	120.1%	125.5%	50649	2.86	124.8%	96.4*	-2	0.631	3591
3.10	54025	3860	3881	99.5%	213.3%	223.7%	54025	1.77	221.5%	91.1*	-1	0.612	3742
2.99	57148	4007	4015	99.8%	317.0%	334.6%	57148	1.19	328.8%	86.7*	1	0.590	3890
2.89	59123	4155	4163	99.8%	440.1%	466.9%	59123	0.85	456.6%	74.5*	-1	0.573	4042
2.80	56233	4297	4304	99.8%	512.1%	550.9%	56233	0.64	533.0%	51.8*	1	0.557	4181
2.71	59276	4412	4419	99.8%	712.6%	769.3%	59275	0.46	740.8%	41.9*	-1	0.546	4291
2.64	62670	4560	4569	99.8%	1234.9%	1333.8%	62670	0.27	1282.6%	24.4*	0	0.533	4427
2.56	64107	4678	4689	99.8%	2557.8%	2794.2%	64107	0.15	2656.6%	16.8*	1	0.516	4557
2.50	59782	4822	4828	99.9%	-99.9%	-99.9%	59782	0.00	-99.9%	5.9	0	0.477	4636
total	884618	65255	65419	99.7%	13.8%	14.6%	884617	9.12	14.3%	99.9*	-2	0.638	62932

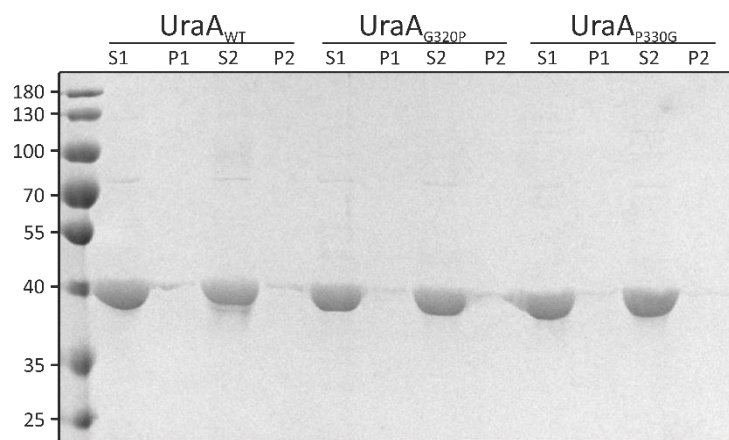
SUBSET OF INTENSITY DATA WITH SIGNAL/NOISE >= -3.0 AS FUNCTION OF RESOLUTION													
RESOLUTION LIMIT	NUMBER OF REFLECTIONS			COMPLETENESS OF DATA	R-FACTOR observed	R-FACTOR COMPARED expected	I/SIGMA	R-meas	CC(1/2)	Anomal Corr	SigAno	Nano	
	OBSERVED	UNIQUE	POSSIBLE										
11.79	7361	614	658	93.3%	3.1%	5.0%	7361	51.50	3.3%	99.9*	-21	0.510	531
8.33	15420	1171	1173	99.8%	3.3%	5.1%	15420	51.27	3.4%	100.0*	-21	0.552	1079
6.81	20104	1500	1498	100.1%	4.5%	5.5%	20104	43.23	4.6%	99.9*	-16	0.675	1407
5.89	22149	1762	1763	99.9%	7.1%	7.0%	22149	30.35	7.4%	99.9*	-6	0.838	1656
5.27	28028	2017	2018	100.0%	9.0%	8.5%	28028	26.44	9.3%	99.9*	-12	0.778	1920
4.81	31429	2212	2216	99.8%	8.3%	8.2%	31429	25.09	8.6%	99.9*	-8	0.782	2119
4.46	30318	2371	2371	100.0%	8.7%	8.6%	30318	21.47	9.1%	99.9*	-6	0.779	2274
4.17	34743	2577	2585	99.7%	12.5%	12.4%	34743	16.79	13.0%	99.9*	-6	0.771	2488
3.93	37978	2730	2736	99.8%	18.6%	18.8%	37978	12.48	19.4%	99.8*	-6	0.734	2626
3.73	40769	2887	2888	100.0%	30.8%	31.4%	40769	8.55	32.0%	99.7*	-3	0.725	2787
3.55	39636	2811	3041	92.4%	48.9%	50.5%	39636	6.25	50.7%	99.4*	0	0.696	2731
3.40	32966	2503	3164	79.1%	62.7%	66.0%	32966	4.87	65.2%	98.4*	-1	0.694	2431
3.27	28374	2116	3279	64.5%	69.2%	71.8%	28374	4.65	72.0%	97.8*	-4	0.678	2045
3.15	21792	1605	3436	46.7%	89.5%	93.3%	21792	3.97	93.0%	96.5*	-4	0.683	1549
3.04	15864	1186	3581	33.1%	95.4%	97.8%	15864	3.93	99.3%	96.5*	-2	0.712	1135
2.95	11198	848	3672	23.1%	112.6%	116.6%	11198	3.33	117.2%	91.0*	-1	0.714	807
2.86	8337	633	3780	16.7%	104.0%	106.4%	8337	3.56	108.3%	82.1*	-3	0.724	598
2.78	5746	425	3902	10.9%	102.1%	103.9%	5746	3.74	106.2%	80.4*	-7	0.720	400
2.70	3133	239	4006	6.0%	113.3%	115.5%	3133	3.08	118.0%	71.6*	3	0.743	218
2.64	928	76	4104	1.9%	146.0%	141.0%	928	2.54	152.8%	67.9*	-7	0.762	67
total	436273	32283	55871	57.8%	8.2%	9.4%	436273	16.42	8.6%	99.9*	-5	0.724	30868

Supplementary figure 17: Merging statistics of the UraA_{G320P}-Sy45 diffraction dataset. Merging statistics of the UraA_{G320P}-Sy45 diffraction data set before and after ellipsoidal truncation and anisotropic scaling performed by the UCLA diffraction anisotropy server (Strong et al., 2006). The structure was refined at 3.1 Å resolution.

SUBSET OF INTENSITY DATA WITH SIGNAL/NOISE \geq -3.0 AS FUNCTION OF RESOLUTION													
RESOLUTION LIMIT	NUMBER OF REFLECTIONS			COMPLETENESS OF DATA	R-FACTOR observed	R-FACTOR expected	COMPARED	I/SIGMA	R-meas	CC(1/2)	Anomal Corr	SigAno	Nano
	OBSERVED	UNIQUE	POSSIBLE										
13.40	2780	428	443	96.6%	3.3%	3.6%	2779	45.66	3.7%	99.9*	-22	0.667	355
9.48	5284	772	773	99.9%	4.1%	4.2%	5284	37.21	4.4%	99.9*	-15	0.751	696
7.74	6590	993	998	99.5%	4.9%	4.9%	6590	31.89	5.4%	99.8*	-14	0.742	907
6.70	7482	1171	1171	100.0%	9.6%	9.1%	7482	18.91	10.4%	99.7*	-5	0.819	1077
5.99	9145	1344	1347	99.8%	18.3%	18.0%	9144	11.69	19.8%	99.2*	-6	0.791	1251
5.47	10201	1454	1452	100.1%	23.3%	22.9%	10200	9.82	25.1%	99.0*	-3	0.807	1344
5.07	11366	1591	1594	99.8%	23.8%	23.1%	11364	9.58	25.6%	99.2*	-8	0.755	1497
4.74	12257	1708	1711	99.8%	22.8%	21.7%	12257	9.80	24.6%	99.4*	-4	0.776	1604
4.47	11970	1795	1802	99.6%	22.3%	21.4%	11969	8.95	24.2%	99.4*	-7	0.744	1682
4.24	12793	1915	1919	99.8%	28.4%	27.2%	12793	7.57	30.8%	98.9*	-5	0.769	1775
4.04	14059	2004	2009	99.8%	38.9%	37.9%	14059	5.77	42.0%	98.5*	-5	0.730	1899
3.87	14163	2108	2105	100.1%	52.1%	51.8%	14163	4.35	56.5%	96.9*	1	0.743	1989
3.72	14066	2185	2189	99.8%	67.5%	67.1%	14066	3.38	73.5%	93.2*	-3	0.704	2046
3.58	15778	2278	2278	100.0%	89.9%	90.2%	15777	2.62	97.2%	89.7*	-4	0.691	2171
3.46	16278	2320	2325	99.8%	143.6%	146.6%	16276	1.68	155.1%	77.0*	1	0.658	2228
3.35	17213	2438	2446	99.7%	167.8%	172.3%	17212	1.47	181.1%	77.5*	-4	0.625	2340
3.25	17972	2509	2514	99.8%	185.4%	191.2%	17972	1.30	199.9%	69.7*	-3	0.627	2418
3.16	18309	2549	2556	99.7%	261.5%	268.3%	18309	0.94	281.8%	58.3*	1	0.622	2455
3.08	19076	2660	2670	99.6%	282.8%	293.9%	19076	0.82	304.8%	52.9*	0	0.599	2559
3.00	16718	2680	2766	96.9%	361.0%	385.5%	16662	0.53	393.5%	42.0*	1	0.583	2340
total	253500	36902	37068	99.6%	25.3%	25.5%	253434	6.65	27.4%	99.9*	-3	0.695	34633

SUBSET OF INTENSITY DATA WITH SIGNAL/NOISE \geq -3.0 AS FUNCTION OF RESOLUTION													
RESOLUTION LIMIT	NUMBER OF REFLECTIONS			COMPLETENESS OF DATA	R-FACTOR observed	R-FACTOR expected	COMPARED	I/SIGMA	R-meas	CC(1/2)	Anomal Corr	SigAno	Nano
	OBSERVED	UNIQUE	POSSIBLE										
13.48	2731	421	436	96.6%	3.3%	3.6%	2730	45.51	3.7%	99.8*	-19	0.649	349
9.53	5220	758	759	99.9%	4.1%	4.3%	5220	37.05	4.4%	99.9*	-15	0.741	685
7.78	6432	976	982	99.4%	4.9%	4.9%	6432	32.00	5.3%	99.8*	-13	0.734	887
6.74	7414	1158	1156	100.2%	9.4%	9.0%	7414	19.01	10.2%	99.7*	-4	0.805	1068
6.03	8837	1302	1307	99.6%	17.8%	17.8%	8836	11.80	19.2%	99.2*	-5	0.760	1212
5.50	10078	1439	1438	100.1%	23.1%	23.1%	10078	9.66	24.9%	99.1*	0	0.805	1332
5.09	11253	1577	1576	100.1%	24.2%	24.3%	11250	9.28	26.1%	99.1*	-9	0.743	1480
4.76	12000	1672	1677	99.7%	22.5%	21.8%	12000	9.80	24.2%	99.4*	-5	0.769	1569
4.49	11977	1767	1776	99.5%	22.3%	21.7%	11976	8.93	24.1%	99.4*	-7	0.743	1662
4.26	12584	1903	1904	99.9%	27.9%	27.4%	12584	7.53	30.3%	98.9*	-5	0.759	1758
4.06	13701	1962	1967	99.7%	37.2%	37.1%	13701	5.77	40.2%	98.7*	-5	0.708	1862
3.89	14059	2061	2062	100.0%	51.5%	52.1%	14059	4.42	55.7%	97.2*	-2	0.723	1943
3.74	12356	1937	2133	90.8%	60.0%	60.7%	12356	3.68	65.4%	93.9*	-2	0.700	1814
3.60	9433	1386	2257	61.4%	56.0%	57.0%	9432	4.06	60.6%	93.8*	0	0.735	1305
3.48	6483	963	2314	41.6%	64.9%	66.7%	6482	3.42	70.4%	88.8*	-3	0.720	907
3.37	4733	717	2402	29.9%	61.7%	63.8%	4733	3.59	67.0%	88.1*	-5	0.704	677
3.27	3461	532	2492	21.3%	45.5%	47.5%	3461	4.41	49.6%	91.7*	-4	0.726	488
3.18	2384	363	2535	14.3%	47.5%	49.1%	2384	4.25	51.7%	87.8*	-4	0.742	335
3.09	1472	216	2593	8.3%	43.0%	46.2%	1472	4.40	46.6%	88.0*	-15	0.701	197
3.01	560	84	2700	3.1%	32.2%	37.8%	560	5.04	35.0%	95.8*	-4	0.726	72
total	157168	23194	36466	63.6%	15.9%	16.0%	157160	10.14	17.2%	99.8*	-5	0.740	21602

Supplementary figure 18: Merging statistics of the UraA_{G320P}-Sy45-uracil diffraction dataset. Merging statistics of the UraA_{G320P}-Sy45-uracil diffraction data set before and after ellipsoidal truncation and anisotropic scaling performed by the UCLA diffraction anisotropy server (Strong et al., 2006). The structure was refined at 3.7 Å resolution.



Supplementary figure 19: Long-term stability analysis of UraA_{WT}, UraA_{G320P} and UraA_{P330G}. Long term stability of the three UraA variants was assessed by comparing the supernatant (S1) and pellet (P1) after ultracentrifugation with the fractions obtained after overnight incubation at room temperature (S2 and P2) on SDS-PAGE.

Supplementary table 1: UraA specific nanobodies. Listed are all individual nanobodies with the master plate indicated by the first characters of the nanobody name, the library the binder originated from, applied selection strategy and the antigen used for selection. The CDR3 sequence is shown and binders with identical CDR3 sequence indicated.

Nanobody	Library	Selection strategy	Antigen	CDR3 AA-sequence	CDR3 redundant Nanobodies
2H9	OXA	pre-panning	UraA _{WT}	YYCAAAYSSGYREAAYDYWGQGT	
3F3	OXA		UraA _{WT}	YYCAAKSDSMGSIYTTTAYKYWGQGT	
3F7	OXA	pre-panning	UraA _{WT}	YYCAAGYRGSYNTTEGFYWGQGT	7B1, 2G2
			UraA _{WT}		1A2, 17H8, 17D7, 17C7, 47H8, 47H7, 47G7, 47F9, 47F8, 47D7, 47B9, 47B8, 47E9, 3H3, 3H2, 3G2, 3G1, 3F2, 3E3, 3E1, 3D1, 3C2, 3C1, 3B2, 3A3, 2H2
3H1	OXA			YTCATKSSNDGTLCTGRVIFNSWGQGT	
3H7	OXA	pre-panning	UraA _{WT}	YYCAARWALGPVCLRRARDAYNDWGQGT	7B3, 7H8, 7E2, 7F9, 6C7, 3F9, 48G2, 6H9, 6H2
6A8	OXA	uracil	UraA _{WT}	YYCGADPRTWYGSNCDLGNLYGLDFRGKGT	7C7, 6E1, 6E9, 7D3
6B1	OXA		UraA _{WT}	YYCAAKRSSGALRDSGAYNDWGQGT	
6D3	OXA		UraA _{WT}	YYCAARFTGSGPWYRTDGYDYWGQGT	6D1
6E3	OXA		UraA _{WT}	YYCAAGYRGSYNNQGGYDYWGQGT	7D7, 21F8, 6A7
6G2	OXA		UraA _{WT}	YYCAAKWESIGAITTPRAYNSWAQGT	2G1, 2F9, 2D2, 2C8, 2B7, 3G7
6G7	OXA	uracil	UraA _{WT}	YYCGADPRTWYGSNCDLANLYGLDFRGKGT	
7A9	OXA	uracil, counterselection	UraA _{WT}	YYCGADPRTWYGSNCDLANLYGLDYWGKGT	7B2
7A10	NUBIA	uracil, counterselection	UraA _{WT}	YYCASKLSSGNLRDNGAYNYRQGT	6D6
			UraA _{WT}		7F6, 7F5, 7F10, 7A6, 7A4, 6A12, 6A11, 7H5, 7G11, 7G10, 6C6, 6C5, 6B10, 6F6, 6F4, 6F12, 7B12, 7E11, 7E10, 7B4, 7D6, 7D10, 7C12, 7E4, 7C10, 6B5, 6A10
7B6	NUBIA	uracil		YYCAARRYDFWPDSTYTYWGQGT	
7B8	OXA	uracil, counterselection	UraA _{WT}	YYCAAKRESIGMITTPRAYDSWGQGT	21G9, 21G7, 7E7, 20H8, 20E7, 20D9, 20C1
7C8	OXA	uracil, counterselection	UraA _{WT}	YYCASKLSSGDLRDIGAYNYWGQGT	
7F3	OXA	counterselection	UraA _{WT}	YYCAVRVPGSGKAWDPSTYDYWGQGT	
7F7	OXA	uracil, counterselection	UraA _{WT}	YYCAASWRGTLNKAEDYWGQGT	
7G8	OXA	uracil, counterselection	UraA _{WT}	YYCAAKRSGGALRDIGAYNDWGQGT	7A8
7G9	OXA	uracil, counterselection	UraA _{WT}	YYCATKRSSGDLRDIGAYNSWGQGT	
7H2	OXA	counterselection	UraA _{WT}	YYCATKSDSIGSIYTTTAYNYWGQGT	
17B12	NUBIA		UraA _{Cysless-1252C⁻} PEG-5000	YHCGTSAQGETCQRGKMTFGSYGPGT	
			UraA _{Cysless-1252C⁻} PEG-5000		17C3, 17C2, 17C1, 17B8, 17B2, 17B1, 17A9, 17A8, 17A7, 17A3, 17A1, 17C9, 17H3, 17H2, 17G9, 17G8, 17G7, 17G1, 17F7, 17F2, 17F1, 17E7, 17E3, 17E2, 17E1, 17D9, 17H9, 17H7
17D3	OXA			YYCGAVSSAQVCAGKLVFHSWGKGT	
17F3	OXA		UraA _{Cysless-1252C⁻} PEG-5000	YYCAGRPGTCFLATRFDSWGKGT	17D1, 17H1
17F11	NUBIA		UraA _{Cysless-1252C⁻} PEG-5000	YYCANVDYGM DYWGKGT	
20C3	OXA		UraA _{WT}	YYCAATFSPGYSSARAYDYWGQGT	
20G1	OXA		UraA _{WT}	YYCAAKSDSIGSIYTTTNYNNWGQGT	
21C1	OXA	counterselection	UraA _{WT}	YYCGADPRTWYGSNCDLGNLYGLDYWGKGT	
21F7	OXA	uracil, counterselection	UraA _{WT}	YYCAVKWDSRGPWTSTYIEYWGQGT	

Appendix A

50 mM buffer	Mg-acetate pH 4.5	Na-cacodylate pH 5.5	ADA pH 6.5	Hepes pH 7.4	Tris-HCl pH 8.4	glycine pH 9.4	Mg-acetate pH 4.5	Na-cacodylate pH 5.5	ADA pH 6.5	Hepes pH 7.4	Tris-HCl pH 8.4	glycine pH 9.4	
PEG400 (v/v)	1	2	3	4	5	6	7	8	9	10	11	12	GS056
18	1 M sodium chloride						150 mM sodium chloride						A
22													B
26													C
30													D
34													E
38													F
42													G
46													H

50 mM buffer	Mg-acetate pH 4.5	Na-cacodylate pH 5.5	ADA pH 6.5	Hepes pH 7.4	Tris-HCl pH 8.4	glycine pH 9.4	Mg-acetate pH 4.5	Na-cacodylate pH 5.5	ADA pH 6.5	Hepes pH 7.4	Tris-HCl pH 8.4	glycine pH 9.4	
PEG400 (v/v)	1	2	3	4	5	6	7	8	9	10	11	12	GS057
18	200 mM ammonium sulfate						50 mM magnesium acetate						A
22													B
26													C
30													D
34													E
38													F
42													G
46													H

50 mM buffer	Mg-acetate pH 4.5	Na-cacodylate pH 5.5	ADA pH 6.5	Hepes pH 7.4	Tris-HCl pH 8.4	glycine pH 9.4	Mg-acetate pH 4.5	Na-cacodylate pH 5.5	ADA pH 6.5	Hepes pH 7.4	Tris-HCl pH 8.4	glycine pH 9.4	
PEG400 (v/v)	1	2	3	4	5	6	7	8	9	10	11	12	GS058
18	500 mM potassium chloride						200 mM calcium chloride						A
22													B
26													C
30													D
34													E
38													F
42													G
46													H

50 mM buffer	Mg-acetate pH 4.5	Na-cacodylate pH 5.5	ADA pH 6.5	Hepes pH 7.4	Tris-HCl pH 8.4	glycine pH 9.4	Mg-acetate pH 4.5	Na-cacodylate pH 5.5	ADA pH 6.5	Hepes pH 7.4	Tris-HCl pH 8.4	glycine pH 9.4	
PEG400 (v/v)	1	2	3	4	5	6	7	8	9	10	11	12	GS059
18	200 mM ammonium formate						50 mM zinc acetate		100 mM potassium iodide				A
22													B
26													C
30													D
34													E
38													F
42													G
46													H

50 mM buffer	Mg-acetate pH 4.5	Na-cacodylate pH 5.5	ADA pH 6.5	Hepes pH 7.4	Tris-HCl pH 8.4	glycine pH 9.4	MES pH 6.5	Na-cacodylate pH 5.5	ADA pH 6.5	Hepes pH 7.4	Tris-HCl pH 8.4	glycine pH 9.4	
PEG400 (v/v)	1	2	3	4	5	6	7	8	9	10	11	12	GS060
18	no salt						100 mM potassium sodium tartrate						A
22													B
26													C
30													D
34													E
38													F
42													G
46													H

50 mM buffer	Mg-acetate pH 4.5	Na-cacodylate pH 5.5	ADA pH 6.5	Hepes pH 7.4	Tris-HCl pH 8.4	glycine pH 9.4	Mg-acetate pH 4.5	Na-cacodylate pH 5.5	ADA pH 6.5	Hepes pH 7.4	Tris-HCl pH 8.4	glycine pH 9.4	
PEG400 (v/v)	1	2	3	4	5	6	7	8	9	10	11	12	GS061
18	200 mM potassium dihydrogen phosphate						100 mM lithium sulfate 100 mM sodium sulfate						A
22													B
26													C
30													D
34	100 mM potassium dihydrogen phosphate						50 mM lithium sulfate 50 mM sodium sulfate						E
38													F
42													G
46													H

Mac400 crystallization screen composition

Appendix B

selection path	immobilization	selection round 1				selection round 2				selection round 3						
		phage input	antigen	selection bias	enrichment	masterplate	phage input	antigen	selection bias	enrichment	masterplate	phage input	antigen	selection bias	enrichment	masterplate
1	neutravidin	1E11 OXA	UraA-wt	no	1.0	MP001_1-3	1E11 output	UraA-wt	no	25.7	MP002_1-3	1E11 output	UraA-wt	no	818.0	MP003_1-3
2	neutravidin	1E11 NUBIA	UraA-wt	no	0.7	MP001_4-6	1E11 output	UraA-wt	no	5.5	MP002_4-6	1E11 output	UraA-wt	no	0.4	MP003_4-6
3	neutravidin	1E11 OXA	UraA-wt	pp	1.0	MP001_7-9	1E11 output	UraA-wt	no	55.0	MP002_7-9	1E11 output	UraA-wt	no	314.0	MP003_7-9
4	neutravidin	1E11 NUBIA	UraA-wt	pp	0.3	MP001_10-12	1E11 output	UraA-wt	no	1.0	MP002_10-12	1E11 output	UraA-wt	no	0.8	MP003_10-12
5	neutravidin	1E12 OXA	UraA-wt	no	2.6	MP020_1-3	4E10 output	UraA-wt	no	4000.0	MP006_1-3	4E10 output	UraA-wt	no	4000.0	MP007_1-3
6	neutravidin	1E12 NUBIA	UraA-wt	no	1.2	MP020_4-6	2E11 output	UraA-wt	no	33.0	MP006_4-6	2E11 output	UraA-wt	no	33.0	MP007_4-6
7	neutravidin	1E12 OXA	UraA-wt	s	1.3	MP020_7-9	4E10 output	UraA-wt	s	12000.0	MP006_7-9	4E10 output	UraA-wt	s	12000.0	MP007_7-9
8	neutravidin	1E12 NUBIA	UraA-wt	s	1.0	MP020_10-12	1E11 output	UraA-wt	s	460.0	MP006_10-12	1E11 output	UraA-wt	s	460.0	MP007_10-12
9	neutravidin	1E12 OXA	UraA-wt	cs	1.4	MP021_1-3	1E11 output	UraA-wt	cs	650.0	MP007_1-3	1E11 output	UraA-wt	cs	650.0	MP008_1-3
10	neutravidin	1E12 NUBIA	UraA-wt	cs	1.3	MP021_4-6	6E10 output	UraA-wt	cs	86.0	MP007_4-6	6E10 output	UraA-wt	cs	86.0	MP008_4-6
11	neutravidin	1E12 OXA	UraA-wt	s,cs	6.0	MP021_7-9	1E11 output	UraA-wt	s,cs	7000.0	MP007_7-9	1E11 output	UraA-wt	s,cs	7000.0	MP008_7-9
12	neutravidin	1E12 NUBIA	UraA-wt	s,cs	0.9	MP021_10-12	8E10 output	UraA-wt	s,cs	214.0	MP007_10-12	8E10 output	UraA-wt	s,cs	214.0	MP008_10-12
13	neutravidin	1E12 OXA	UraA1252CPEG5000	no	1.2		2E11 output	UraA1252CPEG5000	no	4.5	MP047_1-3	2E11 output	UraA1252CPEG5000	no	4.5	MP048_1-3
14	neutravidin	1E12 NUBIA	UraA1252CPEG5001	no	1.0		2E11 output	UraA1252CPEG5001	no	1.0	MP047_4-6	2E11 output	UraA1252CPEG5001	no	1.0	MP048_4-6
15	neutravidin	1E12 OXA	UraA1252CPEG5002	s	0.7		4E11 output	UraA1252CPEG5002	s	5.0	MP047_7-9	4E11 output	UraA1252CPEG5002	s	5.0	MP048_7-9
16	neutravidin	1E12 NUBIA	UraA1252CPEG5003	s	0.5		3E11 output	UraA1252CPEG5003	s	0.3	MP047_10-12	3E11 output	UraA1252CPEG5003	s	0.3	MP048_10-12
17	neutravidin	1E12 OXA	UraA1252CPEG5004	cs	6.0		2E11 output	UraA1252CPEG5004	cs	2.0	MP048_1-3	2E11 output	UraA1252CPEG5004	cs	2.0	MP049_1-3
18	neutravidin	1E12 NUBIA	UraA1252CPEG5005	cs	1.0		2E11 output	UraA1252CPEG5005	cs	0.5	MP048_4-6	2E11 output	UraA1252CPEG5005	cs	0.5	MP049_4-6
19	neutravidin	1E12 OXA	UraA1252CPEG5006	s,cs	3.0		2E11 output	UraA1252CPEG5006	s,cs	1.5	MP048_7-9	2E11 output	UraA1252CPEG5006	s,cs	1.5	MP049_7-9
20	neutravidin	1E12 NUBIA	UraA1252CPEG5007	s,cs	0.3		2E11 output	UraA1252CPEG5007	s,cs	1.0	MP048_10-12	2E11 output	UraA1252CPEG5007	s,cs	1.0	MP049_10-12
21	solid phase	1E12 OXA	UraA-wt	no	10.0		3E10 output	UraA-wt	no	50.0		3E10 output	UraA-wt	no	50.0	
22	solid phase	1E12 NUBIA	UraA-wt	no	1.3		3E11 output	UraA-wt	no	24.0		3E11 output	UraA-wt	no	24.0	
23	solid phase	1E12 OXA	UraA-wt	s	8.0		6E10 output	UraA-wt	s	14.0		6E10 output	UraA-wt	s	14.0	
24	solid phase	1E12 NUBIA	UraA-wt	s	9.0		1E11 output	UraA-wt	s	150.0		1E11 output	UraA-wt	s	150.0	
25	solid phase	1E12 OXA	UraA-wt	cs	4.7		6E10 output	UraA-wt	cs	163.0		6E10 output	UraA-wt	cs	163.0	
26	solid phase	1E12 NUBIA	UraA-wt	cs	1.7		3E10 output	UraA-wt	cs	4.0		3E10 output	UraA-wt	cs	4.0	
27	solid phase	1E12 OXA	UraA-wt	s,cs	2.5		3E10 output	UraA-wt	s,cs	90.0		3E10 output	UraA-wt	s,cs	90.0	
28	solid phase	1E12 NUBIA	UraA-wt	s,cs	10.0		9E10 output	UraA-wt	s,cs	20.0		9E10 output	UraA-wt	s,cs	20.0	
29	solid phase	1E12 OXA	UraA1252CPEG5000	no	10.0		2E11 output	UraA1252CPEG5000	no	6.0		2E11 output	UraA1252CPEG5000	no	1500.0	MP017_1-3
30	solid phase	1E12 NUBIA	UraA1252CPEG5001	no	0.5		9E10 output	UraA1252CPEG5001	no	5.0		1E11 output	UraA1252CPEG5001	no	3000.0	MP017_4-6
31	solid phase	1E12 OXA	UraA1252CPEG5002	s	5.0		9E10 output	UraA1252CPEG5002	s	30.0		2E10 output	UraA1252CPEG5002	s	1800000.0	MP017_7-9
32	solid phase	1E12 NUBIA	UraA1252CPEG5003	s	2.0		6E10 output	UraA1252CPEG5003	s	4.0		5E9 output	UraA1252CPEG5003	s	300000.0	MP017_10-12
33	solid phase	1E12 OXA	UraA1252CPEG5004	cs	0.7		3E10 output	UraA1252CPEG5004	cs	5.0		2E10 output	UraA1252CPEG5004	cs	150.0	MP018_1-3
34	solid phase	1E12 NUBIA	UraA1252CPEG5005	cs	0.3		2E11 output	UraA1252CPEG5005	cs	3.0		3E11 output	UraA1252CPEG5005	cs	3000.0	MP018_4-6
35	solid phase	1E12 OXA	UraA1252CPEG5006	s,cs	0.6		3E10 output	UraA1252CPEG5006	s,cs	5.0		1E9 output	UraA1252CPEG5006	s,cs	1000.0	MP018_7-9
36	solid phase	1E12 NUBIA	UraA1252CPEG5007	s,cs	6.0		3E10 output	UraA1252CPEG5007	s,cs	3.0		1E10 output	UraA1252CPEG5007	s,cs	900000.0	MP018_10-12

Selection bias was introduced by pre-panning with the crosslinked UraA-Avi-L80C-M143C mutant (p), by addition of 1 mM uracil (s) or by counterselection with UraA-cysless-M143CPEG5000 (cs)

Phage display selection overview presenting all 36 selection paths and corresponding information.

References

- Abergel, C. "Molecular Replacement: Tricks and Treats." *Acta Crystallogr D Biol Crystallogr* 69, no. Pt 11 (2013): 2167-73.
- Abramson, Jeff, Irina Smirnova, Vladimir Kasho, Gillian Verner, H. Ronald Kaback and So Iwata. "Structure and Mechanism of the Lactose Permease of *Escherichia Coli*." *Science* 301, no. 5633 (2003): 610.
- Afonine, P. V., R. W. Grosse-Kunstleve, N. Echols, J. J. Headd, N. W. Moriarty, M. Mustyakimov, T. C. Terwilliger, A. Urzhumtsev, P. H. Zwart and P. D. Adams. "Towards Automated Crystallographic Structure Refinement with Phenix.Refine." *Acta Crystallogr D Biol Crystallogr* 68, no. Pt 4 (2012): 352-67.
- Akyuz, Nurunisa, Elka R. Georgieva, Zhou Zhou, Sebastian Stolzenberg, Michel A. Cuendet, George Khelashvili, Roger B. Altman, Daniel S. Terry, Jack H. Freed, Harel Weinstein, Olga Boudker and Scott C. Blanchard. "Transport Domain Unlocking Sets the Uptake Rate of an Aspartate Transporter." *Nature* 518, no. 7537 (2015): 68-73.
- Alexandrov, A. I., M. Mileni, E. Y. Chien, M. A. Hanson and R. C. Stevens. "Microscale Fluorescent Thermal Stability Assay for Membrane Proteins." *Structure* 16, no. 3 (2008): 351-9.
- Alguel, Y., S. Amillis, J. Leung, G. Lambrinidis, S. Capaldi, N. J. Scull, G. Craven, S. Iwata, A. Armstrong, E. Mikros, G. Diallinas, A. D. Cameron and B. Byrne. "Structure of Eukaryotic Purine/H(+) Symporter Uapa Suggests a Role for Homodimerization in Transport Activity." *Nat Commun* 7, (2016): 11336.
- Amillis, Sotiris and Marina Koukaki. "Substitution F569s Converts Uapa, a Specific Uric Acid-Xanthine Transporter, into a Broad Specificity Transporter for Purine-Related Solutes." *Journal of molecular biology* 313, (2001): 765-74.
- Amir Shaghghi, M., C. N. Bernstein, A. Serrano Leon, H. El-Gabalawy and P. Eck. "Polymorphisms in the Sodium-Dependent Ascorbate Transporter Gene Slc23a1 Are Associated with Susceptibility to Crohn Disease." *Am J Clin Nutr* 99, no. 2 (2014): 378-83.
- Andersen, P. S., D. Frees, R. Fast and B. Mygind. "Uracil Uptake in *Escherichia Coli* K-12: Isolation of Uraa Mutants and Cloning of the Gene." *Journal of bacteriology* 177, no. 8 (1995): 2008-2013.
- Arakawa, Takatoshi, Takami Kobayashi-Yurugi, Yilmaz Alguel, Hiroko Iwanari, Hinako Hatae, Momi Iwata, Yoshito Abe, Tomoya Hino, Chiyo Ikeda-Suno, Hiroyuki Kuma, Dongchon Kang, Takeshi Murata, Takao Hamakubo, Alexander D. Cameron, Takuya Kobayashi, Naotaka Hamasaki and So Iwata. "Crystal Structure of the Anion Exchanger Domain of Human Erythrocyte Band 3." *Science* 350, no. 6261 (2015): 680.
- Arkhipova, V., A. Guskov and D. J. Slotboom. "Structural Ensemble of a Glutamate Transporter Homologue in Lipid Nanodisc Environment." *Nat Commun* 11, no. 1 (2020): 998.
- Arnold, F. M., M. S. Weber, I. Gonda, M. J. Gallenito, S. Adenau, P. Eglhoff, I. Zimmermann, C. A. J. Hutter, L. M. Hurlimann, E. E. Peters, J. Piel, G. Meloni, O. Medalia and M. A. Seeger. "The Abc Exporter Irtab Imports and Reduces Mycobacterial Siderophores." *Nature* 580, no. 7803 (2020): 413-417.

- Baba, T., T. Ara, M. Hasegawa, Y. Takai, Y. Okumura, M. Baba, K. A. Datsenko, M. Tomita, B. L. Wanner and H. Mori. "Construction of Escherichia Coli K-12 in-Frame, Single-Gene Knockout Mutants: The Keio Collection." *Mol Syst Biol* 2, (2006): 2006 0008.
- Babaev, V. R., L. Li, S. Shah, S. Fazio, M. F. Linton and J. M. May. "Combined Vitamin C and Vitamin E Deficiency Worsens Early Atherosclerosis in Apolipoprotein E-Deficient Mice." *Arterioscler Thromb Vasc Biol* 30, no. 9 (2010): 1751-7.
- Bai, N., H. Roder, A. Dickson and J. Karanicolas. "Isothermal Analysis of Thermofluor Data Can Readily Provide Quantitative Binding Affinities." *Sci Rep* 9, no. 1 (2019): 2650.
- Bannas, Peter, Julia Hambach and Friedrich Koch-Nolte. "Nanobodies and Nanobody-Based Human Heavy Chain Antibodies as Antitumor Therapeutics." *Frontiers in immunology* 8, (2017): 1603-1603.
- Barik, Sailen. "Site-Directed Mutagenesis by Double Polymerase Chain Reaction." In *Pcr Protocols: Current Methods and Applications*, edited by Bruce A. White, 277-286. Totowa, NJ: Humana Press, 1993.
- Barth, Katja, Susanne Hank, Philipp E. Spindler, Thomas F. Prisner, Robert Tampé and Benesh Joseph. "Conformational Coupling and Trans-Inhibition in the Human Antigen Transporter Ortholog Tmrab Resolved with Dipolar Epr Spectroscopy." *Journal of the American Chemical Society* 140, no. 13 (2018): 4527-4533.
- Beghein, E. and J. Gettemans. "Nanobody Technology: A Versatile Toolkit for Microscopic Imaging, Protein-Protein Interaction Analysis, and Protein Function Exploration." *Front Immunol* 8, (2017): 771.
- Bianchi, F., J. S. Klooster, S. J. Ruiz, K. Luck, T. Pols, I. L. Urbatsch and B. Poolman. "Asymmetry in Inward- and Outward-Affinity Constant of Transport Explain Unidirectional Lysine Flux in Saccharomyces Cerevisiae." *Sci Rep* 6, (2016): 31443.
- Bolla, J. R., C. C. Su, J. A. Delmar, A. Radhakrishnan, N. Kumar, T. H. Chou, F. Long, K. R. Rajashankar and E. W. Yu. "Crystal Structure of the Alcanivorax Borkumensis Ydah Transporter Reveals an Unusual Topology." *Nat Commun* 6, (2015): 6874.
- Bosshart, P. D. and D. Fotiadis. "Secondary Active Transporters." *Subcell Biochem* 92, (2019): 275-299.
- Botou, M., P. Lazou, K. Papakostas, G. Lambrinidis, T. Evangelidis, E. Mikros and S. Frillingos. "Insight on Specificity of Uracil Permeases of the Nat/Ncs2 Family from Analysis of the Transporter Encoded in the Pyrimidine Utilization Operon of Escherichia Coli." *Mol Microbiol* 108, no. 2 (2018): 204-219.
- Boudker, O., R. M. Ryan, D. Yernool, K. Shimamoto and E. Gouaux. "Coupling Substrate and Ion Binding to Extracellular Gate of a Sodium-Dependent Aspartate Transporter." *Nature* 445, no. 7126 (2007): 387-93.
- Bräuer, Philipp, Joanne L. Parker, Andreas Gerondopoulos, Iwan Zimmermann, Markus A. Seeger, Francis A. Barr and Simon Newstead. "Structural Basis for Ph-Dependent Retrieval of Er Proteins from the Golgi by the Kdel Receptor." *Science* 363, no. 6431 (2019): 1103.
- Burzle, M., Y. Suzuki, D. Ackermann, H. Miyazaki, N. Maeda, B. Clemençon, R. Burrier and M. A. Hediger. "The Sodium-Dependent Ascorbic Acid Transporter Family Slc23." *Mol Aspects Med* 34, no. 2-3 (2013): 436-54.
- Byrne, B. "It Takes Two to Transport Via an Elevator." *Cell Res* 27, no. 8 (2017): 965-966.
- Carpenter, E. P., K. Beis, A. D. Cameron and S. Iwata. "Overcoming the Challenges of Membrane Protein Crystallography." *Curr Opin Struct Biol* 18, no. 5 (2008): 581-6.
- Casadaban, Malcolm J. and Stanley N. Cohen. "Analysis of Gene Control Signals by DNA Fusion and Cloning in Escherichia Coli." *Journal of Molecular Biology* 138, no. 2 (1980): 179-207.
- Chang, Y. N. and E. R. Geertsma. "The Novel Class of Seven Transmembrane Segment Inverted Repeat Carriers." *Biol Chem* 398, no. 2 (2017): 165-174.

- Chang, Y. N., E. A. Jaumann, K. Reichel, J. Hartmann, D. Oliver, G. Hummer, B. Joseph and E. R. Geertsma. "Structural Basis for Functional Interactions in Dimers of Slc26 Transporters." *Nat Commun* 10, no. 1 (2019): 2032.
- Cianci, M., G. Bourenkov, G. Pompidor, I. Karpics, J. Kallio, I. Bento, M. Roessle, F. Cipriani, S. Fiedler and T. R. Schneider. "P13, the Embl Macromolecular Crystallography Beamline at the Low-Emittance Petra Iii Ring for High- and Low-Energy Phasing with Variable Beam Focusing." *J Synchrotron Radiat* 24, no. Pt 1 (2017): 323-332.
- Coincon, M., P. Uzdavinys, E. Nji, D. L. Dotson, I. Winkelmann, S. Abdul-Hussein, A. D. Cameron, O. Beckstein and D. Drew. "Crystal Structures Reveal the Molecular Basis of Ion Translocation in Sodium/Proton Antiporters." *Nat Struct Mol Biol* 23, no. 3 (2016): 248-55.
- Coleman, J. A., D. Yang, Z. Zhao, P. C. Wen, C. Yoshioka, E. Tajkhorshid and E. Gouaux. "Serotonin Transporter-Ibogaine Complexes Illuminate Mechanisms of Inhibition and Transport." *Nature* 569, no. 7754 (2019): 141-145.
- Coudray, N., L. Seyler S, R. Lasala, Z. Zhang, K. M. Clark, M. E. Dumont, A. Rohou, O. Beckstein and D. L. Stokes. "Structure of the Slc4 Transporter Bor1p in an Inward-Facing Conformation." *Protein Sci* 26, no. 1 (2017): 130-145.
- Crooks, Gavin E., Gary Hon, John-Marc Chandonia and Steven E. Brenner. "Weblogo: A Sequence Logo Generator." *Genome research* 14, no. 6 (2004): 1188-1190.
- Dallos, Peter and Bernd Fakler. "Prestin, a New Type of Motor Protein." *Nature Reviews Molecular Cell Biology* 3, no. 2 (2002): 104-111.
- Dalpia, A., B. Pavan, M. Scaglianti, F. Vitali, F. Bortolotti, C. Biondi, A. Scatturin and S. Manfredini. "Vitamin C and 6-Amino-Vitamin C Conjugates of Diclofenac: Synthesis and Evaluation." *Int J Pharm* 291, no. 1-2 (2005): 171-81.
- Dalpia, Alessandro, Barbara Pavan, Martina Scaglianti, Federica Vitali, Fabrizio Bortolotti, Carla Biondi, Angelo Scatturin, Sergio Tanganelli, Luca Ferraro, Puttur Prasad and Stefano Manfredini. "Transporter-Mediated Effects of Diclofenamic Acid and Its Ascorbyl Pro-Drug in the in Vivo Neurotropic Activity of Ascorbyl Nipecotic Acid Conjugate." *Journal of Pharmaceutical Sciences* 93, no. 1 (2004): 78-85.
- De Genst, E., K. Silence, K. Decanniere, K. Conrath, R. Loris, J. Kinne, S. Muyldermans and L. Wyns. "Molecular Basis for the Preferential Cleft Recognition by Dromedary Heavy-Chain Antibodies." *Proc Natl Acad Sci U S A* 103, no. 12 (2006): 4586-91.
- de Jong, T. M., A. Jochens, Y. Jockel-Schneider, I. Harks, H. Dommisch, C. Graetz, F. Flachsbar, I. Staufenbiel, J. Eberhard, M. Folwaczny, B. Noack, J. Meyle, P. Eickholz, C. Gieger, H. Grallert, W. Lieb, A. Franke, A. Nebel, S. Schreiber, C. Doerfer, S. Jepsen, C. Bruckmann, U. van der Velden, B. G. Loos and A. S. Schaefer. "Slc23a1 Polymorphism Rs6596473 in the Vitamin C Transporter Svct1 Is Associated with Aggressive Periodontitis." *J Clin Periodontol* 41, no. 6 (2014): 531-40.
- Denhardt, D. T. "The Single-Stranded DNA Phages." *CRC Crit Rev Microbiol* 4, no. 2 (1975): 161-223.
- Deschaght, Pieter, Ana Paula Vintém, Marc Logghe, Miguel Conde, David Felix, Rob Mensink, Juliana Gonçalves, Jorn Audiens, Yanik Bruynooghe, Rita Figueiredo, Diana Ramos, Robbe Tanghe, Daniela Teixeira, Liesbeth Van de Ven, Catelijne Stortelers and Bruno Dombrecht. "Large Diversity of Functional Nanobodies from a Camelid Immune Library Revealed by an Alternative Analysis of Next-Generation Sequencing Data." *Frontiers in Immunology* 8, no. 420 (2017).
- Diallinas, G. "Transceptors as a Functional Link of Transporters and Receptors." *Microb Cell* 4, no. 3 (2017): 69-73.
- Diallinas, G. and C. Scazzocchio. "A Gene Coding for the Uric Acid-Xanthine Permease of *Aspergillus nidulans*: Inactivational Cloning, Characterization, and Sequence of a Cis-Acting Mutation." *Genetics* 122, no. 2 (1989): 341-350.
- Dmitriev, O. Y., S. Lutsenko and S. Muyldermans. "Nanobodies as Probes for Protein Dynamics in Vitro and in Cells." *J Biol Chem* 291, no. 8 (2016): 3767-75.

- Don, R. H., P. T. Cox, B. J. Wainwright, K. Baker and J. S. Mattick. "'Touchdown' Pcr to Circumvent Spurious Priming During Gene Amplification." *Nucleic acids research* 19, no. 14 (1991): 4008-4008.
- Drew, D. and O. Boudker. "Shared Molecular Mechanisms of Membrane Transporters." *Annu Rev Biochem* 85, (2016): 543-72.
- Drew, David, Gunnar Heijne, Pär Nordlund and Jan-Willem de Gier. "Green Fluorescent Protein as an Indicator to Monitor Membrane Protein Overexpression in Escherichia Coli." *FEBS letters* 507, (2001): 220-4.
- Duell, E. J., L. Lujan-Barroso, C. Llivina, X. Munoz, M. Jenab, M. C. Boutron-Ruault, F. Clavel-Chapelon, A. Racine, H. Boeing, B. Buijsse, F. Canzian, T. Johnson, C. Dalgard, K. Overvad, A. Tjonneland, A. Olsen, S. C. Sanchez, E. Sanchez-Cantalejo, J. M. Huerta, E. Ardanaz, M. Dorronsoro, K. T. Khaw, R. C. Travis, A. Trichopoulou, D. Trichopoulos, S. Rafnsson, D. Palli, C. Sacerdote, R. Tumino, S. Panico, S. Grioni, H. B. Bueno-de-Mesquita, M. M. Ros, M. E. Numans, P. H. Peeters, D. Johansen, B. Lindkvist, M. Johansson, I. Johansson, G. Skeie, E. Weiderpass, T. Duarte-Salles, R. Stenling, E. Riboli, N. Sala and C. A. Gonzalez. "Vitamin C Transporter Gene (Slc23a1 and Slc23a2) Polymorphisms, Plasma Vitamin C Levels, and Gastric Cancer Risk in the Epic Cohort." *Genes Nutr* 8, no. 6 (2013): 549-60.
- Eisen, Herman N. and Gregory W. Siskind. "Variations in Affinities of Antibodies During the Immune Response*." *Biochemistry* 3, no. 7 (1964): 996-1008.
- Eisinger, M. L., A. R. Dorrbaum, H. Michel, E. Padan and J. D. Langer. "Ligand-Induced Conformational Dynamics of the Escherichia Coli Na(+)/H(+) Antiporter Nhaa Revealed by Hydrogen/Deuterium Exchange Mass Spectrometry." *Proc Natl Acad Sci U S A* 114, no. 44 (2017): 11691-11696.
- Emsley, Paul and Kevin Cowtan. "Coot: Model-Building Tools for Molecular Graphics." *Acta Crystallographica Section D* 60, no. 12 Part 1 (2004): 2126-2132.
- Erichsen, H. C., S. A. Engel, P. K. Eck, R. Welch, M. Yeager, M. Levine, A. M. Siega-Riz, A. F. Olshan and S. J. Chanock. "Genetic Variation in the Sodium-Dependent Vitamin C Transporters, Slc23a1, and Slc23a2 and Risk for Preterm Delivery." *Am J Epidemiol* 163, no. 3 (2006): 245-54.
- Erichsen, H. C., U. Peters, P. Eck, R. Welch, R. E. Schoen, M. Yeager, M. Levine, R. B. Hayes and S. Chanock. "Genetic Variation in Sodium-Dependent Vitamin C Transporters Slc23a1 and Slc23a2 and Risk of Advanced Colorectal Adenoma." *Nutr Cancer* 60, no. 5 (2008): 652-9.
- Fairhead, M. and M. Howarth. "Site-Specific Biotinylation of Purified Proteins Using Bira." *Methods Mol Biol* 1266, (2015): 171-84.
- Forrest, L. R., R. Kramer and C. Ziegler. "The Structural Basis of Secondary Active Transport Mechanisms." *Biochim Biophys Acta* 1807, no. 2 (2011): 167-88.
- Forsstrom, B., B. B. Axnas, J. Rockberg, H. Danielsson, A. Bohlin and M. Uhlen. "Dissecting Antibodies with Regards to Linear and Conformational Epitopes." *PLoS One* 10, no. 3 (2015): e0121673.
- Gao, K., R. Oerlemans and M. R. Groves. "Theory and Applications of Differential Scanning Fluorimetry in Early-Stage Drug Discovery." *Biophys Rev* 12, no. 1 (2020): 85-104.
- Gao, P., H. Zhang, R. Dinavahi, F. Li, Y. Xiang, V. Raman, Z. M. Bhujwala, D. W. Felsher, L. Cheng, J. Pevsner, L. A. Lee, G. L. Semenza and C. V. Dang. "Hif-Dependent Antitumorigenic Effect of Antioxidants in Vivo." *Cancer Cell* 12, no. 3 (2007): 230-8.
- Garaeva, A. A. and D. J. Slotboom. "Elevator-Type Mechanisms of Membrane Transport." *Biochem Soc Trans* 48, no. 3 (2020): 1227-1241.
- Geertsma, E. R., Y. N. Chang, F. R. Shaik, Y. Neldner, E. Pardon, J. Steyaert and R. Dutzler. "Structure of a Prokaryotic Fumarate Transporter Reveals the Architecture of the Slc26 Family." *Nat Struct Mol Biol* 22, no. 10 (2015): 803-8.
- Geertsma, E. R. and R. Dutzler. "A Versatile and Efficient High-Throughput Cloning Tool for Structural Biology." *Biochemistry* 50, no. 15 (2011): 3272-8.
- Geertsma, E. R., M. Groeneveld, D. J. Slotboom and B. Poolman. "Quality Control of Overexpressed Membrane Proteins." *Proc Natl Acad Sci U S A* 105, no. 15 (2008): 5722-7.

- Geertsma, E. R., N. A. Nik Mahmood, G. K. Schuurman-Wolters and B. Poolman. "Membrane Reconstitution of Abc Transporters and Assays of Translocator Function." *Nat Protoc* 3, no. 2 (2008): 256-66.
- Götzke, Hansjörg, Markus Kilisch, Markel Martínez-Carranza, Shama Sograte-Idrissi, Abirami Rajavel, Thomas Schlichthaerle, Niklas Engels, Ralf Jungmann, Pål Stenmark, Felipe Opazo and Steffen Frey. "The Alfa-Tag Is a Highly Versatile Tool for Nanobody-Based Bioscience Applications." *Nature Communications* 10, no. 1 (2019): 4403.
- Gournas, C., I. Papageorgiou and G. Diallinas. "The Nucleobase-Ascorbate Transporter (Nat) Family: Genomics, Evolution, Structure-Function Relationships and Physiological Role." *Mol Biosyst* 4, no. 5 (2008): 404-16.
- Greenberg, Andrew S., David Avila, Marianne Hughes, Austin Hughes, E. Churchill McKinney and Martin F. Flajnik. "A New Antigen Receptor Gene Family That Undergoes Rearrangement and Extensive Somatic Diversification in Sharks." *Nature* 374, no. 6518 (1995): 168-173.
- Griffin, L. and A. Lawson. "Antibody Fragments as Tools in Crystallography." *Clinical and experimental immunology* 165, no. 3 (2011): 285-291.
- Guy, Drouin, Godin Jean-Remi and Page Benoit. "The Genetics of Vitamin C Loss in Vertebrates." *Current Genomics* 12, no. 5 (2011): 371-378.
- Guzman, L. M., D. Belin, M. J. Carson and J. Beckwith. "Tight Regulation, Modulation, and High-Level Expression by Vectors Containing the Arabinose Pbad Promoter." *Journal of Bacteriology* 177, no. 14 (1995): 4121.
- Hall, J. "A Simple Model for Determining Affinity from Irreversible Thermal Shifts." *Protein Sci* 28, no. 10 (2019): 1880-1887.
- Hamers-Casterman, C., T. Atarhouch, S. Muyldermans, G. Robinson, C. Hammers, E. Bajyana Songa, N. Bendahman and R. Hammers. "Naturally Occurring Antibodies Devoid of Light Chains." *Nature* 363, no. 6428 (1993): 446-448.
- Hamiaux, C., R. S. Drummond, B. J. Janssen, S. E. Ledger, J. M. Cooney, R. D. Newcomb and K. C. Snowden. "Dad2 Is an Alpha/Beta Hydrolase Likely to Be Involved in the Perception of the Plant Branching Hormone, Strigolactone." *Curr Biol* 22, no. 21 (2012): 2032-6.
- Harder, D. and D. Fotiadis. "Measuring Substrate Binding and Affinity of Purified Membrane Transport Proteins Using the Scintillation Proximity Assay." *Nat Protoc* 7, no. 9 (2012): 1569-78.
- Harry de Koning, George Diallinas. "Nucleobase Transporters." *Molecular Membrane Biology* 17, no. 2 (2000): 75-94.
- Hartley, J. L., G. F. Temple and M. A. Brasch. "DNA Cloning Using in Vitro Site-Specific Recombination." *Genome Res* 10, no. 11 (2000): 1788-95.
- Hayward, Steven and Herman J. C. Berendsen. "Systematic Analysis of Domain Motions in Proteins from Conformational Change: New Results on Citrate Synthase and T4 Lysozyme." *Proteins: Structure, Function, and Bioinformatics* 30, no. 2 (1998): 144-154.
- Hediger, M. A., M. F. Romero, J. B. Peng, A. Rolfs, H. Takanaga and E. A. Bruford. "The Abcs of Solute Carriers: Physiological, Pathological and Therapeutic Implications of Human Membrane Transport Protein Introduction." *Pflugers Arch* 447, no. 5 (2004): 465-8.
- Herzik, M. A., Jr., M. Wu and G. C. Lander. "High-Resolution Structure Determination of Sub-100 Kda Complexes Using Conventional Cryo-Em." *Nat Commun* 10, no. 1 (2019): 1032.
- Hirschi, M., Z. L. Johnson and S. Y. Lee. "Visualizing Multistep Elevator-Like Transitions of a Nucleoside Transporter." *Nature* 545, no. 7652 (2017): 66-70.
- Hirschi, Stephan and Dimitrios Fotiadis. "Purification of Membrane Proteins by Affinity Chromatography with on-Column Protease Cleavage." *Methods in molecular biology (Clifton, N.J.)* 2127, (2020): 139-150.
- Ho, B. K. and F. Gruswitz. "Hollow: Generating Accurate Representations of Channel and Interior Surfaces in Molecular Structures." *BMC Struct Biol* 8, (2008): 49.

- Ho, Bosco K. and Robert Brasseur. "The Ramachandran Plots of Glycine and Pre-Proline." *BMC Structural Biology* 5, no. 1 (2005): 14.
- Hofmann, S., D. Janulienė, A. R. Mehdipour, C. Thomas, E. Stefan, S. Bruchert, B. T. Kuhn, E. R. Geertsma, G. Hummer, R. Tampe and A. Moeller. "Conformation Space of a Heterodimeric Abc Exporter under Turnover Conditions." *Nature* 571, no. 7766 (2019): 580-583.
- Hoglund, P. J., K. J. Nordstrom, H. B. Schioth and R. Fredriksson. "The Solute Carrier Families Have a Remarkably Long Evolutionary History with the Majority of the Human Families Present before Divergence of Bilaterian Species." *Mol Biol Evol* 28, no. 4 (2011): 1531-41.
- Holliger, P. and P. J. Hudson. "Engineered Antibody Fragments and the Rise of Single Domains." *Nat Biotechnol* 23, no. 9 (2005): 1126-36.
- Holzhtuter, K. and E. R. Geertsma. "Functional (Un)Cooperativity in Elevator Transport Proteins." *Biochem Soc Trans* 48, no. 3 (2020): 1047-1055.
- Hu, N. J., S. Iwata, A. D. Cameron and D. Drew. "Crystal Structure of a Bacterial Homologue of the Bile Acid Sodium Symporter Asbt." *Nature* 478, no. 7369 (2011): 408-11.
- Hu, Y., C. Liu and S. Muyldermans. "Nanobody-Based Delivery Systems for Diagnosis and Targeted Tumor Therapy." *Front Immunol* 8, (2017): 1442.
- Huang, W., M. Masureel, Q. Qu, J. Janetzko, A. Inoue, H. E. Kato, M. J. Robertson, K. C. Nguyen, J. S. Glenn, G. Skiniotis and B. K. Kobilka. "Structure of the Neurotensin Receptor 1 in Complex with Beta-Arrestin 1." *Nature* 579, no. 7798 (2020): 303-308.
- Huang, Yafei, M. Joanne Lemieux, Jinmei Song, Manfred Auer and Da-Neng Wang. "Structure and Mechanism of the Glycerol-3-Phosphate Transporter from *Escherichia Coli*." *Science* 301, no. 5633 (2003): 616.
- Hutter, C. A. J., M. H. Timachi, L. M. Hurlimann, I. Zimmermann, P. Egloff, H. Goddeke, S. Kucher, S. Stefanic, M. Karttunen, L. V. Schafer, E. Bordignon and M. A. Seeger. "The Extracellular Gate Shapes the Energy Profile of an Abc Exporter." *Nat Commun* 10, no. 1 (2019): 2260.
- Iwata, So, Christian Ostermeier, Bernd Ludwig and Hartmut Michel. "Structure at 2.8 Å Resolution of Cytochrome C Oxidase from *Paracoccus Denitrificans*." *Nature* 376, no. 6542 (1995): 660-669.
- Jardetzky, Oleg. "Simple Allosteric Model for Membrane Pumps." *Nature* 211, no. 5052 (1966): 969-970.
- Jeckelmann, J. M., D. Harder, Z. Ucurum and D. Fotiadis. "2d and 3d Crystallization of a Bacterial Homologue of Human Vitamin C Membrane Transport Proteins." *J Struct Biol* 188, no. 1 (2014): 87-91.
- Joshi, Aditya and Ana Pajor. "Identification of Conformationally Sensitive Amino Acids in the Na⁺/Dicarboxylate Symporter (Sdcs) †." *Biochemistry* 48, (2009): 3017-24.
- Ju, Man-Seok, Sung-Won Min, Sang Min Lee, Hyeong Sun Kwon, Jong Chan Park, Ji Chul Lee and Sang Taek Jung. "A Synthetic Library for Rapid Isolation of Humanized Single-Domain Antibodies." *Biotechnology and Bioengineering* 22, no. 3 (2017): 239-247.
- Kaback, H. R. and L. Guan. "It Takes Two to Tango: The Dance of the Permease." *J Gen Physiol* 151, no. 7 (2019): 878-886.
- Kabir, A., R. P. Honda, Y. O. Kamatari, S. Endo, M. Fukuoka and K. Kuwata. "Effects of Ligand Binding on the Stability of Aldo-Keto Reductases: Implications for Stabilizer or Destabilizer Chaperones." *Protein Sci* 25, no. 12 (2016): 2132-2141.
- Kabsch, W. "Xds." *Acta Crystallogr D Biol Crystallogr* 66, no. Pt 2 (2010): 125-32.
- Kantardjieff, K. A. and B. Rupp. "Matthews Coefficient Probabilities: Improved Estimates for Unit Cell Contents of Proteins, DNA, and Protein-Nucleic Acid Complex Crystals." *Protein Sci* 12, no. 9 (2003): 1865-71.
- Karena, E., E. Tatsaki, G. Lambrinidis, E. Mikros and S. Frillingos. "Analysis of Conserved Ncs2 Motifs in the *Escherichia Coli* Xanthine Permease Xanq." *Mol Microbiol* 98, no. 3 (2015): 502-17.

- Kawate, T. and E. Gouaux. "Fluorescence-Detection Size-Exclusion Chromatography for Precrystallization Screening of Integral Membrane Proteins." *Structure* 14, no. 4 (2006): 673-81.
- Khafizov, K., R. Staritzbichler, M. Stamm and L. R. Forrest. "A Study of the Evolution of Inverted-Topology Repeats from Leut-Fold Transporters Using Alignme." *Biochemistry* 49, no. 50 (2010): 10702-13.
- Klingenberg, Martin. "Ligand-Protein Interaction in Biomembrane Carriers. The Induced Transition Fit of Transport Catalysis." *Biochemistry* 44, no. 24 (2005): 8563-8570.
- Koshland, D. E. "Application of a Theory of Enzyme Specificity to Protein Synthesis." *Proceedings of the National Academy of Sciences of the United States of America* 44, no. 2 (1958): 98-104.
- Kosti, V., I. Papageorgiou and G. Diallinas. "Dynamic Elements at Both Cytoplasmically and Extracellularly Facing Sides of the Uapa Transporter Selectively Control the Accessibility of Substrates to Their Translocation Pathway." *J Mol Biol* 397, no. 5 (2010): 1132-43.
- Kotov, V., K. Bartels, K. Veith, I. Josts, U. K. T. Subramanyam, C. Gunther, J. Labahn, T. C. Marlovits, I. Moraes, H. Tidow, C. Low and M. M. Garcia-Alai. "High-Throughput Stability Screening for Detergent-Solubilized Membrane Proteins." *Sci Rep* 9, no. 1 (2019): 10379.
- Koukaki, M., A. Vlanti, S. Goudela, A. Pantazopoulou, H. Gioule, S. Tournaviti and G. Diallinas. "The Nucleobase-Ascorbate Transporter (Nat) Signature Motif in Uapa Defines the Function of the Purine Translocation Pathway." *J Mol Biol* 350, no. 3 (2005): 499-513.
- Kühlbrandt, Werner. "The Resolution Revolution." *Science* 343, no. 6178 (2014): 1443.
- Kuhn, B. T., I. Zimmermann, P. Egloff, L. M. Hurlimann, C. A. J. Hutter, C. Miscenic, R. J. P. Dawson, M. A. Seeger and E. R. Geertsma. "Biotinylation of Membrane Proteins for Binder Selections." *Methods Mol Biol* 2127, (2020): 151-165.
- Kunji, Edmund R. S., Marilyn Harding, P. Jonathan G. Butler and Pearl Akamine. "Determination of the Molecular Mass and Dimensions of Membrane Proteins by Size Exclusion Chromatography." *Methods* 46, no. 2 (2008): 62-72.
- Lemoine, F., D. Correia, V. Lefort, O. Doppelt-Azeroual, F. Mareuil, S. Cohen-Boulakia and O. Gascuel. "Ngphylogeny.Fr: New Generation Phylogenetic Services for Non-Specialists." *Nucleic Acids Res* 47, no. W1 (2019): W260-W265.
- Lichtenthaler, F. W. "100 Years@ Schlüssel Schlos" Prinzi : What Made Emil Fischer Use This Analogy?" *Angewandte Chemie* 33, (1995): 2364-2374.
- Liebschner, D., P. V. Afonine, M. L. Baker, G. Bunkoczi, V. B. Chen, T. I. Croll, B. Hintze, L. W. Hung, S. Jain, A. J. McCoy, N. W. Moriarty, R. D. Oeffner, B. K. Poon, M. G. Prisant, R. J. Read, J. S. Richardson, D. C. Richardson, M. D. Sammito, O. V. Sobolev, D. H. Stockwell, T. C. Terwilliger, A. G. Urzhumtsev, L. L. Videau, C. J. Williams and P. D. Adams. "Macromolecular Structure Determination Using X-Rays, Neutrons and Electrons: Recent Developments in Phenix." *Acta Crystallogr D Struct Biol* 75, no. Pt 10 (2019): 861-877.
- Lin, L., S. W. Yee, R. B. Kim and K. M. Giacomini. "Slc Transporters as Therapeutic Targets: Emerging Opportunities." *Nat Rev Drug Discov* 14, no. 8 (2015): 543-60.
- Lindenthal, S. and D. Schubert. "Monomeric Erythrocyte Band 3 Protein Transports Anions." *Proceedings of the National Academy of Sciences of the United States of America* 88, no. 15 (1991): 6540-6544.
- Lu, F., S. Li, Y. Jiang, J. Jiang, H. Fan, G. Lu, D. Deng, S. Dang, X. Zhang, J. Wang and N. Yan. "Structure and Mechanism of the Uracil Transporter Uraa." *Nature* 472, no. 7342 (2011): 243-6.
- Luo, P., X. Yu, W. Wang, S. Fan, X. Li and J. Wang. "Crystal Structure of a Phosphorylation-Coupled Vitamin C Transporter." *Nat Struct Mol Biol* 22, no. 3 (2015): 238-41.
- Luo, S., Z. Wang, M. Patel, V. Khurana, X. Zhu, D. Pal and A. K. Mitra. "Targeting Svct for Enhanced Drug Absorption: Synthesis and in Vitro Evaluation of a Novel Vitamin C Conjugated Prodrug of Saquinavir." *Int J Pharm* 414, no. 1-2 (2011): 77-85.

- Madeira, F., Y. M. Park, J. Lee, N. Buso, T. Gur, N. Madhusoodanan, P. Basutkar, A. R. N. Tivey, S. C. Potter, R. D. Finn and R. Lopez. "The EMBL-EBI Search and Sequence Analysis Tools APIs in 2019." *Nucleic Acids Res* 47, no. W1 (2019): W636-W641.
- Mancusso, R., G. G. Gregorio, Q. Liu and D. N. Wang. "Structure and Mechanism of a Bacterial Sodium-Dependent Dicarboxylate Transporter." *Nature* 491, no. 7425 (2012): 622-6.
- Marino, J., K. Holzhter, B. Kuhn and E. R. Geertsmā. "Efficient Screening and Optimization of Membrane Protein Production in *Escherichia Coli*." *Methods Enzymol* 594, (2017): 139-164.
- Matulis, Daumantas, James K. Kranz, F. Raymond Salemme and Matthew J. Todd. "Thermodynamic Stability of Carbonic Anhydrase: Measurements of Binding Affinity and Stoichiometry Using Thermofluor." *Biochemistry* 44, no. 13 (2005): 5258-5266.
- May, James M. "The Slc23 Family of Ascorbate Transporters: Ensuring That You Get and Keep Your Daily Dose of Vitamin C." *British journal of pharmacology* 164, no. 7 (2011): 1793-1801.
- McMahon, C., A. S. Baier, R. Pascolutti, M. Wegrecki, S. Zheng, J. X. Ong, S. C. Erlandson, D. Hilger, S. G. F. Rasmussen, A. M. Ring, A. Manglik and A. C. Kruse. "Yeast Surface Display Platform for Rapid Discovery of Conformationally Selective Nanobodies." *Nat Struct Mol Biol* 25, no. 3 (2018): 289-296.
- Michael Green, N. "[5] Avidin and Streptavidin." In *Methods in Enzymology*, edited by Meir Wilchek and Edward A. Bayer, 184, 51-67: Academic Press, 1990.
- Michel, Hartmut. "Crystallization of Membrane Proteins." In *Techniques and New Developments in Photosynthesis Research*, edited by J. Barber and R. Malkin, 11-15. Boston, MA: Springer US, 1989.
- Michels, A. J., T. M. Hagen and B. Frei. "Human Genetic Variation Influences Vitamin C Homeostasis by Altering Vitamin C Transport and Antioxidant Enzyme Function." *Annu Rev Nutr* 33, (2013): 45-70.
- Monod, Jacques, Jeffries Wyman and Jean-Pierre Changeux. "On the Nature of Allosteric Transitions: A Plausible Model." *Journal of Molecular Biology* 12, no. 1 (1965): 88-118.
- Moraes, I., G. Evans, J. Sanchez-Weatherby, S. Newstead and P. D. Stewart. "Membrane Protein Structure Determination - the Next Generation." *Biochim Biophys Acta* 1838, no. 1 Pt A (2014): 78-87.
- Moutel, S., N. Bery, V. Bernard, L. Keller, E. Lemesre, A. de Marco, L. Ligat, J. C. Rain, G. Favre, A. Olichon and F. Perez. "Nali-H1: A Universal Synthetic Library of Humanized Nanobodies Providing Highly Functional Antibodies and Intrabodies." *Elife* 5, (2016).
- Mulligan, C., C. Fenollar-Ferrer, G. A. Fitzgerald, A. Vergara-Jaque, D. Kaufmann, Y. Li, L. R. Forrest and J. A. Mindell. "The Bacterial Dicarboxylate Transporter Vcindy Uses a Two-Domain Elevator-Type Mechanism." *Nat Struct Mol Biol* 23, no. 3 (2016): 256-63.
- Nakanishi, T. and I. Tamai. "Solute Carrier Transporters as Targets for Drug Delivery and Pharmacological Intervention for Chemotherapy." *J Pharm Sci* 100, no. 9 (2011): 3731-50.
- Newby, Z. E., J. D. O'Connell, 3rd, F. Gruswitz, F. A. Hays, W. E. Harries, I. M. Harwood, J. D. Ho, J. K. Lee, D. F. Savage, L. J. Miercke and R. M. Stroud. "A General Protocol for the Crystallization of Membrane Proteins for X-Ray Structural Investigation." *Nat Protoc* 4, no. 5 (2009): 619-37.
- Newport, T. D., M. S. P. Sansom and P. J. Stansfeld. "The Memprotmd Database: A Resource for Membrane-Embedded Protein Structures and Their Lipid Interactions." *Nucleic Acids Res* 47, no. D1 (2019): D390-D397.
- Nicoludis, J. M. and R. Gaudet. "Applications of Sequence Coevolution in Membrane Protein Biochemistry." *Biochim Biophys Acta Biomembr* 1860, no. 4 (2018): 895-908.
- Niesen, F. H., H. Berglund and M. Vedadi. "The Use of Differential Scanning Fluorimetry to Detect Ligand Interactions That Promote Protein Stability." *Nat Protoc* 2, no. 9 (2007): 2212-21.
- Nizak, Clément, Sandrine Moutel, Bruno Goud and Franck Perez. "Selection and Application of Recombinant Antibodies as Sensors of Rab Protein Conformation." In *Methods in Enzymology*, 403, 135-153: Academic Press, 2005.

- Oliveira, Diogo, André M. Machado, Tiago Cardoso, Mónica Lopes-Marques, L. Filipe C. Castro and Raquel Ruivo. "Identification of a Novel Nucleobase-Ascorbate Transporter Family Member in Fish and Amphibians." *Fishes* 4, no. 1 (2019): 1.
- Padayatty, S. J., A. Katz, Y. Wang, P. Eck, O. Kwon, J. H. Lee, S. Chen, C. Corpe, A. Dutta, S. K. Dutta and M. Levine. "Vitamin C as an Antioxidant: Evaluation of Its Role in Disease Prevention." *J Am Coll Nutr* 22, no. 1 (2003): 18-35.
- Pardon, E., T. Laeremans, S. Triest, S. G. Rasmussen, A. Wohlkonig, A. Ruf, S. Muyldermans, W. G. Hol, B. K. Kobilka and J. Steyaert. "A General Protocol for the Generation of Nanobodies for Structural Biology." *Nat Protoc* 9, no. 3 (2014): 674-93.
- Pavic, A., A. O. M. Holmes, V. L. G. Postis and A. Goldman. "Glutamate Transporters: A Broad Review of the Most Recent Archaeal and Human Structures." *Biochem Soc Trans* 47, no. 4 (2019): 1197-1207.
- Perez, C., K. Khafizov, L. R. Forrest, R. Kramer and C. Ziegler. "The Role of Trimerization in the Osmoregulated Betaine Transporter Betp." *EMBO Rep* 12, no. 8 (2011): 804-10.
- Pettersen, E. F., T. D. Goddard, C. C. Huang, G. S. Couch, D. M. Greenblatt, E. C. Meng and T. E. Ferrin. "Ucsf Chimera--a Visualization System for Exploratory Research and Analysis." *J Comput Chem* 25, no. 13 (2004): 1605-12.
- Ponzoni, L., S. Zhang, M. H. Cheng and I. Bahar. "Shared Dynamics of LeuT Superfamily Members and Allosteric Differentiation by Structural Irregularities and Multimerization." *Philos Trans R Soc Lond B Biol Sci* 373, no. 1749 (2018).
- Quistgaard, E. M., C. Low, F. Guettou and P. Nordlund. "Understanding Transport by the Major Facilitator Superfamily (Mfs): Structures Pave the Way." *Nat Rev Mol Cell Biol* 17, no. 2 (2016): 123-32.
- Rask-Andersen, M., S. Masuram, R. Fredriksson and H. B. Schioth. "Solute Carriers as Drug Targets: Current Use, Clinical Trials and Prospective." *Mol Aspects Med* 34, no. 2-3 (2013): 702-10.
- Rasmussen, S. G., H. J. Choi, J. J. Fung, E. Pardon, P. Casarosa, P. S. Chae, B. T. Devree, D. M. Rosenbaum, F. S. Thian, T. S. Kobilka, A. Schnapp, I. Konetzki, R. K. Sunahara, S. H. Gellman, A. Pautsch, J. Steyaert, W. I. Weis and B. K. Kobilka. "Structure of a Nanobody-Stabilized Active State of the Beta(2) Adrenoceptor." *Nature* 469, no. 7329 (2011): 175-80.
- Rasmussen, S. G., B. T. DeVree, Y. Zou, A. C. Kruse, K. Y. Chung, T. S. Kobilka, F. S. Thian, P. S. Chae, E. Pardon, D. Calinski, J. M. Mathiesen, S. T. Shah, J. A. Lyons, M. Caffrey, S. H. Gellman, J. Steyaert, G. Skiniotis, W. I. Weis, R. K. Sunahara and B. K. Kobilka. "Crystal Structure of the Beta2 Adrenergic Receptor-Gs Protein Complex." *Nature* 477, no. 7366 (2011): 549-55.
- Redhead, M., R. Satchell, C. McCarthy, S. Pollack and J. Unitt. "Thermal Shift as an Entropy-Driven Effect." *Biochemistry* 56, no. 47 (2017): 6187-6199.
- Reithmeier, R. A., J. R. Casey, A. C. Kalli, M. S. Sansom, Y. Alguel and S. Iwata. "Band 3, the Human Red Cell Chloride/Bicarbonate Anion Exchanger (Ae1, Slc4a1), in a Structural Context." *Biochim Biophys Acta* 1858, no. 7 Pt A (2016): 1507-32.
- Reyes, N., C. Ginter and O. Boudker. "Transport Mechanism of a Bacterial Homologue of Glutamate Transporters." *Nature* 462, no. 7275 (2009): 880-5.
- Sambrook, Joseph and David W. Russell. *Molecular Cloning : A Laboratory Manual*. Cold Spring Harbor, N.Y.: Cold Spring Harbor Laboratory Press, 2001.
- Schenck, S., L. Kunz, D. Sahlender, E. Pardon, E. R. Geertsma, I. Savtchouk, T. Suzuki, Y. Neldner, S. Stefanic, J. Steyaert, A. Volterra and R. Dutzler. "Generation and Characterization of Anti-Vglut Nanobodies Acting as Inhibitors of Transport." *Biochemistry* 56, no. 30 (2017): 3962-3971.
- Schneider, C. A., W. S. Rasband and K. W. Eliceiri. "Nih Image to Imagej: 25 Years of Image Analysis." *Nat Methods* 9, no. 7 (2012): 671-5.

- Schumann, T., J. König, C. Henke, D. M. Willmes, S. R. Bornstein, J. Jordan, M. F. Fromm and A. L. Birkenfeld. "Solute Carrier Transporters as Potential Targets for the Treatment of Metabolic Disease." *Pharmacol Rev* 72, no. 1 (2020): 343-379.
- Scott, Duncan E., Christina Spry and Chris Abell. "Differential Scanning Fluorimetry as Part of a Biophysical Screening Cascade." *Fragment-based Drug Discovery Lessons and Outlook*, (2016): 139-172.
- Screpanti, E. and C. Hunte. "Discontinuous Membrane Helices in Transport Proteins and Their Correlation with Function." *J Struct Biol* 159, no. 2 (2007): 261-7.
- Seo, M. H., J. Park, E. Kim, S. Hohng and H. S. Kim. "Protein Conformational Dynamics Dictate the Binding Affinity for a Ligand." *Nat Commun* 5, (2014): 3724.
- Serrano-Vega, M. J., F. Magnani, Y. Shibata and C. G. Tate. "Conformational Thermostabilization of the Beta1-Adrenergic Receptor in a Detergent-Resistant Form." *Proc Natl Acad Sci U S A* 105, no. 3 (2008): 877-82.
- Shi, Y. "Common Folds and Transport Mechanisms of Secondary Active Transporters." *Annu Rev Biophys* 42, (2013): 51-72.
- Sigoillot, M., M. Overtus, M. Grodecka, D. Scholl, A. Garcia-Pino, T. Laeremans, L. He, E. Pardon, E. Hildebrandt, I. Urbatsch, J. Steyaert, J. R. Riordan and C. Govaerts. "Domain-Interface Dynamics of Cftr Revealed by Stabilizing Nanobodies." *Nat Commun* 10, no. 1 (2019): 2636.
- Smirnova, Irina N. and H. Ronald Kaback. "A Mutation in the Lactose Permease of Escherichia Coli That Decreases Conformational Flexibility and Increases Protein Stability." *Biochemistry* 42, no. 10 (2003): 3025-3031.
- Sonoda, Y., S. Newstead, N. J. Hu, Y. Alguet, E. Nji, K. Beis, S. Yashiro, C. Lee, J. Leung, A. D. Cameron, B. Byrne, S. Iwata and D. Drew. "Benchmarking Membrane Protein Detergent Stability for Improving Throughput of High-Resolution X-Ray Structures." *Structure* 19, no. 1 (2011): 17-25.
- Sotiriou, Sotiria, Suzana Gispert, Jun Cheng, Yaohui Wang, Amy Chen, Shelley Hoogstraten-Miller, Georgina F. Miller, Oran Kwon, Mark Levine, Susan H. Guttentag and Robert L. Nussbaum. "Ascorbic-Acid Transporter Slc23a1 Is Essential for Vitamin C Transport into the Brain and for Perinatal Survival." *Nature Medicine* 8, no. 5 (2002): 514-517.
- Steyaert, J. and B. K. Kobilka. "Nanobody Stabilization of G Protein-Coupled Receptor Conformational States." *Curr Opin Struct Biol* 21, no. 4 (2011): 567-72.
- Strong, M., M. R. Sawaya, S. Wang, M. Phillips, D. Cascio and D. Eisenberg. "Toward the Structural Genomics of Complexes: Crystal Structure of a Pe/Ppe Protein Complex from Mycobacterium Tuberculosis." *Proc Natl Acad Sci U S A* 103, no. 21 (2006): 8060-5.
- Tereshko, V., S. Uysal, A. Koide, K. Margalef, S. Koide and A. A. Kossiakoff. "Toward Chaperone-Assisted Crystallography: Protein Engineering Enhancement of Crystal Packing and X-Ray Phasing Capabilities of a Camelid Single-Domain Antibody (Vhh) Scaffold." *Protein Sci* 17, no. 7 (2008): 1175-87.
- Thurtle-Schmidt, B. H. and R. M. Stroud. "Structure of Bor1 Supports an Elevator Transport Mechanism for Slc4 Anion Exchangers." *Proc Natl Acad Sci U S A* 113, no. 38 (2016): 10542-6.
- Ting, D., G. Wang, M. Shapovalov, R. Mitra, M. I. Jordan and R. L. Dunbrack, Jr. "Neighbor-Dependent Ramachandran Probability Distributions of Amino Acids Developed from a Hierarchical Dirichlet Process Model." *PLoS Comput Biol* 6, no. 4 (2010): e1000763.
- Uchański, Tomasz, Simonas Masiulis, Baptiste Fischer, Valentina Kalichuk, Alexandre Wohlkönig, Thomas Zögg, Han Remaut, Wim Vranken, A. Radu Aricescu, Els Pardon and Jan Steyaert. "Megabodies Expand the Nanobody Toolkit for Protein Structure Determination by Single-Particle Cryo-Em." *bioRxiv*, (2019): 812230.
- Virant, David, Bjoern Traenkle, Julia Maier, Philipp D. Kaiser, Mona Bodenhöfer, Christian Schmees, Ilijana Vojnovic, Borbála Pisak-Lukáts, Ulrike Endesfelder and Ulrich Rothbauer. "A Peptide Tag-Specific Nanobody Enables High-Quality Labeling for Dstorm Imaging." *Nature Communications* 9, no. 1 (2018): 930.

- Vivoli, M., H. R. Novak, J. A. Littlechild and N. J. Harmer. "Determination of Protein-Ligand Interactions Using Differential Scanning Fluorimetry." *J Vis Exp*, no. 91 (2014): 51809.
- vonHeijne, Gunnar. "Control of Topology and Mode of Assembly of a Polytopic Membrane Protein by Positively Charged Residues." *Nature* 341, no. 6241 (1989): 456-458.
- Voss, N. R. and M. Gerstein. "3v: Cavity, Channel and Cleft Volume Calculator and Extractor." *Nucleic Acids Res* 38, no. Web Server issue (2010): W555-62.
- Walter, J. D., M. Sawicka and R. Dutzler. "Cryo-Em Structures and Functional Characterization of Murine Reveal Mechanism of Uncoupled Chloride Transport." *Elife* 8, (2019).
- Wang, C., B. Sun, X. Zhang, X. Huang, M. Zhang, H. Guo, X. Chen, F. Huang, T. Chen, H. Mi, F. Yu, L. N. Liu and P. Zhang. "Structural Mechanism of the Active Bicarbonate Transporter from Cyanobacteria." *Nat Plants* 5, no. 11 (2019): 1184-1193.
- Wang, W. W., L. Gallo, A. Jadhav, R. Hawkins and C. G. Parker. "The Druggability of Solute Carriers." *J Med Chem* 63, no. 8 (2020): 3834-3867.
- Wang, Xiaoyu and Olga Boudker. "Large Domain Movements through Lipid Bilayer Mediate Substrate Release and Inhibition of Glutamate Transporters." *bioRxiv*, (2020): 2020.05.19.103432.
- Waterhouse, A., M. Bertoni, S. Bienert, G. Studer, G. Tauriello, R. Gumienny, F. T. Heer, T. A. P. de Beer, C. Rempfer, L. Bordoli, R. Lepore and T. Schwede. "Swiss-Model: Homology Modelling of Protein Structures and Complexes." *Nucleic Acids Res* 46, no. W1 (2018): W296-W303.
- Wei, H., J. Mo, L. Tao, R. J. Russell, A. A. Tymiak, G. Chen, R. E. Iacob and J. R. Engen. "Hydrogen/Deuterium Exchange Mass Spectrometry for Probing Higher Order Structure of Protein Therapeutics: Methodology and Applications." *Drug Discov Today* 19, no. 1 (2014): 95-102.
- Winn, M. D., C. C. Ballard, K. D. Cowtan, E. J. Dodson, P. Emsley, P. R. Evans, R. M. Keegan, E. B. Krissinel, A. G. Leslie, A. McCoy, S. J. McNicholas, G. N. Murshudov, N. S. Pannu, E. A. Pottertson, H. R. Powell, R. J. Read, A. Vagin and K. S. Wilson. "Overview of the Ccp4 Suite and Current Developments." *Acta Crystallogr D Biol Crystallogr* 67, no. Pt 4 (2011): 235-42.
- Wohlert, D., M. J. Grotzinger, W. Kuhlbrandt and O. Yildiz. "Mechanism of Na(+)-Dependent Citrate Transport from the Structure of an Asymmetrical Cits Dimer." *Elife* 4, (2015): e09375.
- Wohlrab, C., E. Phillips and G. U. Dachs. "Vitamin C Transporters in Cancer: Current Understanding and Gaps in Knowledge." *Front Oncol* 7, (2017): 74.
- Wu, H., G. Beuerlein, Y. Nie, H. Smith, B. A. Lee, M. Hensler, W. D. Huse and J. D. Watkins. "Stepwise in Vitro Affinity Maturation of Vitaxin, an Alphav Beta3-Specific Humanized Mab." *Proceedings of the National Academy of Sciences of the United States of America* 95, no. 11 (1998): 6037-6042.
- Yamashita, A., S. K. Singh, T. Kawate, Y. Jin and E. Gouaux. "Crystal Structure of a Bacterial Homologue of Na+/Cl⁻-Dependent Neurotransmitter Transporters." *Nature* 437, no. 7056 (2005): 215-23.
- Yan, N. "A Glimpse of Membrane Transport through Structures-Advances in the Structural Biology of the Glut Glucose Transporters." *J Mol Biol* 429, no. 17 (2017): 2710-2725.
- Yernool, Dinesh, Olga Boudker, Yan Jin and Eric Gouaux. "Structure of a Glutamate Transporter Homologue from *Pyrococcus Horikoshii*." *Nature* 431, no. 7010 (2004): 811-818.
- Yin, Yong, Xiao He, Paul Szewczyk, That Nguyen and Geoffrey Chang. "Structure of the Multidrug Transporter Emrd from *Escherichia Coli*." *Science (New York, N.Y.)* 312, no. 5774 (2006): 741-744.
- Yoshida, T., N. Yasui, Y. Kusakabe, C. Ito, M. Akamatsu and A. Yamashita. "Differential Scanning Fluorimetric Analysis of the Amino-Acid Binding to Taste Receptor Using a Model Receptor Protein, the Ligand-Binding Domain of Fish T1r2a/T1r3." *PLoS One* 14, no. 10 (2019): e0218909.
- Yu, X., G. Yang, C. Yan, J. L. Baylon, J. Jiang, H. Fan, G. Lu, K. Hasegawa, H. Okumura, T. Wang, E. Tajkhorshid, S. Li and N. Yan. "Dimeric Structure of the Uracil:Proton Symporter Uraa Provides Mechanistic Insights into the Slc4/23/26 Transporters." *Cell Res* 27, no. 8 (2017): 1020-1033.

-
- Zhang, Y., Y. Zhang, K. Sun, Z. Meng and L. Chen. "The Slc Transporter in Nutrient and Metabolic Sensing, Regulation, and Drug Development." *J Mol Cell Biol* 11, no. 1 (2019): 1-13.
- Zhou, W., G. Fiorin, C. Anselmi, H. A. Karimi-Varzaneh, H. Poblete, L. R. Forrest and J. D. Faraldo-Gomez. "Large-Scale State-Dependent Membrane Remodeling by a Transporter Protein." *Elife* 8, (2019).
- Zimmermann, I., P. Egloff, C. A. Hutter, F. M. Arnold, P. Stohler, N. Bocquet, M. N. Hug, S. Huber, M. Siegrist, L. Hetemann, J. Gera, S. Gmur, P. Spies, D. Gyax, E. R. Geertsma, R. J. Dawson and M. A. Seeger. "Synthetic Single Domain Antibodies for the Conformational Trapping of Membrane Proteins." *Elife* 7, (2018).
- Zimmermann, I., P. Egloff, C. A. J. Hutter, B. T. Kuhn, P. Brauer, S. Newstead, R. J. P. Dawson, E. R. Geertsma and M. A. Seeger. "Generation of Synthetic Nanobodies against Delicate Proteins." *Nat Protoc* 15, no. 5 (2020): 1707-1741.
- Zomot, E. and I. Bahar. "Intracellular Gating in an Inward-Facing State of Aspartate Transporter Glt(Ph) Is Regulated by the Movements of the Helical Hairpin Hp2." *J Biol Chem* 288, no. 12 (2013): 8231-7.

List of abbreviations

2HCT	2-Hydroxycarboxylate Transporter
7-TMIR	7-transmembrane segment inverted repeat
<i>A. aeolicus</i>	Aquifex aeolicus
<i>A. nidulans</i>	Aspergillus nidulans
ABC transporter	ATP binding cassette transporter
AbgT	p-Aminobenzoyl-glutamate Transporter
ADP	Adenosine diphosphate
AEBSF	4-(2-aminoethyl)benzenesulfonyl fluoride hydrochloride
APC	Amino Acid-Polyamine-Organocation
APS	Ammonium persulfate
ATP	Adenosine triphosphate
<i>B. subtilis</i>	Bacillus subtilis
Cam	chloramphenicol
cDNA	complementary DANN
CDR	complementarity determining region
CPM	7-Diethylamino-3-(4'-Maleimidylphenyl)-4-Methylcoumarin
cryo-EM	cryogenic electron microscopy
Cysless	cysteine free
DDM	n-dodecyl- β -D-maltopyranoside
dHDX	differential hydrogen-deuterium exchange
DM	n-decyl- β -D-maltopyranoside
DMSO	Dimethyl sulfoxide
DNA	Deoxyribonucleic acid
dNTPs	Deoxyribonucleoside Triphosphate
DPPC	Dipalmitoylphosphatidylcholine
DSF	differential scanning fluorimetry
DTT	dithiothreitol
<i>E. coli</i>	Escherichia coli
ELISA	enzyme linked immunosorbent assay
Fab fragment	antigen binding fragment
for	forward

FSEC	Fluorescence-Detection Size-Exclusion Chromatography
GFP	green fluorescent protein
GPCR	G-protein coupled receptor
<i>H. pylori</i>	Helicobacter. pylori
<i>H. sapiens</i>	Homo sapiens
HCAb IgG	heavy-chain Immunoglobulin G
HDX	hydrogen-deuterium exchange
HEPES	(4-(2-hydroxyethyl)-1-piperazineethanesulfonic acid)
HPLC	high-performance liquid chromatography
HRP	horseradish peroxidase
HRV-3C protease	Human rhinovirus 3C protease
IgG	Immunoglobulin G
IMAC	immobilized metal affinity chromatography
IOV	inside-out membrane vesicles
IPTG	Isopropyl β -D-1-thiogalactopyranoside
KPi	potassium phosphate
<i>L. lactis</i>	Lactococcus lactis
LB	lysogeny broth
LLG	log-likelihood gain
<i>M. tuberculosis</i>	Mycobacterium tuberculosis
MES	2-(N-Morpholino)ethansulfonsäure
MFS	Major faciliator superfamily
MS	mass spectrometry
MWCO	molecular weight cutoff
<i>N. wadsworthii</i>	Neisseria wadsworthii
NaPi	sodium phosphate
NAT	Nucleobase ascorbate transporter
NCS2	Nucleobase cation symporter-2
NG	n-nonyl- β -D-glucoside
Ni-NTA	Nickel nitrilotriacetic acid
OD600	optical density at a wavelength of 600 nm
OG	n-octyl- β -D-glucoside
<i>P. denitrificans</i>	Paracoccus denitrificans
<i>P. horikoshii</i>	Pyrococcus horikoshii
PBS	phosphate buffered saline
PCR	polymerase chain reaction
PDB	protein database
PEG-400	polyethylene glycol 400
PEG-5000	polyethylene glycol 5000
PEG-8000	polyethylene glycol 8000
PMSF	phenylmethylsulfonyl fluoride
PTS system	phosphotransferase system
PVDF	Polyvinylidene fluoride
PVT	polyvinyl toluene
rev	reverse
RMSD	root mean square deviation
RNA	ribonucleic acid
<i>S. enterica</i>	Salmonella enterica
scFv	single-chain variable fragment
SDS	sodium dodecyl sulfate
SDS-PAGE	sodium dodecyl sulfate–polyacrylamide gel electrophoresis
SEC	size exclusion chromatography
SLC	Solute carrier
SLS	Swiss Light Source

Soy PC	L- α -phosphatidylcholine from soy
SPA	scintillation proximity assay
SVCT	sodium-dependent vitamin C transporter
<i>T. maritima</i>	<i>Thermotoga maritima</i>
<i>T. thermophilus</i>	<i>Thermus thermophilus</i>
TAE	TRIS-Acetate-EDTA
TB	terrific broth
TEMED	Tetramethylethylenediamine
TFZ	translation function Z
TLS	Translation-Libration-Screw-rotation model
T _m	melting temperature
TM	transmembrane segment
Tris	tris(hydroxymethyl)aminomethane
WT	wildtype

Declaration of collaborative work

Except where stated otherwise by reference or acknowledgment, the work presented was generated by myself under the supervision of my advisor during my doctoral studies. All contributions from colleagues are explicitly referenced in the thesis. The materials listed below was obtained in the context of collaborative research with following people.

Figure 9: Alpaca immunization – sample preparation and immune response. Sample preparation was performed in collaboration with Katharina Holzhüter as part of her Master studies. Immunizations were performed by Saša Štefanić from the Nanobody Service Facility, University of Zurich, Switzerland. I performed the ELISA for immune response analysis.

Figure 11: Phage display selection of nanobodies against UraA_{WT} and output analysis by ELISA. Preparation of alpaca immune libraries from isolated B-lymphocytes was performed by Katharina Holzhüter including isolation of mRNA and its conversion to cDNA, PCR amplification and cloning into the pDX phagemid and transformation into *E. coli* TG1. I prepared phages and antigens and performed phage display selections and the ELISA.

Figure 13: ELISA based binding analysis of selected sybodies. Sybody selection and output analysis by ELISA was performed by Prof. Dr. Eric R. Geertsma in collaboration with Iwan Zimmermann, Institute of Medical Microbiology, University of Zurich, Switzerland. I prepared the antigens used for selection.

Figure 15: Thermal stabilization of UraA_{WT} by selected nanobodies and sybodies. Expression and purification of Sybodies für initial analysis was performed by Prof. Dr. Eric R. Geertsma in collaboration with Iwan Zimmermann, Institute of Medical Microbiology, University of Zurich, Switzerland. I purified all alpaca derived nanobodies and performed the melting curve analysis.

Figure 19: Functional analysis of inter-domain linker variants. Mutagenesis of the UraA variants G112P, P121G, G320P and P330G was performed by Dogukan Özkul as part of his Master studies. The UraA variants A111P, T113P, G114P and W115P were created by Sebastian Falkner. Katharina Holzhüter prepared the UraA-E241A-H245A-E290A mutant that was used as negative control. I created the UraA variants K110G, G320A and P330A and performed the transport assay and expression controls.

Figure 20: Purification of inter-domain linker variants of UraA. Purification of UraA_{G112P} was performed by Dogukan Özkul as part of his Master studies. I purified the UraA variants UraA_{WT}, UraA_{G320P} and UraA_{P330G}.

Figure 22: Substrate binding site accessibility analysis by specific cysteine labeling. The cysteine accessibility assay was performed by Tim Gemeinhardt as part of his Master studies. I created the UraA variants UraA_{Cysless}, UraA_{Cysless-A31C}, UraA_{Cysless-M143C} and UraA_{Cysless-A31C-G320P}. I further produced and purified UraA_{Cysless} and UraA_{Cysless-M143C}.

Figure 23: Scintillation proximity assay of UraA_{WT}, UraA_{G320P}. Scintillation proximity assay was performed in collaboration with Niko Schenck as part of his Master studies. Niko Schenck performed the SPA measurements. I produced the UraA-variants UraA_{WT}-Avi and UraA_{G320P}-Avi.

Figure 24: Co-crystallization of UraA_{G320P} and Sy45. Pipetting of crystallization plates for initial crystallization screening was performed by Barbara Rathmann from the MPI of Biophysics, Frankfurt. I prepared the proteins for crystallization and the crystallization screen.

Figure 25: Co-crystallization of UraA_{G320P} and Sy5. Pipetting of crystallization plates for initial crystallization screening was performed by Barbara Rathmann from the MPI of Biophysics, Frankfurt. I prepared the proteins for crystallization and the crystallization screen.

Figure 34: Differential HDX-MS of UraA_{WT}. All dHDX measurements were performed by Jonathan Zöllner from the MPI of Biophysics, Frankfurt. I prepared the UraA_{WT} protein sample.

Figure 35: Differential HDX-MS of UraA_{G320P}. All dHDX measurements were performed by Jonathan Zöllner from the MPI of Biophysics, Frankfurt. I prepared the UraA_{G320P} protein sample.

Figure 36: Differential HDX-MS of UraA_{P330G}. All dHDX measurements were performed by Jonathan Zöllner from the MPI of Biophysics, Frankfurt. I prepared the UraA_{P330G} protein sample.

Figure 37: Differential HDX of UraA_{G320P} and UraA_{P330G} in comparison to UraA_{WT}. All dHDX measurements were performed by Jonathan Zöllner from the MPI of Biophysics, Frankfurt. I prepared the UraA_{WT}, UraA_{G320P} and UraA_{P330G} protein samples.

Supplementary figure 15: Scintillation proximity assay of UraA_{P330G}. Scintillation proximity assay was performed in collaboration with Niko Schenck as part of his Master studies. Niko Schenck produced the UraA-variant UraA_{P330G}-Avi and performed the SPA measurements as part of his Master studies.

Supplementary figure 16: uracil affinity of UraA_{WT} in presence or absence of Sy45 by saturation binding assay. Scintillation proximity assay was performed together with Niko Schenck as part of his Master studies. Niko Schenck prepared the scintillation beads and performed the measurements. I prepared UraA_{WT}-Avi, Sy45 and the uracil substrate stocks.

List of publications

Hofmann, S., D. Januliene, A. R. Mehdipour, C. Thomas, E. Stefan, S. Bruchert, B. T. Kuhn, E. R. Geertsma, G. Hummer, R. Tampe and A. Moeller. "Conformation Space of a Heterodimeric Abc Exporter under Turnover Conditions." *Nature* 571, no. 7766 (2019): 580-583.

Kuhn, B. T., I. Zimmermann, P. Egloff, L. M. Hurlimann, C. A. J. Hutter, C. Miscenic, R. J. P. Dawson, M. A. Seeger and E. R. Geertsma. "Biotinylation of Membrane Proteins for Binder Selections." *Methods Mol Biol* 2127, (2020): 151-165.

Marino, J., K. Holzhter, B. Kuhn and E. R. Geertsma. "Efficient Screening and Optimization of Membrane Protein Production in Escherichia Coli." *Methods Enzymol* 594, (2017): 139-164.

Zimmermann, I., P. Egloff, C. A. J. Hutter, B. T. Kuhn, P. Brauer, S. Newstead, R. J. P. Dawson, E. R. Geertsma and M. A. Seeger. "Generation of Synthetic Nanobodies against Delicate Proteins." *Nat Protoc* 15, no. 5 (2020): 1707-1741.

Acknowledgements

First of all, I want to thank my supervisor Prof. Dr. Eric R. Geertsma for the opportunity to join his group for my PhD and all the scientific advice and discussions and granted experimental freedom. Your careful supervision was a massive support.

I want to thank Prof. Dr. Klaas Martinus Pos for sharing instruments and lab space but also for scientific advice during the group seminars.

I want to thank Prof. Dr. Volker Dötsch, for accepting my invitation as a second thesis reviewer.

Many thanks to Beate Braungart for keeping all the paperwork under control and taking care of all non-scientific and personal things.

I like to thank all my colleagues from the Geertsma, Pos and Hänel lab for the nice working atmosphere, scientific discussions and for all the fun had together. Especially, I like to thank Dr. Nita Chang, Katharina Holzhüter, Anja Roden, Melanie Engelin, Dr. Viveka Nand Malvia and Dr. Jenifer Cuesta Bernal.

Special thanks in addition to Katharina Holzhüter for creation of immune libraries and all kind of UraA related discussions and assay optimizations.

Thanks to Barbara Rathmann and Dr. Yvonne Thielmann for help in crystallization plate pipetting.

Thanks to Jonathan Zöller and Dr. Julian Langer for the fruitful HDX collaboration.

I like to thank Dr. Igor Tascon and Dr. Denys Pogoryelov for advice in protein crystallography and structural biology and for organization of synchrotron trips. Many thanks to all participants of the synchrotron trips especially to Igor, Yvonne, Julia and Charlotte. I am glad we survived the exhausting long rides on the german highway.

I further like to thank my former Master students Katharina Holzhüter, Tobias Primke, Alexandra Bork, Dogukan Özkul, Tim Gemeinhardt and Niko Schenk. It was a pleasure to have you in the lab. Special thanks to Katharina, Dogukan, Tim and Niko for the lively scientific discussions and your experimental contribution to this study.

I want to thank my family and especially my parents for ongoing support throughout my scientific career. I finally want to thank my partner Annette and our daughter Charlotte for giving me strength and joy. You make our home a peaceful place.